DOCTORAL THESIS

Design of a Novel Spillway Turbine and Optimisation of Its Intake Hydrodynamics

Filipa Adžić

Hydro-Environmental Research Centre

School of Engineering

Cardiff University

Supervised by:

Prof. Thorsten Stoesser and Dr. Zhihua Xie

*A thesis submitted in fulfilment of the requirements
for the degree of Doctor of Philosophy*

November 6, 2020

"True knowledge exists in knowing that you know nothing.."

-Socrates

To my mother Mirela

Acknowladgements

First and foremost, I would like to express my deepest gratitude to my supervisor, Prof. Thorsten Stoesser for giving me an opportunity to do this PhD project. As I was only 21 years old at the time he offered me this project, I can truly say that not only I advanced in an academic sense but I also gained confidence and learned true professionalism under his supervision. I appreciate the motivation and encouragement through difficult and good periods of this project. Many thanks to my second supervisor Dr. Zhihua Xie who always found time to provide valuable guidance at times when I doubted myself most. I cannot express how lucky I feel that I had to chance to work with both and I believe that this project would not come to a positive conclusion without their supervision and encouragement.

Many thanks to Emily and Emrgy Inc. who kindly funded this project along with Cardiff University. Also I would like to acknowledge the support of the Supercomputing Wales, who provided all the super-computing power required in this project.

A big thank you to Dr. Stefan Runge, as without his initiative I would not apply for this project. Thank you Stefan for always supporting me and teaching me everything about the laboratory and Solidworks. I would also like to thank Pablo, Richard and Ken for teaching me how to code and use Hydro-3D. I would also like say thanks to Paul, Harry and Gareth for all the help during the set up of experiments. A big thank you to all the staff from the Research and Finance offices, you're help with administrative work was very valuable.

Above all, I would like to thank my mother Mirela to whom I dedicate this thesis. She always believed in my passion to learn and gave me an opportunity to get the best education possible. It took a great amount of courage from her and after 10 years of me leaving home, I can just begin to comprehend it now. Thank you to my brother Danilo and my father Dejan who always believed in me and are truly proud of any success I achieve.

I would also like to express gratitude to my friends from back home Anja S. and Anja R. who were such a support during the COVID-19 lockdown during which I wrote this thesis. A big thank you to Holly, Sanaya and Grace for always being there for me, I could not wish for better friends. All have given me immense encouragement and great emotional support for years.

Thank you to all my colleagues and friends Arthur, Nefeli, Giovanni, Guile, Laura, Jelena, Andjela, Asma, Milos, Claudia, Ben, Lucy, Aristos, Stefani,

Valentine, Sam, Richard, Aaron, Luke and Emanuela. I have learned so much from each of you.

Cardiff, 2020

Filipa Adzic

Abstract

The motivation to expand electricity production from renewable energy sources exists worldwide. A novel, horizontal axis, spillway turbine that attempts to convert high-speed, supercritical flow in steeply sloped channels into electricity is presented in this thesis. The spillway turbine is intended for use in low-head, low-flow, man-made, concrete-lined channels such as chutes, spillways and other similar steeply sloped open-channels. The design of the spillway turbine is inspired by the impulse turbine runner but without a pipe or a nozzle.

The spillway turbine presented in this thesis consists of the runner and the accelerator channel/wedge that is used to direct the water towards and through the channel blades. The runner design process shows that once the runner is fitted with Pelton-inspired inserts, performance improves both in terms of efficiency and specific speeds. The specific speed and the speed factors calculated confirm that this novel spillway turbine can be categorised as an impulse turbine. The maximum performance efficiency obtained is 43.3 %.

The observations made during laboratory testing indicate that the accelerator channel in the final design version could be improved in terms of energy losses inside it if the insight into the hydrodynamics of the flow can be gained. This is the motivation for computational fluid dynamics research into the hydrodynamics of the flow through a contraction.

The in-house large-eddy simulation (LES) code Hydro-3D is employed to simulate supercritical flow in a straight-wall, open-channel contraction. The initial channel contraction angle simulated is 6°, and the ratio of contraction is 2:1, which is the same ratio used in the final accelerator channel design. The LES code solves the filtered Navier-Stokes equations for two-phase flows and uses the level-set method to track the interface between water and air. Overall, a satisfactory agreement of simulated results with experimental data is obtained. Contours of the time-averaged velocities indicate that the flow loses energy and momentum in the contracting channel. The effect of different contraction angles is analysed, and recommendations from numerical simulation research are implemented in the field application prototype of the spillway turbine.

Publications

Journal Articles

1. Adzic, F. Stoesser, T., Morris, E. and Runge, S. Design and performance of a novel spillway turbine. *Journal of Power and Energy Engineering, 8. 14-31.*

2. Adzic, F. Xie, Z. and Stoesser, T. LES of supercritical free-surface flow in an open-channel contraction.*Journal of Hydraulic Research-in Peer Review.*

Reports to Industry Sponsor (confidential)

1. Adzic, F. Stoesser, T. Runge, S. Morris, E. Initial design and performance of a novel spillway turbine. August 2017.

2. Adzic, F. Stoesser, T. Runge, S. Morris, E. Design revision of a novel spillway turbine. December 2017.

3. Adzic, F. Stoesser, T. Runge, S. Morris, E. Design and performance of a novel spillway turbine. August 2018.

4. Adzic, F. Stoesser, T., Morris, E. Titanchi flume and spillway turbine design report. August 2019.

Contents

List of Figures

List of Tables

Nomenclature

ω	Rotational velocity
Φ	Speed factor
ρ	Density
τ	Bed shear stress
A	Cross-sectional area
C_p	Pressure coefficient
C_{pd}	Form drag coefficient
Cp	Power coefficient
D	Diameter
d	Distance function
F	Froude number
F_d	Frictional surface force
F_I	Impact force
F_n	Normal surface force
F	Viscous drag force
F_{co}	Coriolis force
F_{ct}	Centrifugal force
F_p	Form drag force
H	Head
h	Water depth
h_l	Head loss
L	Reference length scale
N	Rotational speed
N_s	Specific speed
P	Power
Q	Discharge
R_e	Reynolds number

$s_{(d0)}$	Smooth sign function
T	Torque
t_a	Artificial time
t_e	Eddy turnover time
tke	Turbulent kinetic energy
U	Time-averaged streamwise flow velocity
$u'u'$	Streamwise normal Reynolds stress
$u'w'$	Primary normal Reynolds stress
u_*	Shear velocity
U_{bulk}	Bulk velocity
V	Time-averaged spanwise flow velocity
$v'v'$	Spanwise normal Reynolds stress
C_f	Friction coefficient
f	Force from immersed boundary points
g	Gravitational acceleration
t	Time
$\nabla\tau$	Sub-grid scale stress tensor
Γ	Interface between gas and liquid domains
Ω_{gas}	Gas fluid domain
Ω_{liquid}	Liquid fluid domain
$H_{(\phi)}$	Single grid space
K_l	Head loss coefficient
$\bar{p}$	Filtered pressure
$\bar{u}$	Filtered velocity vector
ϕ	Level-set distance function
ε_r	Single grid space
ε	Half thickness of the interface
μ_g	Dynamic viscosity of gas
μ_l	Dynamic viscosity of liquid
μ	Dynamic viscosity
ν	Kinematic viscosity
ρ_g	Density of gas
ρ_l	Density of liquid

Chapter 1

Introduction

1.1 Motivation

Population growth and its effects on the world have become a trending topic, often mentioned in conjunction with increasing pollution of the environment and climate change. The world population has reached 7.2 billion in 2014, and it is predicted to reach approximately 9.6 billion by 2050 if current growth trends are applied (Gerland et al., 2014). It is in human nature to continually seek ways to make everyday life more convenient. Finding ways to access information quickly, to easily communicate with each other, to achieve new medical breakthroughs and to improve transport have led to fast and ever-increasing development of technology through history. As Nicola Tesla wrote in 1919 "*Invention is the most important product of man's creative brain. The ultimate purpose is the complete mastery of mind over the material world, the harnessing of human nature to human needs*" (Tesla, 1919). From the invention of the wheel, the clock, the steam engine, the electric battery, to the design of the modern computer, it is clear that the technology is evolving rapidly, especially since humans found novel ways to extract energy from nature and use it to fuel transportation and communication industries. With the rapid and constant development of technology, 21st century society has become tremendously dependant on electricity production. Breakdown of the largest consumers of electricity from 2016 is shown in Figure 1.1.

Energy sources can be classified as clean or environmentally damaging. Electricity is commonly produced from nuclear fission, burning fossil fuels or renewable energy sources. Although nuclear fission is clean in terms of greenhouse gas emissions, the debate of its sustainability is long-standing. Firstly, the financial and environmental cost of safely decommissioning nuclear plants is often unpredictable. The possibility of a nuclear incident cannot be neglected even
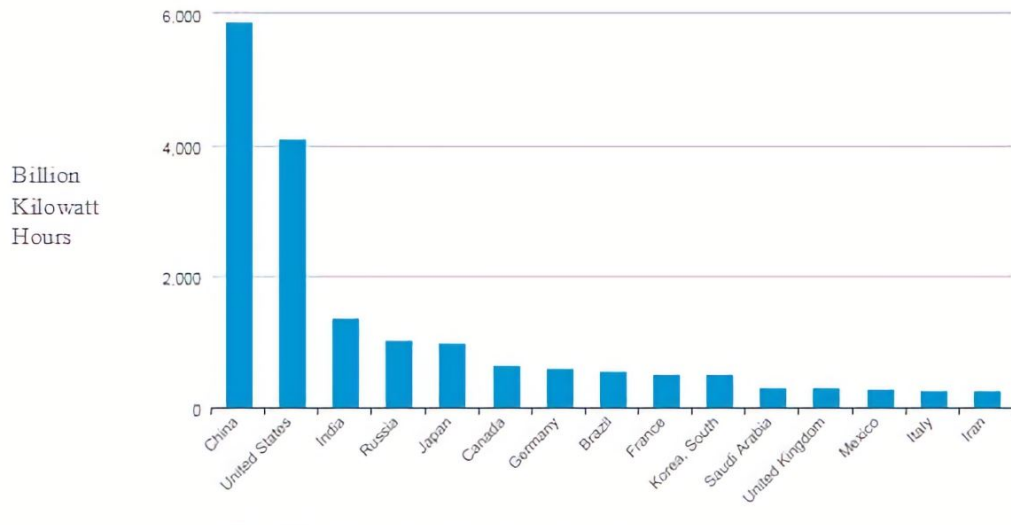
FIGURE 1.1: Energy consumption by country in 2016 (Eia.gov, 2019)

though safety has been considerably improved over the years. The sustainability of nuclear fission plants is also in question when the amounts of harvestable uranium deposits are considered. However, investment in nuclear fission plants is one of the prevalent political debates of our time, with countries of the world making different decisions on this matter. Burning fossil fuels such as coal, gas and oil also commonly used for electricity production. Coal is the cheapest of all fossil fuels as its more accessible and larger quantities are available comparing to gas and oil reserves. Although it is the most affordable, it is also the biggest polluter because it releases large amounts of methane when burned. Oil and gas also release carbon dioxide into the atmosphere during combustion, but only half the cost of coal combustion produces. According to Shafiee & Topal (2009), it is predicted that the oil reserves will deplete in about 40 years, gas reserves in nearly 70 years and coal reserves will diminish in about 200 years.

Producing electricity from renewable sources such as sun, wind, and water has been on the rise in the last couple of decades. The popularity of such methods of electricity production comes from the desire to reduce negative human impact on the environment. In other words, renewable energy sources are considered clean as no greenhouse gasses are emitted into the atmosphere when electricity is produced. The pie chart of how much electricity was generated from each source in 2018 is shown in Figure 1.2.

As can be noted, 64% of electricity was produced from burning fossil fuels. Due
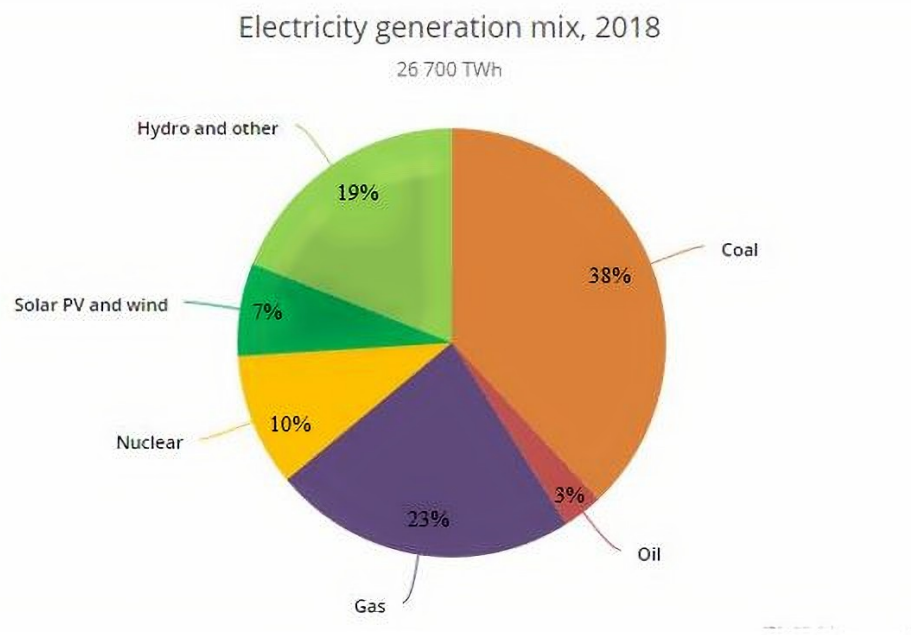
FIGURE 1.2: Energy production from different sources (Iea.org, 2019)

to the rise of electricity demand in China, India and the United States, a historical peak of 33.1 GT of CO_2 emissions were measured as a result of fossil fuel burning. The power sector is thought to be responsible for two-thirds of those emissions in 2018 (Iea.org, 2019). Some countries such as France, Germany, United Kingdom, Japan and Mexico have recorded declining CO_2 emissions due to the switch from fossil fuels to nuclear and renewable energy sources. The International Energy Agency stated that burning fossil fuels increases global annual average surface temperatures by 0.3°C to 1°C, which makes coal combustion the most significant contributor to global temperature rises.

Several international agreements addressing climate change have been put in place. The Paris Agreement (United Nations, 2016) was signed by 200 countries that focus on greenhouse gas emissions and keeping global temperatures in check. European Union Directive (European Commission, 2009) was put in place in 2009, and it set an objective for all parties involved to produce at least 20% of energy from renewable energy sources by 2020. This directive was updated in 2014, proposing to increase energy produced from renewable energy sources to at least 27% by 2030 (Eurpean Commission, 2019).

To sum up, the motivation behind the work presented in this thesis comes from a difficult question: How to fulfil world energy demands with minimal environmental harm sustainably? Population growth and ongoing technological revolution cause rising energy demands of modern society, and these demands

are answered with a mix of energy sources. The majority of the world population is to some extend aware of how electricity generation influences climate change; hence international agreements and objectives have been set in place. Research, development and improvement of old and new tools for electricity generation from renewable energy sources is of great importance, as the world is turning to a greener and less polluted future. Although the focus of this research is on hydraulic turbine technology and hydropower, available renewable energy sources are briefly discussed in the following section.

Emrgy Inc., the industrial sponsor of this project, requested a new hydraulic turbine technology that can be placed in spillways and similar sloped man-made channels, and does not require any piping installations. The motivation for avoiding pipes and nozzles, which are common in turbine systems, comes from the difficulty of obtaining testing and installation permits if such structures are present on site. Hence, the spillway turbine presented in this project does not have a nozzle component. Rather than directing the flow to the runner through a nozzle, an accelerator channel was developed. It is important to highlight that the term spillway turbine refers to a system consisting of both the turbine runner and the accelerator channel. The industrial sponsor also requested a technology that is novel and can be patented in the future. This request was answered throughout this project and the novelty of this turbine comes from both the runner blade insert design (Figure 4.24) and the accelerator channel design (Figure 4.37). Moreover, the runner design and the accelerator channel design have been developed for the purposes of this project by the thesis author and do not exist in previously published literature. The novelty of this research does not only come from developing a new hydraulic turbine technology, but also from the numerical simulation approach utilised to improve the system efficiency. This was achieved by simulating a free-surface, supercritical flow through a channel contraction, mimicking the flow through the accelerator channel. Utilising large-eddy simulation approach and free-surface modelling for the analysis of supercritical flows through a channel contraction has not been published in literature before. Moreover, the published studies mostly fail to validate their models with experimental studies. To conclude, this thesis offers novel contributions on two fronts. It presents a new turbine technology developed from an original idea and it also presents a new, validated methodology for simulating supercritical free-surface flows through channel contraction.

1.2 Renewable Energy Overview

Renewable energy sources have contributed to over 26% of total world electricity production, as shown in Figure 1.2. When debating between renewable energy sources and fossil fuels, the arguments in favour of switching to renewable energy sources are clear. This is due to the finite supply of fossil fuels left on the Earth and significant amounts of greenhouse gases emitted into the atmosphere as a result of fossil fuel combustion. Renewable energy sources can be defined as clean and inexhaustible with minor greenhouse gas and CO_2 emissions. On the other hand, deciding between nuclear power and renewable is not as evident to many. Both methods of energy production produce negligible amounts of CO_2. Nuclear plants usually have large power outputs, but the decommissioning and dealing with nuclear waste or possible nuclear accidents can be very complicated. Also, nuclear sources are not inexhaustible, contrary to the renewable energy sources which are extracted from natural sources such as sun, water, wind, geothermal and biomass.
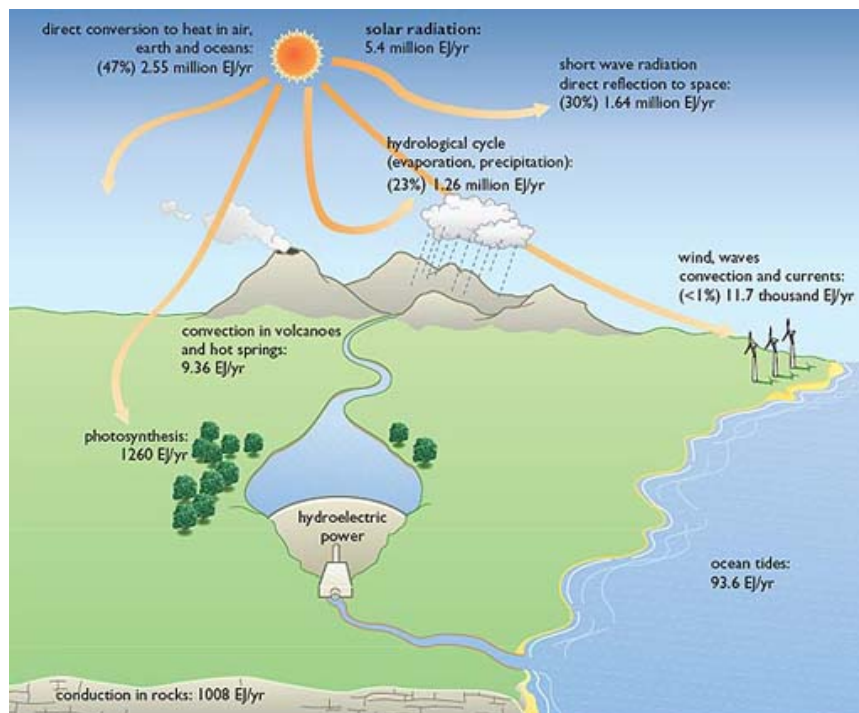
FIGURE 1.3: Renewable energy sources (The Open University, 2020)

Solar energy is the most available for harvesting. The amount of solar power intercepted by the Earth is 1.8 x 10^{14} kW, out of which 60% reaches the Earths surface, and the rest is reflected into space (Thirugnanasambandam et al., 2010).

The most used method for solar energy conversion to electricity is by using photovoltaic (PV) effect through the use of PV panels. Photovoltaic panels had an increase in the installation of 4300% from 2007 to 2017 (Nunez, 2019), indicating that the photovoltaic panel market is fast expanding and the technology is widely available.

Harnessing energy from the wind dates back to hundreds of years BC when Persians used ancient versions of windmills for food production and water pumping (Kaldellis & Zafirakis, 2011). The first wind turbine for electricity generation was installed in 1888, but modern type horizontal axis turbines evolved after the Second World War in the 1960s and 1970s. Therefore, wind turbine technology has had decades to mature and evolve into a reliable source for electricity production. Both onshore and offshore wind farm installation is on the increase in the last several years, with the forecasted production capacity of 839 GW by 2023 (Iea.org, 2019).

Bioenergy can be harvested directly from burning biomass or converting it to biogas, biodiesel or bioethanol. Biomass can be defined as organic waste, for example, wood, agricultural, animal or food waste. The great advantage of bioenergy is that energy is extracted from waste, however, improving the efficiency of the available extraction methods is of interest.

Geothermal energy or energy extracted from below the Earth's surface has been utilised by humans for a long time. First electricity generated from geothermal energy was in Italy in 1904, and nowadays it is harvested in over 20 different countries (National Geographic, 2019). The principles of harvesting energy from geothermal sources is based on accessing hot water or steam underneath the ground that can be used to drive turbines and generate electricity.

Water as a source of renewable energy contributes to 31% of energy harvested from renewable energy sources. It can be used in marine energy schemes or hydropower schemes. Marine energy can be extracted from a tidal stream, tidal range or wave energy. Tides are foreseeable and are not just seasonal. The main advantage of marine energy is that during the seasons in which other renewable energy sources are less reliable, tides are steady and regular (Corsatea & Magagna, 2019). Although there are many different types of wave phenomena, wave energy is focused on converting energy from wind waves into electricity. Wave energy has great potential for electricity generation, up to 32 000 TWh/year worldwide (Mørk et al., 2010); however, wave energy extraction technology is far from maturity.

Tidal power technology is far ahead of wave energy exploitation. Tidal energy can be harvested from a tidal range or a tidal stream. Tidal barrages or lagoons

work on principles of potential energy being harvested, and tidal stream turbines work on the principle of harvesting kinetic energy from flowing water. Tidal energy potential is significant in countries with large tidal ranges such as the United Kingdom and France. Moreover, the largest tidal ranges occur in semi-closed areas of water such as bays, estuaries and fjords. Places with the most considerable tidal potential are the Severn Estuary and the Bristol Channel, Orkney and Pentland Firth, all in the United Kingdom, the Bay of Fundy in Canada and several locations in North-West Spain (Graves & Iglesias, 2018).

Tidal stream energy can be harvested from tidal currents larger than 1 m/s and United Kingdom's tidal stream energy potential has been estimated to 12 TWh.

Tidal stream turbine technology was derived from horizontal axis turbines (HATs), commonly used as wind turbines. Vertical tidal turbines (VATs) have also been a part of the discussion in the tidal stream technology debate, but their low efficiency calls for more research on the blade design.

Despite the outlined challenges related to extracting electricity from a marine energy source, vast sea and ocean regions pose a high potential for renewable energy industry expansion. Hence, the development of marine energy technologies is eminent in the future. If marine and hydropower schemes are contrasted, hydropower schemes are technologically superior and more present through history and hence more researched and standard. Hydropower has been discussed at depth in the following chapter, as it is the main focus of this research. However, it was important to highlight that other renewable energy sources described in this chapter have an important role in answering electricity demands of the modern world.

1.3   Objectives and thesis structure

The principal objective of this research was to design and develop a novel horizontal axis turbine for use in low-head, low-flow, man-made channels such as chute spillways or other similar sloped channels. Low-head refers to head of up to 40 m and low-flow refers to flows with velocities of up to 2.5 m^3/s (Razak et al., 2010). The turbine system consists of two main components, the runner and the accelerator channel/wedge used to accelerate and direct the water towards the runner blades. Both the runner and the accelerator channel/wedge are novel designs developed for purposes of this project and do not exist in previously published literature. The goal was to design a runner and a flow directing system that will be the most efficient in extracting energy from the flowing

water. The next step was to test the initial turbine design in the laboratory setting, followed by the analysis of the results. Both runner and accelerator channel/wedge designs were revised according to the conclusions made from laboratory tests until at least 40 % performance efficiency was reached. During experimental testing, it was noted that the runner placement relative to the accelerator channel and the accelerator channel design had a large impact on the overall system performance. Hence, another objective was to investigate the runner intake through large-eddy simulation and gain an understanding of free-surface flow dynamics of a high Froude number flow through an open-channel contraction. The conclusions made from the large-eddy simulation will then be implemented into the final design to be tested in field environment.

The thesis was structured to highlight both the design process, the testing methodology, the conclusions and recommendations made and is as follows:

- Chapter 2: Background: The background section summarises the principles of extracting energy from rivers and streams. Sustainability of large hydropower plants was discussed, and a motivation for finding innovative methods of extracting energy from small, mini and micro-scale hydropower plants was explained. This section also gives an overview of hydraulic turbines commonly used in hydro-plants. As the spillway turbine is a novel and original turbine, review of existing technology focused on turbines that inspired the spillway turbine design. An opportunity for the novel design was argued, potential installation sites were identified, and equations used for performance analysis were presented in this section.

- Chapter 3: Laboratory set up: The description of the laboratory set up, and experiment installation was presented in this section, together with the equipment and methods used for data logging. Design of the experiments was depicted through numerous technical drawings. An overview of how the flow energy was converted into electrical energy through the use of generator was also described.

- Chapter 4: In this chapter, three design versions of the spillway turbine were presented to highlight the design process and the conclusions made from different variable testing. Testing methodology and variables were presented clearly for all three design versions.
  Design version I: Initial design and concept of the spillway turbine were given in this section. The results were presented in a way that indicates how changing testing variables such as different runner to channel bed, slope or wedge distances affect the turbine performance. The effect of

the blade number, size of the runner and height of the wedge was also quantified in terms of performance coefficients. Finally, the conclusions and recommendations for the design revision were outlined at the end of the section.

Design version II: The potential sources of energy losses in the first design version of the turbine system were identified and addressed in this chapter. Changes were implemented in terms of installing inserts into the runner, and the wedge was re-designed to direct the water into the runner in a more precise manner. The results were presented so conclusions of each variable effect on the performance can be made. Furthermore, the conclusions and the recommendations about sources of energy losses for this design version were presented.

Design version III: This section shows the final design revision of the spillway turbine tested in the laboratory. Changes to the second design version were implemented, mainly in changing the wedge design into an accelerator channel that guides the water more precisely to the runner blades. Results indicate that the spillway turbine can be considered as efficient as some available hydrokinetic turbines. Finally, it was recommended that future testing continues in field, as the results achieved during laboratory testing were satisfactory.

Summary and recommendations: The summary and comparison of all three design versions were presented in this section. From the design process and the laboratory testing, it was concluded that the point of major energy losses in the system was at the entrance of the accelerator channel. The accelerator channel can be defined as a contracting open-channel, and it was decided that the investigation of hydrodynamics in this component was necessary for further spillway turbine performance improvement.

- Chapter 5: Numerical simulation background: This chapter entails the explanation behind the motivation to research the supercritical flow through an open channel contraction. A review of literature available on this topic was shown, and it was concluded that significant gaps exist in available methods. The challenges and objectives of numerical simulation of supercritical flow through an open-channel contraction were outlined.

- Chapter 6: Numerical simulation framework: Governing equations of motion and methods of providing the solutions were described in this chapter, with an overview of methods available for turbulence modelling. As large eddy simulation was the chosen approach, the method and the solution of the Navier-Stokes equations was described. The level-set method was

utilised to simulate the free-surface, and the immersed-boundary method was used to implement the contracting channel geometry.

- Chapter 7: Numerical simulation results: The numerical simulation used was validated against experimental data presented in Abdo et al. (2019) to ensure the fidelity of the results. The experiment used for validation was described. The computational domain with boundary conditions description and the number of points was also specified. This chapter concludes that the model can capture the position of the free-surface of supercritical flow through a contraction correctly and therefore can be used for the analysis of such flows. The published studies of supercritical flow through an open-channel contraction lack descriptions of flow characteristics and turbulence intensities. Therefore, the analysis of velocity profiles and turbulent kinetic energy components was presented in this section. Pressure distribution and forces acting on contraction channel walls were compared and quantified in this section. The energy losses in a 6° open-channel contraction were also quantified with head loss and loss coefficients calculated. One of the main objectives of numerical simulation of the supercritical flow through a channel contraction is to make conclusions on what contraction design would lead to smallest possible energy losses in the flow so that the spillway turbine runner can access and convert larger portions of flow energy into electricity. Hence, the contraction angle effect on the energy losses in the flow was quantified in this chapter, with five different contraction angles analysed. A summary on numerical simulation of supercritical flow through a contraction was given at the end of this chapter. The summary entailed analysis of the model accuracy, flow characteristics, energy losses and the effects of using different contraction angles.

- Chapter 8: Conclusions and recommendations for future work: Conclusions, contributions of this thesis and recommendations for future work were given in the last chapter.

Chapter 2

Background

2.1 Hydropower

Hydropower is a significant contributor to the worldwide electricity production, contributing 19% of electricity produced from all energy sources in 2018 (Iea.org, 2019). From the water wheel used for flour milling in Greece around 2000 years ago to the first modern turbine in the 1700s in France (Energy.gov, 2019), hydropower and hydro turbines have exciting and long evolution paths. At the end of 2016, the total installed hydropower capacity was 1246 GW (Breeze, 2018). Hydropower schemes are widely distributed, and the countries with most significant electricity production from hydropower in 2015 were China, Canada, Brazil and the United States with 1130, 381, 360 and 271 TWh produced respectively (Iea.org, 2017). Based on the capacity, hydropower plants can be split into four categories listed in Table 2.1, although different countries will have different definitions of what is defined as small hydropower with a general capacity up to 10 MW, with 30 MW in the United States and up to 50 MW in Canada (Khare et al., 2019). However, the norm is a range of 10-30 MW capacity for small hydropower schemes.

TABLE 2.1: Hydropower plant categories (Breeze, 2018)

Size	Power Capacity
Micro	1 KW - 100 KW
Mini	100 KW - 1 MW
Small	1 MW - 10-30 MW
Large	Above 10-30 MW

All hydropower schemes work on the principle of getting the largest amount of available water to pass through the turbines installed. This can be achieved either through a dam or a reservoir scheme or a run-of-river scheme. Hydropower is most commonly generated through harvesting gravitational potential energy.

Hence, power available from the potential energy of water can be calculated using Equation (2.1).

$$P_{in} = \rho * g * H * Q \tag{2.1}$$

where P_{in} is the power of water available in $Watts$, ρ is the density of water in kg/m^3, H is the head available in m and Q is the discharge in m^3/s.

On the other hand, hydropower can also be generated by utilising the kinetic energy of the flowing water. This is commonly achieved through the use of hydrokinetic turbines (Runge et al., 2018). The power available from kinetic energy can be found using Equation (2.2).

$$P_{in} = 0.5 * \rho * A * U^3 \tag{2.2}$$

Where P_{in} is the power of water available in $Watts$, ρ is the density of water in kg/m^3, A is the cross-sectional area in m^2, and U is the flow velocity in m/s. Although hydro-kinetic turbines got attention in the last few years, the focus of the presented research is on hydropower generated from the potential energy of water.

Large hydro-plants usually involve a reservoir of water, a dam, a powerhouse and a penstock, as shown in Figure 2.1. Large hydro-dams are the most significant contributors to the electricity produced from water sources.
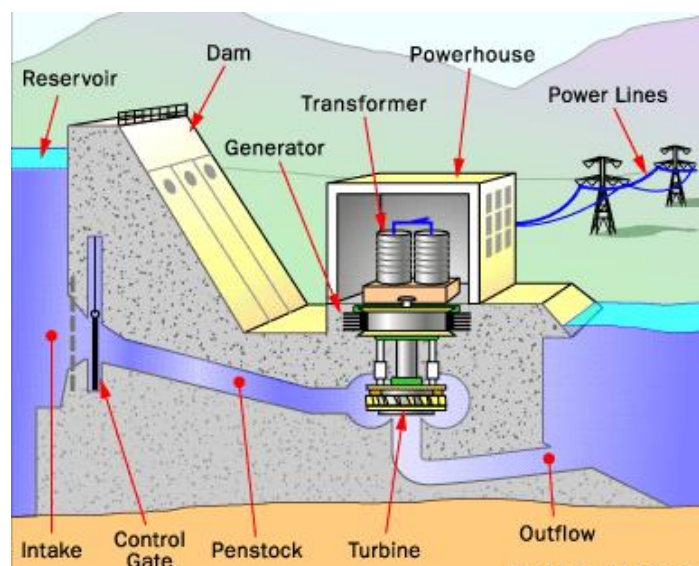
FIGURE 2.1: Inside a hydropower plant (Bonsor, 2001)

Some of the largest dams in the world are The Three Gorges Dam in China with a maximum capacity of 22 500 MW followed by Itaipo Dam in Brazil with a maximum capacity of 14 000 MW. High or medium head turbines such as Pelton, Turgo, Kaplan and Francis turbines are mostly used in these large scale projects because these turbines have already gone under extensive research and are highly efficient.

Most common dams used in large scheme hydropower plants are embankment, concrete arch, gravity and buttress dams. Embankment dams are usually most common in sites with wide valleys and they commonly create shallow, wide reservoirs. Embankment dams can be damaged by water overtopping the dam as they are usually made from natural materials. To avoid this, concrete spillways are often constructed for water release in peak flow times.

FIGURE 2.2: Embankment dam; Mica Dam, Canada (Christensen, 2019) on the left and Gravity dam; Grande Dixence, Switzerland (Grande-dixence, 2019) on the right.

Gravity dams are commonly made of concrete and masonry, and usually have a near-vertical upstream face and a sloping downstream face. As the name indicates, they are held in position through gravity, and therefore these type of dams have to be built on strong rock foundations. Gravity dams are suitable for both wide and narrow side valleys and can be constructed taller than embankment dams. Buttress dams are very similar to gravity dams and are also made of concrete and masonry. They are appropriate in wide or narrow side valleys, and also need solid rock foundations for stability. Arch concrete dams use the principle of force distribution along a parabola to ensure stability. Arch dams require steep side valleys, with a strong rock that can endure the forces from the arch on both sides and the dam bottom. Having clean energy extraction from water, with minimal disruption to local life resulted in smaller-scale hydropower developments becoming increasingly popular.

Sustainability of Large Hydropower Plants

The sustainability of large hydropower plants has been questioned due to many arising environmental and socio-economic factors. Contrasting the hydroelectric dam construction in developing and developed countries, it can be noted that the overall image is significantly different. Moreover, developed countries have had a decline in dam construction since 1960 as dams on available sites have already been developed. The dams built before the 1950s are at the end of the predicted life span in Europe and America, and are mainly being decommissioned as the cost of repairing is too high. The number of dams removed to this date in France, Sweden, Finland, Spain, the United Kingdom and seven other European countries is 4984 (Damremoval.eu, 2020). On the other hand, the situation is different in countries with emerging economies such as countries in South East Asia, The Balkans, South America and Africa. Overall, 3700 dams with capacity over 1MW have been planned for construction or are already in construction all over the world as seen in Figure 2.3, out of which 874 with a capacity over 100 MW (Zarfl et al., 2015).
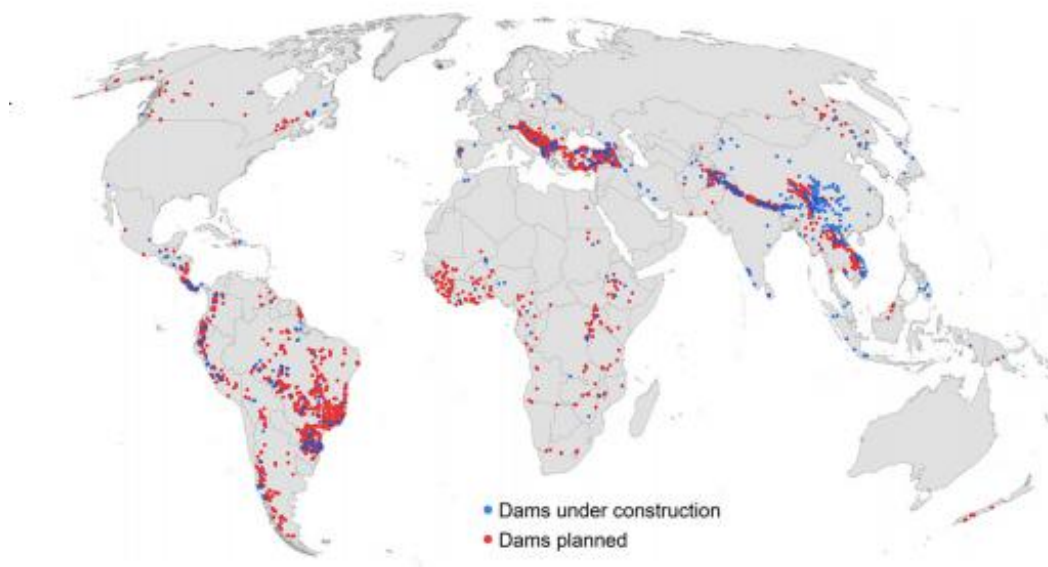
FIGURE 2.3: Planned/ongoing dam construction (Zarfl et al., 2015)

If the financial, environmental and human costs of large dams are considered, it is believed that benefits are not always higher than costs. Firstly, hydrologic consequences of large dams include seasonal changes in river discharges and lower freshwater availability which further leads to water temperature changes, salinity changes, floodplain and coastal erosion changes. Secondly, these changes

lead to ecosystem changes such as loss of habitat and loss of both water and land biodiversity. Thirdly, this directly affects populations along the river basins that rely on farming and fishing. An example of this is a decline in fish catch of 60% in the Tucuruí Dam region in the Brazilian Amazon (Moran et al., 2018). Finally, in the past six decades, between 40 and 80 million people have been moved from their homes as a direct result of large dam projects, (International Rivers, 2019). Majority of these people were not resettled as they should. If the purely financial side of large dam projects is considered, Ansar et al. (2014) found that costs are 96% more then predicted for a sample of 254 large dams built from 1934 to 2007. It was also found that 1 in 10 of these dams cost three times more than estimated in the original calculations. Another factor to consider is that hydropower development in developing regions of the world often overlooks the implications of climate change on how much water power there will be available that year. There is evidence that the intensity and frequency of extreme events are unpredictable. Lake Mead that is used as a reservoir for the Hoover Dam had experienced 40% reduction in water levels, and the peak power outputs for the Hoover dam reduced from 2 GW to 1.5 GW. Another example is The Belo Monte Dam on Xingu River, which has only produced a peak of 4.43 GW comparing to the optimistic peak capacity estimation of 11.23 GW (Moran et al., 2018). To conclude, it is essential to seek and develop more sustainable solutions than building large dam projects. The dam technology is mature, and it has provided humans with electricity for many years, but it is significant to keep new, greener technologies in mind when discussing hydropower schemes.

Innovative solutions

One of the solutions to ensure the sustainability of large dam projects is that environmental and socio-economic impacts of these projects should be assessed fairly and ethically, not by dam builders but by civil servant firms. Another way of improving sustainability is to take into account climate change factors and local issues that could arise during and after construction is completed. Moreover, there is evidence that smaller-scale hydropower schemes are more sustainable and pose a lower risk to the environments where they are installed. Smaller-scale hydropower plants do not just have a smaller generation capacity, but also site head differences are not as significant as in large hydropower sites, and hence they are mostly run-of-river sites rather than reservoir schemes. An illustration of a typical micro-scale plant set-up is given in Figure 2.4.

It is challenging to quantify the impacts of either small or large hydropower
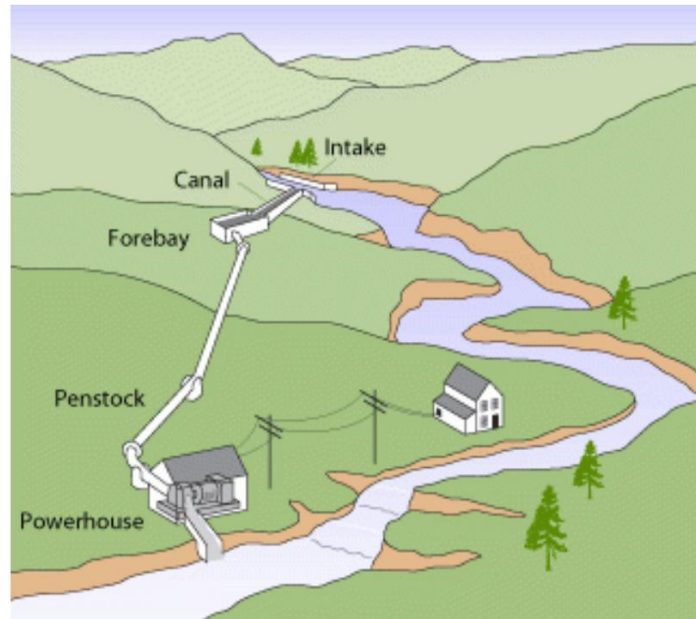
FIGURE 2.4: Micro-hydropower plant (Energy.gov, 2019)

plants, but Bakken et al. (2012) presented a study that compared the environmental impact produced by one large hydropower scheme and a group of small scale plants that produce a similar amount of power. Sites with similar topography, climate and ecosystems were selected for the comparison, which makes this method acceptable. Impact factors were compared on a nine-level scale ranging from substantial positive impact to a tremendous negative impact. However, the study does not take into account social impact, which could change the overall perception, but in this case, it is unlikely it would be in favour of a large dam project. The study can be criticised for requiring a significant degree of subjective judgement, but it can be used to depict overall comparison on how a group of 27 small hydropower plants compare to 1 average large dam project. Data for one large dam was taken as an average of impacts of 3 large Norwegian dams. Energy production of an average large hydropower project is 350 GWh, and the comparable amount produced by 27 small scale hydropower projects is 390 GWh. The impacts presented in this study are shown in Figure 2.5. The impacts presented in this figure do not show a significant difference between one large hydropower plant and 27 smaller ones; however, many vital factors are not presented. This includes the impact on farming and fishing, which is crucial in developing countries. Furthermore, no evidence on social impact is provided, and in developing countries, resettlement of people affected is rarely fair and humane. Also, it is essential to emphasise that the data is for a cumulative value of 27 small schemes, and impacts of 1 small scale scheme will be much lower than presented data.
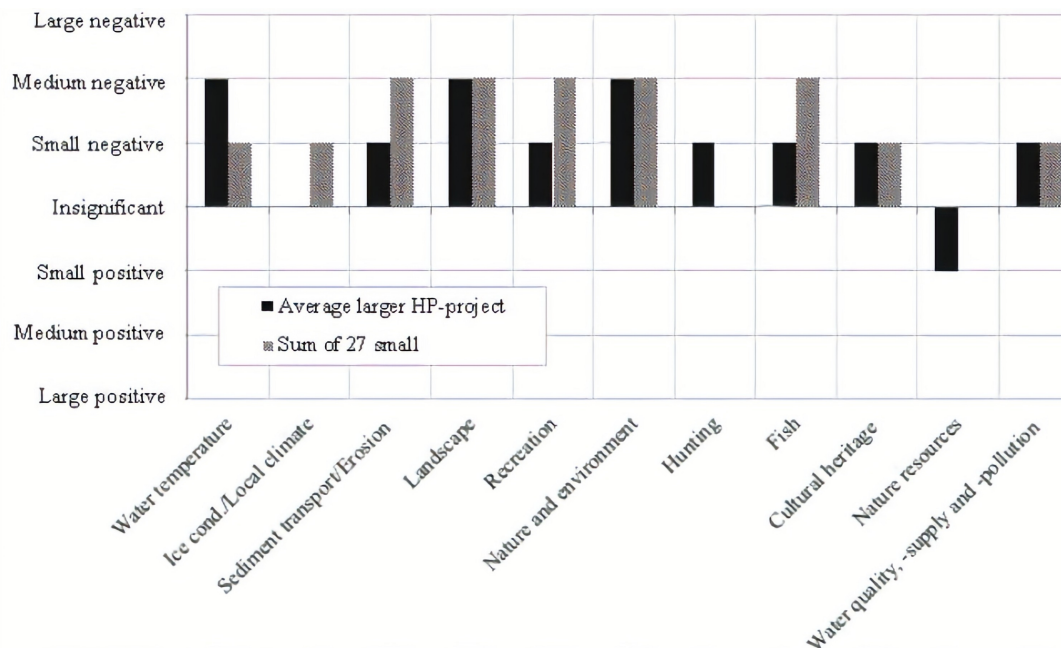
FIGURE 2.5: Impact of large vs. small hydropower plants
(Bakken et al., 2012)

Small, mini and micro-scale hydropower plants are an innovative solution to providing electricity to rural areas without access to electricity. In India, about 18 000 villages are about to be electrified through renewable energy sources, many of which through small, mini or micro hydropower schemes (Tanwar, 2006). Mini-hydropower plant feasibility studies have also been conducted for hilly forest areas in Thailand that rely on natural gas power plants (Suwanit & Gheewala, 2011). Potential for developing small scale hydropower projects in Turkey has been investigated in depth by Dursun & Gokcol (2011) implying that this could be the cleanest and most effective way of generating electricity in rural areas. These smaller hydropower schemes have development potential not only in areas without access to electricity but also in areas where significant scale developments are being avoided for environmental reasons. Small scale projects are thought to be one of the most effective energy technologies (Paish, 2002), but initial costs of installation can be high. On the other hand, they provide long term reliability and relatively negligible environmental effects when compared to large dam hydropower schemes. Depending on head available, different turbines will be selected for different sites. Mini Francis and Pelton turbines are available for installation in low head environments; however, a market for novel low head turbines is expanding. The concept of micro-hydropower schemes spiked interest in research of new and innovative turbine designs. The principle advantage of

small scale hydropower plants is the ability to directly supply energy to the consumers, even if the consumers are far from the grid. This could potentially bring socio-economic growth in places that still struggle with electricity stability in underdeveloped parts of the world. Moreover, the environmental impact of such schemes is significantly lower that of large hydropower projects. This triggered growth in new turbine design research, intending to place such turbines in low-head streams or man-made channels.

2.2   Hydraulic Turbines

The predecessor of modern hydraulic turbines, the water wheel, was invented in the 1st century BC (Viollet, 2017). The water wheel was of great importance in the industrial sense as it was used form many different purposes, from grinding grain to cotton clothes manufacturing. The most prominent industries around the world were dependent on the efficiency of water wheels in 19th century. The water wheel inspired new and innovative turbine designs such as the first reaction turbine developed in England in 1744, which influenced the development of the Francis turbine in 1855 (Lewis, 2014).

2.2.1   Types of Turbines

Hydraulic turbines can be classified as impulse or reaction turbines. The critical difference between reaction and impulse turbines is in the way the energy is transferred to the runner. Reaction turbines work on the principle of flow energy being partly converted to kinetic energy, with flow pressure energy still having some effect on the rotor. However, in impulse turbines, energy is completely converted to kinetic energy, and flow pressure does not affect the impeller (Douglas et al., 2001). Moreover, hydraulic turbines can be categorised depending on the direction of flow in the turbine runner, and those categories are radial flow, tangential flow, mixed-flow and axial-flow turbines.

Kinetic turbines are different from typical impulse or reaction turbines and work on principles of extracting kinetic energy from flowing stream of water. These turbines are modern and still mainly in development stages, but they can be deployed both in rivers or engineered channels. Some examples of hydro-kinetic in-plane and vertical axis turbines are shown in Figure 2.6. Hydro-kinetic turbines can be horizontal axis or vertical axis turbines. Horizontal axis turbines can be used in streams but are predominantly used in marine energy schemes. Vertical axis turbines, especially Darrieus and Savonius turbines, are used in

river applications (Kumar & Saini, 2016). The difference between Darrieus and Savonius turbines is in the main driving force. In other words, Darrieus turbine main driving force is the lifting force, and in case of Savonius rotor, drag is the main driving force.
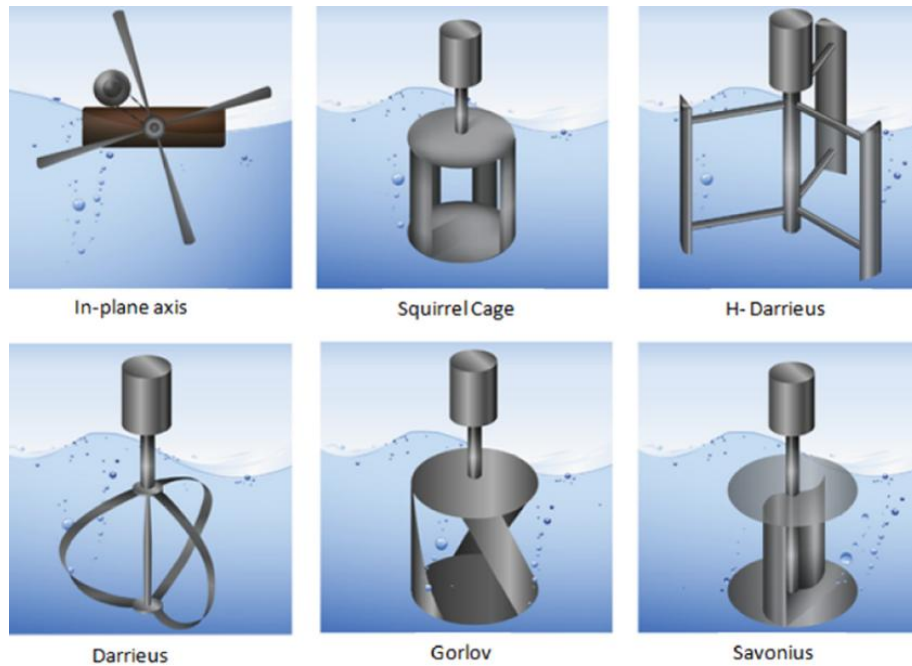
FIGURE 2.6: In-plane and vertical axis hydrokinetic turbines (Kumar & Saini, 2016)

Reaction turbines can be split into categories based on the direction of flow in the runner. Hence runners of reaction turbines can be described as radial-flow machines, mixed-flow or axial-flow machines. Francis turbines can be either radial or mixed flow turbines, depending on the design-specific speed (Goswami & Kreith, 2017). Propeller turbines or axial-flow turbines imply runner design in which the flow enters and exits the turbine in the same axial direction. Propeller turbines require constant pressure of the flow, meaning that the water is in contact with all blades at once. Examples of propeller turbines with fixed blade pitch are Bulb, Straflo and Tube turbines. The best-known example of a propeller turbine with adjustable blades is the Kaplan turbine shown in Figure 2.7. Propeller turbines are frequently used in low-head conditions.

The early versions of Francis turbines were radial flow turbines that were used for 10-100 m head range. Modern Francis turbines are commonly mixed-flow turbines, and a typical Francis turbine is given in Figure 2.8. Guide vanes in Francis turbines are adjustable, and the number of blades commonly ranges between 16 and 24. They are the most widely used turbines and are installed in
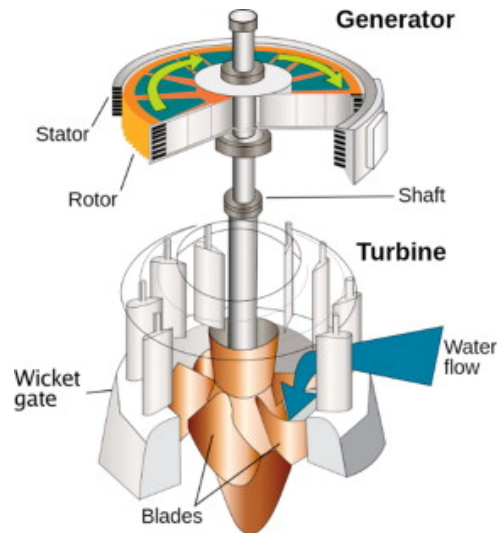
FIGURE 2.7: Kaplan turbine (Salameh, 2014)

some of the largest hydropower schemes such as the Three Gorges Dam, Grand Coulee Dam and Itaipu Dam.
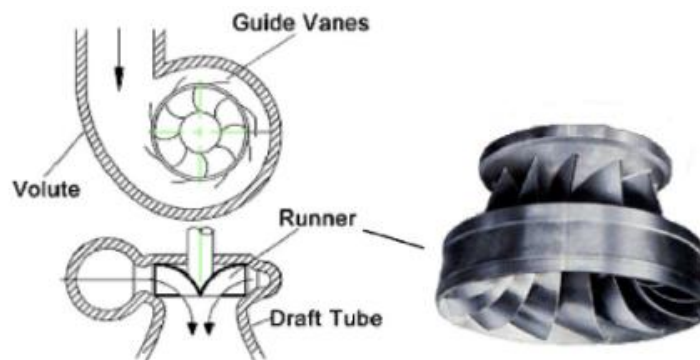
FIGURE 2.8: Francis Turbine (Okot, 2013)

The efficiency of Francis turbines can go up to 95%, but these type turbines do not perform well in heads less than 20 m or in very high head environments over 900 m (Dixon & Hall, 2010), and are intended mostly for medium head sites.

Impulse turbines were inspired by the design of the stream wheel and were invented at the end of 19th century for use in very high head flows. Impulse turbines work on the idea of a water jet interacting with the turbine blades and hence spinning the runner, which results in conversion of mechanical rotational energy into electric energy. A water jet, in this case, is commonly created by passing a high-pressure water column through a nozzle. The most widely used and known impulse turbine is the Pelton wheel. The renowned impulse turbines

are Turgo and the Cross-flow turbine. A more extensive review of Pelton and Cross-flow turbines is given in the following subsection, as both these turbines served as inspiration for some design aspects of the spillway turbine. The Turgo turbine resembles the Pelton wheel as it also works on principles of a jet pushing the turbine buckets. The principal difference is in the direction of how the jet acts on the buckets, as it is axially rotated for Turgo turbines at an angle of about 20 to 30 ° from the front of the runner (Robinson & Gilkes, 2018), as shown in Figure 2.9.
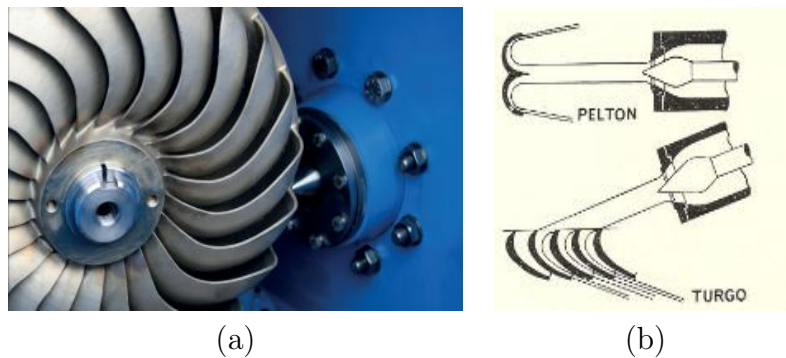
FIGURE 2.9: (a) Turgo turbine runner (Robinson & Gilkes, 2018); (b) Turgo vs. Pelton jet angle (Wilson, 1967).

2.2.2 Spillway Turbine Design Vision

The inspiration for the spillway turbine design comes from the shape of the Savonius hydrokinetic turbine, the manner of how forces act on Pelton wheel buckets and the design of Cross-flow turbine. Hence, these three turbines were investigated in more depth than turbines mentioned above.

Savonius Turbine

Savonius turbine was invented in 1924 as a vertical axis wind turbine operating mainly due to drag force acting on the turbine buckets. The original design of the Savonius turbine consisted of two semi-circular buckets. Over time, the Savonius turbine has been researched by many, and the applications expanded to the marine energy sector for tidal or wave power generation. Most extensive research has been focused on the Savonius wind turbine, as it has the most extended industrial history. Design parameters that can be adapted to achieve better performance of the Savonius turbine are presented in Figure 2.10.

The aspect ratio is the ratio between the turbine height and its diameters, and aspect ratios of about 2 give good performance efficiency (Akwa et al.,
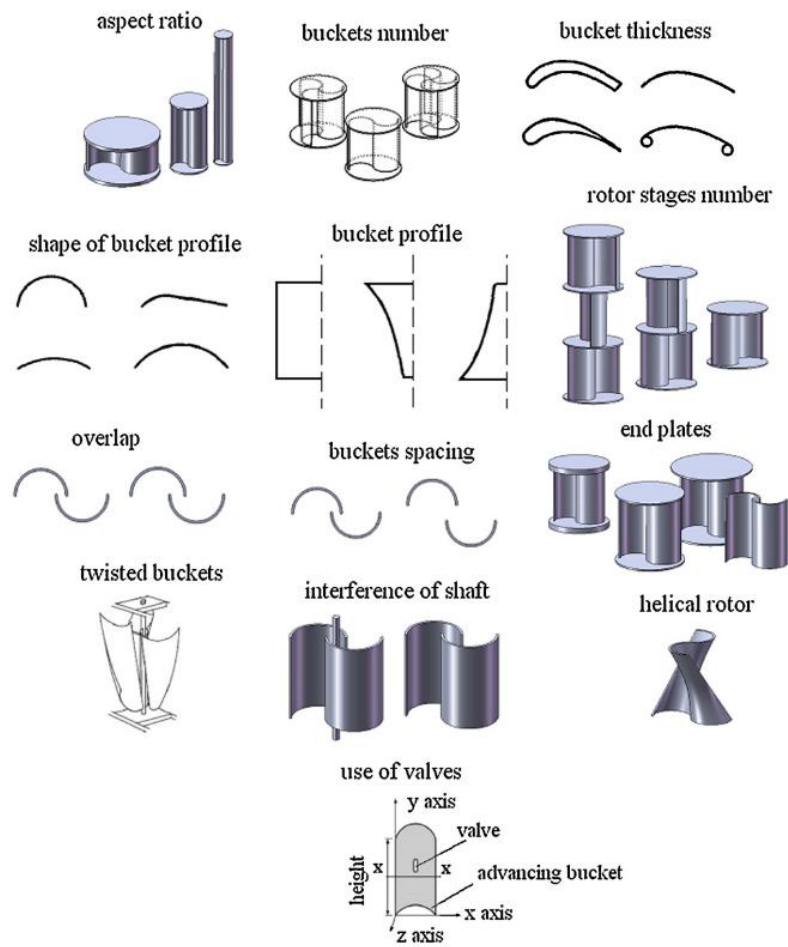
FIGURE 2.10: Design parameters of the Savonius runner (Akwa et al., 2012)

2012). By installing a plate at turbine ends, the flow is contained within the runner, preventing it from going out. The performance efficiency is 10% higher with end plates installed. The optimal endplate diameter should be around 1.1 times the runner diameter (Alexander & Holownia, 1978). Some studies indicated that having two buckets rather than three gives better performance as the extra buckets added to deflect the airflow inefficiently. It is suggested that the rotor stages number should be increased rather than the bucket number. Furthermore, the best power coefficient of 0.32, was obtained for a two-stage, two bucket rotor with twisted blades (Saha et al., 2008).

Although initially intended for use as a wind vertical axis turbine, the Savonius turbine has been used in marine energy schemes. There are studies in which the vertical axis Savonius rotor has been configured and used in tidal power schemes (Harries et al., 2016), but in recent years, many studies of horizontal axis Savonius rotor for wave energy harnessing emerged. For this application, the primary vertical axis Savonius rotor was changed to the horizontal axis orientation. Wave orbital motion is utilised to spin the rotor, and hence the wave height, wave period, and water depth have a significant effect on the turbine performance. Tutar & Veci (2016) presented a study of a 3-bladed Savonius type wave turbine which showed that the wave height had a more substantial effect on the performance than the wave period or turbine submergence level. Another study on the Savonius rotor for utilising ocean waves in shallow waters concluded that the optimal number of buckets depends on the wave height and the submergence level. A 3 blade rotor performs better than a four or a five-blade rotor when the submergence level is at the still water level. However, if the submergence level is decreased to -50 mm below the still water level, a five-blade rotor performs significantly better than a three or a four-blade rotor (Hindasageri et al., 2011).

Even though the Savonius turbine was designed as a wind turbine and several researchers are focused on using the turbine for tidal and wave energy harnessing, the Savonius turbine has also been used as a hydraulic turbine. Nakajima et al. (2008) presented a study of the performance of the Savonius rotor with a horizontal axis orientation. This turbine was tested in a laboratory flume, wholly submerged and working on principles of harnessing the kinetic flow energy. Performance of the turbine was evaluated for both clockwise and counter-clockwise flow directions at different bottom clearance ratios. It was concluded that the clearance ratio played a significant role in the turbine performance, and hence the flow around the turbine rotor was also analysed in this study. Vertical axis hydrokinetic Savonius turbines have also been a subject

of several studies. Telukdar et al. (2018) conducted a parametric evaluation of
the Savonius rotor through both experimental and numerical analysis. Two and
three-bladed rotors were both tested, and it was concluded that the two-blade
rotor performs significantly better over all immersion levels. It was also noted
that the semi-circular blade profile outperforms the elliptical blades.
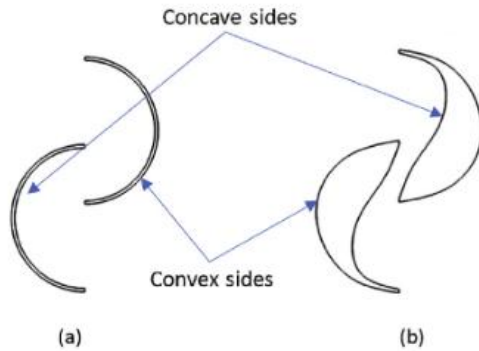
FIGURE 2.11: (a)
Standard blade shape;
(b) Optimised blade
shape (Kerikous &
Thévenin, 2019)

Kerikous & Thévenin (2019) used
numerical simulations to optimise
the hydrokinetic Savonius rotor, and
the optimal shape found was flatter
on the concave side with a hook-like
tip. This led to a significant im-
provement in operational efficiency.
The optimal design was also self-
starting at all angles. The optimal
blade design with the comparison to
the standard blade design is given in
Figure 2.11

The Savonius rotor has gone under research in wind, marine and hydropower
sectors. The power coefficients range from 0.17-0.32 for wind Savonius, with
many different design variations available. The horizontal axis Savonius showed
power coefficient of 0.25, and the vertical axis rotor ranged from 0.2-0.24 de-
pending on the design configuration. The design principles adopted from the
Savonius turbine design are the aspect ratio of 2, the presence of end plates with
1.1 ratios to the runner diameter and the blade shape resembling the optimised
blade shape shown in Figure 2.11.

Pelton Turbine

Pelton turbine was invented in 1880, and its modern form is considered one of
the most efficient impulse turbines on the market. The potential energy of water
is converted into a jet of water that is directed towards Pelton wheel buckets.
A Pelton turbine is presented in Figure 2.12.

Since the Pelton turbine is a mature technology, research available on this topic
is extensive. The review of literature on the Pelton turbine can be split into
three categories: theoretical, experimental and numerical studies.

Several theoretical studies focused on analysing the effect of friction and other
driving forces on the Pelton buckets. Zhang (2007) published research on how

FIGURE 2.12: Pelton Turbine (Hydrolink, 2009)

Pelton turbine efficiency is directly affected by friction of flow which either accelerates or slows down the turbine bucket blades. It was also emphasised that the Pelton efficiency is indirectly affected by the pressure distribution on the buckets. This work was taken further (Zhang, 2009), explaining the contributions and influences of forces acting on the buckets.
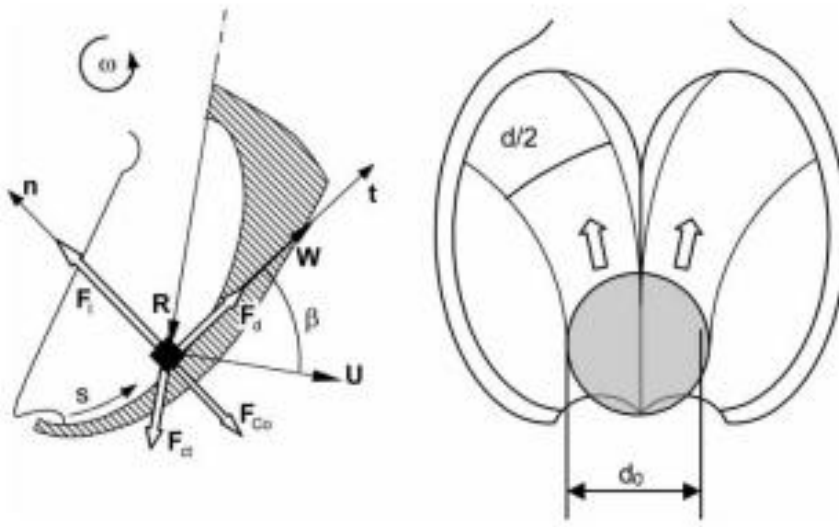
FIGURE 2.13: Pelton Turbine Forces (Zhang, 2009). Jet diameter d_0, water sheet width d, centrifugal force F_{ct}, Coriolis force F_{Co}, direct frictional force F_d, impact force F_I, normal force F_n.

The change in kinetic energy in the flow along the bucket surface is equal to the work performed by the centrifugal force, F_{ct}. The centrifugal force influences the speed of relative velocity of a water particle. The Coriolis force F_{Co} always acts normal to the flow direction, and hence it only changes the direction of a water particle but not the speed. Both centrifugal and Coriolis forces do positive work on the bucket surface. The water flow along the bucket surface experiences a continuous change in the flow direction, and hence this change in momentum

results in a force called the impact force F_{I}. Zhang (2009) concluded that the effect of the centrifugal force is negligible comparing to the effect the Coriolis force has on the bucket blades. Mechanical work on the bucket is performed by the normal surface force F_{n} and the frictional surface force F_{d}, which are the two active driving forces. The normal force can be calculated using Equation (2.3), and it can also be described as the force that arises from the pressure in the water sheet acting on the blade surface.

$$F_n = F_I - F_{ct} * n - F_{Co} * n \qquad (2.3)$$

Experimental studies on the Pelton turbine are numerous and mostly focus on improving efficiency through improved nozzle blade interaction. Several pieces of research focused on finding the optimal shape of the nozzle, and the shape of the jet discharged (Kotousov, 2005; Zhang & Casey, 2007). It was observed (Staubli & Abgottspon, 2008) that the position of the injector has a significant effect on the turbine efficiency, or in other words, the turbine with the upper injector outperforms the lower one. Several studies focused on the erosion of nozzle and bucket blades in Pelton turbines. Padhy & Saini (2009) related the effects that concentration and size of silt particles and the velocity of the jet have on the rate of erosion in the buckets, while Bajracharya et al. (2008) studied the problem of erosion in Pelton buckets in the Himalayan region where river water is abundant in Quartz and Feldspar. When considering experimental investigations of flow in the Pelton buckets, the objective of several studies was to depict the pressure distribution in these buckets. Perrig et al. (2006) conducted pressure tests on five zones of equal surface areas in a Pelton bucket. This study concluded that the outer bucket regions contribute most to the bucket power, as that is where the flow particles have high momentum. On the other hand, the bucket root regions are less productive in power transfer. Zoppé et al. (2006) research outcome showed that varying the head had no influence on pressure distribution in the bucket, but the leakage flow does increase with the jet diameter and bucket incidence.

Although CFD has been evolving in the last couple of decades, numerically simulating flow in Pelton turbines still is a challenging task. This is because the flow is two dimensional, and the jet bucket interaction results in spraying losses, pressure losses and secondary flows. However, CFD studies are available on both jet and bucket hydrodynamics. Perrig et al. (2006) experimental data was used to validate numerical simulation results obtained using CFX-5 code. Zoppé et al. (2006) also used experimental data to validate FLUENT code

simulations which indicated that the zone of highest pressure in the bucket is the deepest part of the bucket. Parkinson et al. (2006) investigated pressure field, flow and bucket response to unsteady hydraulic loading using the finite element method. Jet shape to bucket interaction was investigated by Santolin et al. (2009) using CFX-11 code. It was concluded by Beucher et al. (2010) that by reducing the number and size of buckets in a Pelton turbine, friction losses could be decreased by 30%.

The design principle adopted from the Pelton wheel is the shape of the inserts used in the spillway turbine as shown in Figures 4.22, 4.23 and 4.24. The analysis of force and pressure distributions on the Pelton buckets was used as a guideline of how the flow will behave in the spillway turbine with the cup inserts presented later in this thesis.

Cross-flow Turbine

A cross-flow turbine can be defined as an impulse turbine consisting of two main parts, the nozzle and the runner. In these turbines, the shaft is horizontal to the ground, which ensures radial flow over the turbine. Cross-flow turbines have two stages of power production, with the first stage occurring when the water jet interacts with the blade at the entrance. The water jet then goes through the hollow inside of the turbine towards the exit blades. The second stage of power production, therefore, occurs when the jet hits the blades again from the inside of the turbine. Cross-flow turbine and nozzle are shown in Figure 2.14. This type of turbine is also known as a Bánki-Mitchell turbine, named after two scientists that developed the initial idea at the beginning of 20th century.
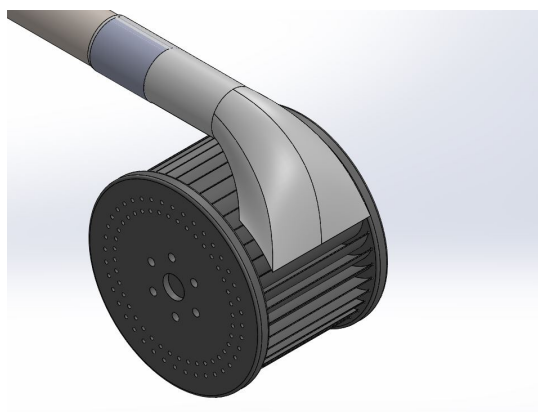
FIGURE 2.14: Cross-flow turbine, runner and nozzle.

Mockmore & Merryfield (1949) pioneered experimental research on the cross-flow turbine. This is the first time a cross-flow turbine was tested, and it achieved 68% efficiency at an optimal speed of 270 rpm and 4.88 m head. This

turbine had 20 blades and blade spacing of 52.8 mm. Varga (1959) achieved 77% efficiency with a 30 blade runner, while also measuring pressure distributions. This efficiency was further improved by Nakase et al. (1982), increasing it to 82% by using a runner with 26 blades. In the same year, Johnson et al. (1982) achieved efficiencies up to 80% for a runner with 18 blades and heads around 1 m. For a runner with 15 blades, the performance efficiency dropped to 79% (Khosrowpanah et al., 1988). Fiuzat & Akerkar (1991) study focused on obtaining power outputs of two power production stages. Total maximum efficiency achieved was 78%, of which 45% was contributed from the second power production stage when the flow hits the blades for the second time on the path to leave the turbine. Totapally & Aziz (1994) observed that the efficiency could be increased to 92 % for a 35 blade runner if the nozzle size is reduced to be narrower than the runner. With the rising popularity of CFD tools, several authors used such models further to improve cross-flow turbine performance (Choi et al., 2008; De Andrade et al., 2011), but the efficiencies still ranged from 80-90 % depending on which outer and inner diameter, number of blades, and nozzle arc were chosen. Sammartano et al. (2013) obtained 85 % efficiency through CFD testing of a runner with 35 blades and a net head of 14.2 m and Sinagra et al. (2015) furthered this work by testing the effects of the internal shaft going through the runner, coming to a conclusion that the runner without a shaft going through the middle shows better performance. The cross-flow turbine blade shape was used as inspiration for the initial design of the runners shown in Figures 4.1 and 4.3.

2.2.3   Novel Design Opportunity

Hydropower turbine manufacturing has been focused on turbines already available for use in large hydropower schemes. However, such turbines achieve low efficiencies in low-head conditions and frequently call for significant investment costs. This resulted in research and development of new devices more appropriate for use in low-head conditions. These new devices are at different stages of development, some in laboratory stages and some already commercialised. Wiemann et al. (2007) gave an overview of low head turbine technology available in 2007 describing gravitational vortex converter, Transverpello, Hydrostatic pressure machine which can all be classified as hydrokinetic turbines. Bozhinova et al. (2013) gave an overview of hydropower converters used in heads below 2.5 m in which wheels, reaction turbines, hydrostatic pressure converters were analysed. Jawahar & Michael (2017) gave a summary of turbines published in the literature that can be suitable for use in micro-hydro plants. Relevant

energy converters described in these publications are summarised in Table 2.2.

TABLE 2.2: Turbine technology available for low-head environments (Bozhinova et al., 2013; Jawahar & Michael, 2017; Wiemann et al., 2007)

Author	*Turbine Type*	*H(m)*	*Efficiency(%)*
Zotlöterer (2010)	Gravitation Water Vortex	1.5	80
Müller et al. (2007)	Impulse Water Wheel	0.4-1.5	35-40
Bozhinova et al. (2013)	Poncelet Wheel	0.7-1.7	55-65
Quaranta & Müller (2018)	Zuppinger Wheel	0.3-1.5	52-84
Bozhinova et al. (2013)	Francis turbine	0.75-5	75-85
Bozhinova et al. (2013)	Kaplan turbine	1.8-5.0	82-92
MJ2 Technologies (2011)	VLH	1.4-3.2	80-86
Lashofer et al.(2011)	Archimedes screw	1-10	80
Senior et al. (2010)	HPM	1-2.5	70-82
Senior et al. (2010)	HPW	0.2-1	60-90
Bozorgi et al.(2013)	Axial pump turbine	4	61
Date et al. (2013)	Simple reaction turbine	1-4	50
Motwani et al. (2013)	Centrifugal pump turbine	15	60
Alexander et al. (2009)	Propeller turbine	4-9	68
Ikeda et al. (2010)	Nano hydraulic turbine	1.2	20
Pereira and Borges (2014)	Cross Flow Turbine	5.5	85
Acharya et al. (2015)	Cross Flow Turbine	10	77
Bryan and Kendra (2013)	Pelton and Turgo Turbine	13–28	80
Williamson et al. (2013)	Turgo Turbine	1–3.5	87–91
Giosio et al.(2015)	Pump as Turbine	5.98	79

Gravitation water vortex turbine data from Obergrafendorf in Austria shows that this type of turbine can achieve 80% efficiency at 1.5 m head according to Zotlöterer (2010). However, this high efficiency is claimed by the manufacturer, but there is a lack of published literature on this turbine, and the realistic efficiency of the device is likely much lower. This device is suitable for regulated rivers where flow and sediment transport are managed with several low-weirs. On such sites, the gravitation water vortex turbine is very convenient, especially as these devices aerate water which affects the fish positively. Besides, these devices do not require a dam or a run-off scheme. However, civil works required are extensive in non-regulated rivers, and there are no studies available on how the sediment transport is affected in rivers where gravitation water vortex turbines are installed.

Impulse water wheel or stream water wheel is given in Figure 2.15 performance depends on the flow characteristics and the depth of the water. It was found (Müller et al., 2007) that if the impulse water wheel is placed in shallow subcritical flow, the efficiency is much lower than 35-40% stated, which can be

achieved in supercritical flows or deep waters. Overall, these devices are not commonly installed on rivers, but there is a potential for future development for use in deep waters.
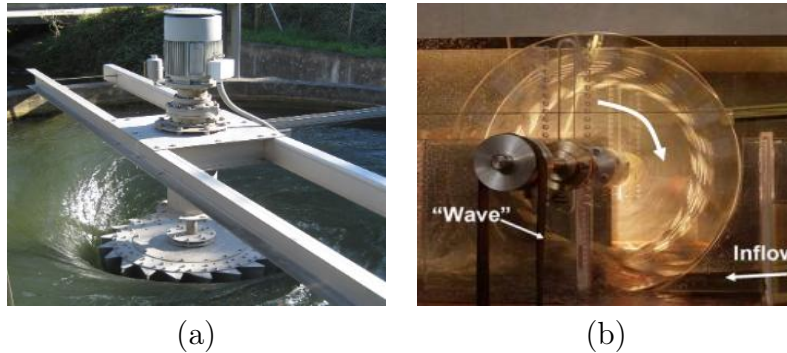
FIGURE 2.15: (a) Gravitation water vortex turbine (Zotlöterer, 2010); (b) Impulse water wheel (Müller et al., 2007)

The Poncelet wheel was invented in 1827 and is rarely built in present-day (Bozhinova et al., 2013) as there is no available literature on the performance tests. The efficiency of the Poncelet wheel is likely to be much lower, and the turbine is considered to have a larger negative effect on fish than other wheel turbines, due to the presence of a fast jet and the angle of turbine blades.

The Zuppinger wheel was tested (Quaranta & Müller, 2018) for a 0.3-1.5 m range of heads, showing maximum efficiency of 84% at a flow velocity of 1.2 m/s. The strengths of the Zuppinger wheel are its fish friendliness, high efficiency and ability of sediment to pass through the turbine. The weaknesses are the size of the wheel, which goes up to 7.5 m diameter, and the high noise levels it produces. Moreover, a drop in performance for a slight change in flow rate is significant. The maximum efficiency achived at 4.71 l/s was 84%, and for 4.58 l/s, the efficiency dropped to 61%.

The Francis turbine can be used for heads as low as 0.75 m and is a mature technology that is commonly used in large power schemes. The Francis turbines show high efficiencies, but the civil works required for installation and costs can be high. Also, these turbines are not fish-friendly and do not allow sediment transport through the turbine (Bozhinova et al., 2013).

Kaplan turbines are also a mature technology with extensive research available on this propeller turbine. This turbine performs very well in low head environments, with efficiencies reaching 90% in some cases. However, Kaplan turbine does not only consist of the runner, but also the inflow structure, which ensures the flow interacts with the blades in a specific manner. Hence, the civil works

(a) (b)
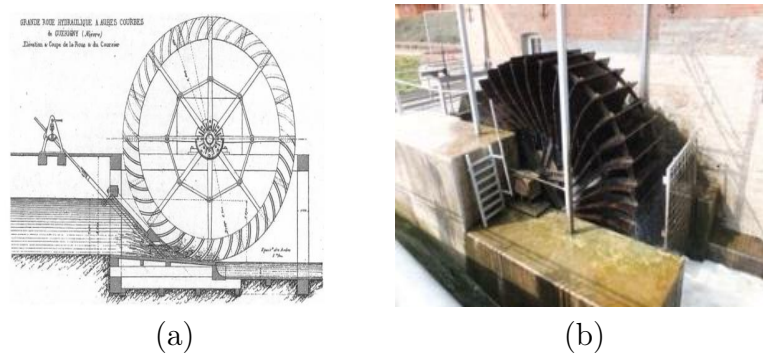
FIGURE 2.16: (a)The Poncelet wheel (Bozhinova et al., 2013);
(b) The Zuppinger wheel (Quaranta & Müller, 2018)

required for installation of this turbine and the costs are high comparing to the
Francis turbine (Bozhinova et al., 2013).

(a) (b)
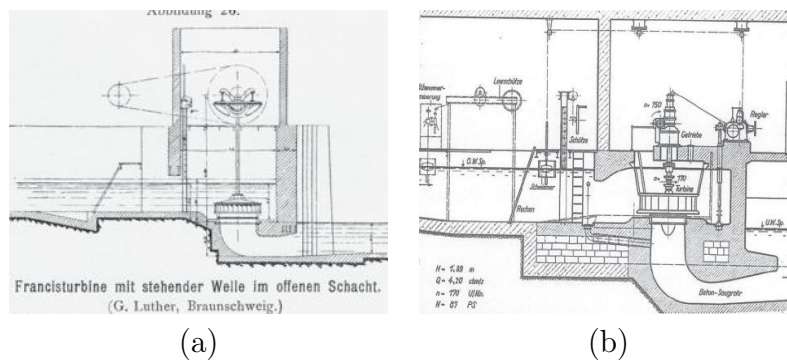
FIGURE 2.17: (a) Francis turbine (Bozhinova et al., 2013); (b)
Kaplan turbine (Bozhinova et al., 2013)

Very low head turbine (VLH) is an invention by MJ2 Technologies (2011) which
works for head ranges of 1.4-3.2 m and can achieve an efficiency of 80-86%. The
manufacturers claim that this turbine is very fish-friendly, with 92% fish sur-
vival rate. The turbine has an in-built generator and is installed as 1 unit. It
has a low-cost impact, and it is considered to be environmentally friendly by
the manufacturer. The performance drops significantly for part-load situations
when the flow rate is less than 1/3 of the maximum flow rate.

Although the Archimedes screw is one of the oldest inventions, it has not been
utilised for energy extraction until the end of 20$^{\text{th}}$ century. The efficiency of
the screw drops with steeper angles and wider turns (Lashofer et al., 2011).
Although the screw is considered fish-friendly and is simple to install, the tur-
bine does not perform well in low flow rates, and it does not allow sediment
passage. However, it is considered one of the most environmentally friendly and
cost-effective designs for low-head environments.

Figure 2.18: Very low head turbine (MJ2 Technologies, 2011)
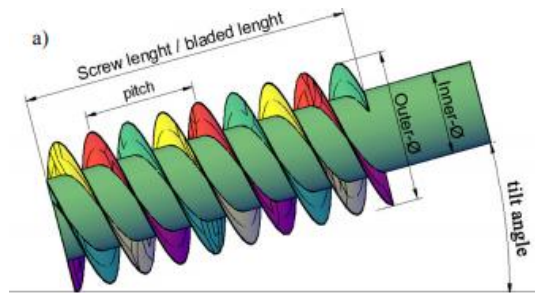
Figure 2.19: Archimedes screw (Lashofer et al., 2011)

Two hydrostatic pressure devices were developed in the last decade by Senior et al. (2010), called hydrostatic pressure wheel (HPW) and hydrostatic pressure machine (HPM). These converters can be compared to the impulse water wheel, the Zuppinger wheel and the Poncelet wheel, but they allow sediment transport and are not limited in the volume of water they can process. HPW is a simple wheel machine with straight blades, made for heads of 0.2-1 m and is more cost effective than the Zuppinger wheel, but it has a very low rotational speed. This implies that effective power transmission will be difficult to achieve at low costs. Also, turbulent structures are likely to appear on the straight blades, meaning that there is room for improvement when the blade shape is considered. The HPM differs from HPW in blade shape, which are more curved. Also, it is meant for use in slightly higher head environments ranging from 1-2.5 m. It was noted that HPM can only process about 50% of the flow, and hence there is potential for design improvements. The ecological advantages of these devices are the ability for sediment and fish to pass underneath the devices. However, both of these devices are bulky and require 100% flow area blockage, meaning extensive civil works are required. However, it is considered that HPW and HPM could have commercial potential if further researched and improved.

(a)   (b)

FIGURE 2.20: (a) HPM (Senior et al., 2010); (b) HPW (Senior et al., 2010)

Bozorgi et al. (2013) researched a reverse axial pump as a turbine in pico-hydropower schemes. The turbine was investigated both numerically and experimentally, with good correlation between the results. The Axial pump-turbine requires a penstock meaning that a significant amount of civil works is required. Ecological implications were not discussed, but it is considered that these turbines can be utilised in developing countries effectively as they are cheaper than turbines more complex in design.

Date et al. (2013) presented research on a simple reaction turbine with low fabrication costs that is suitable for use in 1-4 m heads and can achieve 50%. This turbine requires a pipe or other form of water intake that will make the components rotate similarly to how the garden sprinklers work.

(a)   (b)
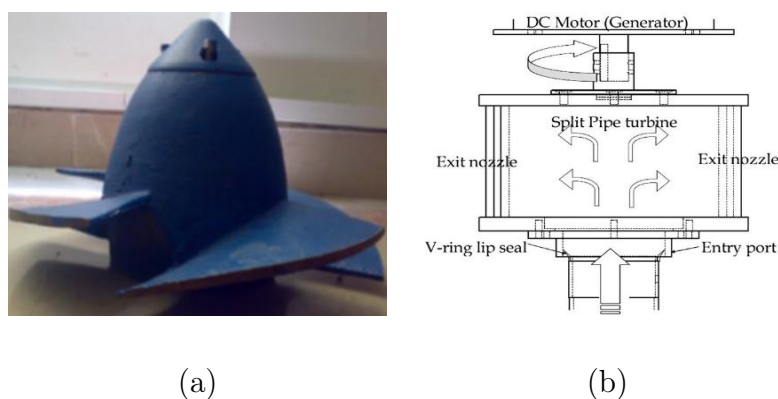
FIGURE 2.21: (a) Axial Pump (Bozorgi et al., 2013); (b) Simple reaction turbine (Date et al., 2013)

Motwani et al. (2013) compared centrifugal pump as a turbine device to the Francis turbine for use in pico-hydropower plants. It was concluded that the

efficiency of 60% could be achieved if the pump as turbine was used, which is significantly lower than if the same capacity Francis turbine was used. However, centrifugal pumps as turbines are 6 to 8 times cheaper than the comparable Francis turbine. Ecological implications and installation were not discussed in this publication.

Alexander et al. (2009) presented a new propeller turbine design for use in heads from 2 to 40 m. Based on the specific speed ranging from 60 to 540, a different scale of the turbine was used, but the geometrical shape was kept constant. This propeller turbine differs from Kaplan turbine in casing design. The guide vanes were removed from the inlet configuration, as blockages and leaves are commonly piled in such structures. Results showed that four different scale turbines showed efficiencies of over 68% for four different specific speeds, with the maximum efficiency of around 70% for specific speeds in the range of 60 to 240. The laboratory tests were performed for a head range of 2 to 9 m. The conditions were scaled, and it was claimed that the turbines would perform as well in much higher head conditions, up to 40 m, but such conditions were not tested.

(a)   (b)
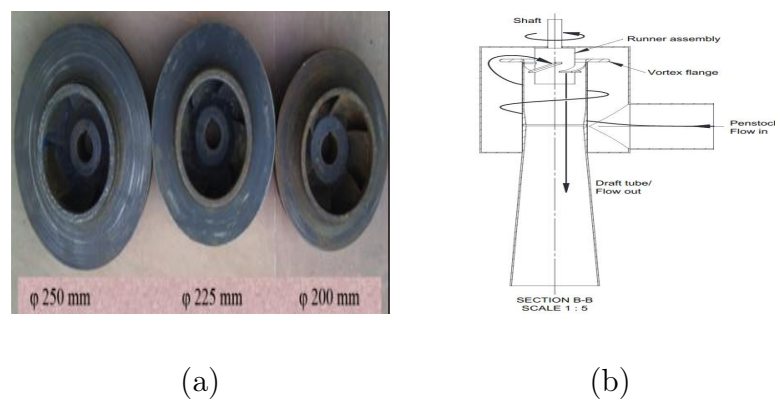
FIGURE 2.22: (a) Centrifugal pump turbine (Motwani et al.,
2013); (b) Propeller Turbine (Alexander et al., 2009)

Ikeda et al. (2010) developed a nano hydraulic turbine for use in waterfalls, shaped similarly to a cross-flow device. Although the laboratory tests claimed the efficiency of 53 to 60%, the field tests showed that field efficiency is a third of the laboratory obtained results. The flow rate and the placement of the turbine in reference to the waterfall affected the results significantly.

Pereira & Borges (2014) conducted a study on a cross-flow turbine for micro hydropower plants and achieved efficiency of 85% for 5.5m head and discharge
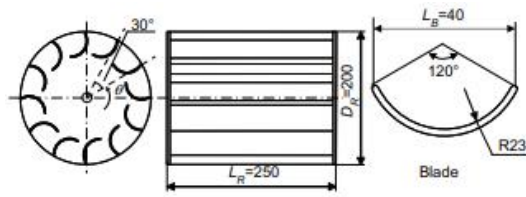
FIGURE 2.23: Nano-hydraulic turbine (Ikeda et al., 2010)

of 100 l/s in the experimental study and Acharya et al. (2015) published a numerical study showing how changing the nozzle and the number of blades can boost the efficiency from 64% to 77%. Both of these turbines require a nozzle which implies pipe or penstock is necessary for installation.

(a) (b)
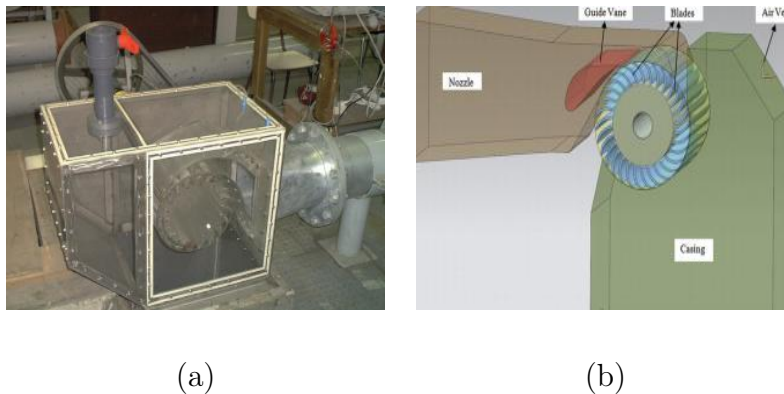
FIGURE 2.24: (a) Cross Flow Turbine (Pereira & Borges, 2014);
(b) Cross Flow Turbine(Acharya et al., 2015)

Bryan & Kendra (2013) concluded that impulse turbines such as Turgo and Pelton could be used in pico-hydro schemes. Factors that impacted turbine performance were highlighted, showing that the jet misalignment can lead to a drop in efficiency of 10 to 20%. Also, it was noted that keeping the speed ratio in a range of 0.4-0.5 ensures the best performance possible. Williamson et al. (2013) presented a study on a low-head Turgo turbine, showing both experimental and numerical methods were utilised. Very high efficiencies were achieved, concluding that 91% efficiency can be reached for 3.5 m head. However, both of these turbines require a nozzle, leading to the conclusion that penstock or pipe set up is necessary for installation.

Giosio et al. (2015) presented a pump as turbine device for use in micro-hydro schemes. Very good performance was observed, and it was claimed that this device is significantly more cost effective than using a turbine such as Francis in given conditions. A drawback of having pump as turbine is that performance

(a)   (b)

FIGURE 2.25: (a) Pelton and Turgo Turbine (Bryan & Kendra,
2013); (b) Turgo Turbine (Williamson et al., 2013)

is very poor if it is not at point of highest efficiency. This was addressed by
having constant uniform inlet for a range of flow conditions, achieved through
installing 13 hydrofoil guide vanes fitted within the case.

FIGURE 2.26: Pump as turbine (Giosio et al., 2015)

The review of literature and technology available for use in small and micro-
hydropower plants indicates that most devices discussed require some nozzle
installation, which raises questions of piping installations required for the tur-
bines to function. This is convenient in run-off river schemes which require large
amounts of civil works to prepare the sites. Another disadvantage of turbines
that require nozzles is their inability to pass sediment adequately, leading to
damage and high maintenance costs. There are also questions of fish friendli-
ness of such turbines. Some studies listed in this section also claim that using
a pump as the turbine is more cost-effective (Bozorgi et al., 2013; Giosio et al.,
2015; Motwani et al., 2013). On the other hand, pump as turbine performance
will drop significantly when distanced from the point of highest efficiency. This
makes them adequate for use in the flows with uniform conditions which can
be regulated in laboratory testing but cannot in the field. Runners with guide

vanes and casings also imply difficulty when dealing with sediment or fish. Water wheel type turbines are commonly bulky and require large blockage areas to achieve good performance, implying that a significant amount of site work is required for installation and hence disruption to the environment is also significant. Therefore, a compact turbine with no nozzle and no casing was invented for use in streams and man-made chute spillways and presented in this thesis as an original idea published by the thesis author (Adzic et al., 2020). The advantages of the spillway turbine are the simple design as seen in Chapter 4 and cheap production as depicted in Appendix B. The ease of installation is also implied, given that most testing and runner re-installations were completed without any help from technical staff in the laboratory.

2.2.4 Power Coefficient, Specific Speed and Speed Factor

A way of quantifying how well different turbines are performing is to calculate a power coefficient or coefficient of performance, C_{p}. The power coefficient is a ratio of the power of flow available P_{in} Equation (2.2), to power extracted by the turbine P_{out}. The power extracted is given in Equation (2.4), and the power coefficient can be calculated using Equation (2.5).

$$P_{out} = T * \omega \qquad (2.4)$$

Where P_{out} is power extracted by the turbine in W, T is torque in Nm and ω is the runner rotational velocity in rad/s.

$$C_p = \frac{P_{out}}{P_{in}} = \frac{T * \omega}{0.5 * \rho * g * H * Q} \qquad (2.5)$$

Turbines cannot extract all of the available flow energy as, during the energy conversion, a portion of it will be lost. Friction is a common cause of losses, and it is usually dissipated as heat, indicating that turbine components such as the shaft or bearings can get hot and might need cooling down.

The specific speed N_{s} is used to characterise the speed of the turbine. It is the speed at which a similar runner would rotate when operating under a head of $1\ m$ and would produce $1\ kW$. The specific speed can be calculated using Equation (2.6).

$$N_s = \frac{N * P^{1/2}}{H^{5/4}} \qquad (2.6)$$

Where N is the rotational speed in rev/min, P is the power produced in kW and H is the effective head in m.

The speed factor ɸ, is the ratio of peripheral speed of the buckets and the theoretical velocity of water under the effective height (Novak et al., 1996). The speed factor can be calculated using Equation (2.7).

$$\phi = \frac{D * N}{84.6 * H^{0.5}} \tag{2.7}$$

Where D is the nominal turbine diameter in m, N is the rotational speed in rev/min, and H is the effective head in m.

Turbines can be classified according to the specific speed and the speed factor that give the highest efficiencies. These are given in Table 2.3 given below.

TABLE 2.3: Turbine classification (Novak et al., 1996)

Type of Turbine	ϕ	Ns	Efficiency(%)
Impulse	0.43-0.48	8-17	85-90
		17	90
		17-30	90-82
Francis	0.60-0.90	40-130	90-94
		130-350	94
		350-452	94-93
Propeller	1.4-2.0	380-360	94
		600-902	94-85

2.2.5   Application Sites

As its name indicates, the spillway turbine is primarily indented for use in man-made sloped structures such as chutes or spillways. A spillway is defined as a channel that transfers the water from a reservoir to a stream, and they are common in reservoir and dam schemes as they can be used to release excess water. The flow over a spillway can be classified as a supercritical shallow flow. Examples of existing spillways include the Alqueva Dam spillway in Portugal and Llyn Brianne spillway in Wales, both shown in Figure 2.27.

If the spillway is substantial in length, it would be possible to place two or more turbines in series. This would maximise the usage of flow power and therefore result in higher energy extraction. The design scaling and adjustments would be recommended for each application site individually. The spillway turbine could also be placed in a stream with some construction work done on-site to adjust it for spillway turbine application. An example of this is a stream close

(a)   (b)

FIGURE 2.27: (a) Alqueva Dam spillway, Portugal (Ecourse, 2019); (b) Llyn Brianne spillway in Wales (Gibson , 2019)

to Asheville, North Carolina in the United States (Figure 2.28), where potential testing was planned at early stages of the development.

FIGURE 2.28: Asheville free-stream potential testing site

The testing on this site was not realised due to difficulties obtaining testing permissions in this specific location; however, testing was allowed on another site which was discussed in more detail later on in this thesis. A general drawing of diverting free-stream flow for spillway turbine installation is given in Figure 2.29.
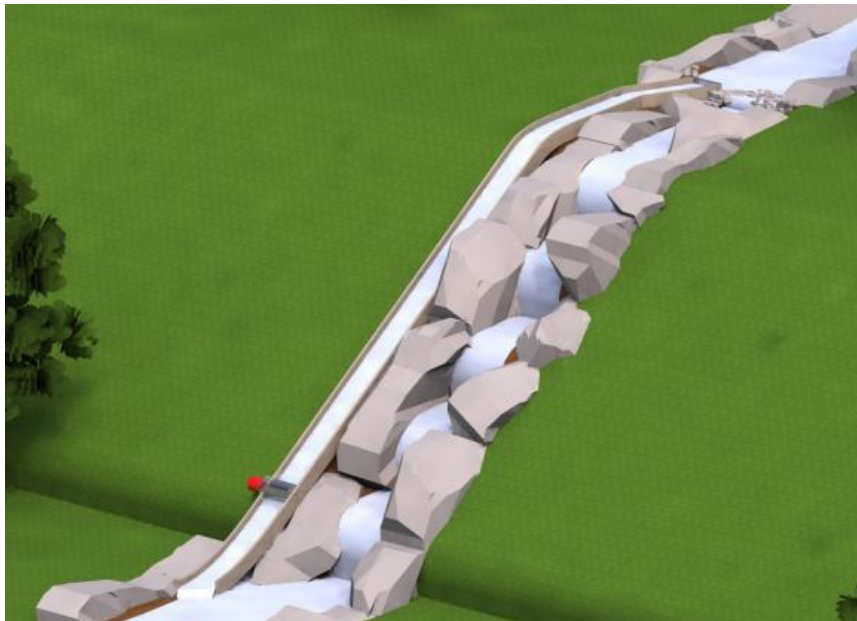
FIGURE 2.29: Site application of spillway turbine in free-stream
locations

Chapter 3

Laboratory set-up

3.1   Testing Facility

Laboratory tests were conducted in a recirculating flume at Cardiff University, School of Engineering hydraulics laboratory shown in Figure 3.1.

(a)

(b)
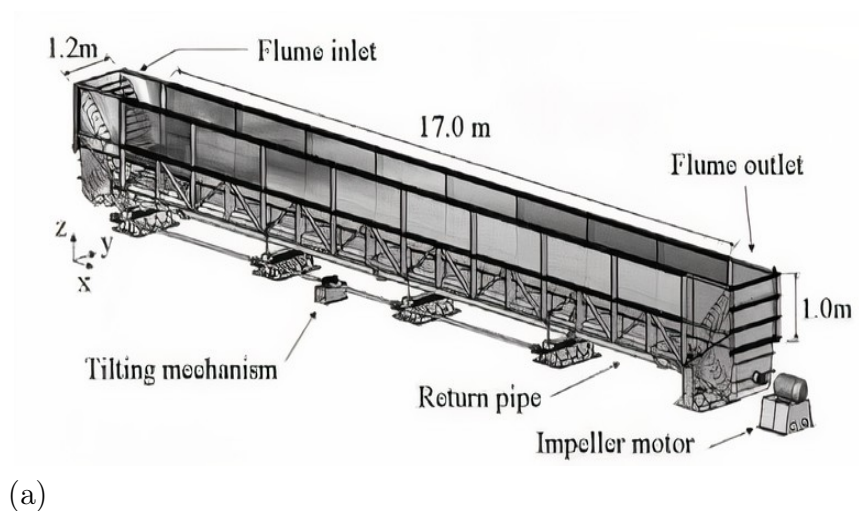
FIGURE 3.1: (a) 3-D Flume view (Rauen et al., 2008); (b) Flume photograph

The flume is 1.2 m wide, 1 m deep and 17 m long and is able to sustain flow

ranges of 5 to 100 l/s. The flow is moved by an axial flow impeller connected to a electric motor which circulates the water through a pipe of 0.6 m diameter, placed under the bottom glass side. The flume is also equipped with a tilting mechanism (Rauen et al., 2008). The flume was adjusted to match conditions in a man-made chute spillway.

At the flume inlet, a 1.2 m weir was installed in order to generate a difference in water elevation. At the height of 1 m, a 0.3 m wide channel (spillway) was attached to the weir where water was discharged as soon as the weir-channel opening overspills. After a short horizontal section, the channel slope changes to 45° in order to accelerate the flow and eventually drive the turbine runner, as shown in Figure 3.2.
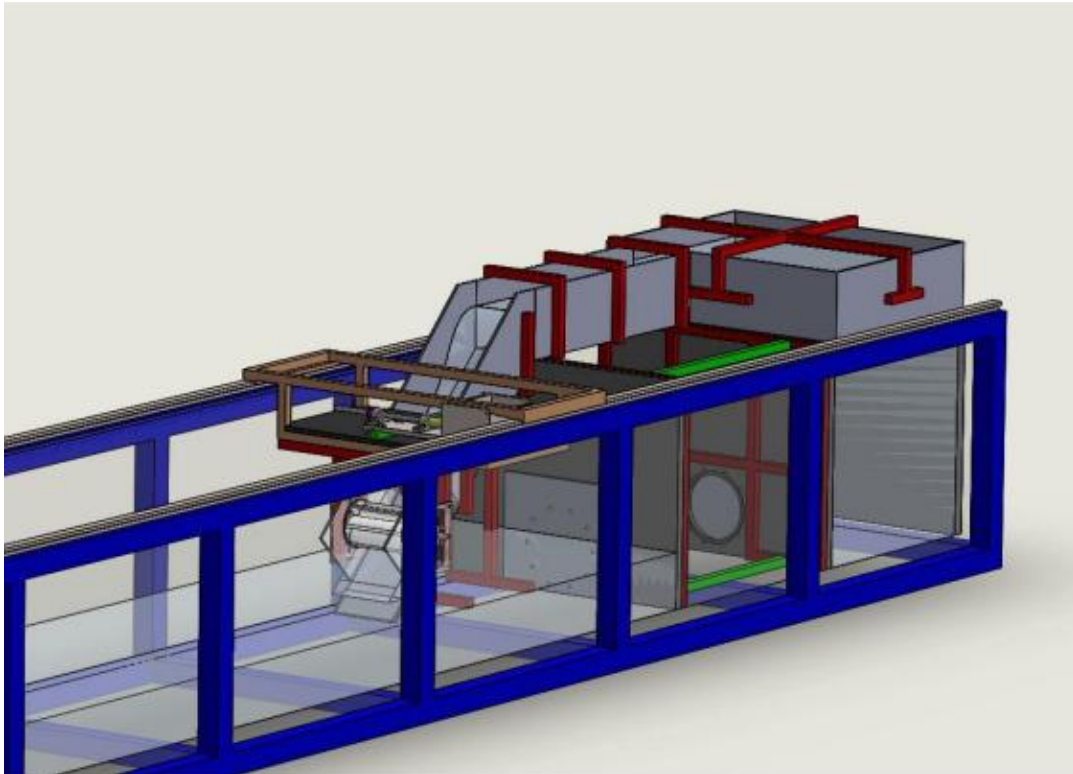
FIGURE 3.2: Spillway constructed in flume.

3.1.1   Data Logging and Discharge Measurements

Discharge, head, torque and rotational speed of the turbine were logged to obtain the power available from flow, using Equation (2.1) and power produced by the turbine, using Equation (2.4). The head measurement needed for the power of flow calculation was obtained using self-adhesive tape measures attached to the tank constructed behind the spillway channel. The discharge in the flume was measured using a fully contracted rectangular weir placed 10

m downstream from the constructed spillway, which is about eight times the width of the flume. The weir was constructed according to British Standards (2017) BS ISO 1438:2017 and weir sketch with dimensions is given in Figure 3.3. The installation of the weir was completed according to given guidelines in the mentioned standard, meaning that the thin-plate rectangular weir was placed vertically to the bottom and perpendicular to the sides of the flume. The connections of the flume to weir were made watertight to ensure that the flow can only go through the rectangular opening in the middle of the plate. The upstream face of the plate was smooth. The sides of the notch were filled to ensure the sharpness as recommended. The discharge was calculated using Equitation (3.1) known as Kindsvater-Carter formula given in British Standards (2017).
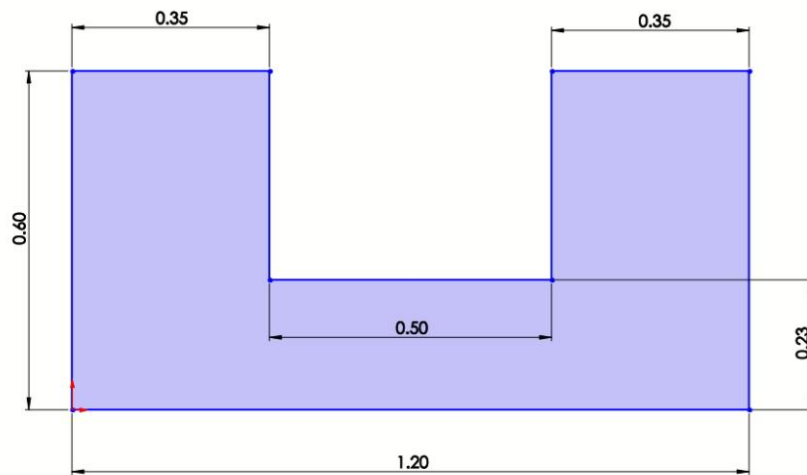
FIGURE 3.3: Rectangular weir (dimensions in metres).

TABLE 3.1: Weir dimensions

Variable	Value (m)
B	1.2
p	0.23
b	0.5
s	0.35

$$Q = C_d \frac{2}{3} \sqrt{2g} b_e h_e^{\frac{3}{2}} \tag{3.1}$$

Where Q is discharge in m^3/s, C_d is the coefficient of discharge, g is the gravitational acceleration in m/s^2, b_e is the effective width in m and h_e is the effective

head measured from height of flow above the weir notch. The effective width b_e and effective head h_e can be calculated using equations below, where k_b and k_h are experimentally obtained coefficients, b is the width of the weir notch (0.5 m), and h is the height of discharge measured in the weir. The British Standards (2017) recommends using k_b value of 0.0027 m for the ratio $b/B = (0.5/1.2)$ of 0.4 m, and k_h of 0.001 m when the weir is installed in conformance with recommended specifications. Both k factors are meant to compensate for the effects of viscosity and surface tension effects.

$$b_e = b + k_b = 0.5027 \tag{3.2}$$

$$h_e = h + k_h = h + 0.001 \tag{3.3}$$

For b/B ratio of 0.4, C_d should be taken as $0.591 + 0.0058(h/p)$. Using variables and constants from the guidelines, Equation (3.1) was used to derive Equation (3.4) which was used for discharge Q (m^3/s) calculations.

$$Q = 1.84(b - 0.2h)(h^{3/2}) \tag{3.4}$$

Limitations of the Kindsvater-Carter formula such as having b width larger than 0.15 m, p larger than 0.1 m and $(B-b)/2$ larger than 0.10 m were acknowledged for this weir design. The rectangular weir installed in the laboratory set up is shown in Figure 3.4. All tests were conducted with discharges ranging from 6 to 16 l/s. The head ranged from 0.49 to 0.55 m.

FIGURE 3.4: Laboratory rectangular weir set up

Rotational speed and the torque were both measured using a combined torque and encoder device Futek TSR605, capable of recording a range of rotational speeds up to 7000 rpm and torque intensities up to 20 Nm. The specification sheet was given in Appendix D. The torque transducer was connected to a power cell and a Lab Jack U6 device that converts the analogue data. The data was logged by DAQFactoryExpress software, and Microsoft Excel was used

to analyse the data. The rotational speed and the torque data was recorded over 8 to 10 one minute intervals, starting from zero torque to the stall point. The torque was applied electrically, through a low-speed DVE200 AC generator connected to 6 adjustable resistors, with three resistors in series in two rows. The set up used for data logging is given in Figure 3.5

(a)   (b)
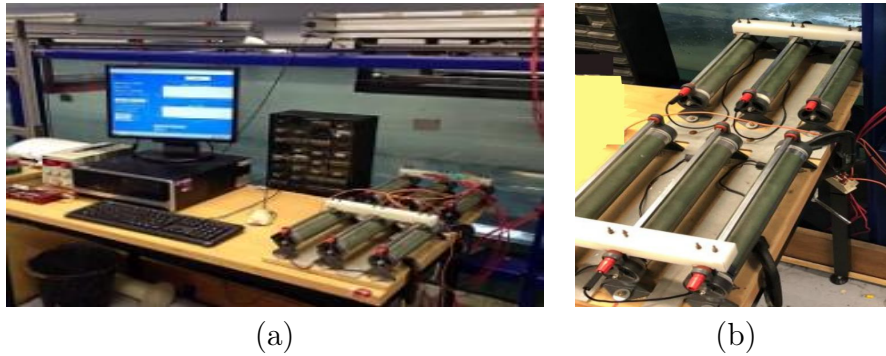
FIGURE 3.5: (a) Data logging set up; (b) Resistors used for torque appliance

3.1.2   System Design

The turbine laboratory set up consists of 5 components which are depicted in Figure 3.6.
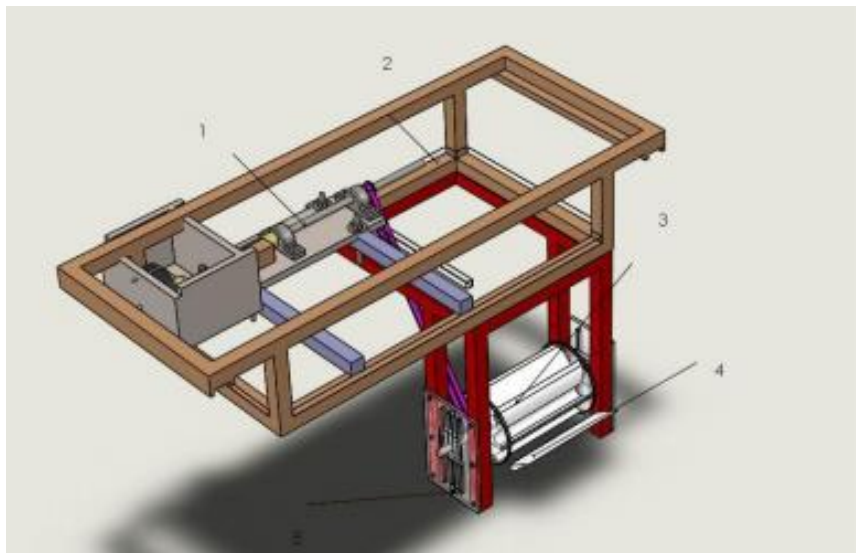
FIGURE 3.6: Spillway turbine testing structure: 1- Drive train and generator, 2- Bridge, 3- Supporting, structure, 4- Runner, 5- Wedge

The bridge was placed on top of the vertical flume walls, where the railing was installed to ensure the bridge mobility. The drive train and generator, bridge

and the supporting structure were kept the same in all tests conducted while
different runner and wedge designs were tested. The drive train and the gen-
erator are positioned and fixed to the bridge. Making the bridge movable was
a crucial factor in the system design as the position of the bridge affected the
belt tension. It was of key importance to stop the belt from slipping due to
low tension or the belt snapping due to high tension, and adjusting the bridge
position ensured appropriate tensioning of the belt. The runner was attached
to the supporting structure with 2 four holes 20 mm flange bearings allowing
initial misalignment, making adjustments of runner position easier during lab-
oratory testing. The drive train (1) is presented in more detail in Figure 3.7.
The drive train consists of the generator, the torque transducer, the shaft, the
pulley and the belt. A 20 mm stainless steel shaft goes through the runner
from both sides, with a 30 teeth pulley placed on this shaft. The Continental
HTD 1500-5M belt was wrapped around this pulley, and the pulley placed on
the main drive train shaft, which is connected to a torque transducer and the
generator. Correctly aligned drive trains and suitable grade components can
provide drive train efficiency of up to 95%. If the belt is not tensioned and
bearings, pulleys and shafts aligned correctly, the efficiency of the drive train
can drop significantly, resulting in overall lower efficiency of the turbine system
(Harvey et al., 2009).
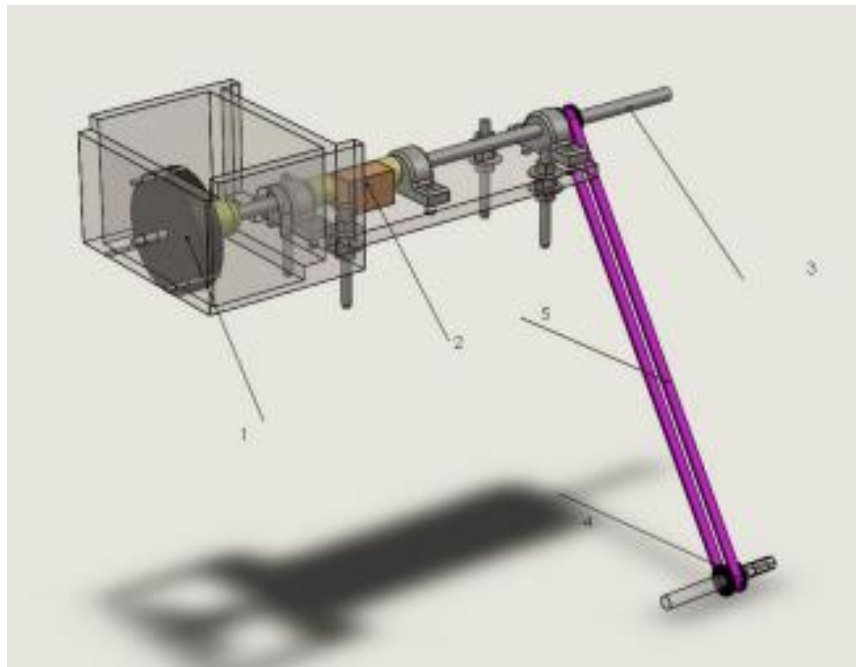
FIGURE 3.7: Spillway turbine testing structure: 1- Generator,
2- Torque transducer, 3- Shaft, 4- Pulley, 5- Belt
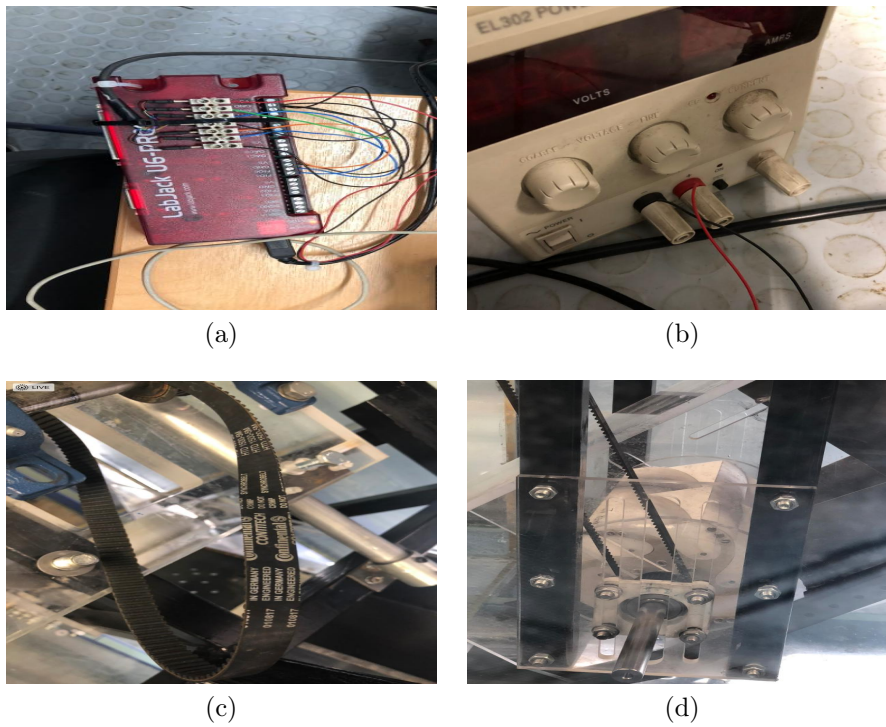
FIGURE 3.8: (a)- LabJack U6, (b)- Load celll, (c)- Belt, (d)-
Bearing

The drive train and the generator are used to transfer mechanical rotational
energy of the runner to the electrical energy as shown in Figure 3.9.
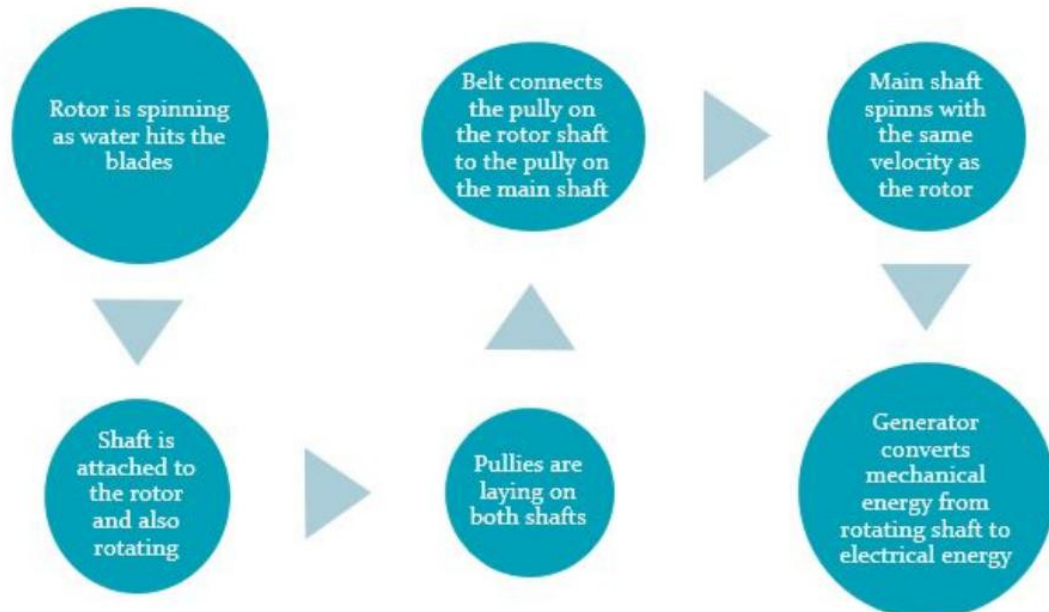
FIGURE 3.9: Mechanical to electrical energy conversion in a
spillway turbine system

Generator

When choosing a generator, the first choice to be made is between using a direct
current (DC) or alternating current (AC) generator. There are many reasons
why either DC or AC system would be chosen. Key advantages of using a
DC system is the ability to operate it without a load controller, and storage
batteries can be directly used in such systems. The AC system advantages
are the broader availability of AC system components and low costs. However,
direct battery storage is not possible using an AC system, but it is possible to
use rectifying units to charge DC batteries through an AC generator. Therefore,
an AC generator was used for spillway turbine testing. AC generators can be
3-phase or single-phase depending on how many coils are present. As the name
indicates, a single-phase AC generator has a single coil and power line and a
neutral line, which is a similar set-up to a DC generator. Three-phase AC
generators have three coils, three power lines and a neutral line. The principal
difference between a single-phase and a three-phase AC generator is in the
way the load is distributed in the wiers which determines their required size.
Therefore, the three-phase generators are often more cost-effective as they are
smaller than their single-phase equivalents (Harvey et al., 2009). AC generators
can also be classified as synchronous or induction generators. For spillway
turbine tests, DVE200 standard permanent magnet, synchronous, three-phase

AC generator was used. The technical drawing is given in Appendix D, and the generator used in laboratory tests is given in Figure 3.10.

FIGURE 3.10: DVE200 Permanent magnet, three phase off-the-shelf generator

Although losses between 3-7 % are expected (Harvey et al., 2009) the generator efficiency was tested (Runge, 2018) to quantify the losses and conclude at which rotational speed is this specific generator most efficient. The test was conducted by attaching the generator to the milling machine with variable speed control, and mechanical power was obtained by measuring torque and rotational speed with a torque transducer. Current and voltage meters were used to obtain electrical power at different resistances of 5, 7.5, 10,15, 20, 30, 40 and 50 Ω at rotational speeds of 60, 75, 100, 125, 150, 200, 250, 300, 350, 400 and 450 rpm.

The difference between mechanical and electrical efficiency is shown in Figure 3.11, indicating that the efficiency of this generator goes up to 85 % for low rotational speeds tested. The difference in hydrokinetic turbine efficiency when a mechanical break and this generator was used was about 12% for peak performance according to Runge (2018), which is in the same range as the milling machine test. The difference may come from friction and temperature losses in the milling machine tests. Overall, it was decided that although there are some expected losses, DVE200 generator is appropriate for use in laboratory testing of the spillway turbine as the rotational speeds are in the range where the generator shows high efficiency. Therefore, mechanical power was not tested in this case as it would overestimate the efficiencies that could be obtained in field testing in the future.
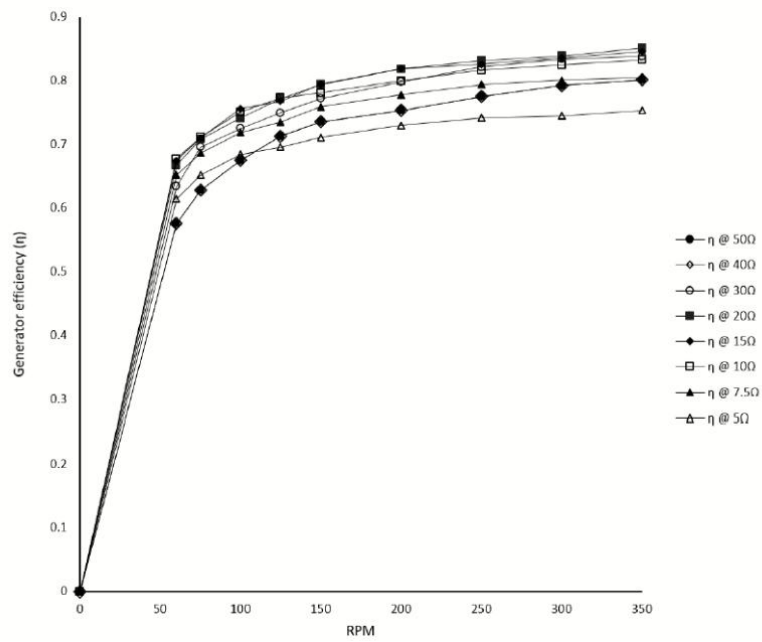
Figure 3.11: Mechanical and electrical efficiency of DVE200
generator (Runge, 2018)

Chapter 4

Spillway Turbine Development and Testing

4.1 Design Version I

4.1.1 Design of the Turbine

The initial design of the runner was inspired by the shape of the Savonius turbine with shaft positioning similar to the cross-flow turbine. The first objective was to determine how the number of blades and the blade clearance affects the performance of the runner. Therefore, two runners were manufactured, a six-bladed and a seven-bladed runner. Both runners were made of polyamide powder with a 3D printing technique called selective laser sintering or SLS, outlined in Appendix B.

Runner 1 (6 Blades)

The six-bladed runners with the supporting structure in exploded view are shown in Figure 4.1. This runner has six blades, it is 0.3 m wide and has a diameter of 0.2 m. Stainless steel, 0.02 m diameter runner shaft was split into two parts, supporting the runner through the middle opening from both sides. The acrylic disks of 0.01 m thickness were placed on both runner sides to protect the runner from side fiction in case of unwanted shifting during testing. The disks also provided a degree of structural stability and rigidity. See-through acrylic was chosen for the disks as it provides an insight into how the water moves the turbine. The diameter of the disks was 0.21 m which is marginally larger than the diameter of the runner. The disks were attached to the runner with 24 head cap screws on each side. The screws conform to British Standards (2004) BS ISO 4762:2004 and are stainless steel M4 x 40 mm. The blade clearance of

Runner 1 is 0.10 m.
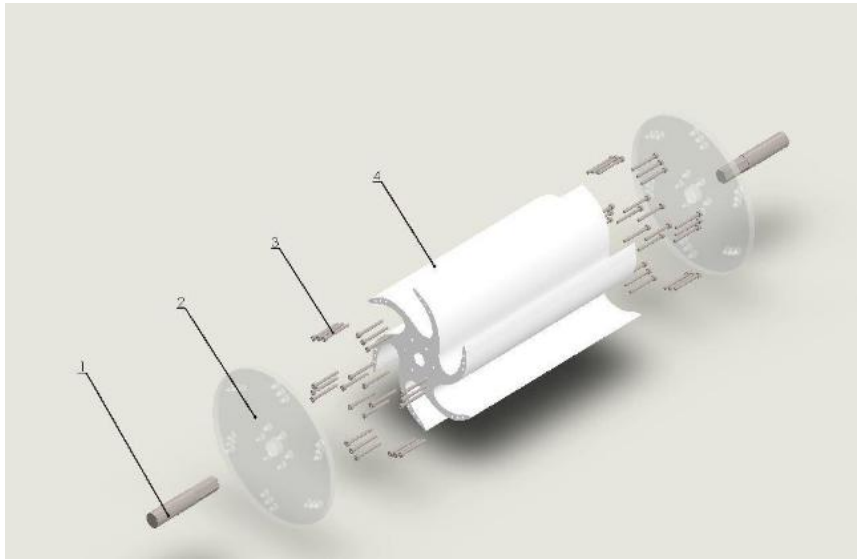
FIGURE 4.1: Exploded view of Runner 1-6 blades: 1- Runner shaft, 2- Acrylic disk, 3- Screws, 4- Runner
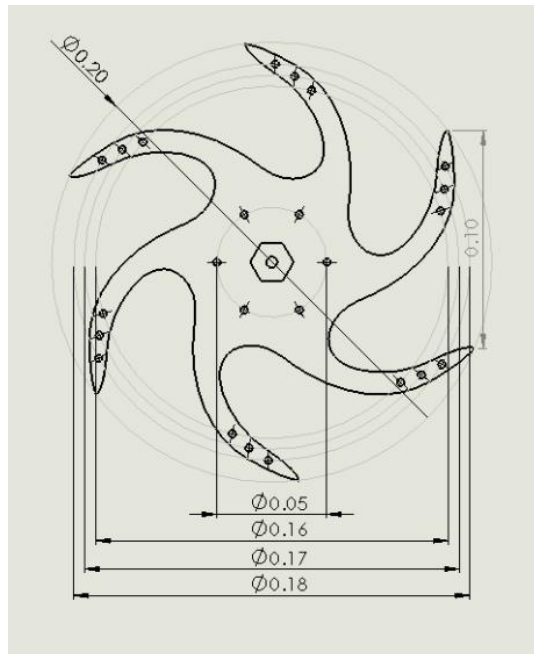
FIGURE 4.2: Runner 1 cross-section;all dimensions in metres

Runner 2 (7 Blades)

The seven-bladed runner is smaller in diameter than the six-bladed runner, while the other components were kept the same. The seven-bladed runner is shown in Figure 4.3. The runner is 0.3 m wide and has a diameter of 0.14 m.

The acrylic disks used on sides of the seven-bladed runners were also smaller and had a diameter of 0.141 m. Rather than using 24 M4 x 40 mm head cap screws, 20 were used on each disk. Both runner blades were designed with an idea of water pushing the blade when it hits it initially, but also when the water exits the blade, resulting in double force action within the blades. The blade clearance of Runner 2 is 0.06 m.

FIGURE 4.3: Runner 2-7 Blades
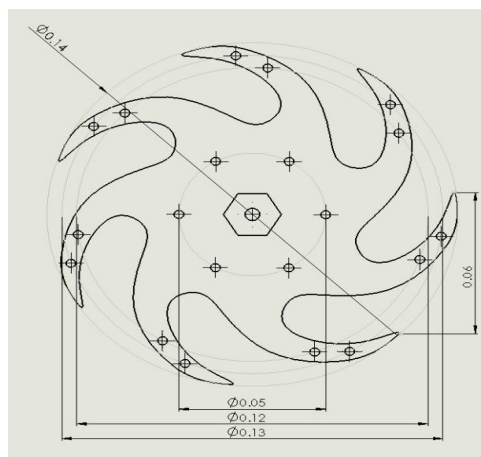
FIGURE 4.4: Runner 2 cross-section; all dimensions in metres
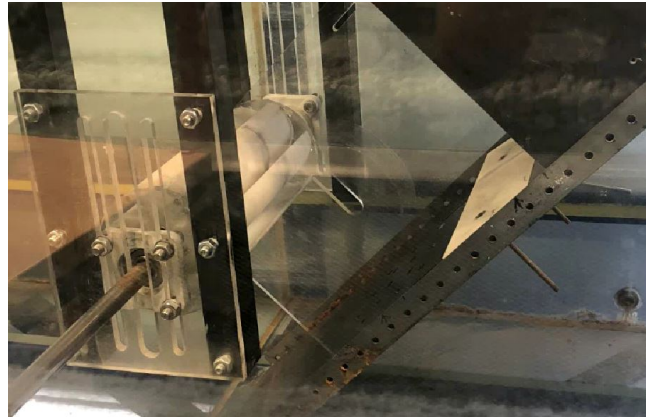
FIGURE 4.5: Runner 2-7 Blades in laboratory set up

Wedges

The wedge was introduced to the turbine design with an idea of directing and accelerating the water towards the blades. The wedges were placed on the down-sloping spillway channel, just before the runner. The wedge was sealed to ensure a smooth transition between the channel and the wedge, and minimum friction losses at the connection edge. Three different wedges were designed in the initial design stages and tested at different distances from the rotors. All three wedges have the same shape and width of 0.3 m. The design variable, in this case, is the wedge height which varied from 0.015 to 0.025 m. Wedge designs are given in Figure 4.6, and their dimensions were summarised in Table 4.1.
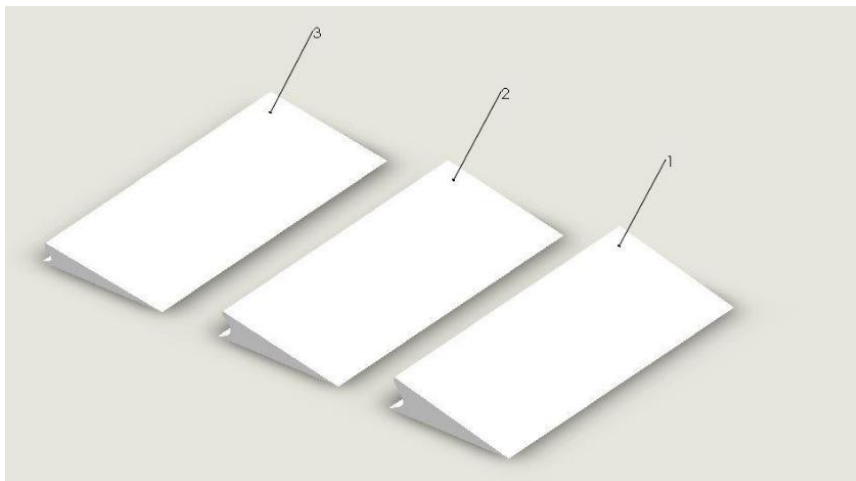
FIGURE 4.6: Wedge designs

TABLE 4.1: Wedge dimensions

Wedge	Height (m)
1	0.025
2	0.020
3	0.015

4.1.2 Design I Testing Method

Both rotors were tested in more than 250 different set-ups so conclusions can be drawn on the effect of the number of blades and the most appropriate position of the wedge. The full test list is given in Appendix A. As the testing method had many variables, a sketch of all changeable components is depicted in Figure 4.7. All variables and their descriptions are shown in Table 4.2 to clarify the testing method of Design I further.
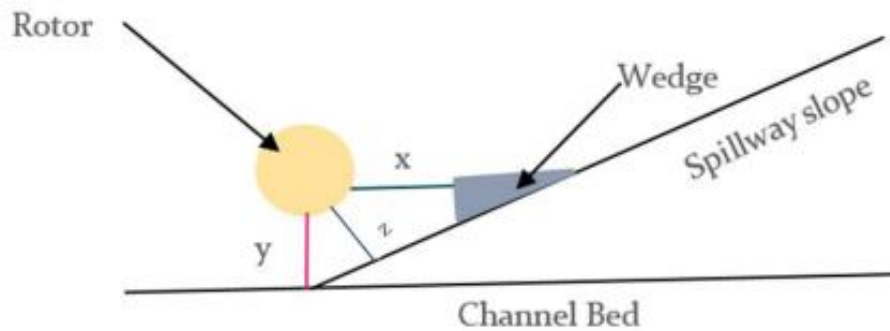
FIGURE 4.7: Design I testing method

TABLE 4.2: Variable names and descriptions

Variable name	Rotor		Wedge height variation			Wedge to rotor distance			Rotor to slope distance			Rotor to channel distance	
	R1	R2	W1	W2	W3	x_1	x_2	x_3	z_1	z_2	z_3	y_1	y_2
Description	6 blades	7 blades	0.025 m	0.020 m	0.015 m	0.02 m	0.04 m	0.06 m	0.005 m	0.02 m	0.04 m	0.385 m	0.395 m

The testing methodology is outlined in Figure 4.8. Results for all tests were presented on power coefficient (Cp) and torque (T) graphs.

Firstly, the six-bladed, Runner 1, was tested with a variety of discharges. Then, different wedges were tested at different runner horizontal distances (x). After, the vertical slope distance (z) was varied for all horizontal distances, all wedges and all discharges. By changing vertical slope distance (z), the runner to channel distance was changed too. Finally, when all tests were completed, the seven-bladed, Runner 2, was tested in the same manner for all variables described.
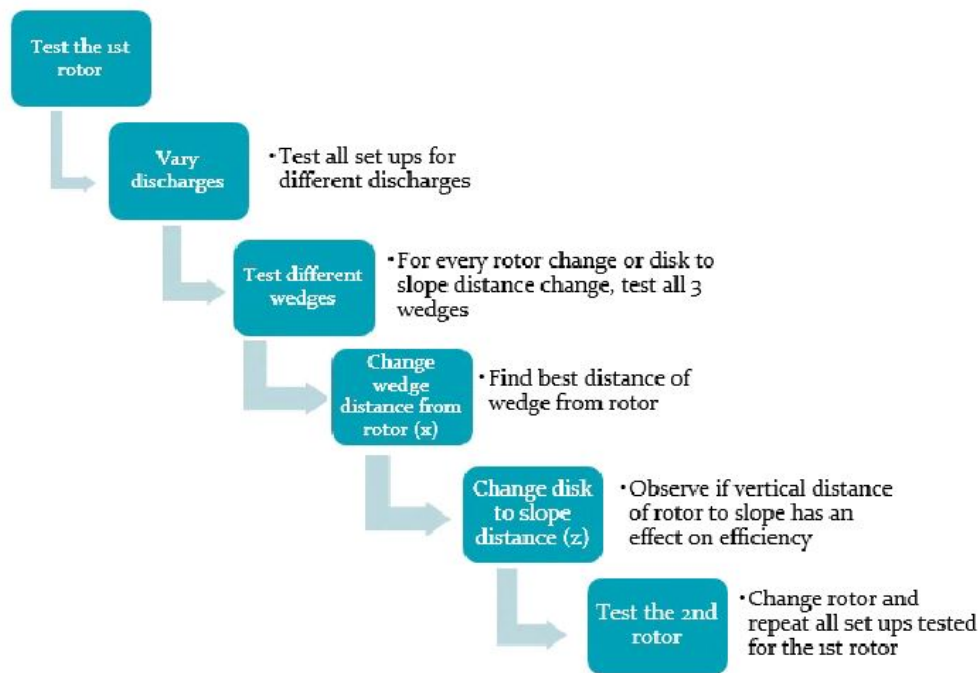
FIGURE 4.8: Design I testing method

Variation of all components mentioned resulted in significant system efficiency differences, outlined in the following section.

4.1.3   Design I Results

The testing results were presented in different subsections, in which different design components depicted in Figure 4.7 were varied. Firstly, the wedge design or the varying wedge height effect on the performance of both six-bladed and seven-bladed runners were analysed. Secondly, the distance of wedge to runner (x) effect on the performance was tested and analysed. Finally, the runner to vertical slope distance (z) effect on the turbine efficiency was investigated for both runners and all three wedges.

Wedge Height Effect on Turbine Efficiency

Both runners were tested with all wedge designs with varying heights, placed at several distances from the rotor disks (x). The wedges were labelled Wedge 1, 2 and 3 (W1, W2, W3) with heights of 0.025 m, 0.020 m and 0.015 m respectively, as shown in Figure 4.6. The results shown indicate that the wedge design had a significant effect on the overall efficiency of the turbine.

Runner 1, which had six blades, was placed at 0.385 m from channel bed (y_1). Minimum rotor to slope distance of 0.005 m (z_1) was used for comparison of

wedge height influence on the efficiency for both rotors and all wedges. Rotor 1 with different wedge heights testing results are shown in Figure 4.9. The maximum efficiency was achieved with Wedge 3 installed with the six blades Runner 1, reaching 25.06 %. The second-best performing set up was with Wedge 2, reaching 24.71 % efficiency and the worst performing was the set up using Wedge 1, with the efficiency of 11.16 %.
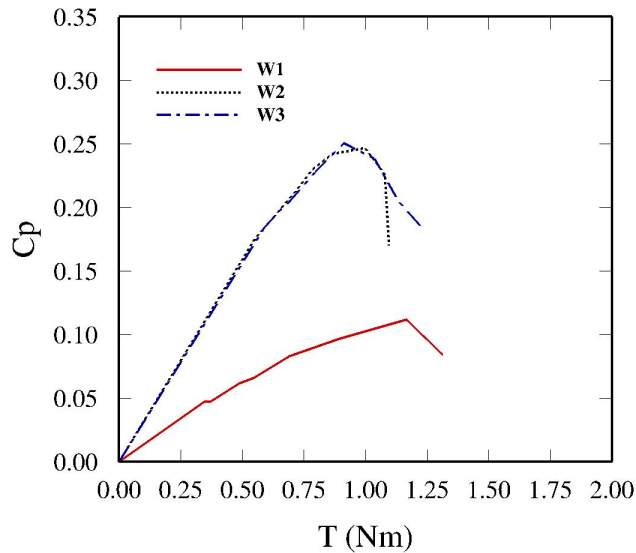
Wedge	Efficiency
Wedge 3	25.06 %
Wedge 2	24.71 %
Wedge 1	11.16 %

FIGURE 4.9: Wedge height effect
on Rotor 1 performance

Runner 2, which has seven blades, was placed at 0.395 m from channel bed (y_2) and the disk to slope vertical distance was kept to 0.005 m (z_1). Runner 2 with different wedge heights testing results are shown in Figure 4.10. The maximum efficiency was achieved with Wedge 3, reaching 9.99 %. The second-best performing set up was with Wedge 2, reaching 9.05 % efficiency.
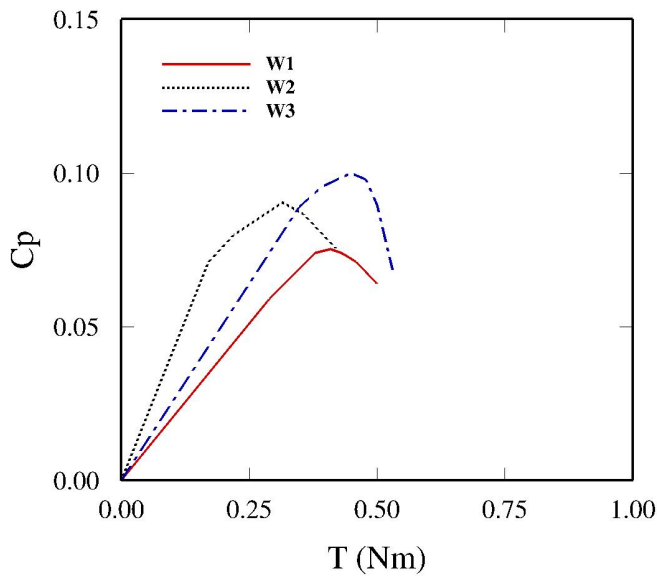
Wedge	Efficiency
Wedge 3	9.99 %
Wedge 2	9.05 %
Wedge 1	7.53 %

FIGURE 4.10: Wedge height effect
on Rotor 2 performance

Distance of Wedge to Runner (x)

All three wedges were tested with both runners at different horizontal distances
(x_1, x_2, x_3). Variation of the horizontal distance is the variation of x variable
depicted in Figure 4.7. The wedges were placed at 0.02, 0.04 and 0.06 m away
from the rotors for all tests. For Runner 1, disk to slope distance (z_1) was
kept at 0.005 m, and distance of shaft from channel bed (y_1) was kept at 0.385
m. Comparison of the effect the horizontal distance of wedge to runner has on
Runner 1 is given in Figure 4.11.

The best performance for Runner 1 was achieved with Wedge 3 at 0.02 m hor-
izontal distance (x_1), with the efficiency of 25.06 %. The next best performing
set up was Wedge 2 at 0.02 m distance, with the efficiency of 24.71 %.

TABLE 4.3: 0.08 m
distance

Wedge	Efficiency
Wedge 3	5.03 %
Wedge 2	15.36 %
Wedge 1	13.43 %

In one case when the 6 bladed run-
ner was tested at 0.02 m from slope
vertical distance (y_2), wedges were
test at 0.08 m horizontal distance.
These results are summarised in Ta-
ble 4.3.

Runner 2 was also tested at 0.005 m disk to slope distance (z_1), with the shaft
at 0.395 m from the channel bed distance (y_2). Analysis of the effect of distance
of the wedges to the seven-bladed rotor is shown in Figure 4.12.
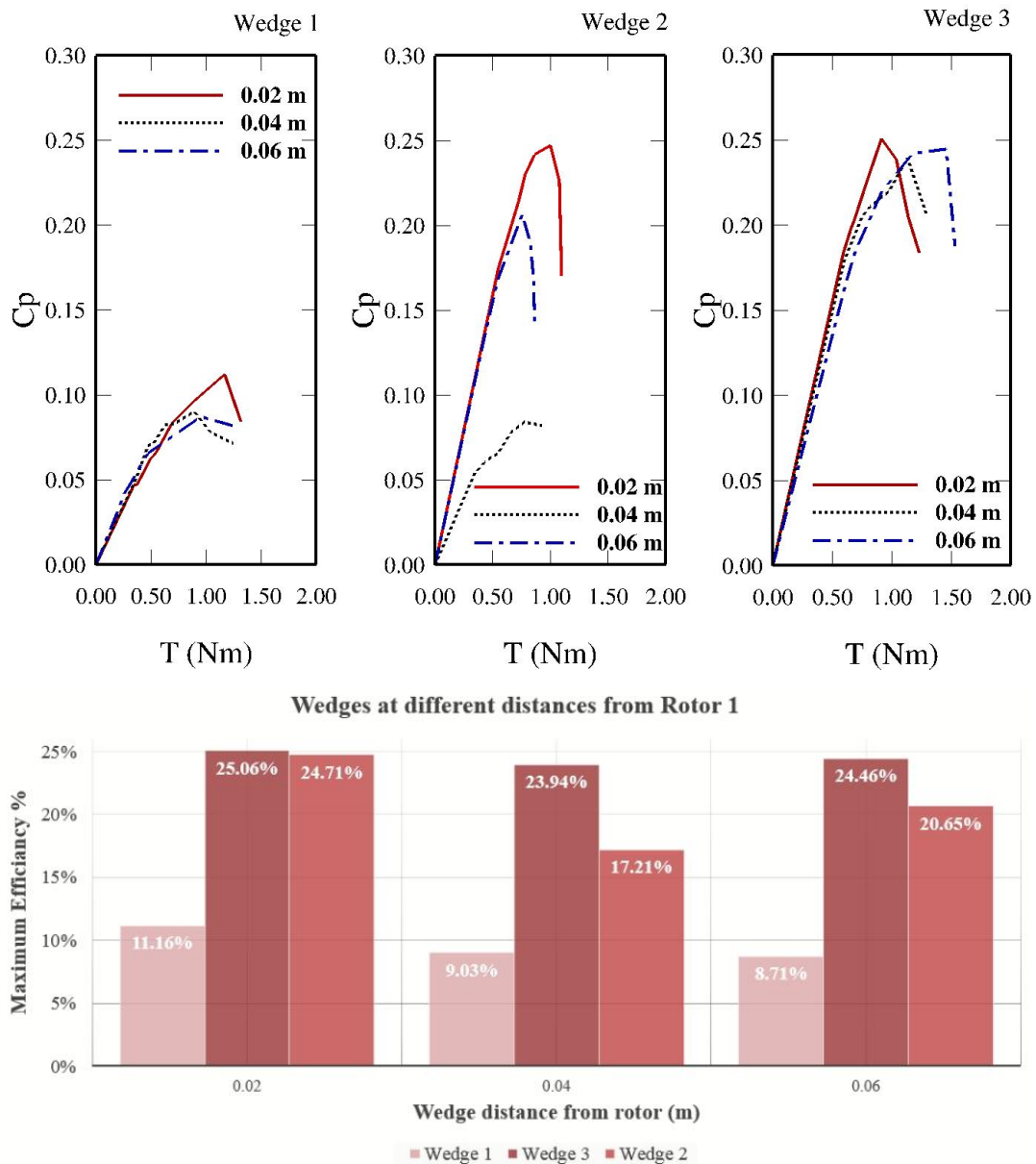
FIGURE 4.11: Wedge distances effect on Rotor 1

In case of testing Runner 2 at 0.005 m vertical slope distance, there was not enough clearance to test wedges at 0.06 m horizontal distance, so the distance tested was 0.055. As wedges did not perform well at higher distances from the rotor, this adjustment is not believed to have a significant negative impact on the results and the analysis. The best performance for Runner 2 was achieved with Wedge 3 at 0.02 m horizontal distance, with the efficiency of 9.99 %. The next best performing set up was Wedge 3 at 0.04 m distance, with the efficiency of 9.43 %.
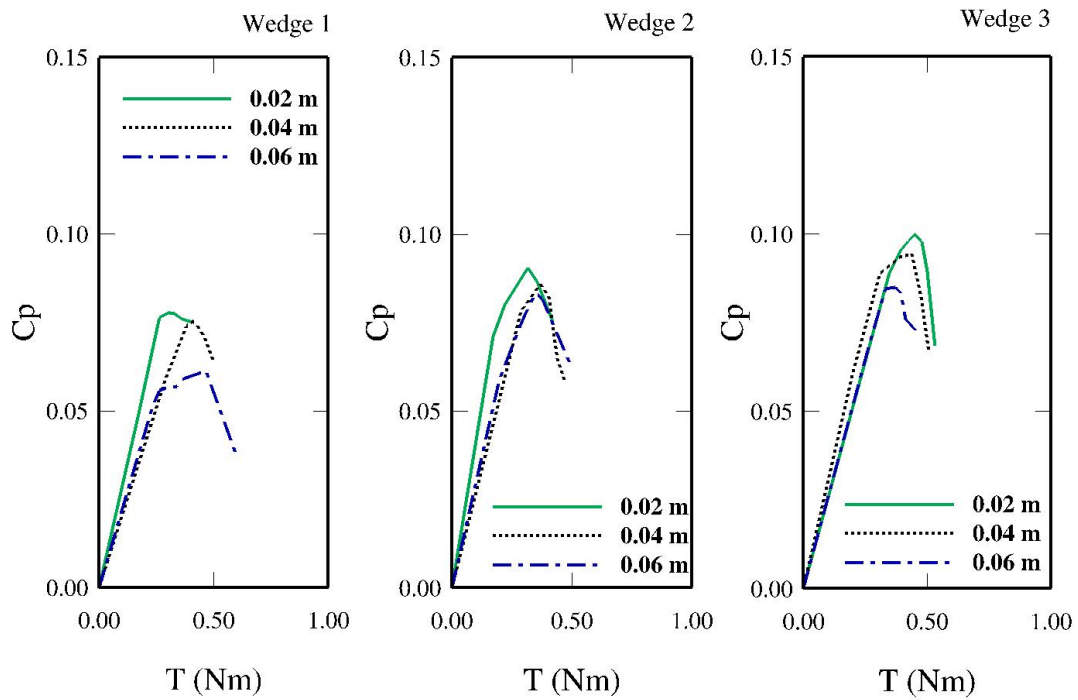
FIGURE 4.12: Wedge distances effect on Rotor 2

Runner to Slope Vertical Distance (z)

Both runners were tested at different distances (z) from the slope. For Runner 1, the shaft distance from channel bed (y_1) was kept at 0.385 m. For Rotor 1, the minimum possible vertical distance of 0.005 m and 0.02 m distance were both tested.

TABLE 4.4: Rotor 1 to slope distance (z) effect with Wedge 3

Horizontal distance x (m)	Efficiency z=0.005 m	Efficiency z=0.02 m
0.02	25.06 %	11.16 %
0.04	23.94 %	16.89 %
0.06	24.46 %	6.53 %

In order to analyse the effect of the runner to slope distance, 0.015 m high Wedge 3, that shows best performance was tested for all three horizontal intervals at 0.005 m and 0.02 m vertical slope to runner gaps. Figure 4.14 indicates that the efficiency achieved for minimum slope to runner distance is 55.6 % higher than the performance obtained when runner to slope gap is increased to 0.02 m. It can be noted that there is a significant drop in performance for all three horizontal distances of the wedge to the runner when the z is 0.02 m.
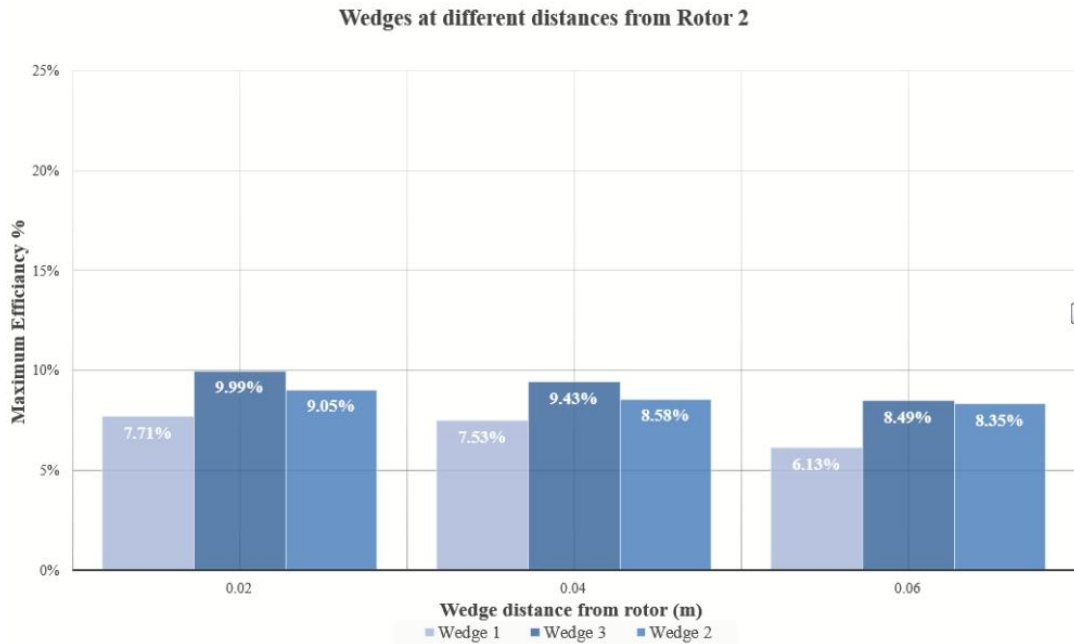
FIGURE 4.13: Wedge distances effect on Rotor 2
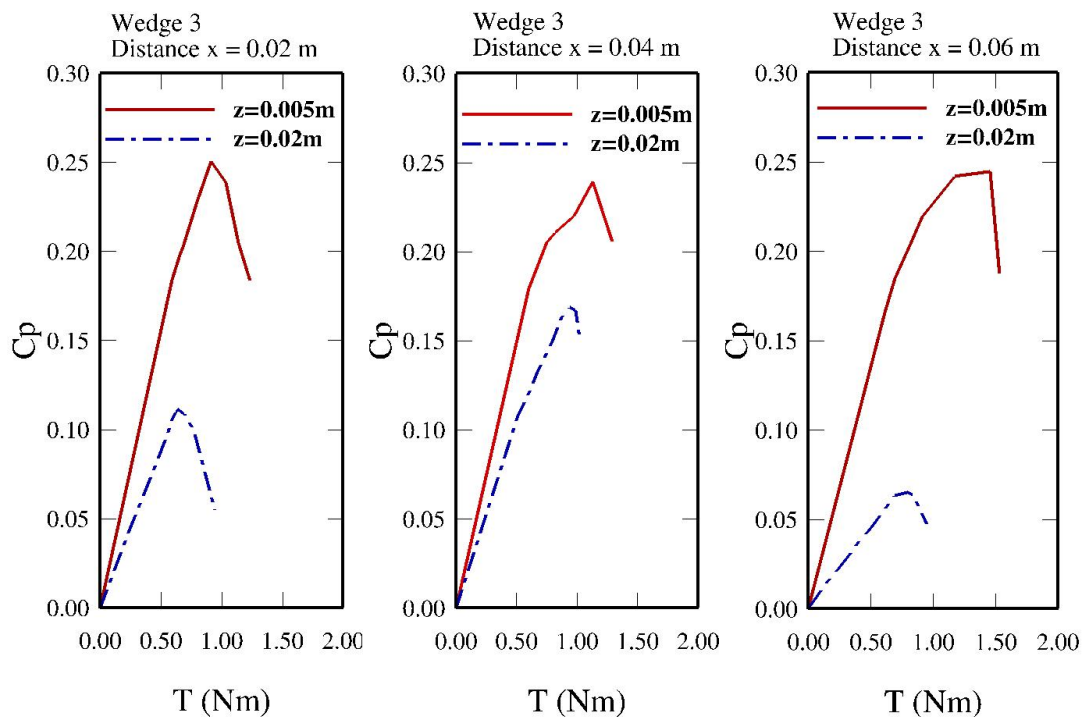
FIGURE 4.14: Rotor 1 to slope distance (z) effect with Wedge 3

Wedge 2 at 0.02 m horizontal distance from runner also shows better performance for slope to runner vertical distance of 0.005 m. The turbine performance for this set up was 24.71 %, comparing to a considerably lower value of 10.04 % achieved with z_2 value of 0.02 m. The same trend was observed with other wedge to rotor horizontal spans as summarised in Table 4.5. Overall, Wedge 2
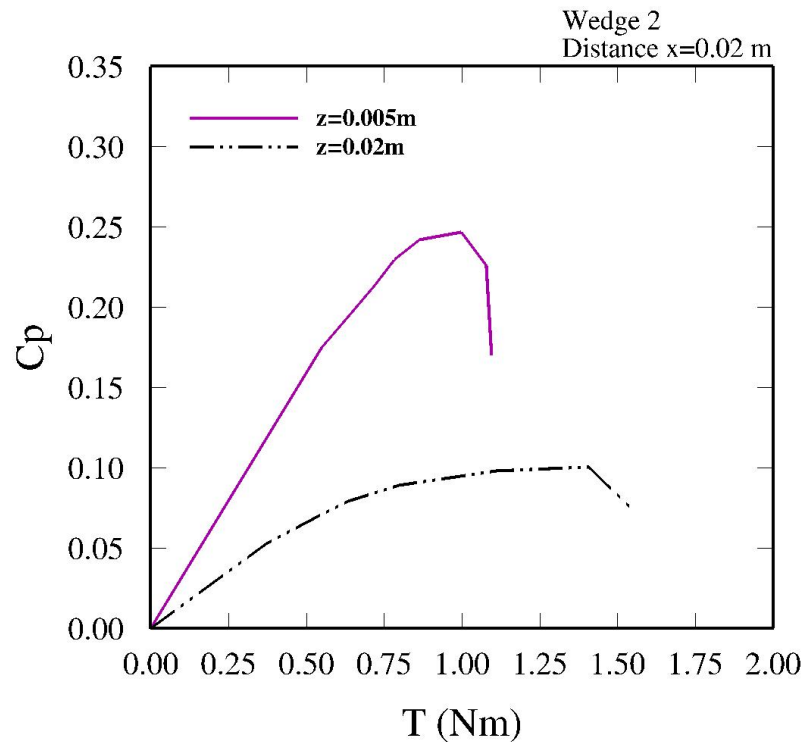
FIGURE 4.15: Runner 1 to slope distance (z) effect with Wedge
2

tests with z_1 distance of 0.005 m exhibited twice the efficiency compared to the
testes conducted with z_2 equal to 0.02 m.

TABLE 4.5: Runner 1 to slope distance (z) effect with Wedge 2

Horizontal distance x (m)	Efficiency z=0.005 m	Efficiency z=0.02 m
0.02	24.71 %	10.04 %
0.04	17.21 %	9.48 %
0.06	20.65 %	10.55 %

Although Wedges 3 and 2 perform significantly better for the lower Runner 1
to slope gap, this is not the case when Wedge 1 was tested. As indicated in
Figure 4.16, having z variable of 0.02 m outperforms the set up with 0.005 m
vertical distance of slope to the runner, for all three horizontal wedges to runner
distances (x) in case of Wedge 1.

Table 4.6 indicates that the efficiency achieved for minimum slope to runner
distance is 55.3 % lower than the performance obtained when runner to slope
gap is increased to 0.02 m for 0.02 m x distance. It can be noted that there
is a rather significant drop in performance for all three horizontal distances of
Wedge 1 to Runner 1 when z is 0.005 m.
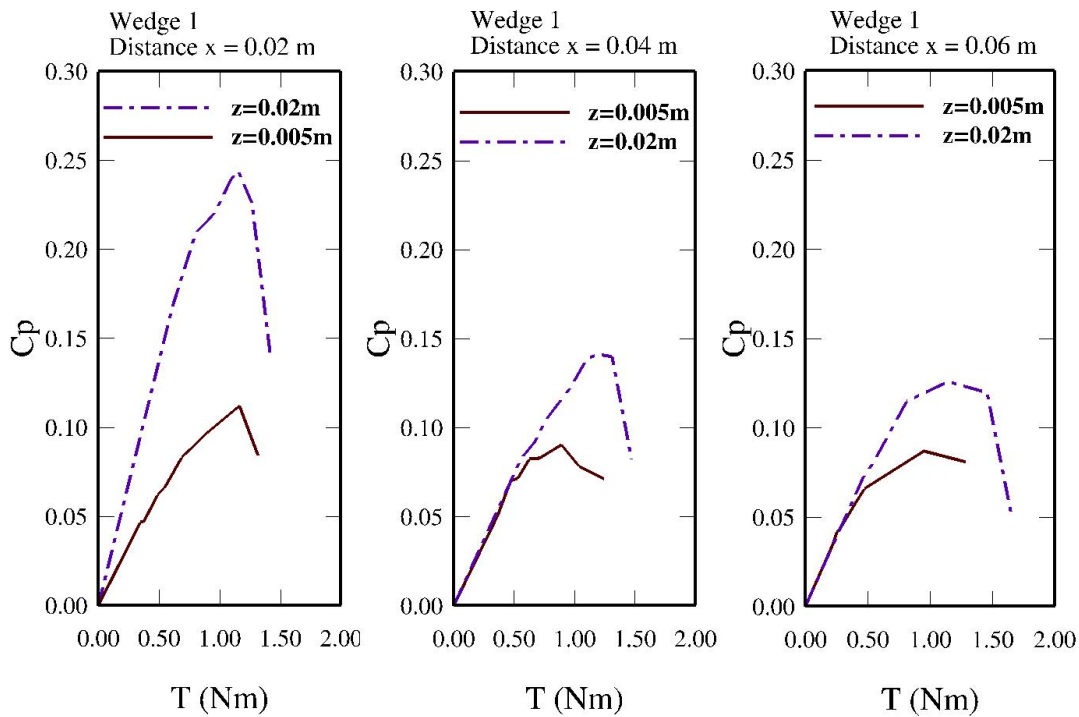
FIGURE 4.16: Runner 1 to slope distance (z) effect with Wedge
1

TABLE 4.6: Runner 1 to slope distance (z) effect with Wedge 1

Horizontal distance x (m)	Efficiency z=0.005 m	Efficiency z=0.02 m
0.02	11.16 %	24.43 %
0.04	9.03 %	14.14 %
0.06	8.71 %	12.61 %

As Wedge 1, which was the tallest manufactured wedge, showed improvement in performance when it was tested for vertical slope to runner distance of 0.02 m, an idea to test an even taller wedge for this specific set up arose. An improvised wedge of height 0.035 m, labelled Wedge 4, was installed in the set-up. Results of testing this wedge are given in Figure 4.17, with maximum efficiency of 15.51 % achieved for 0.02 m horizontal distance and 14.08 % for 0.04 m horizontal distance x. This is a drop in performance comparing to Wedge 1 when the same x and z values were tested.

Because Runner 2 is smaller in diameter than Runner 1, laboratory set-up allowed for a further slope to runner distance of 0.04 m to be tested along with 0.02 m and 0.005 m z distances. Shaft to channel bed space (y_2) was kept to 0.395 m for all results presented below.
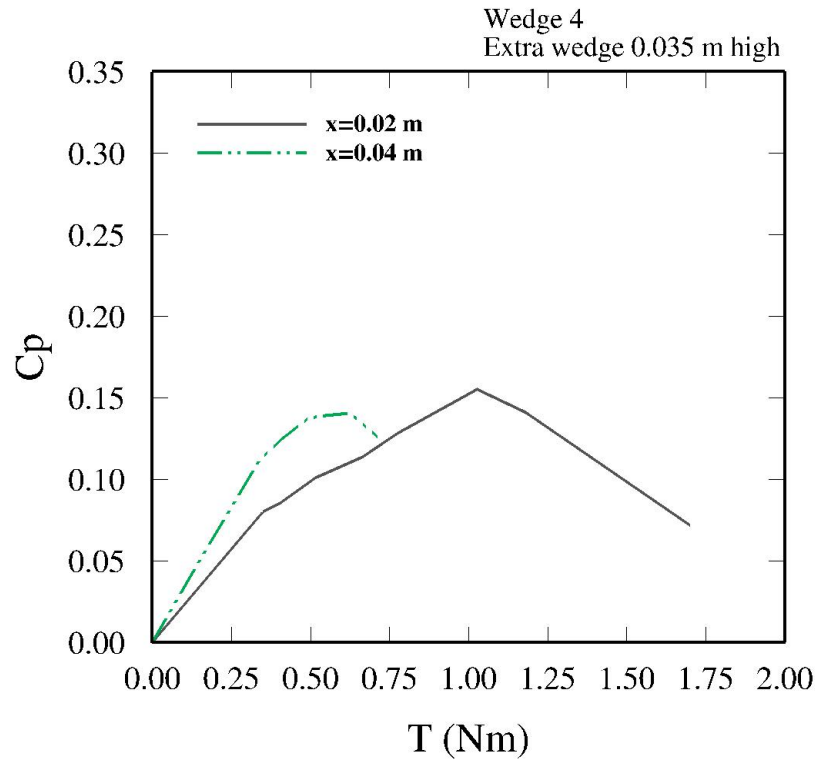
FIGURE 4.17: Improvised Wedge 4 and slope to Runner 1 distance z= 0.02 m
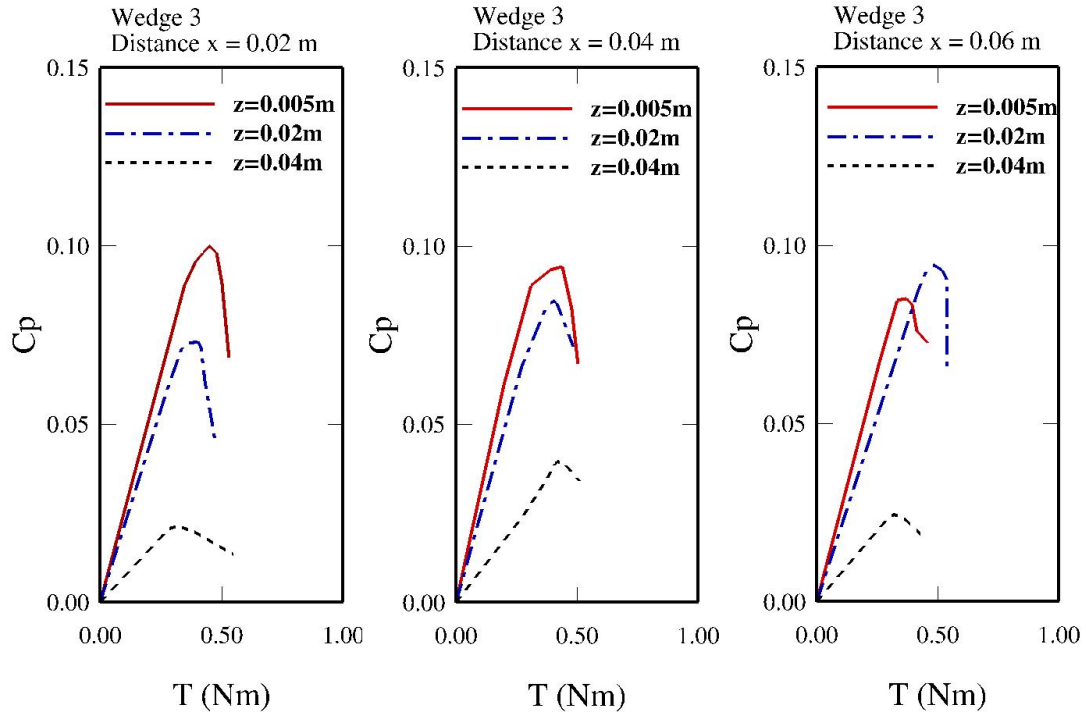
FIGURE 4.18: Rotor 2 to slope distance (z) effect with Wedge 3

Wedge 3 in conjunction with Runner 2 was tested at all three horizontal distances and the best performing set up was at 0.02 m x distance and 0.005 m

TABLE 4.7: Runner 2 to slope distance (z) effect with Wedge 3

Horizontal distance x (m)	Efficiency z=0.005 m	Efficiency z=0.02 m	Efficiency z=0.04 m
0.02	9.99 %	8.20 %	2.10 %
0.04	9.43 %	8.46 %	3.94 %
0.06	8.49 %	9.44 %	2.44 %

slope to channel distance, which was also the case when Runner 1 was tested. The differences in the efficiency are not as significant as when Runner 1 was tested with different z distances. The peak obtained efficiency was 9.99 % as shown in Figure 4.20
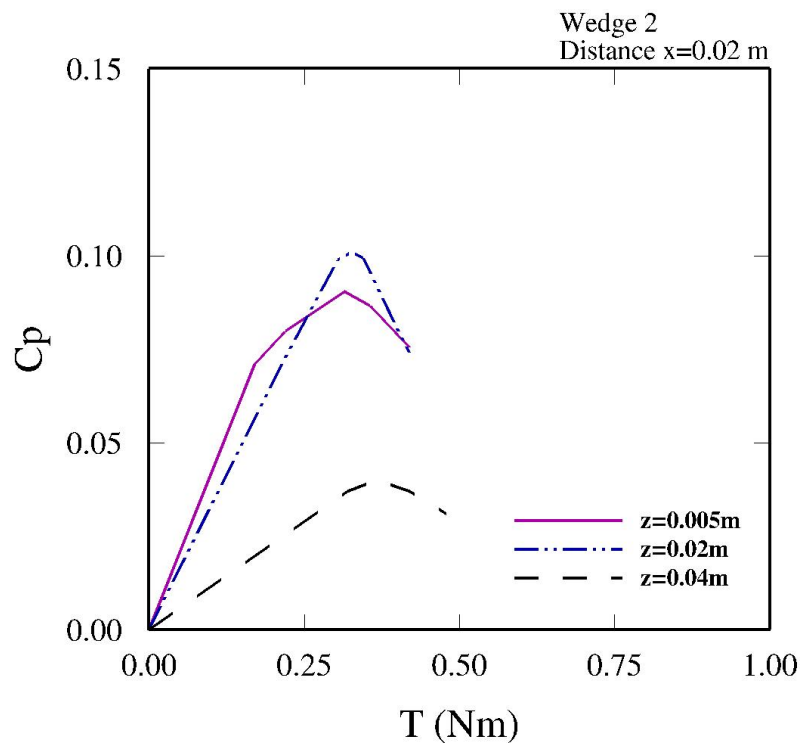
FIGURE 4.19: Rotor 2 to slope distance (z) effect with Wedge 2

Wedge 2 at 0.02 m horizontal distance from runner also shows better performance for slope to runner vertical distance of 0.02 m. The turbine performance for this set up was 10.09 %, comparing to a lower value of 9.05% achieved with a z value of 0.005 m and 3.95% when z distance of 0.04 m was used. The same trend was observed with other wedge to rotor horizontal spans as summarised in 4.9. Overall, out of all tests conducted for Runner 2, Wedge 2 at 0.02 m horizontal distance and runner to slope distance of 0.02 m shows the highest efficiency of all set-ups tested.

TABLE 4.8: Runner 2 to slope distance (z) effect with Wedge 2

Horizontal distance x (m)	Efficiency z=0.005 m	Efficiency z=0.02 m	Efficiency z=0.04 m
0.02	9.05 %	10.09 %	3.95 %
0.04	8.58 %	9.03 %	4.96 %
0.06	8.35 %	9.42 %	6.17 %
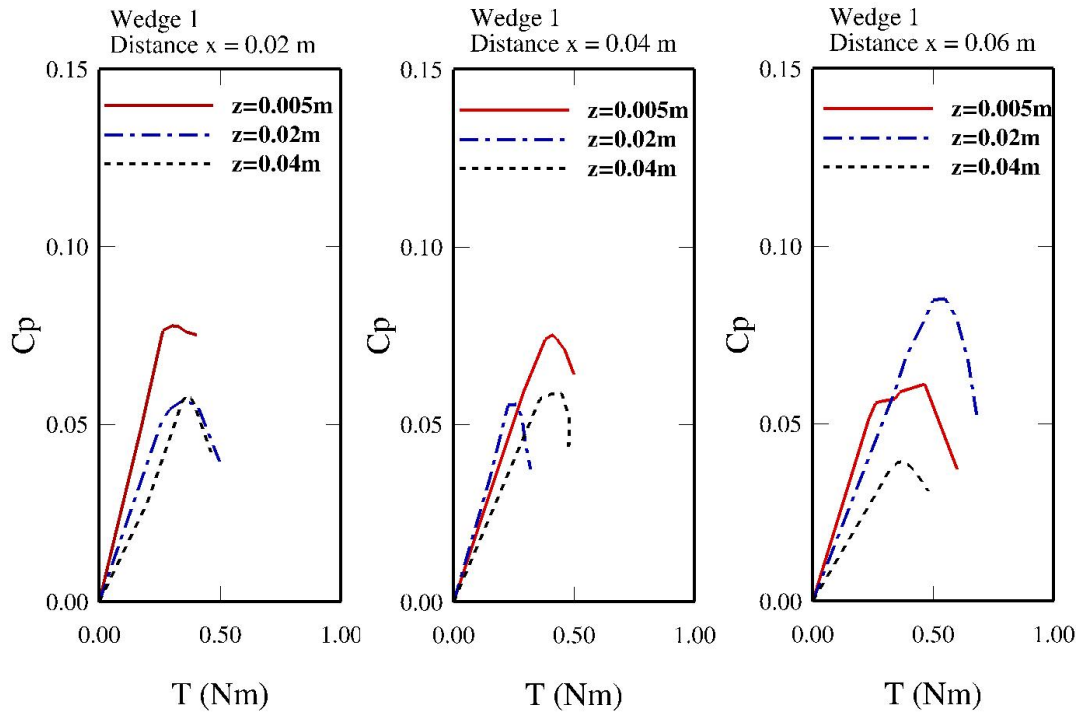
FIGURE 4.20: Rotor 2 to slope distance (z) effect with Wedge 1

TABLE 4.9: Runner 2 to slope distance (z) effect with Wedge 1

Horizontal distance x (m)	Efficiency z=0.005 m	Efficiency z=0.02 m	Efficiency z=0.04 m
0.02	7.77 %	5.64 %	5.85 %
0.04	7.53 %	5.57 %	5.88 %
0.06	6.13 %	8.53 %	7.76 %

Wedge 1 and Rotor 2 tests depicted in Figure 4.20 indicate that the best performing set up was for x 0.06 m and runner to slope distance of 0.02 m. For this x distance, the performance was improved for 0.04 m z value (8.53 %), comparing to the z value of 0.005 m (6.13 %). However, the tests conducted at a z value of 0.005 m are most consistent, and there are no significant differences in efficiency for different x values tested.

Variation of Discharge

All tests were undertaken in a range of discharges from 9 to 39 l/s, varied using the axial pump and measured using a weir, both described in Chapter 3. The discharge was varied for all tests conducted in order to determine for which flow the turbine performs best. It was noted that the amount of water hitting the blades significantly impacts the overall turbine efficiency. Best performing Runner 1 set up with Wedge 3, the horizontal distance of wedge to the runner of 0.02 m and minimal runner to slope distance of 0.005 m was plotted in Figure 4.21. For comparison purposes, the best performing Runner 2 set up with Wedge 2 at 0.02 m horizontal distance (x_1) from the runner and slope to runner distance (z_2) of 0.02 m. It can be noted from the plotted Figure that there is a sharp increase in efficiency when the discharge reaches a certain limit. This is because, at a specific discharge, smoother operation of the turbine is achieved. The same trend was observed for other variable arrangements tested with both runners.
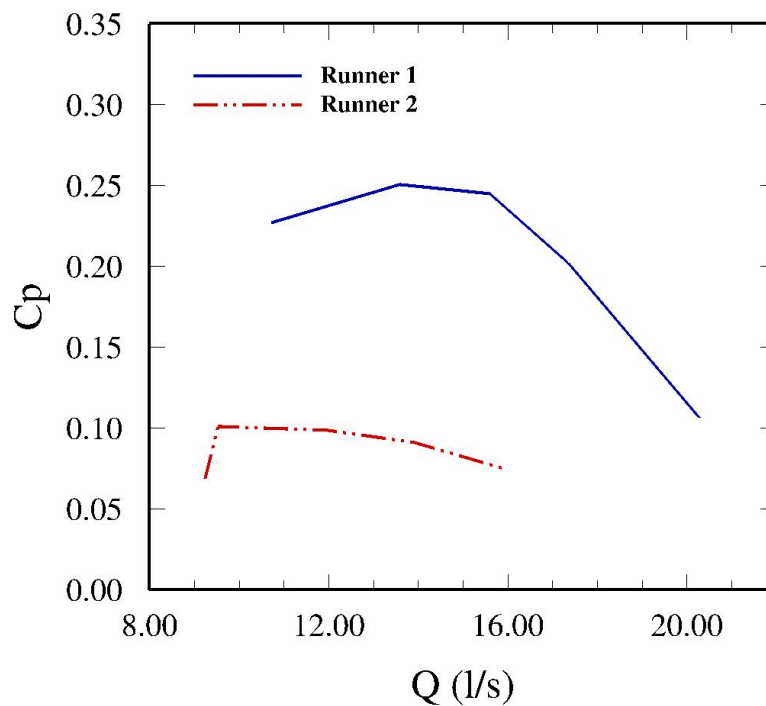
FIGURE 4.21: Variation of discharge and efficiency for both runners

4.1.4 Design I Discussion and Summary

After testing both rotors at varying discharges, with all three wedges at different distances, while also alternating slope to runner vertical distance, it was noted

that the six-bladed, Runner 1 shows significantly better performance than the seven-bladed, Runner 2. For the best performing Runner 1 set up, with Wedge 3 at 0.02 m (x_1) horizontal distance and 0.005 m (z_1) slope to runner distance, the efficiency achieved was 25.06 %. The best performing Runner 2 set up, with Wedge 2 at 0.02 m (x_1) distance and 0.02 m (z_2) distance only achieves efficiency of 10.09 %. Therefore, it can be noted that Runner 1 performance is 59.7 % increased in efficiency comparing to the performance achieved by Runner 2. It was observed during testing that the seven-bladed runner performs poorly due to a too narrow blade clearance of 0.06 m, which causes significant splashing and flow blocking. A lower number of blades and larger diameter of Runner 1 allowed for larger blade clearance of 0.1 m, which resulted in higher and more consistent efficiency values.

The height of the wedge had a significant impact on the performance, as shown in Figure 4.10 for Runner 1 and 4.11 for Runner 2. For Runner 1, Wedge 3 performance at x_1=0.02 m and z_1=0.005 m distances is 1.39 % increased to performance of Wedge 2 and 55.47 % increase to performance obtained with Wedge 1. For Runner 2, Wedge 3 performance at x_1=0.02m and z_1=0.005 m distances are 9.49% increased from the performance of Wedge 2 and by 24.62 % better than the performance of Wedge 1.

However, the height of the wedge is not the only factor, and the distance of the wedge to the runner (x) plays a significant role in the operation of the spillway turbine. In case of Runner 1 at the runner to slope distance of 0.005 m (z_1), all three wedges perform best when the gap from runner to wedge was kept to a minimum of 0.02 m (x_1). Moreover, in case of Runner 2 at the same runner to slope (z_1) spacing, the best performance was also achieved when the horizontal gap between the wedge and the runner was kept to 0.02 m (x_1). For both runners, the differences in performance from 0.04 m (x_2) and 0.06 m (x_3) tests were slight.

Variation of the runner to slope vertical distance (z) showed to be a large influence on the performance quality for both runners tested. In case of the 6 bladed runner, 0.005 m (z_1) and 0.02 m(z_2) values were tested for all three wedges at all three horizontal distances (x_1, x_2, x_3). The laboratory environment did not allow for a z_3 = 0.04 m slope to runner distance to be tested in case of the larger, six-bladed runner. The results indicate that the performance is better when z_1 gap was used. In the case of Wedge 3 at 0.02 m x separation, the performance decreases by 55.47 % when z value is increased from 0.005 m to 0.02 m. The decrease is even larger in case of Wedge 3 at 0.06 m separation, where the performance decreases by 73.3 %. Wedge 2 also performs

significantly better for slope to runner distance of 0.005 m. However, Wedge 1 performs much better when z_2 distance was implemented. For Wedge 1 at 0.02 m x variable, the performance increases by 54.32 % when the z variable is increased from 0.005 m to 0.02 m. The horizontal distance of 0.08 m was tested just for Runner 1 placed at z_2 =0.02 m as the laboratory set up allowed for this additional variation. These tests showed no further improvements to the overall turbine performance. Runner 2 was tested for 0.005, 0.02 and 0.04 m (z) as it was smaller in diameter, and it was possible to further increase the slope to runner vertical distance. Similarly to conclusions drawn from Runner 1 tests, the seven-bladed runner with Wedge 3 also gives the best performance when z_1 value of 0.005 m was used at 0.02 m x horizontal gap. However, the best performing set up was achieved when Wedge 2 was tested at x=0.02 for z_2 slope to runner distance of 0.02 m. The difference between this arrangement and when Wedge 3 was tested at 0.02 m (x), and 0.005 m (z) is only 1 %. The performance of Runner 2 tested with Wedge 1 is best when x of 0.06 m was used at z_2=0.02 m. During testing, it was noticed that the water tends to build up under the rotor, and the importance of testing different vertical slope to runner distances is in observing how this amount of water can be reduced. More water build-up was noticed in Runner 2 tests.

All tests were conducted under a variety of discharges, ranging from 9 l/s to 39 l/s. During testing, it was observed that a significant jump in efficiency is observed when a certain amount of flow is reached. This amount of flow necessary for the smooth operation of the turbine is dependant on the wedge height, the distance of the wedge and the slope distance to the runner. The performance drops gradually after the peak performance flow is reached, mainly due to increased splashing that accompanies the larger discharges.

The most common observable issue during testing was the water build-up at the rotor, just after the wedge. Another observable issue is a large amount of splashing. The splashing indicates that a significant amount of flow energy is not being converted into electrical energy. These two issues are addressed in the next section, in which the Design II is outlined. The design revision provides a solution to both, by providing an improved water run-off system underneath the rotor and by introducing guide vanes into the runner blades to reduce the splashing.

To conclude, Rotor 1 performs best in combination with the lowest, Wedge 3, when it is placed 0.02 m from the rotor. The optimum distance from the runner to the slope is found to be 0.005 m for the six-bladed runners. Rotor 2 also performs best with the lowest, Wedge 3 when it is placed 0.02 m from the

rotor and when the rotor to slope distance is kept to 0.005 m. However, the best performance for 0.02 m vertical slope to runner distance is when Wedge 2 is installed at 0.02 m from the runner. As the six-bladed rotors performed significantly better in all tests, it was chosen over the smaller Rotor 2, for design improvements. The wedge height chosen for further design advancements was 0.015 m high Wedge 3. Finally, it can be concluded that the insufficient release of water from the rotor causes the accumulation of water between wedge and rotor when a specific flow rate is reached. Consequently, a further increase in flow rate is restricted as the efficiency drops. Therefore, the design of blades and the flow directing mechanism, the wedge, was adjusted in such a way that the water is guided on its path in and out of the turbine rotor.

4.2   Design Version II

4.2.1   Design II of Runner and Isle Wedge

Runner 1, in combination with Wedge 3, showed the best performance in the previously described Design I tests given in the first section of this chapter and were both taken into further consideration in the revised design. A couple of observable issues were identified during design I testing stage. One of these issues was the water pile up before the runner, and the other was a significant amount of splashing. These issues were addressed in the revised design by:

- **Guiding the water into the rotor** - Wedge 3 (0.015 m high) was replaced by a stainless steel isle wedge which funnels the flow to the centre of the rotor and provides run-off space to the right and left-hand side.

- **Guiding the water through the rotor** - A semi-circular inserts (cups) were placed in each runner blade which deflects the water jet by 180 °from the centre to the right and left-hand side.

- **Providing more productive water run-off when it exits the rotor** - The spillway floor under the runner was opened in order to release the water as quickly as possible and reduce water pile up during laboratory testing.

Two variations of the second design update were considered and described in this chapter. For both variations, the six-bladed Runner 1 was used and adjusted for further testing. Version A is given in Figure 4.22 and Version B is shown in Figure 4.23.

Meeting of objectives listed was attempted through the improved design of both the runner and the wedge, as shown in Figure 4.22. The design presented in

this Figure consists of the Design II Runner A and Isle Wedge A.
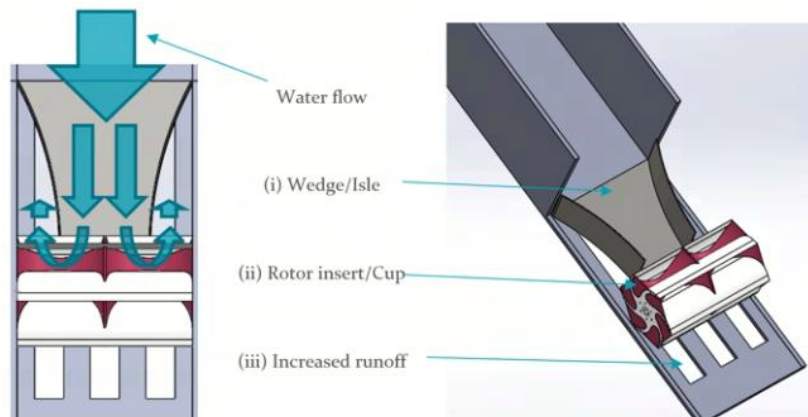
FIGURE 4.22: Top and side view of spillway turbine Design II
(Runner A and Isle Wedge A)

FIGURE 4.23:
Runner B

Another variation of Design II consisted of Runner version B shown in Figure 4.23. The difference in Design II versions A and B is in the number of guide vanes in both the runner and the isle wedge.

The Runner

The first decisions in developing and testing Design II was the decision to stick to the larger six-bladed runners from Design I and conduct all future testing using Runner 1. The critical change in the runner design was the placement of either version A inserts (2 cups) or version B inserts (4 cups), which guide the funnelled inflow through the blade by redirecting it towards the side-walls. Here, the flow is not just discharged and out of the way from the inflow direction, but also deflected by 180 °, which results in a significant boost of extractable energy. The drawings of two inserts are shown in Figure 4.24. Both were manufactured using the same technique used for runner manufacturing (SLS), outlined in Appendix B. The inserts were made in such way to ensure easy installation and changing of them, and were attached to the runner with same screws used for disk to runner attachments. End-plates were also used in the runner set up, although they are not presented in the drawings shown in this section.
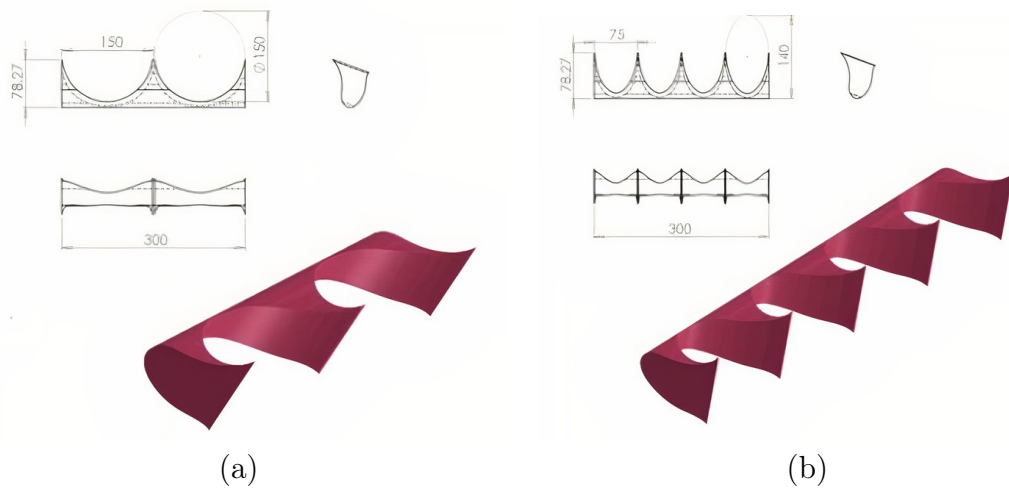
FIGURE 4.24: (a) Version A - 2 cup inserts; (b) Version B - 4
cup inserts

Isle Wedge

The isle wedge was made out of 0.0025 m thick stainless steel which was cut
and welded to a shape shown in Figure 4.25.
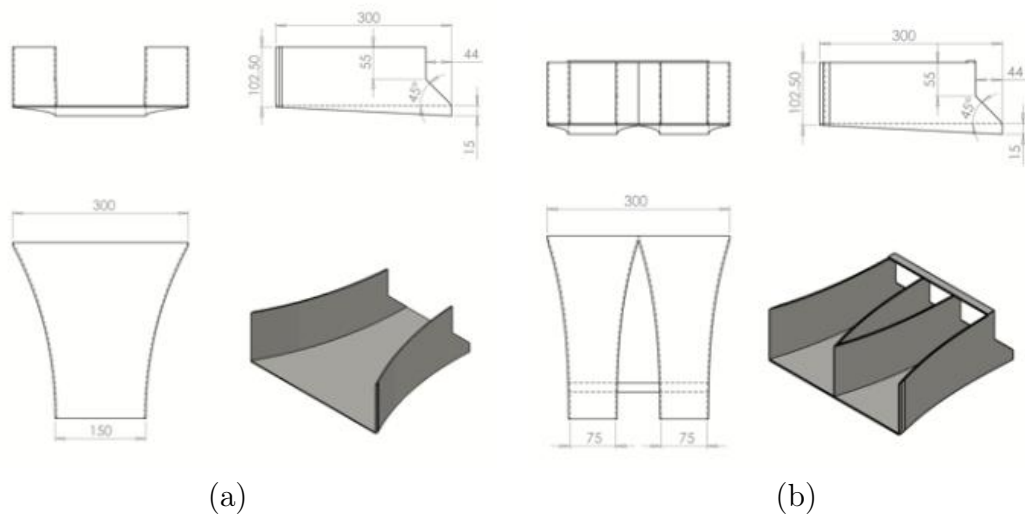
FIGURE 4.25: (a) Version A isle wedge; (b) Version B isle wedge

The purpose of this wedge re-design was to direct and accelerate the water flow
towards the runner cups in a more precise manner than Design I wedge did. Be-
sides, the flow was funnelled in the horizontal plane by bending side-walls. The
isle wedge was 0.015 m high, as this wedge height showed the best performance
during initial testing. Two versions of the wedge were manufactured. Version
A isle wedge was meant for use in conjunction with the runner with version A
cup inserts and version B isle wedge was intended for use with 4 cup, version B
runner inserts. The wedge was placed 0.02 m horizontally from the runner as

this positioning showed the best performance in design I testing.

FIGURE 4.26: Enclosed isle wedge A

During testing, it appeared that the splashing at the isle wedge entrance is significant. Introducing a see-through acrylic lid to the isle wedge A was imagined as a potentially feasible solution. This isle wedge is given in Figure 4.26, and it will be refereed to as 'enclosed isle wedge A'.

Increased Run-off

To ensure sufficient discharge of water directed to the runner, the spillway bed was opened as depicted in Figure 4.27. In design, I, the water build-up under the runner was an observable issue, as the water had no other path then being discharged downstream of the runner. With the introduced opening, the water was discharged as soon as it would hit the blades and transfer its energy, independent from the position of the blade.
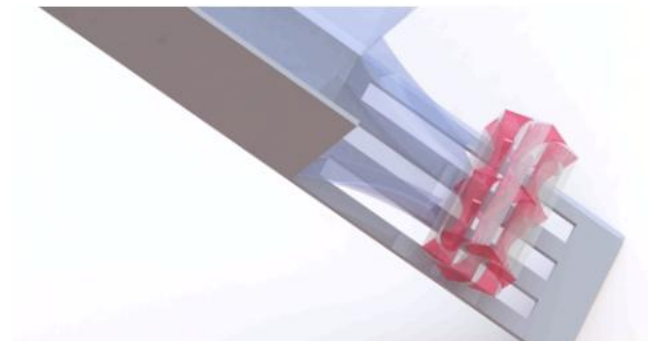
FIGURE 4.27: CAD drawing of spillway turbine version A with increased run-off area in the spillway

4.2.2 Design II Testing Method

Similarly to Design I testing method outlined in Section 4.1.2, the testing method for the updated Design II was devised before the testing started. The full test list is given in Appendix A. As the testing method had many variables, a sketch of all changeable components is depicted in Figure 4.29. From the previous testing, it was observed that the best efficiencies were achieved when rotor

to slope distance (z) was kept to the minimum value of 0.005 m. All variables
and their descriptions are shown in Table 4.10 to clarify the testing method of
Design II further.
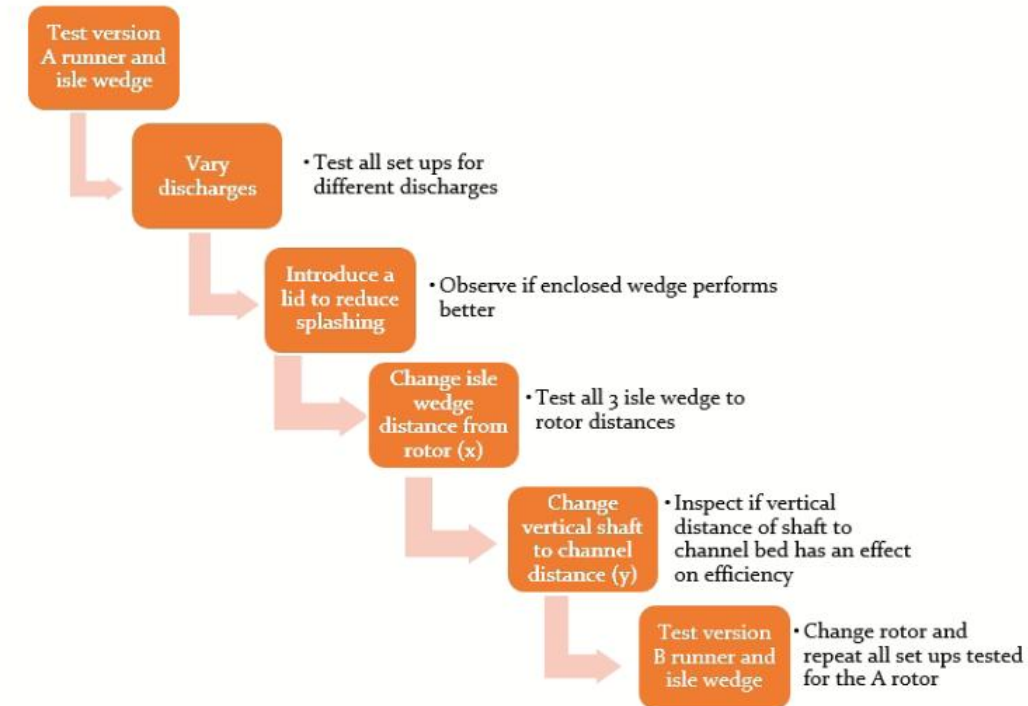
FIGURE 4.28: Design II testing method

Firstly, Runner A was tested with the open Isle Wedge A under a variety of
discharges.

TABLE 4.10: Variable names and descriptions

	Runner		Isle wedge		Lid		Wedge to rotor distance			Rotor to channel distance	
Variable name	A	B	A	B	O	E	x_1	x_2	x_3	y_1	y_2
Description	2 cup inserts	4 cup inserts	1 path	2 path	No lid	Lid	0.02 m	0.03 m	0.04 m	0.385 m	0.375 m

Secondly, the lid was introduced to the isle wedge to address splashing and
observe its effect on efficiency. Then, different horizontal distances of isle wedge
to runner were tested by moving the bridge described in Chapter 3. The testes
were then conducted for two different shafts to channel distances. Finally, the
runner with 4 cup, version B inserts and Isle Wedge B was planned for testing
for all previously listed variables.

4.2.3 Design II Results

Similarly to the Design I result section, the testing results will be presented in different subsections depending on which design component was varied. Firstly, the effect of having a lid on the isle wedge influence of the performance of Runner A with the open Isle Wedge A was analysed. Secondly, the effect of the horizontal distance between the runner and the isle wedge was investigated. Finally, the influence of the runner shaft to channel bed spacing was tested. All of the set-ups were tested under a variety of discharges.

Open vs. Enclosed Wedge

Open Isle Wedge A was the first to be tested with Runner A under a variety of discharges. During testing, it was noted that splashing in the isle wedge was considerable.

FIGURE 4.29: Open isle wedge A

Therefore, a lid was introduced to address this issue. The difference in the performance of isle wedge A with and without a lid is presented in Figure 4.30 The horizontal distance was kept constant to 0.03 m (x_2), and runner shaft to channel bed distance (y) was 0.385 m.

The discharges were varied from 5 l/s to 18 l/s, with peak performance for 12 to 14 l/s. From the graph, it can be noted that the Enclosed Isle Wedge A performs better than the Open Isle Wedge A. The peak efficiency of E (enclosed) Isle Wedge A is 23.70 % and the peak efficiency of the O (open) Isle Wedge A is only 11.86 %. As the enclosed isle wedge performs significantly better, this design was taken forward in testing.
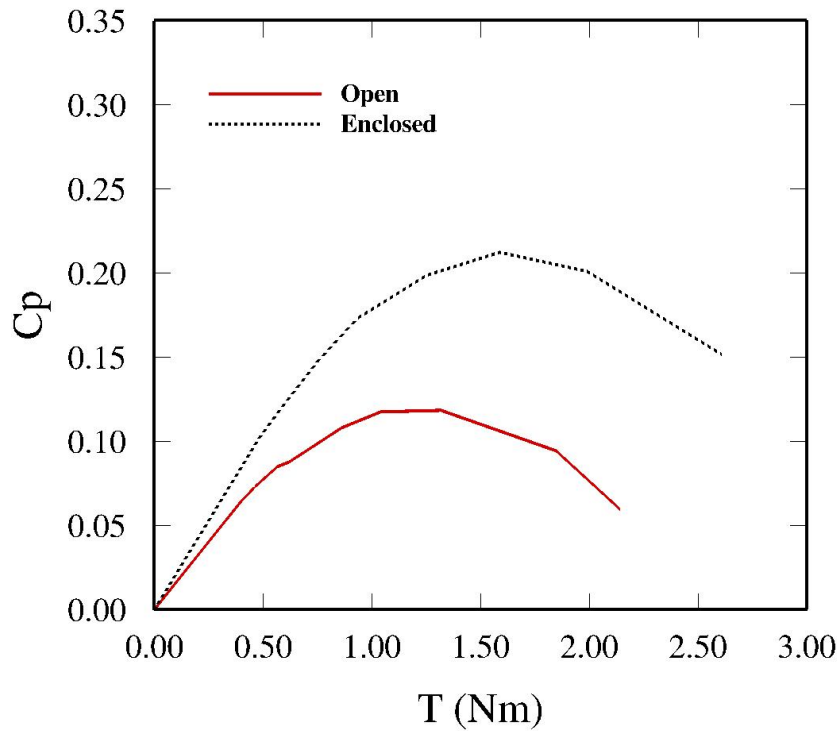
FIGURE 4.30: Open and Enclosed Isle Wedge A

Distance of Isle Wedge to Runner (x)

Enclosed Isle Wedge A was tested with Runner A with 2 cup inserts at different
horizontal distances (x1, x2, x3). Variation of the horizontal distance is the
variation of x variable depicted in Figure 4.7. The wedges were placed at 0.02,
0.03 and 0.04 m away from the rotor for all tests. For Runner A, disk to slope
distance (z1) was kept at 0.005 m, and distance of shaft from channel bed (y1)
was kept at 0.385 m. Comparison of the effect the horizontal distance of wedge
to runner has on Rotor A is depicted in Figure 4.31. The discharge tested varied
between 7 l/s to 18 l/s, with peak efficiency values reached for the discharge of
around 13 l/s for x of 0.03 m.

TABLE 4.11: Runner A and Enclosed Isle Wedge A x distances

Distance x (m)	Efficiency
0.02	17.44 %
0.03	23.70 %
0.04	19.33 %

The best performance was achieved at x_2 distance that was equal to 0.03 m.
The difference in efficiencies achieved at x distances of 0.02 m and 0.04 m was
not very large. The summary of efficiencies achieved is shown in Table 4.12.
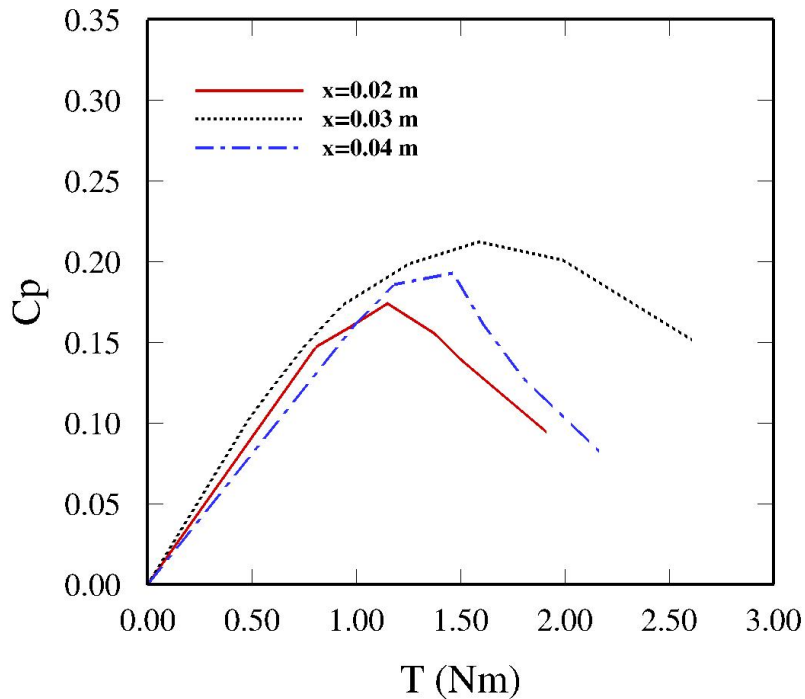
FIGURE 4.31: Enclosed Isle Wedge A effect of horizontal distance (x)

Distance of Runner to Channel Bed (y)

The design I testes indicated that the best performing slope to runner distance was 0.005 m (z), but a variation of the channel to runner distance (y) was not tested in the previous design. Runner A with Isle Wedge A was tested at all three horizontal x distances and two different y distances.

TABLE 4.12: Runner A and Enclosed Isle Wedge A x distances

Distance x (m)	Efficiency y=0.385 m	Efficiency y=0.375 m
0.02	17.44 %	22.53
0.03	23.70 %	23.96
0.04	19.33 %	20.64

The y_1 of 0.385 m was tested first, and the y_2 of 0.375 m testing followed. The discharges for these tests varied between 8 l/s to 17 l/s. From Figure 4.32 it can be noted that the channel to bed distance change from 0.385 m to 0.375 m shows improvement in efficiency for all Runner A to Isle Wedge A horizontal distances (x_1, x_2, x_3). The peak performance was obtained at x_2 distance of 0.03 m and y_2 runner shaft to channel bed distance of 0.375 m.
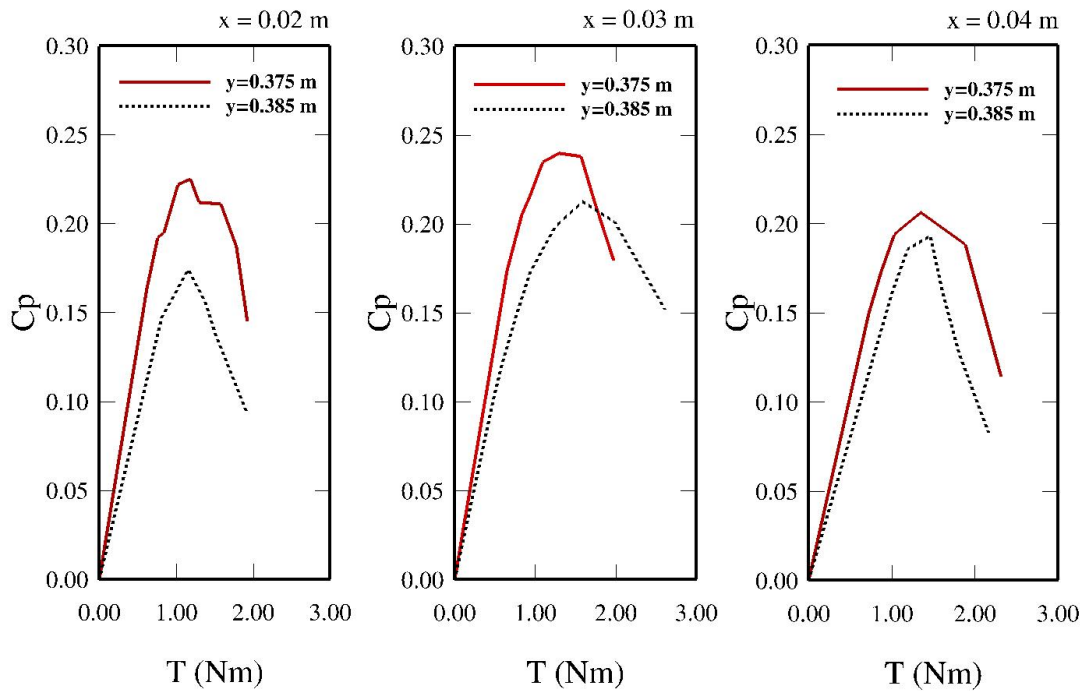
FIGURE 4.32: Runner A and Isle Wedge A variation of y

Variation of Discharge

All tests were undertaken in a range of discharges from 8 to 20 l/s, varied using the axial pump. Similarly to the effect that discharge had on Design I, the updated design also shows better performance for a specific discharge range. As the previous analysis of Design II, Runner A with Isle Wedge A indicated that the turbine performs best at 0.375 m y_2 runner to channel bed and runner to slope distance of 0.005 m (z), those parameters were chosen for discharge effect analysis. Figure 4.33 pictures how different discharges influence the performance for all three x distances of isle wedge to the runner.

It can be noted that depending on the position of the wedge, which influences the interaction of flow with the blades, the turbine performs differently for a variety of discharges. The peak efficiency was achieved for x = 0.03 m for a range of discharges of 12 to 14 l/s.

Runner B and Isle Wedge B

Due to some observable issues during the installation and testing of Isle Wedge A and laboratory schedule restrictions, the decision not to test Isle Wedge B with Runner B was made. Runner B with 4 cup inserts was tested in Design III updated with a modified Isle Wedge B that dealt with issues noted in this
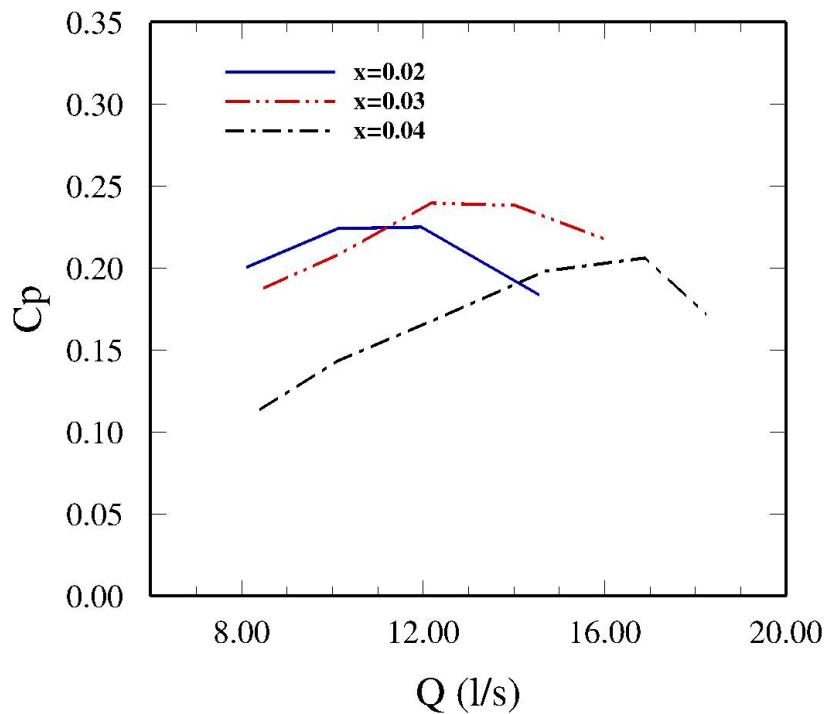
FIGURE 4.33: Variation of discharge Runner A and Isle Wedge
A

design version. This decision led to better time management and completion of
the experiments in a given testing schedule.

4.2.4 Design II Discussion and Summary

The objectives set after design I was tested were met with changes made and
implemented in Design II. The Isle Wedge design directed the water towards
the runner more precisely, and the semi-circular inserts in the runner deflected
the water inside the runner blades as intended. The water pile up under the
runner was also reduced through the opening of slots on the slope. However,
the overall maximum efficiency achieved was 23.96 %, which is lower than the
maximum efficiency of 25.06 % achieved while testing Design I. This is mainly
due to new observable issues during testing. The open isle wedge testing resulted
in large amounts of splashing that was addressed by installing a lid on top of
the isle wedge. However, this solved the problem partly as the main issue was
flow separation inside the isle wedge. Flow separation was observable, and a
thin jet would form slightly above the main flow path. The isle wedge to slope
connection and the sudden change of straight slope walls to curved isle wedge
sides were the sources of energy losses. Testing of Design I lead to a conclusion

that runner disk to slope distance z should be kept to 0.005 m, and this was applied to all Design II tests.

Initial testing of Runner A and Isle Wedge A concluded with maximum efficiency of 11.86 %, which was a disappointing drop in performance when compared to Design I. Introduction of the lid improved the performance of the turbine significantly because it reduced energy losses inside the isle wedge. The Enclosed Isle Wedge A emerged to be performing more than twice as well compared to the Open Isle Wedge A. It was concluded that the enclosed wedge should be installed in all future tests.

Testing of Design I indicated that Wedge 3, of the same height as Isle Wedge A, performs best at 0.02 m horizontal distance from the runner. However, the differences between 0.04 m x distance and 0.02 m were not very large; hence the decision to test Isle Wedge A at 3 x gaps between and including 0.02 m and 0.04 m was made. This method of testing resulted in a conclusion that horizontal distance of 0.03 m outperforms tests conducted at 0.02 and 0.04 m horizontal distances for Isle Wedge A and Runner A. The performance curve also appears to be smoother. The difference in efficiencies achieved was not vast. When y_1 value of 0.385 m was considered, Isle Wedge A 0.03 m away from Runner A results in the efficiency of 23.70 %, which is a rise by 35 % from 0.02 m distance and a rise by 22.61 % from 0.04 m x distance.

The distance of runner shaft to channel bed (y) was also analysed for all three horizontal distances for Runner A and Isle Wedge A. The initial y_1 of 0.385 m was reduced to 0.375 m for y_2 variable. The change resulted in an efficiency increase across all 3 x values. Horizontal x distance of 0.03 m with y_2 of 0.375 m and z_1 of 0.005 m arrangement resulted in peak efficiency of 23.96 %, maximum obtained for Design II testing. The x_1 0.02 m and y_2 efficiency dropped by only 5 % comparing to the peak performance recorded.

The discharge was varied for all arrangements analysed. It was noted that Design II performs best in the range of 12 to 14 l/s for majority of set-ups. This is in the same range as Design I best performance discharges.

To conclude, Runner A with 2 cup Version A inserts and Isle Wedge A addressed the observable issues outlined in design I testing. Despite this, a new problem of water separation occurred and resulted in significant energy losses inside the isle wedge. The cause of water separation is a sudden change in slope to isle wedge geometry. The curved isle wedge walls do not show any benefits to turbine performance. Hence, its design was revised in Design III. The runner design change did not result in any observable energy losses. The water build-up under

the runner was reduced but not eliminated, and further improvements on this are possible to implement.

4.3   Design Version III

4.3.1   Design III of Runner and Accelerator Channel

Testing of Design II led to observations of problems associated with Isle Wedge design showed in the previous section. The runner re-design with inserts could not be exploited as intended due to energy losses in the isle wedge. Hence, the following steps were planned for Design III:

- **Avoid significant losses while guiding the water into the runner** - The accelerator channel replaced isle wedge with the same height as Wedge 3 (0.015 m).
- **Guiding the water through the rotor** - Inserts presented in Design II were kept the same in this design revision with the idea of the cup inserts deflecting the water jet by 180 ° from the centre to the right and left-hand side.
- **Providing better water run-off under the runner** - The spillway floor under the runner was opened further than in Design II.

Three variations of the Design III were considered in order to improve the efficiency of the spillway turbine system. The six-bladed runner presented in Design I was used in all four variations. Depending on which accelerator channel was installed, 2 cup inserts (Version A Runner), no cup inserts (Version B Runner) or 4 cup inserts (Version C Runner) were tested. The variations of the Design are summarised in Table 4.13.

TABLE 4.13: Design Variations

Runner	Accelerator Channel	Description
A	A	2 cup inserts and single water path
A	B	2 cup inserts and single water path
B	A	No inserts and single water path
C	C	4 cup inserts and double water path

Design Version A, consisting of the six-bladed runner with 2 cup inserts and the Accelerator Channel A is shown in Figure 4.34. Design III Version B of the runner was tested with no inserts installed and the Accelerator Channel A

as shown in Figure 4.35. Finally, Design Version C, also consisting of the six-bladed runner but with 4 cup inserts and the Accelerator Channel C is given in Figure 4.36.
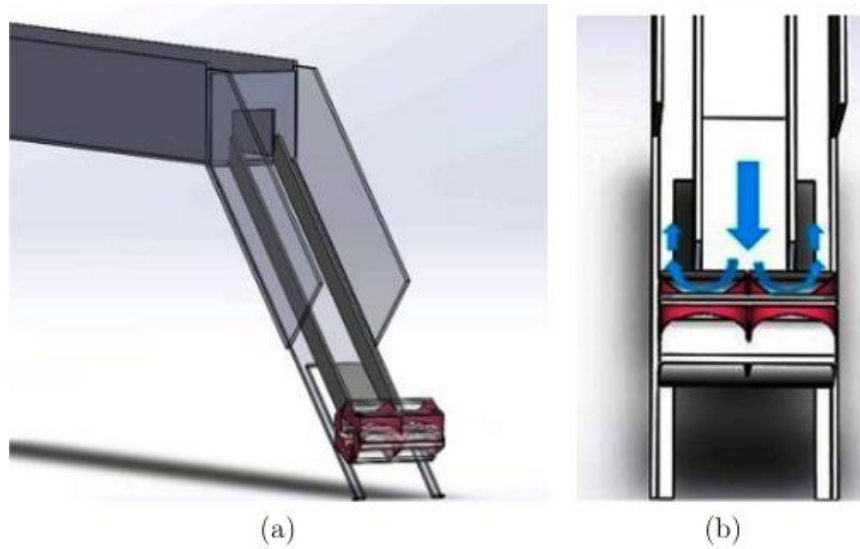
FIGURE 4.34: (a) Runner A and Accelerator channel A; (b) Top View of Runner A and Accelerator Channel B
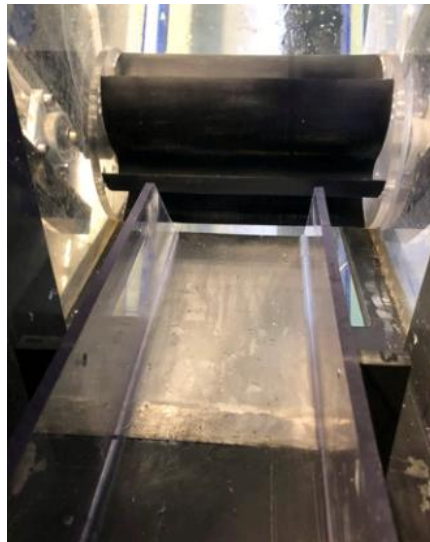
FIGURE 4.35: Version B Runner and Accelerator Channel B
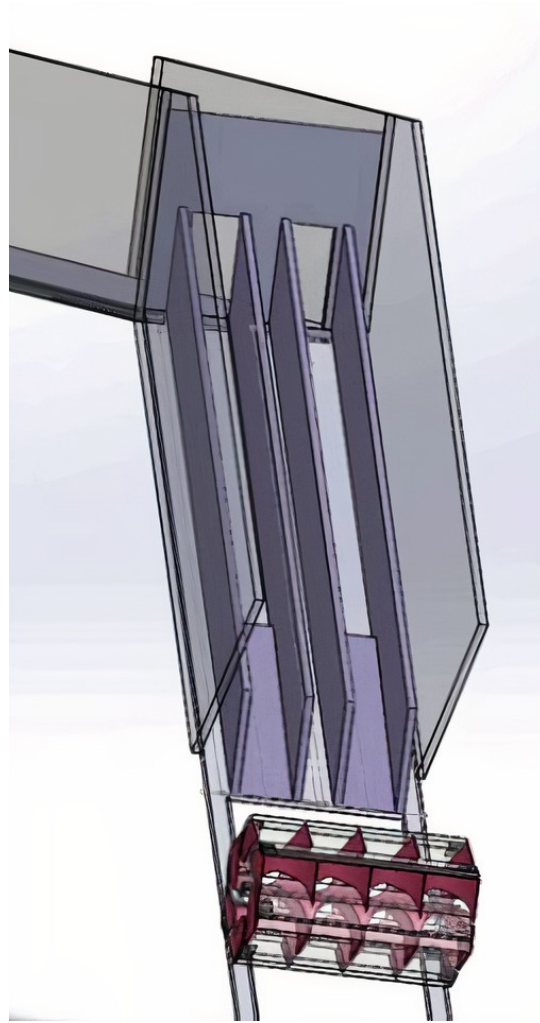
FIGURE 4.36: Version C Runner and Accelerator Channel C

Accelerator Channel Design

The accelerator channel was designed to address the problem of flow separation and splashing that appeared when Wedge Design I and Isle Wedge Design II were tested. The ratio of around 2:1 runner to wedge outlet presented in Design II was kept. The principle difference is in the size of the accelerator channel when compared to previous Design. The accelerator channel runs along the entire spillway slope and therefore allows for the water to flow down the channel smoothly, as there are no sharp changes when the water enters the accelerator channel. The channel was fitted with a metal wedge at the very end, mimicking the Wedge 3 height from Design I (also implemented in the Isle Wedge Design II). Three different accelerator channels were used in the testing of Design III. Accelerator channels A and B are the same in shape but have different outlet widths, as shown in Figure 4.37. A channel complied with having rotor to wedge outlet ratio of 2:1 and the outlet width of 0.15 m, whereas B channel had a rotor

to wedge outlet ratio of 2.4:1 and the outlet width of 0.126 m. A channel was tested with Runner Version A with 2 cup inserts, and B channel was also tested. Runner B with no inserts was tested with the Accelerator Channel A.

(a)   (b)
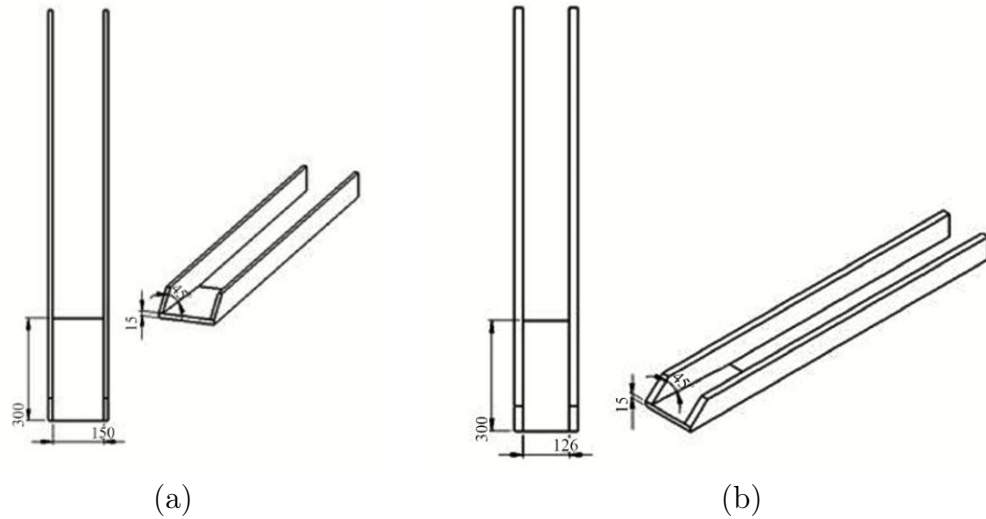
FIGURE 4.37: (a) Accelerator Channel A; (b) Accelerator Channel B

The Accelerator Channel C was different as it was meant for use together with the runner with 4 cup inserts. Hence, rather than having one water path as in Accelerator Channels A and B, Accelerator channel C had two water paths. The representation of Accelerator Channel C is shown in Figure 4.38. Cup insert to channel outlet ratio was kept to 2:1.
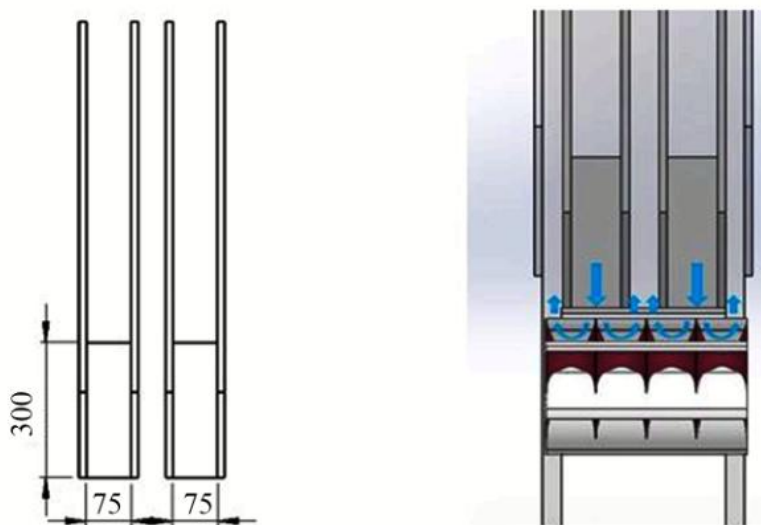
FIGURE 4.38: Accelerator Channel C

Water Run-off

Spillway sloped floor was further opened to provide more release of water build-up under the runner. In the field environment, water run-off under the runner will be dealt with either by providing a space for the water build-up or by slightly rising the runner above the spillway but keeping the parameters recommended. Different recommendations will be necessary for different sites, depending on surrounding conditions.
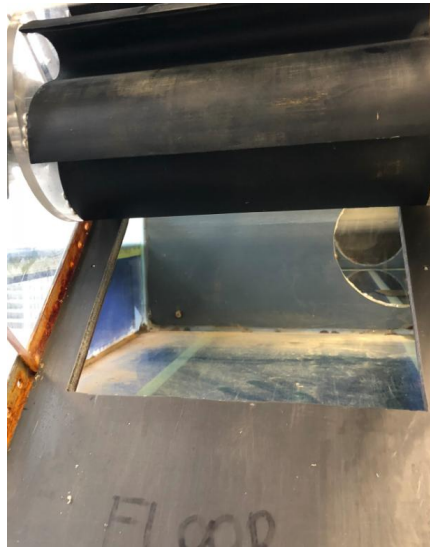
FIGURE 4.39: Spillway floor

4.3.2 Design III Testing Method

Similarly to Design I testing method outlined in section 4.1 and Design II testing method described in Chapter 4.2, the testing method for the updated Design III was devised before the testing started. The full test list is given in Appendix A. Variables that changed during tests, together with their descriptions, are shown in Table 4.14. From the previous testing, it was observed that the best performance was achieved when the rotor to slope distance (z) was kept to the minimum value of 0.005 m.

Firstly, Runner A with 2 cup inserts and 0.15 m wide Accelerator Channel A was tested under a variety of discharges, at 0.02 m and 0.03 m horizontal distances (x) and 0.375 m and 0.385 m vertical channel to runner shaft (y) distances. Secondly, Runner A with 2 cup inserts was tested with 0.126 m wide Accelerator Channel B, varying discharges and x and y variables. To quantify the difference runner inserts make to the turbine performance, Runner B with no inserts was tested with Accelerator Channel A. Finally, Runner C with 4

TABLE 4.14: Variable names and descriptions

	Runner			Accelerator Channel			Accelerator Channel to runner distance		Rotor to channel distance	
Variable name	A	B	C	A	B	C	x_1	x_2	y_1	y_2
Description	2 cup inserts	No cup inserts	4 cup inserts	1 path (0.15 m)	1 path (0.126 m)	2 path (0.075 m)	0.02 m	0.03 m	0.385 m	0.375 m

cup inserts was tested with two path Accelerator Channel C under a variety of discharges, for both x horizontal distances and y vertical gaps of the runner to channel.
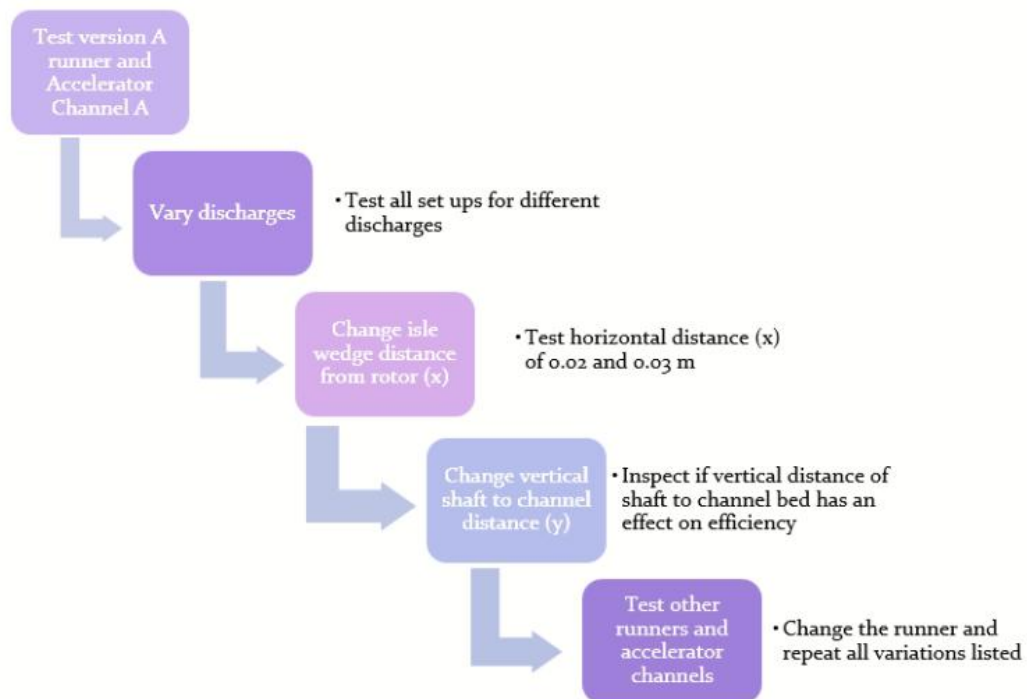
FIGURE 4.40: Testing Method Flow Chart

4.3.3   Design III Results

Design III testing results were presented similarly as Design I and II testing results. The effect of horizontal distance (x) of the runner to the accelerator channel was discussed for all four variations. Vertical distance (y) of runner shaft to channel bed influence was also compared. The best performing set-ups of 4 variations of Design III were also presented and contrasted. Finally, speed

factors and specific speeds were presented. The distance of slope to the runner (z) was kept to a minimum value of 0.005 m for all presented test results.

Distance of Accelerator Channel to Runner (x)

Testing of previous design variations indicated that the turbine performance peaks for horizontal distances (x) of 0.02 m and 0.03 m. Hence, it was decided that larger gaps will not be tested in this Design version. Discharges were varied between 7 l/s and 16.5 l/s, with most peak efficiency values reached for discharges ranging from 9 to 13 l/s.

Runner A with 2 cup inserts was tested with the 0.15 m wide Accelerator Channel A and 0.126 m wide Accelerator Channel B. The ratio of runner width to channel outlet width was 2:1 for Runner A and Accelerator Channel A and 2.4:1 for the Runner A and Accelerator Channel B. The results presented were from tests undertaken with y_2 value of 0.375 m. Runner A with Channel A is depicted in Figure 4.41 and Runner A with Channel B in Figure 4.42.

x	Efficiency
0.02 m	43.38 %
0.03 m	39.07 %
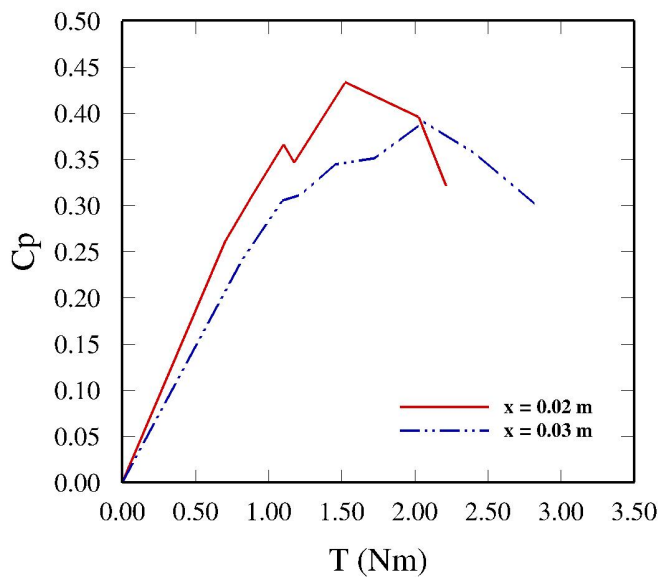
FIGURE 4.41:   Runner A and
Channel A at x_1 and x_2

It can be noted that Runner A and Channel A show best performance at x_1 value of 0.02 m with the efficiency of 43.38 %, comparing to 39.07 % for 0.03 m x_2. Runner A and Channel B perform better for x_2 of 0.03 m with the peak efficiency of 39.02 %. The peak performance for x_1 was 34.91 %.
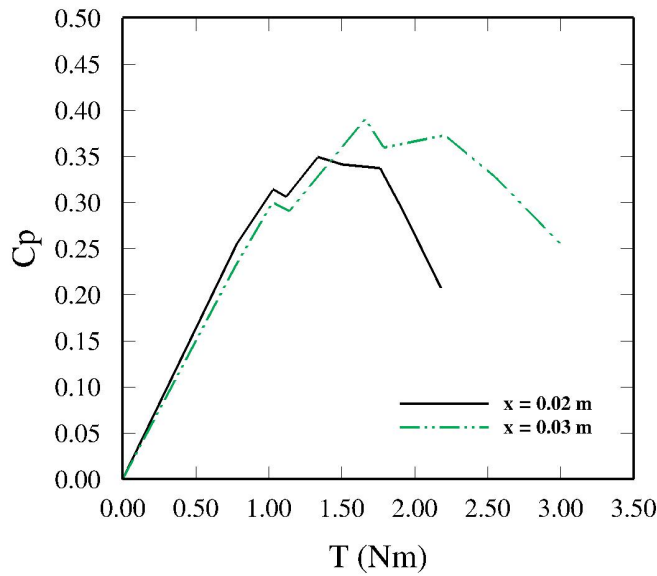
x	Efficiency
0.02 m	34.91 %
0.03 m	39.02 %

FIGURE 4.42:   Runner A and
Channel B at x_1 and x_2

Runner B, that had no inserts installed was tested with the 0.15 m wide Accelerator Channel A. The results presented were obtained in tests where y was kept at 0.375 m. The performance comparison for 0.02 and 0.03 m x variables is given in Figure 4.43. The change in performance is slight in case of Runner B, with peak performance of 22.43 % for x_1 and 22.03 % for x_2.
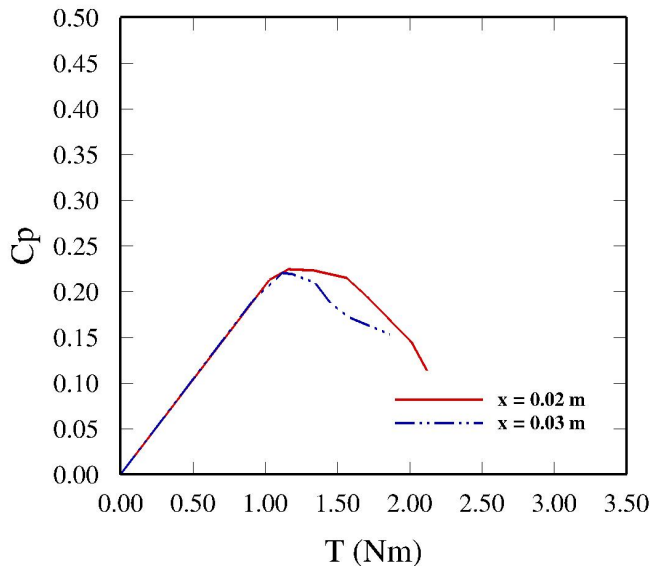
x	Efficiency
0.02 m	22.43 %
0.03 m	22.03 %

FIGURE 4.43:   Runner B and
Channel A at x_1 and x_2

Runner C had 4 cup inserts installed and was tested with Channel C. The channel consisted of two smaller channels of 0.075 m width each. The results presented are from tests performed at y_2 channel to runner distance of 0.375

m. The horizontal distance of the accelerator channel to runner effect on the performance is given in Figure 4.44. As this Runner C with 4 cup inserts was not tested in Design II, x_3 of 0.04 m was tested at this stage.
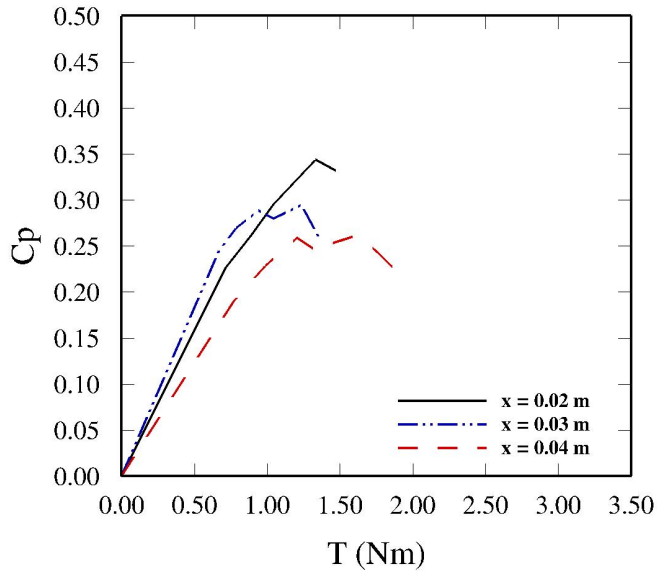
x	Efficiency
0.02 m	34.36 %
0.03 m	29.49 %
0.04 m	26.21 %

FIGURE 4.44: Runner C and Channel C at x_1, x_2 and x_3

It can be noted that Runner C and Channel C perform best at x_1 distance of 0.02 m, as in other Design III versions tested for y_2 of 0.375 m. The peak performance obtained was 34.36 %, comparing to 29.49 % at x_2 and 26.21 % to x_3.

Distance of Runner to Channel (y)

Similarly to Design II tests, Design version III was also tested for two variations of runner shaft to channel bed distance (y). All four variations of Design III were tested for y_1 of 0.385 m and y_2 of 0.375 m for both 0.02 and 0.03 m horizontal distances. Slope to runner distance (z) was kept to 0.005 m for all results presented.

Runner A with 2 cup inserts and 0.15 m wide Accelerator Channel A was tested at y_1 and y_2 and the effect of changing the vertical distance is depicted in Figure 4.45

TABLE 4.15: Runner A and Accelerator Channel A

Distance x (m)	Efficiency y=0.385 m	Efficiency y=0.375 m
0.02	34.87 %	43.38 %
0.03	32.16 %	39.07 %
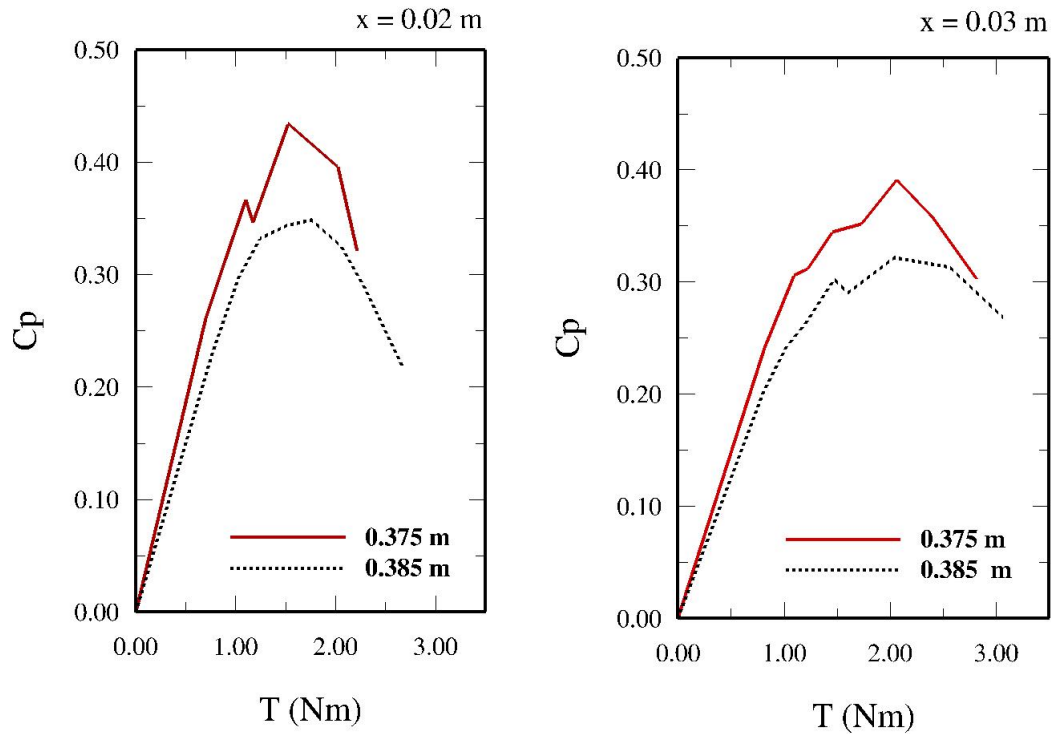
FIGURE 4.45: Runner A and Channel A variation of y

Performance at y_1 and y_2 under 0.02 m and 0.03 m horizontal spacing (x) was summarised in Table 4.16. It can be noted that turbine preforms significantly better for y_2 value of 0.375 m.

Runner A and 0.126 m Accelerator Channel B were also tested at both y values, and the effect of varying vertical channel to runner shaft distance is presented in Figure 4.46.

TABLE 4.16: Runner A and Accelerator Channel B

Distance x (m)	Efficiency y=0.385 m	Efficiency y=0.375 m
0.02	38.56 %	34.91 %
0.03	33.25 %	39.02 %

It can be noted that Channel B performs better than Channel A at 0.385 m y distance, but peak performance is still obtained for y value of 0.375 m at 0.03 m x horizontal gap between the runner and the channel.

Runner B with no inserts was tested with the 0.15 m wide Channel A for both y vertical distances, as Runner A was, at both horizontal runner to channel x distances. The difference in performance is depicted in Figure 4.47 and summarised in Table 4.17.
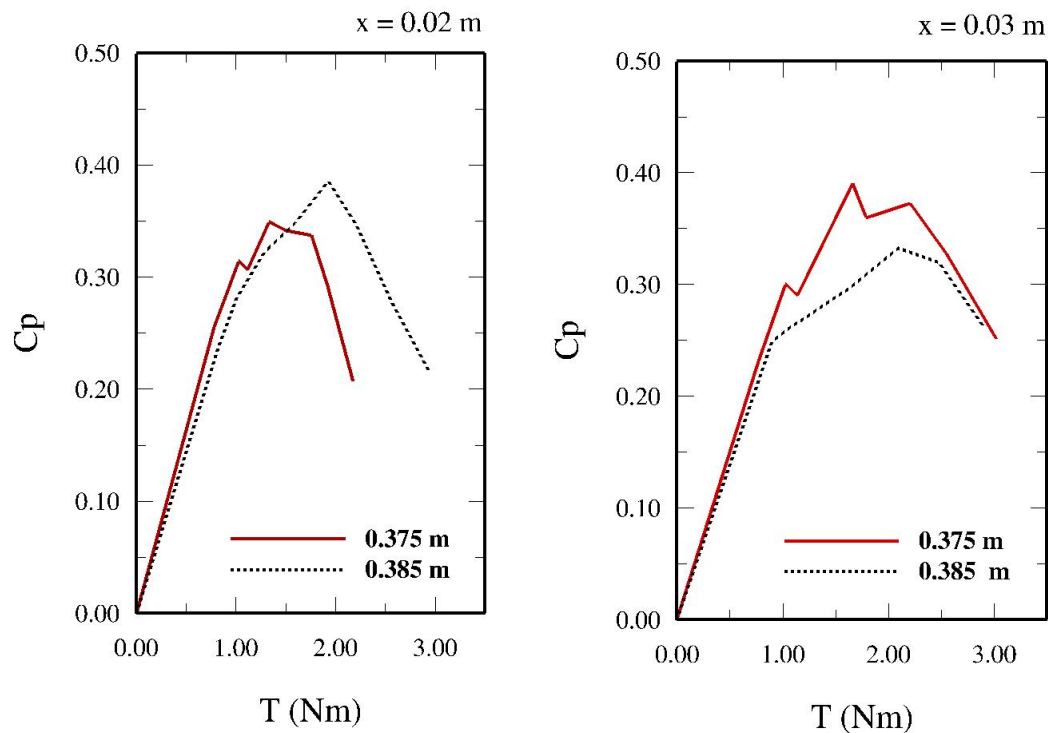
FIGURE 4.46: Runner A and Channel B variation of y

TABLE 4.17: Runner B and Accelerator Channel A

Distance x (m)	Efficiency y=0.385 m	Efficiency y=0.375 m
0.02	21.96 %	22.43 %
0.03	21.35 %	22.03 %

In the case of Runner B, a vertical distance of runner shaft to channel bed does not significantly change the peak efficiency obtained. The differences are less than 1 % for all four tests presented. Channel A to Runner B performs best at x of 0.02 m and y of 0.375 m, with a maximum efficiency of 22.43 %.

Runner C, with 4 cup inserts, was tested in conjunction with Accelerator Channel C at three horizontal distances (x) of the channel to the runner at y_1 of 0.385 and y_2 of 0.375 m. The effect of varying vertical distance y is presented in Figure 4.48. It can be noted that the turbine efficiency drops for all horizontal distances when y_1 of 0.385 m is used. Runner C shows the best performance of 34.36 % when it is placed 0.02 m in the x-direction from the runner and 0.375 m in the y-direction. Moreover, all 0.375 m y_2 tests show more than 10 % increase in performance.
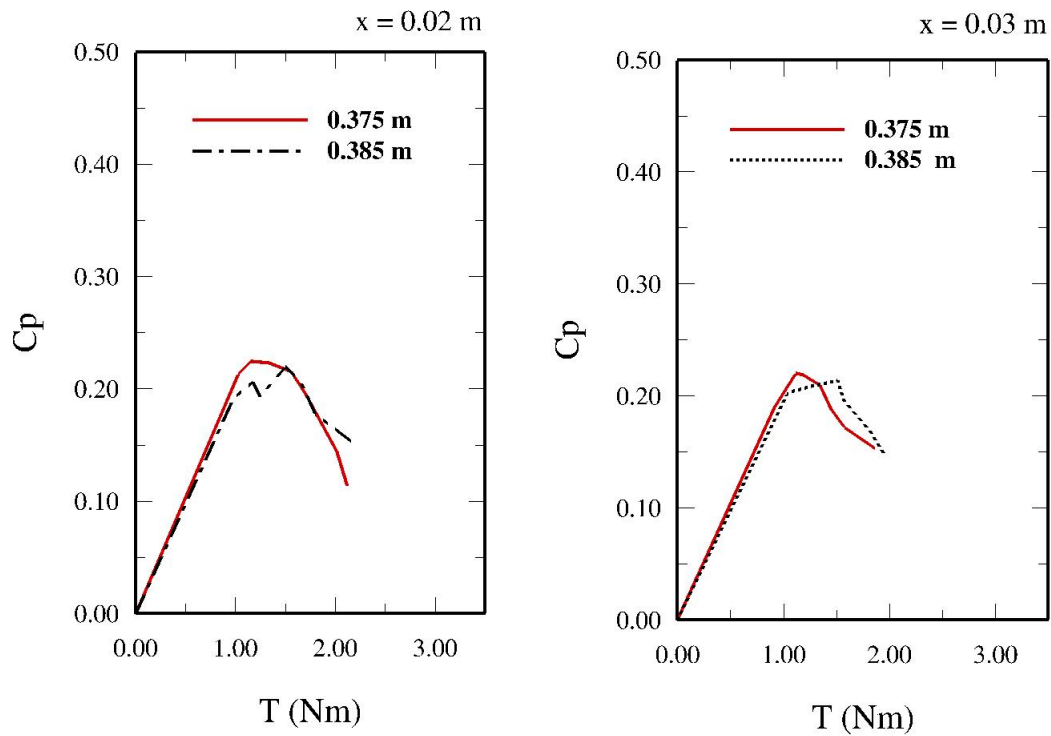
FIGURE 4.47: Runner B and Channel A variation of y

TABLE 4.18: Runner C and Accelerator Channel C

Distance x (m)	Efficiency y=0.385 m	Efficiency y=0.375 m
0.02	20.64 %	34.36 %
0.03	20.35 %	29.49 %
0.04	16.71 %	26.21 %

Variation of Discharge

All tests were carried out in a range of discharges from 6 l/s to 17 l/s, varied using the axial pump described in Chapter 3. The vertical distance (y) for discharge analysis was kept constant at 0.375 m, and runner disk to slope distance (z) was 0.005 m. The plot shown in Figure 4.49 depicts how efficiency is affected by the discharge depending on the horizontal distance (x) of the runner to accelerator channel. All four design variations were analysed. It can be noted from the Figure that most tests carried out to perform best at 0.02 m horizontal distance for a range of discharge between 9 l/s and 12 l/s, which was similar in other design tests carried out previously. Maximum efficiency of 43.39 % was achieved with Runner A in conjunction with Channel A, 0.02 m away in the x-direction for a discharge of 9.5 l/s.
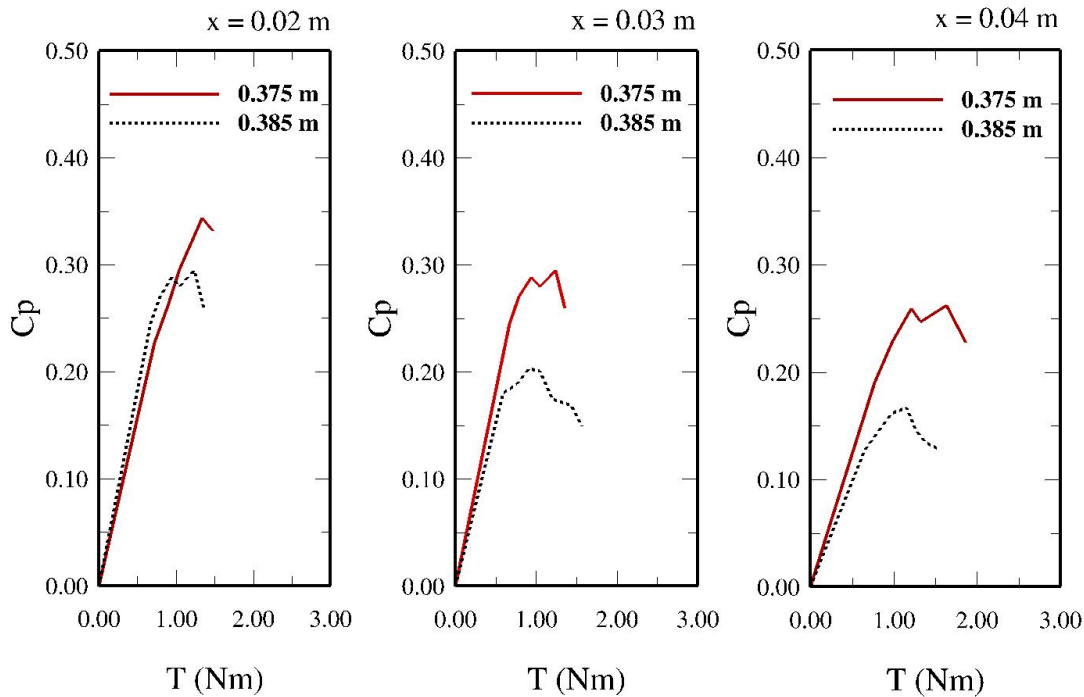
FIGURE 4.48: Runner C and Channel C variation of y
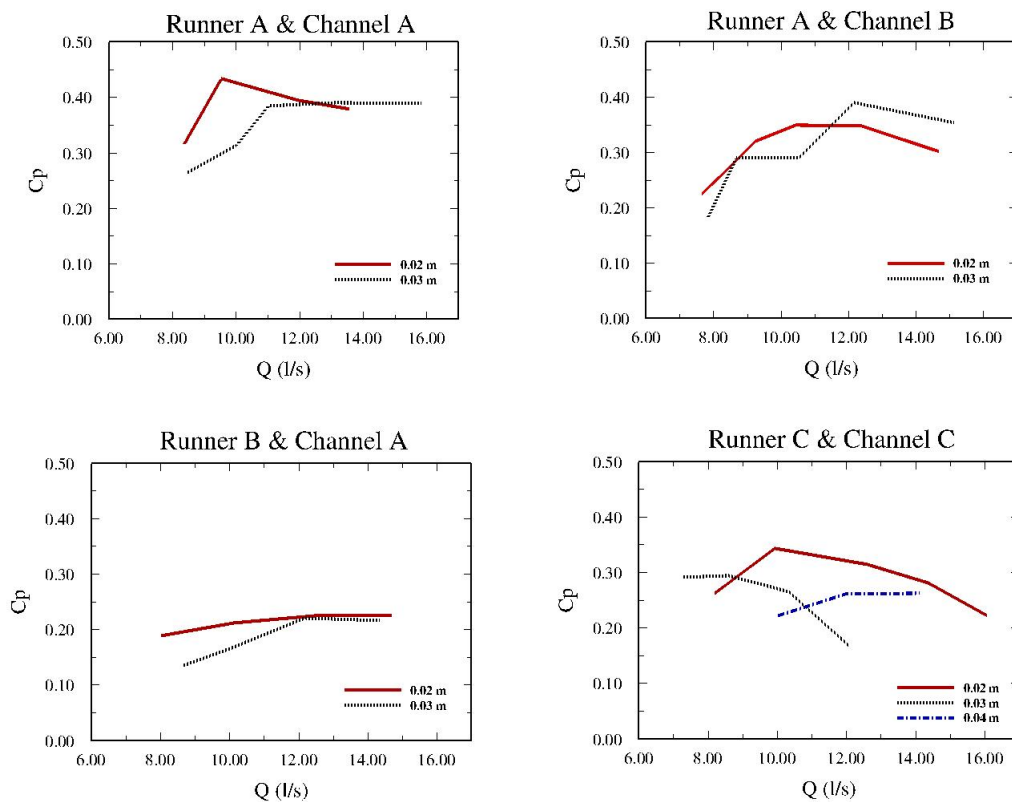
FIGURE 4.49: Variation of discharge effect on performance

Comparison of Runner and Channel Performance

The best performing Runner A, B and C tests were given in Figure 4.50 to depict how different runners and channel variations influence the overall performance. The best performing set-ups were also summarised in Table 4.19. From

the results, it can be seen that Runner A with 2 cup inserts in together with Accelerator Channel A performs best out of the four set-ups, followed by Runner A and Accelerator Channel B. The worst performing Design III variation is Runner B, that had no inserts installed.
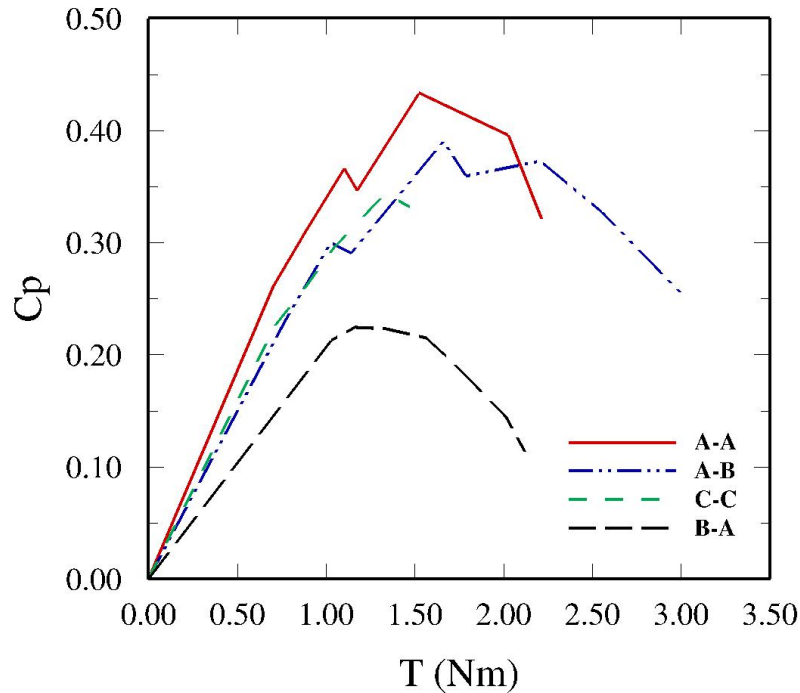
FIGURE 4.50: Comparison Between Design Variations

TABLE 4.19: Peak Efficiencies

Design Variation	Runner	Channel	Efficiency
A-A	Runner A	Channel A	43.38 %
A-B	Runner A	Channel B	39.02 %
B-A	Runner B	Channel A	22.43 %
C-C	Runner C	Channel C	34.36 %

Specific Speed

The specific speed and the speed factor were calculated using Equations (2.6) and (2.7) respectively, given in Chapter 2. The calculated values for peak power coefficients are given in Table 4.20. The speed factors against the power coefficient and the specific speeds for all three runners Design III variations are shown in Figure 4.51. From the Figure and Table given, it can be noted that the runners with cup inserts have higher specific speeds and speed factors than the runner with no cup inserts. Hence, the idea of achieving similar water blade

interaction as it occurs in Pelton turbine blades (Chapter 2). As the speed factors fall into 0.43 - 0.48 range of impulse turbine speed factors, it can be concluded that the spillway turbine with 2 cup inserts can be classified as an impulse turbine. The specific speed range is shown in Table 4.20 also confirms that the spillway turbine can be defined as an impulse turbine.
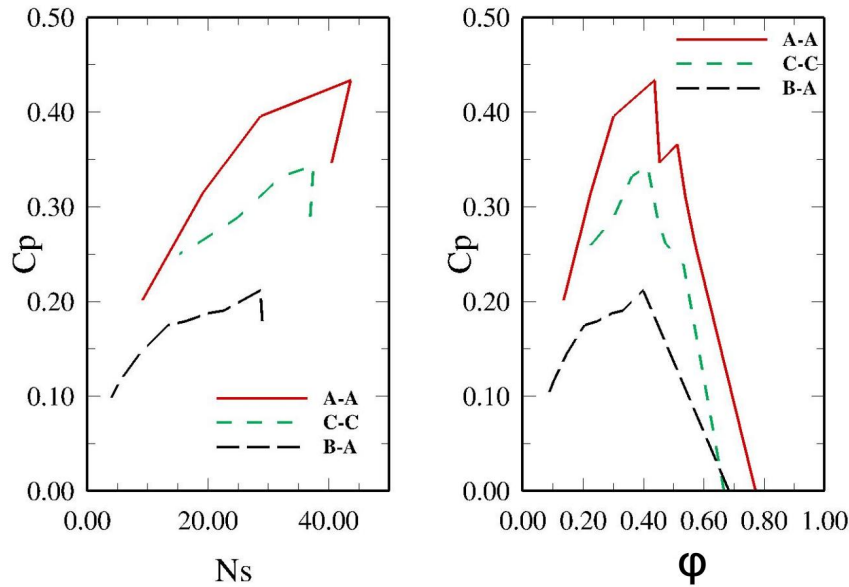
FIGURE 4.51: Specific speeds (left) and Speed Factors (right)

TABLE 4.20: Speed Factors and Specific Speeds

Design Variation	Specific Speed	Speed Factor	Efficiency
Runner A,Channel A	43.66	0.437	43.38 %
Runner B,Channel A	28.64	0.398	39.02 %
Runner C,Channel C	37.49	0.414	34.36 %

4.3.4 Design III Discussion and Summary

The objectives set after Design II was revised were met with changes implemented in Design III. The isle wedge was converted into an accelerator channel, and the issue of water separation at the walls was reduced. The splashing was also significantly less present. The runner inserts guided the water through the rotor as intended, deflecting the jet by 180 ° from the centre to the sides. Further opening of the spillway eliminated the water build-up under the runner. These design revisions lead to a considerable advancement in performance,

reaching 43.36 %, which is double the efficiency reached in Design I and Design II.

Similarly to the previous design versions, positioning of the rotor concerning the accelerator channel, channel bottom and the spillway slope, had a substantial influence on how well the turbine performs in all four Design III variations. From previous tests, it was concluded that the vertical spillway slope to runner disk space (z) should be kept to a minimum value of 0.005 m. If the horizontal distance (x) of the runner to accelerator channel is considered, all design variations but one show better performance when the distance is kept at 0.02 m. In the case of Runner A and Channel A, the efficiency drops by 10 % when the horizontal distance is increased to 0.03 m. Runner B and Channel A also show there is a drop in efficiency if the horizontal distance is increased, but the drop is very slight and lower than 2 %. Moreover, Runner C and Channel C also perform best at 0.02 m x distance, with the efficiency decreasing by 14 % when x of 0.03 m is used and 24 % when 0.04 m horizontal gap is implemented. However, when Runner A was tested with the Accelerator Channel B, better performance is observed when x is 0.03 m. The performance increased by almost 12 % from the 0.02 m x test. Varying the runner to channel (y) distance also showed to have an immense impact on the performance of the turbine. For Runner A and Channel A tests, it was noted that the performance increases by 24 % when y is reduced from 0.385 m to 0.375 m for the x value of 0.02 m and 21 % for the x value of 0.03 m. The same behaviour was observed in Runner B and Channel A tests, but the increases of efficiencies for changing the y from 0.385 to 0.375 m were much lower, 2 % and 3 % for 0.02 and 0.03 m x-direction gaps respectively. Furthermore, Runner C and Channel C tests also show that the turbine performs considerably better for 0.375 m vertical y distance. The performance increased by 40 %, 31 % and 36 % for x of 0.02, 0.03 and 0.04 m respectively. However, Runner A and Channel B tests indicate that using y of 0.385 m for 0.02 m x distance performs better than y value of 0.375 m. On the other hand, the best performance of this design variation was also achieved for y of 0.375 m and x of 0.03 m.

Testing the effect of discharge variation indicated that the best performance was achieved for 9.5 l/s discharge for Runner A and Channel A variation, but peaks are commonly observed in the range of 9 to 12 l/s. This corresponds to observations made in previous design variations.

Having all four design variations as part of Design III tested can be used to quantify the contribution of cup inserts and channel width to the overall performance. From the tests conducted with Runner A that had 2 cup inserts and

Runner B that had no cup inserts, with the same accelerator channel, it can be concluded that the inserts lead to an increase in efficiency by 20 %, which is almost double. Changing the channel width to runner width ratio from 2:1 to 2.4:1 resulted in a 5% efficiency drop when Runner A was tested. Moreover, 2 cup inserts and a single water path outperformed Runner C with 4 cup inserts and a two-path accelerator channel.

The specific speed and the speed factors indicate that the runners with inserts have higher specific speeds and speed factors than the runner without the inserts. This indicates that the cup inserts significantly influence force distribution in the turbine blades described in Chapter 2. Analysis of the specific speeds and the speed factors indicate that the Spillway turbine consisting of Runner A and Accelerator Channel A can be classified as an impulse turbine, and the water blade interaction is similar as in the Pelton turbines.

The observable issues in this design version were far fewer than previous design version. The principle issue is head losses in the accelerator channel due to a sudden change from 0.3 m wide straight channel that funnels the water into the spillway, to 0.15 m wide accelerator channel that stretches across the entire length of the spillway. Design revision of the accelerator channel will be considered in-field testing, according to recommendations made after the investigation of hydrodynamics of a channel contraction.

From all above, it can be concluded that the spillway turbine Design III Runner A and Accelerator Channel A performs best at a horizontal distance of runner to channel (x) of 0.02 m, channel to runner shaft distance (y) of 0.375 m and slope to runner disk distance (z) of 0.005 m. The efficiency of this Design with the stated set up reaches 43.38 %, and these design parameters will be used in field testing with appropriate scaling of parameters applied.

4.4 Experimental Testing Conclusion

The design process of the Spillway turbine consisted of the initial design and two design revisions. Testing of 2 runner and 3 wedge designs was the initial stage of the turbine testing and development stage. From these tests, conclusions about the wedge height and the number of blades were made. Design I lead to conclusions that a 6 blade runner with a 0.015 m high wedge should be placed not further than 0.04 m horizontally from the runner, with the disk slope distance (z) kept to a minimum value of 0.005 m. Peak performance of Design I was 25.06 %. Observable issues such as large amounts of splashing,

lack of precise guidance of water into and through the runner, and release of water from under the runner were addressed in Design II.

Revision of Design I, named Design II, resulted in a redesign of the wedge, which became an isle wedge. The isle wedge was 0.015 m high and 0.15 m wide at the outlet. The runner with 6 blades was taken forward over the 7 bladed runner. Two versions of cup inserts were designed to be placed inside the runner blades, to guide the water through the rotor and accomplish Pelton like water blade interaction. Slots were introduced in the spillway to increase water run-off under the runner. Testing of Design II led to conclusions that the vertical runner shaft to channel distance (y) also plays an important role in turbine performance. Peak performance was 23.96 % and it was lower than that of Design I. Although guiding the water through the rotor was accomplished with the inserts, the isle wedge design could be improved further. The water separation at the entrance of the isle wedge walls indicated that some flow power was lost before it reached the blades.

Revision of Design II, referred to as Design III, was the ultimate design version tested in the laboratory setting. Avoiding significant losses while guiding the water into the runner was the primary objective of this design revision. This was the main motivation behind replacing the isle wedge with an accelerator channel that ran along the entire spillway length. Better run-off of water below the runner was achieved by further opening the spillway slope floor. These design revisions ultimately led to a maximum efficiency of 43.38 %, which is double than the efficiencies achieved in Design I and Design II tests. Although the implementation of the accelerator channel had a positive influence on the performance of the spillway turbine, it was recognised that a portion of flow power is lost when the flow transitions from a 0.3 m wide straight channel into the 0.15 m wide accelerator channel. Hence, the laboratory testing and observations of water behaviour inside the accelerator channel motivated further research into the hydrodynamics of the contracting channels. It was believed that numerically simulating the water surface of flow going through different contraction angles will be a guide to a final design revision and implemented in field testing. The investigation of hydrodynamics of flow through a contraction is presented in the following chapters.

Chapter 5

Numerical Simulation Background

5.1 Motivation

Design, development and testing of the novel spillway turbine have consisted of
not only the traditional turbine runner design and how the fluid moves through
the runner blades. The focus was also on how the water is guided to the runner
so maximum flow energy can be extracted. This was achieved through the ac-
celerator channel/wedge presented in Chapter 4 of this thesis. However, the ex-
perimental design-test-redesign method was not sufficient in understanding the
hydrodynamics of the flow exiting the accelerator channel. Therefore, numerical
modelling was utilised to gain understanding and make recommendations for a
redesign before the spillway turbine is tested in the field environment.

Channel transitions can be classified as channel contractions, in which the cross-
sectional area is reduced from one area to another, or channel expansions in
which the cross-sectional area is increased. Channel contraction can be a grad-
ual or a sudden change of channel width or depth. The behaviour of the water
surface in the channel transition will depend on the classification of flow if it is
supercritical or subcritical. The accelerator channel presented in Chapter 4 can
be defined as a contracting channel, with 90 ° contraction angle. A drawing of
the channel transition view from above is given in Figure 5.1.
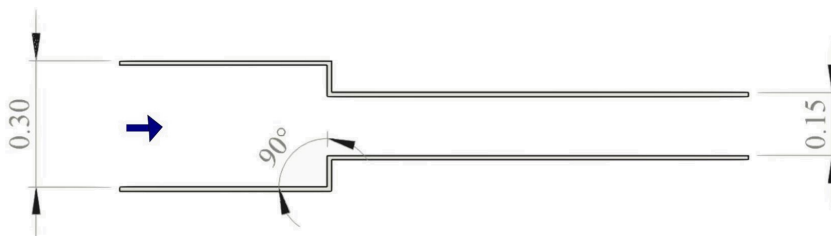
FIGURE 5.1: Transition of accelerator channel used in Design
III design and testing

This transition can be defined as a sudden channel contraction, and the flow

in the channel was characterised as supercritical flow, with the Froude number larger than 1. In this type of flow, inertial forces are dominant over the gravitational forces and hence a standing wave is expected to form downstream (Chow , 1959). Design of the channel contraction significantly affects the energy losses within the transition. Investigations of how the design of channel contraction can reduce energy losses by making the contraction gradual rather than sudden was conducted. In straight wall contractions, this can be achieved by reducing the angle of contraction from 90 ° to a smaller angle over a length. This was the principal motivation for numerical investigations conducted about how an angle of contraction would affect the energy losses inside the contraction and the flow hydrodynamics.

The challenges of numerically modelling supercritical flow through a channel contraction are numerous and complicated. They involve detailed and precise capturing of wave propagation and the deforming water surface, along with correctly implementing boundaries, all with a purpose of quantifying energy losses posed by the contracting geometry. Several pieces of research focused on numerically modelling such flow, but many questions remain unanswered. Firstly, studies do indicate that 2D shallow-water equations are not capable of capturing the wave propagation correctly and hence a 3D model needs to be utilised, but available studies of this nature are very limited. Is the in-house Large Eddy Simulation (LES) HYDRO 3D code utilised in this study capable of correctly simulating this type of flow? Secondly, describing velocity profiles, pressure distributions and the friction effect of flow through a channel contraction have not been analysed. Finally, what effect an angle of contraction would have on the hydrodynamics of supercritical flow through a contraction? These questions have been answered throughout the following chapters.

5.2   Background

Flow through a contraction was experimentally and numerically investigated by several researchers over the last half a century. This section is focused on describing work by others done on flow through a contraction and methods commonly used for free-surface tracking, to identify gaps in already published studies.

5.2.1 Flow Through a Contraction

Analysis of flow through a contraction was pioneered by Dawson (1943), in which wave propagation along the channel after the contraction was analysed and presented. The experiments were conducted for a contraction with both curved side walls and straight contraction side walls. Dawson (1943) concluded that the straight contraction walls are preferable due to simpler wave super-imposition, and hence such type of contraction design is recommended. This work was continued by Ippen & Dawson (1951), who presented the location and shape of the free-surface wave propagation and water depth along the channel after the contraction. As this experiment was conducted several decades ago, it is relevant to state that the measuring equipment was limited to the use of a point gauge with a scale meter and a vernier. However, their work served as validation experimental data for many researchers presenting numerical models and approximations of the position of the free-surface. The laboratory test was conducted in a 0.6 m wide channel transitioning into 0.3 m wide channel at a convergence angle of 6 °, with a Froude number of 4.0.

Majority of numerical modelling studies used shallow-water equations, derived from Navier-Stokes equations, for approximating free surface flows. Shallow-water equations assume hydrostatic pressure and neglect vertical momentum, making them two dimensional. Despite this, they were utilised for numerical modelling of three-dimensional flows, such as flow through a contraction. Researches opted for different discretization methods such as finite element, finite difference and finite volume, for solving these 2D shallow-water equations, hence the studies were presented by this classification rather than by the year they were published.

The most common approach in available literature utilises finite difference schemes for solving shallow-water equations. Lax and MacCormack steady explicit finite difference schemes were used by Jiménes (1987) and Jiménes & Chaudhry (1988) for simulating flow through a contraction with curved side walls. Both schemes were verified through an oblique hydraulic jump and shock reflecting from a wall test cases with accurate solutions achieved for both. On the other hand, the flow through a contraction with curved side walls computation presented in this case did not achieve the desired accuracy when compared to experimental data, especially in the region after the contraction. The authors outlined the main limitations to the approach used was in the assumption of hydrostatic pressure and that including vertical acceleration in the shallow water solution is desirable. This work was taken further by Bhalamudi & Chaudhry

(1992) who used unsteady explicit MacCormack finite difference scheme with an orthogonal grid. The questionable assumptions made in this publication include hydrostatic pressure distribution and uniform velocity distribution over depth. The contraction in consideration was a straight wall contraction of dimensions matching the experiment published by Ippen & Dawson (1951). The model described in this publication showed capacity of capturing shock waves in supercritical flows, but the results presented are not in agreement with the experimental measurements. Switching from steady to unsteady flow equations with 2nd order MacCormack finite difference scheme did not significantly change and improve results published in previously assessed studies. Second-order explicit MacCormack finite difference scheme was also utilised by Rahman & Chaudhry (1997) to simulate flow in the open-channel contraction. The principal difference of methods used in this study, compared to other described above, is in using an adaptive grid rather than a fixed one. This was implemented through Rai and Anderson method in which grid locations are calculated from the grid speed equation. The comparison of using a fixed grid MacCormack scheme presented in Bhalamudi & Chaudhry (1992) and the adaptive grid is given in Figure 5.2. The authors state that the grid adaptation technique presented in this study shows improvement over the fixed grid method but it is debatable if results presented support this claim.
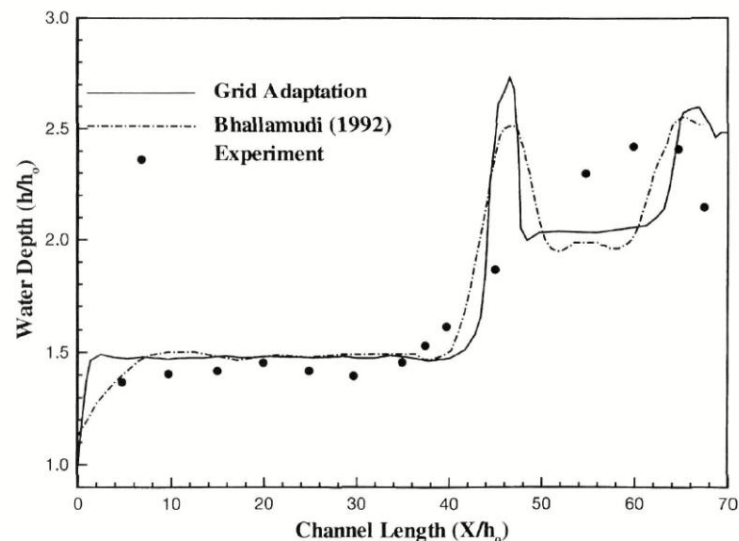
FIGURE 5.2: Comparison of adaptive and fixed grid with Mac-
Cormack scheme (Rahman & Chaudhry, 1997)

Time marching, Alternating-direction-implicit (ADI) scheme with added artificial viscosity was used by Molls & Chaudhry (1995) and there were some improvements compared to previously analysed studies. Moreover, two finite

differencing schemes, one marching in space and one marching in time, with a boundary fitted grid, were applied by Hsu,Ten & Lai (1998) to the contracting channel case. Two experimental measurements were taken for validation purposes. The first case was curved channel contraction presented by Ippen & Dawson (1951) and the second was an experiment of flow through straight wall contraction but with different geometry and flow conditions to the experiment used for validation in the available literature. The comparison of numerically simulated results of both time and space marching schemes was not in agreement with the experimental values of flow through a curved channel contraction. On the other hand, simulated results are in better agreement with the straight wall channel contraction measurements. Although gaps between simulated results and measured data exist, the overall height of the shock wave was captured and this is a significant improvement over other studies available in literature at that point in time.

The literature available is consistent in making the hydrostatic pressure assumption and neglecting vertical acceleration for this rapidly varied, free-surface flow. Some researches identified this as a possible anomaly in methodology and attempted improving the hydrostatic pressure assumption by including Boussinesq approximations. By using the Boussinesq approach, other simplifying assumptions are implied. These include the assumption that the streamwise velocity is uniform in the x-direction and that the flow velocity in vertical direction varies from 0 at channel bottom to maximum at water surface (Gharangik & Chaudhry, 1991; Molls & Zhao, 1996). The assumption that the Boussinesq approach would improve results when using 2D shallow water equations also implies that the density variations in flow do not affect the accuracy of numerical results, which is not the case. These assumptions are likely the reason authors came to a conclusion that including these Boussinesq equations in shallow-water models does not have an effect on the results of channel contraction flow.

Finite volume methods have also been utilised to solve 2D shallow-water equations by several authors (Alcrudo & Garcia-Navarro, 1993; Zhao et al., 1996). Moreover, some used finite volume methods to solve supercritical flows (Causon et al., 1999; Zhao et al., 1994). However, most focused on modelling 1D or 2D Partial Dam-Break Problem and applications of flow through a contraction were only presented by Causon et al. (1999). Finite-volume Godunov-type method was deployed to curved channel contraction to obtain solutions of 2D shallow water equations with an approximate Riemann solver and a boundary-conforming mesh. The hydrostatic pressure assumption applies to this case and the results show some agreement with the experimental data in first wave

reflection, but overall there are noticeable differences between numerical and measured data.

Berger & Stockstill (1993) used a finite element model named HIVEL2D, designed to capture water surface around boundary transitions in high-velocity channels. The two-dimensional shallow water equations were iterated using the Newton-Raphson method and the Eddy viscosities were defined empirically based on Manning's coefficient. The numerical simulation was conducted with the same domain specification as described in Ippen & Dawson (1951) laboratory experiment.
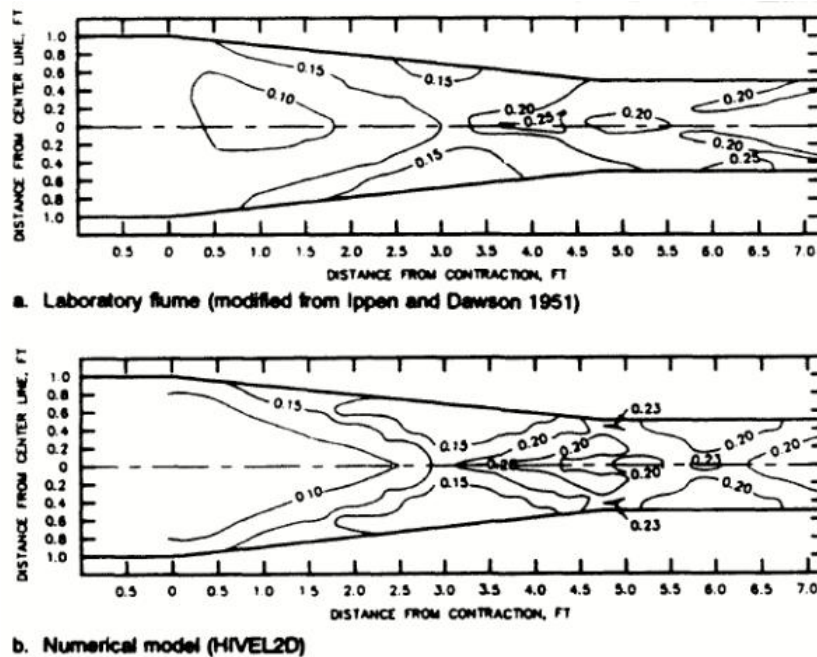
FIGURE 5.3: Depth contours of supercritical flow through a contraction (Berger & Stockstill , 1993)

The authors state that their model was capable of capturing the accurate wave propagation, but the results were presented in a manner that is difficult to compare to the original experimental data, with depth contours rather than depth over length measurements. From Figure 5.3 it cannot be concluded if the results do fully support the claim that the model can capture the water surface with great precision. Vary of the limitations of the shallow water equations in case of supercritical flow through a channel contraction, Krüger & Rutschmann (2006) presented an extended version of shallow water equations solved with a finite element solver. The extended shallow water equations model included assumptions of additional parameters for vertical velocity and pressure distributions. The comparison with Rahman & Chaudhry (1997) classic shallow water equation model and experimental results given in Figure 5.4 indicates that

there are significant improvements in the numerical method used. Although the improvements are clear, the model still fails to be validated according to the experimental measurements of Ippen & Dawson (1951).
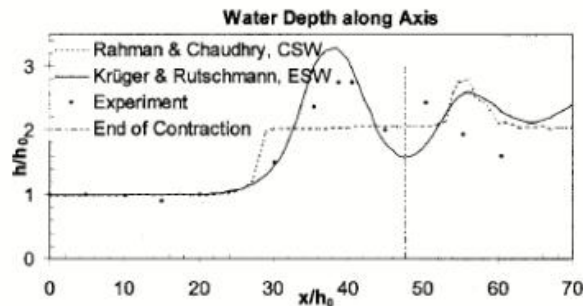
FIGURE 5.4: Water depth comparison along channel contraction
(Krüger & Rutschmann, 2006)

The novelty in the research of flow through a channel contraction was introduced by Abdo et al. (2019) who presented a 3D Reynolds Averaged Navier Stokes (RANS) equations model with a volume of fluids (VOF) solver. Abdo et al. (2019) also questioned the validity of the experimental data used in previous studies, originally presented by Ippen & Dawson (1951). The study implies that the point gauge measuring equipment used by Ippen & Dawson (1951) failed to capture accurate water surface positions and is likely outdated. Hence, the experiment with exact geometrical and physical characteristics was repeated. The authors also presented a finite volume 2D depth-averaged model, but this failed to achieve the desired accuracy. The experiment and the 3D model is given in the study by Abdo et al. (2019) were used for validation of the LES HYDRO 3D model thoroughly described and used in this thesis. The study by Abdo et al. (2019) focused only on depicting the behaviour of the free-surface for 6 ° angle of contraction but does not consider the effect of other angles of interest. It also fails to describe velocity profiles and effects of pressure and friction forces. As far as known at this point in time, no research available focuses on the stated questions. Many authors agree that more systematic research with a new approach is needed on this topic with regard to numerical modelling.

5.2.2 Free-surface Modelling

The occurrences of free-surfaces flows in nature are numerous, including deformations of the surface due to natural bed topography, turbulence or hydraulic structures. Commonly, the free-surface term refers to a boundary between two

fluids such as the boundary between an area of water and air. Free-surface flow can be defined as the surface of a fluid in which both the kinematic and dynamic conditions are applied. Kinematic condition implies that the free surface is a sharp boundary and no flow though it is possible. Dynamic condition suggests momentum conservation, or in other words, the equilibrium of forces acting on the free-surface. Computation of the free-surface can be achieved through interface-tracking methods, interface-capturing methods or hybrid methods (Ferziger & Perić, 2002).

Interface tracking methods, also known as surface methods or moving mesh methods, explicitly calculate the location of the free surface as the mesh deforms. The mesh deformation occurs for only one fluid phase at every time step. The advantage of using interface tracking methods comes from modelling only one fluid phase at every time step, as this implicates that number of the domain points required for an accurate solution is lower than for other methods. Furthermore, for water-air interface tracking, the nodes would only be required in the water body portion of the domain. However, interface tracking methods have a disadvantage when dealing with complex surface topologies, as this can lead to large amounts of grid distortion (McSherry et al., 2017). Moreover, one of the most popular interface tracking methods presented by Hou et al. (2001) does not apply to viscous flows governed by Navier-Stokes equations. On the other hand, several authors focused their research on ship hull hydrodynamics with RANS approaches and obtained satisfactory results with interface tracking methods. Free-surface was computed as a function of height in studies published by Alessandrini & Delhommeau (1996); Farmer et al. (1993); Nichols & Hirt (1973); Raven (1996); Raven & Van Brummelen (1999), all focusing on the RANS approach. Direct numerical simulation (DNS) framework with interface tracking was presented by Fulgosi et al. (2003) with the focus of analysing turbulence intensities near the interface. Large-Eddy Simulation (LES) with interface tracking studies are limited in the literature. Hodges & Street (1999) presented a dynamic LES technique applied to simulations of a laminar standing wave and turbulent open-channel flow with a finite-amplitude surface wave. Finite-volume approach was used to solve Navier-Stokes equations and it showed effective in simulating cases listed but was limited to simulations of steep waves due to errors associated using the boundary-orthogonal approach. Interface tracking methods are in theory appealing due to the reduced number of nodes required, but they can be computationally expensive. The removal of nodes close to the interface is sometimes included in the numerical procedures to ensure the accuracy of results and this can increase the overall computational cost

McSherry et al. (2017).

Interface capturing methods, also known as volume methods, do not define the water surface explicitly on a deforming mesh-like interface tracking methods do. Volume methods are employed on a Eulerian mesh, with both phases of flow included. The challenge in interface capturing methods is maintaining the thickness of the interface and mass conservation along the interface (McSherry et al., 2017). Interface capturing methods can be categorised as a particle in fluid, volume of fluid or level-set methods. An example of a particle-in-fluid method is the marker-and-cell (MAC) method of a single fluid was pioneered by Harlow & Welch (1965) and MAC method for two fluids was presented by Daly (1967). Several models based on the original MAC method were developed over the years, including simplified marker-in-cell method (SMAC) and GENS-MAC presented by Tomé & McKee (1994). The advantages of the particle in fluid methods is their ability to capture breaking waves and similar complex surface topologies. However, the computational cost of three-dimensional simulations using this method can be high. Hence, particle in fluid method studies has been mostly conducted in two-dimensions (McKee et al., 2008). The volume of fluid (VOF) method utilises scalar functions to calculate the free-surface location, making it computationally cheaper than particle in fluid methods. VOF method was introduced by Hirt & Nichols (1981) and it is based on tracking the volume percentage that one fluid takes up in a sub volume cell. Modified versions of VOF methods have been emerging in studies ever since the original method was presented with the intention to improve the accuracy robustness of the scheme. Such versions of VOF methods include flux-corrected transport method (Boris & Book, 1973), the piecewise linear interface calculation method (Youngs et al., 1982), the simple line interface calculation method (Noh & Woodward, 1979) and the compressive interface capturing scheme for arbitrary meshes (CICSAM) (Ubbink, 1997). The piecewise linear and simple line interface calculation methods can deal with breaking wave topologies but can be hard to implement in three dimensions and can result in unsatisfactory accuracy of solutions. The method presented by Ubbink (1997) is considered reliable due to its ability to simulate a very sharp boundary, but it is also very sensitive to the Courant-Friedrichs-Lewy (CFL) number (McSherry et al., 2017). The volume of fluids method has been used with LES simulations. One of the examples is the study of Xie et al. (2014) simulating open channel flow over 2D dunes using the compressive interface capturing scheme originally presented by Ubbink (1997). Other available LES studies with VOF methods involve relatively simple geometries Sanjou & Nezu (2010); Shi et al. (2000). Inclusion

of Cartesian grid methods, such as immersed boundary or cut-cell method, in LES, while utilising VOF method led to further and wider applications and several state-of-the-art studies. Xie (2015) identified that limitations of available methods on three-dimensional breaking waves over complex topography and presented an LES study with finite volume discretization and volume of fluids CICSAM scheme with partial cell treatment. The model presented in this study showed a high degree of accuracy in depicting wave overturning and was capable of capturing air entertainment and jet splashing during overturning and post-breaking. Moreover, Xie & Stoesser (2020) further worked on the previously stated study, including a moving body algorithm with the source function. This allowed for 3D collapse of the water column and 3D dam-break flow over a vertical square cylinder cases to be accurately modelled, with the ability of capturing the jet and the splashing.

The level-set method (LSM) is another popular interface capturing method, originally presented by Osher & Sethian (1988). It is based on the smooth distance function, set to zero at the interface between two-phases of the fluid. The level-set method can be applied to both 2D and 3D cases and is capable of capturing the interface in great detail (Chang et al., 1996). In a study published by Yue et al. (2005), a gap in the literature was identified regarding numerical modelling of coherent structures in open-channel flow over a dune. The author states that studies of this particular case exist with RANS approach, but they do not attempt to present a deformable free-surface and use a flat shear-free plane approach (Johns et al., 1993; Mendoza & Shen, 1990; Yoon & Patel, 1996). Large-eddy simulation (LES) approach with the level set method and two different subgrid-scale models were utilised to study the formation of the free surface (Yue et al., 2005), and the results obtained were in agreement with experimental results. A study of the effect of air-water interface on vortex shedding has been presented by Suh et al. (2011) shows an LES approach with the level set method. Periodically organised vortex shedding was found in deep water sections and small-scale vortices were present closer to the free-surface. The level set method with LES and immersed boundaries was used by Kang & Sotiropoulos (2015) to model 3D free surface flow past a complex stream restoration structure under different discharges. The methodology showed the ability to model secondary flow structures accurately and with larger Froude numbers, a hydraulic jump can also be captured. A similar methodology was presented by Kara et al. (2015a) in which a large eddy simulation approach with WALE sub-grid model and level set method was used to model flow dynamics through a submerged bridge opening with overtopping. Authors concluded

this approach is validated with experimental data and is capable of capturing vortices around bridge abutment. Moreover, Chua et al. (2019) used the same approach as Kara et al. (2015a) to investigate flow and turbulence structure and its effect on bridge abutment scour. A drawback of the level set method is in sometimes problematic mass-conservation consistency. The LSM distance function ϕ can get distorted. To avoid this, McSherry et al. (2017) states that Peng et al. (1999); Russo & Smereka (2000); Sussman et al. (1994) introduced ϕ re-initialisation techniques that reset the function at regular time intervals have been implemented. Re-initialising the ϕ function can lead to numerical inaccuracies in some cases, hence it is important to validate the numerical model with experimental data, as shown in Chapter 7.

Chapter 6

Numerical Simulation Framework

6.1 Governing Equations

Equations of motion of the incompressible, viscous, unsteady flow of a Newtonian fluid are solved using the in-house HYDRO 3D LES code, presented in many diverse studies (Bomminayuni & Stoesser, 2011; Kara et al., 2015a; Stoesser & Nikora, 2008; Stoesser, 2010, 2014; Stoesser et al., 2016). HYDRO 3D was used and validated for flow in contact tanks (Kim et al., 2010, 2013), flow in compound channels (Kara et al., 2012), flow over dunes Stoesser & Nikora (2008) and free-surface flows (Chua et al., 2019; McSherry et al., 2017). The code used is a finite-difference solved based on a staggered Cartesian grid. Spatially filtered and normalised by the Reynolds number, Navier-Stokes equations for two-phase incompressible flows used in the code are given as (Xie, 2015):

$$\nabla \cdot \overline{\mathbf{u}} = 0 \tag{6.1}$$

$$\rho(\frac{\partial \overline{\mathbf{u}}}{\partial t} + \nabla \cdot (\overline{\mathbf{u}} \cdot \overline{\mathbf{u}})) = -\nabla \overline{p} + \nabla \cdot [\mu(\nabla \overline{\mathbf{u}} + \nabla^T \overline{\mathbf{u}})] - \nabla \tau^{SGS} + \rho g + \boldsymbol{f} \tag{6.2}$$

where $\bar{\boldsymbol{u}}$=($\bar{\mathrm{u}}$,$\bar{\mathrm{v}}$,$\bar{\mathrm{w}}$) is the filtered velocity vector , t is time, $\bar{p}$ is the filtered pressure,$\nabla \tau$ is the sub-grid scale stress tensor, g is the gravitational acceleration vector, ρ is the density of fluid, μ is the dynamic viscosity and $\boldsymbol{f}$ is the body force from immersed boundary points.

Modelling turbulent flows is a challenging task as turbulence is random and involves a wide range of scales that need to be taken into account. The most straight forward approach is the direct numerical simulation (DNS) in which the Navier-Stokes equations are solved for all motions in a turbulent flow. It

is considered the most accurate method as it does not entail any approximations or averaging, but it requires very fine grids, small time steps and large domains, particularly for medium or high Reynolds number. Therefore, it is considered very computationally expensive and not sustainable for use in many engineering applications. Another approach is to average equations of motions over time by introducing Reynolds-averaged Navier-Stokes equations (RANS). RANS approach has many applications in literature but it is not appropriate for use in unsteady flows with a large range of turbulent motions. Unsteady Raynolds-averaged Navier-Stokes (URANS) approach can be utilised in some cases of unsteady flows such as tidal channel flows, but URANS cannot cope with turbulent fluctuations (Rodi et al., 2013).

6.2 Large Eddy Simulation

Large-eddy simulation is an approach that resolves large scale motions and approximates small scale ones. This approach can be adopted as large scale motions carry significantly more energy than small ones. Large and small motions are separated by a spatial filter. Schematic representation of how LES resolves flow motion is shown in Figure 6.1 where $k_{cut\text{-}off}$ is the separation point between large and small eddies. Small eddies are quantified in terms of Reynolds stress, that is modelled using a subgrid-scale (SGS) model. Large eddies will be directly resolved, as they would be in the DNS approach. Due to the modelling of small fluctuations through an SGS model, LES is capable of handling simulations on large domains as extremely fine grids are not required. It is also capable of capturing unsteady flow motions which RANS methods cannot. Therefore, it is considered to be an accurate and economical approach to obtaining solutions for turbulent flows.

The main purpose of the SGS models is to dissipate kinetic energy from small eddies in a correct manner, especially for eddies of size close to the spatial filter limit. Smagorinsky model is one of the first eddy-viscosity models utilised for subgrid-scale approximation. However, Nicoud & Ducros (1999) presented a new subgrid-scale model named Wall-Adapting-Local-Eddy-viscosity or WALE model, which the author claimed had several advantages over the original Smagorinsky model. Some of those advantages include an improved approach to detecting all turbulent structures, it is appropriate for LES with complex geometries, the need for a dynamic constant of damping function is eliminated and the ability of the new model to reproduce laminar to turbulent transitions in flow. HYDRO 3D support the use of both models mentioned but the WALE model was used
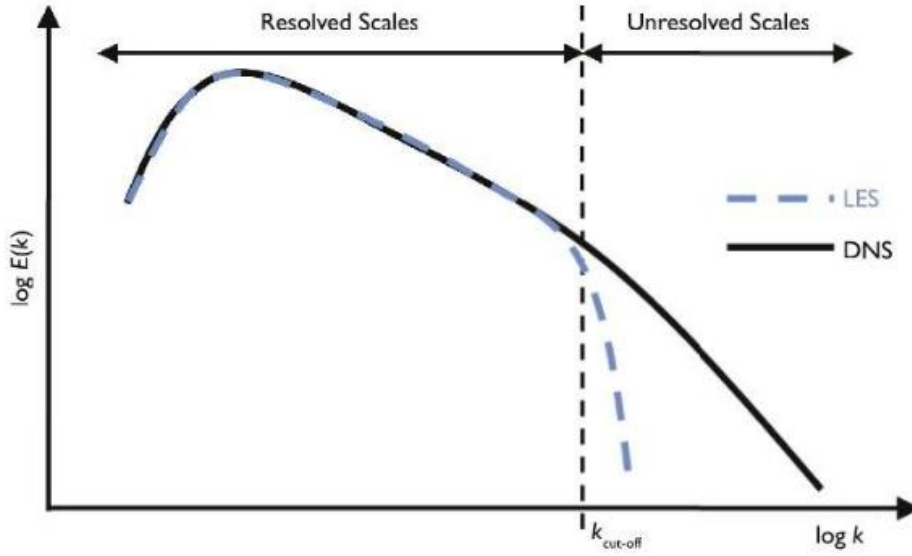
FIGURE 6.1: Large Eddy Simulation Concept(Rodi et al., 2013)

for all presented numerical results, hence it has been described in more detail. The eddy-viscosity in WALE is formulated as:

$$\nu_{\mathrm{T}} = (C_{\mathrm{w}}\Delta^2)\frac{(S_{\mathrm{ij}}{}^{\mathrm{d}}S_{\mathrm{ij}}{}^{\mathrm{d}})^{3/2}}{(\overline{S_{\mathrm{ij}}S_{\mathrm{ij}}})^{5/2}(S_{\mathrm{ij}}{}^{\mathrm{d}}S_{\mathrm{ij}}{}^{\mathrm{d}})^{5/4}} \tag{6.3}$$

where ν_{T} is eddy viscosity, C_w is a constant of value of 0.46, Δ is subgrid characteristic length scale, $\overline{S_{\mathrm{ij}}}$ is the rate of strain tensor for resolved scale defined as:

$$\overline{S_{\mathrm{ij}}} = \frac{1}{2}\left(\frac{\partial\overline{u_{\mathrm{i}}}}{\partial x_{\mathrm{j}}} + \frac{\partial\overline{u_{\mathrm{j}}}}{\partial x_{\mathrm{i}}}\right) \tag{6.4}$$

$S_{\mathrm{ij}}{}^{\mathrm{d}}$ is the traceless symmetric part of the square of the velocity gradient tensor, $\overline{g_{\mathrm{ij}}} = \frac{\partial\overline{u_{\mathrm{i}}}}{\partial x_{\mathrm{j}}}$ and δ_{ij} is the Knocker delta symbol Cevheri et al. (2016)

$$S_{\mathrm{ij}}{}^{\mathrm{d}} = \frac{1}{2}(\overline{g_{\mathrm{ik}}g_{\mathrm{kj}}} + \overline{g_{\mathrm{ik}}g_{\mathrm{kj}}}) - \frac{1}{3}(\delta_{\mathrm{ij}}\overline{g_{\mathrm{kk}}})^2 \tag{6.5}$$

6.3   Solution of Navier-Stokes equations

A staggered rectangular Cartesian grid with velocities stored at the middle of cell faces and pressure components stored in the centre of cell centres was used. Filtered Navier-Stokes equations are advanced in time using the fractional-step method that utilises decoupled velocity and pressure equations.

A fourth-order central differencing scheme approximates diffusive terms, while

the fifth-order weighted, essentially non-oscillatory (WENO) scheme calculates convection terms in both momentum and level-set equations. The governing equations are advanced in time using the fractional step method coupled with an explicit, low-storage, third-order Runge-Kutta scheme. An iterative multi-grid technique is used to solve the Poisson pressure equation. Domain decomposition and message passing interface (MPI) protocols for sub-domain communication are used to run the code in parallel on high-performance computers (Ouro et al., 2019). The fractional-step method utilises two steps to obtain a solution. The first step is to initially predict intermediate velocities u_i^*, without enforcing the incomprehensibility constraint and using a two-stage explicit Runge-Kutta method shown in Equations (6.6) (Cevheri et al., 2016).

$$u_i^{*,n+1/2} = u_i^n + \frac{\Delta t}{2}[\mathbf{R^n} - \frac{\partial}{\partial x_i}p^{n\text{-}1/2}]$$
$$u_i^{*,n+1} = u_i^n + \Delta t[\mathbf{R^{*,n+1/2}} - \frac{\partial}{\partial x_i}p^{n\text{-}1/2}] \qquad (6.6)$$
$$R = [-\frac{\partial(u_i u_j)}{\partial x_j} + (\frac{1}{R_e} + \nu_T)\frac{\partial^2 u_i}{\partial x_i \partial x_j}]$$

The second step of the fractional-step method entails the projection of intermediate velocities onto the divergence-free vector fields through a Poisson equation to calculate an increment to the pressure field, δp

$$\nabla^2 \delta p = \frac{1}{\delta t}\frac{\delta}{\delta x_i}u_i^{*,n+1} \qquad (6.7)$$

where ∇^2 is the Laplacian operator. Equation (6.7) is solved using the multigrid method, iteratively. The next step is to update the velocity field as shown in Equation (6.8)

$$u_i^{*,n+1} = u_i^{n+1} + \Delta t\frac{\partial(\delta p)}{\partial x_i} \qquad (6.8)$$

$$p^{n+1/2} = p^{n\text{-}1/2} + \delta p \qquad (6.9)$$

Finally, the Poisson equation is solved again with the new pressure. The presented iteration is repeated until the divergence-free condition is achieved. This is defined by the CFL (Courant-Friedreich-Lewy) condition.

6.4   Level-set Method

The free-surface is calculated in every time step using the level-set method (Osher & Sethian, 1988). The method is based on a level-set distance function ϕ and it is formulated as:

$$\phi(x,t) \begin{cases} < 0 & \text{if} \quad x \, \epsilon \, \Omega_{gas} \\ = 0 & \text{if} \quad x \, \epsilon \, \Gamma \\ > 0 & \text{if} \quad x \, \epsilon \, \Omega_{liquid} \end{cases} \tag{6.10}$$

where Ω_{gas} is the gas fluid domain, Ω_{liquid} is the liquid fluid domain and Γ represents the interface. The interface movement is calculated through a pure advection equation (Sethian & Smereka., 2003):

$$\frac{\partial \phi}{\partial t} + u \cdot \nabla \phi = 0 \tag{6.11}$$

Discontinuities between density and viscosity at the interface can lead to numerical instabilities. This is avoided by setting a transition zone in which density and viscosity change between water and air is smoothed.

$$\begin{aligned} \rho(\phi) &= \rho_g + (\rho_l - \rho_g)H(\phi) \\ \mu(\phi) &= \mu_g + (\mu_l - \mu_g)H(\phi) \end{aligned} \tag{6.12}$$

The transition zone is defined as $|\phi| \leq \varepsilon$, where ε is half the thickness of the interface. This is implemented through the Heaviside function $H(\phi)$ as formulated (Osher & Fedkiw, 2002; Zhao et al., 1996b):

$$H(\phi) = \begin{cases} 0 & \text{if} \quad \phi \, < -\varepsilon \\ \frac{1}{2}[1 + \dfrac{\phi}{\varepsilon} + \dfrac{1}{\pi} sin(\dfrac{\pi\phi}{\varepsilon})] & \text{if} \quad \phi \, \leq \, \varepsilon \\ 1 & \text{if} \quad \phi \, > \, \varepsilon \end{cases} \tag{6.13}$$

Although the level set method is successful in capturing the air-water interface, instabilities can arise if ϕ does not maintain its property of $|\nabla\phi| = 1$ as time advances. This is addressed through a re-initialisation technique applied in the transition zone. The re-initialised signed distance function d is calculated by solving the partial differential equation given by Sussman et al. (1994):

$$\frac{\partial d}{\partial t_a} + s(d_0)(|\nabla d| - 1) = 0 \tag{6.14}$$

where $d_0(x,0) = \phi(x,t)$, t_a is the artificial time and $s(d_0)$ is the smoothed sign function formulated as:

$$s(d_0) = \frac{d_0}{\sqrt{d_0{}^2 + (|\nabla d_0| \, \varepsilon_{\mathrm{r}})^2}} \tag{6.15}$$

This partial differential equation is solved for several iteration steps, $\varepsilon_r/\Delta t_a$ where ε_r is a single grid space. These adjustments to the level set method are applied only in the interface zone (Kara et al., 2015a).

6.5 Immersed Boundary Method

The contraction geometry in numerical simulations performed was implemented with the immersed boundary method approach. The immersed boundary method was pioneered by Peskin (2002), intended for modelling fluid-structure interactions in biological fluid dynamics applications. Many variations of the method became available over the years, some with continuous body boundary approach and some with the discrete Lagrangian particle approach, which was used in simulations presented in this thesis. The direct forcing immersed boundary method used in this study was presented by Ulhmann (2005), ensures a no-slip boundary at the contraction walls through the forcing term $\boldsymbol{f}$. A predictor-corrector methodology is given in several steps listed below. To start, the predicted Eulerian velocity u^* is interpolated with a delta function δ, to obtain the Lagrangian velocity $\mathrm{U_L}$.

$$U_L = \sum_{ijk=1}^{n_e} u_{ijk}^* \cdot \delta(x_{ijk} - X_L) \cdot \Delta x_{ijk} \tag{6.16}$$

where U_L is the Lagrangian point velocity, n_e is the number of Eularian neighbours, u_{ijk}^* is the fluid velocity, δ is the interpolation function, x_{ijk} is the vector of coordinates on Eularian mesh cells, X_L is the location of Lagrangian marker L in 3 dimensions and Δx_{ijk} is the Eulerian cell volume.

The three-dimensional delta function δ is defined as (Ouro & Stoesser , 2017):

$$\delta(x_{ijk} - X_L) = \frac{1}{\Delta x_{ijk}}\phi_k(\frac{x_{ijk} - X_L}{\Delta x})\phi_k(\frac{y_{ijk} - Y_L}{\Delta y})\phi_k(\frac{z_{ijk} - Z_L}{\Delta z}) \tag{6.17}$$

One dimensional ϕ_k kernel function that prevents large oscillations of 27 neighbours was chosen. After the Lagrangian velocity was calculated, the force to be exerted by the Lagrangian markers (F_{L}) to fulfil the no-slip condition at

the marker location. This force can be computed from the difference in two velocities over time. For static bodies, as in this study, U_L is equal to zero.

$$F_L = \frac{U_L{}^* - U_L}{\Delta t} \tag{6.18}$$

Eulerian force $\boldsymbol{f}$ was then obtained from the equation below, transformed from the Lagrangian force with an interpolation function δ and the volume assigned to the markers ΔV_L, approximately eqaul to Eulerian cell volume Δx_{ijk}.

$$f(x_{ijk}) = \sum_{L=1}^{n_L} F_L \cdot \delta(X_L - x_{ijk}) \cdot \Delta V_L \tag{6.19}$$

The final step in the method is to update the Eulerian fluid velocity.

$$\overline{u^*} = u^* + f\Delta t \tag{6.20}$$

Chapter 7

Numerical Simulation Results

7.1 Numerical Simulation Validation

7.1.1 Experiment Description

The experimental data published by Abdo et al. (2019) was used to validate the numerical model, described in the previous chapter, in terms of water surface profiles, both near wall and along the domain centerline. The computational set up shown in Figure 7.1 replicates the experimental study conducted at the University of South Carolina, presented in Abdo et al. (2019). The experimental model had a length of 4.0 m and a contraction angle of 6°. A sluice gate was placed at the upstream of the flume to provide specific depth inflow while also controlling discharge. Water surface elevations were measured with an ultrasonic distance measuring sensor UNAM 18U6903/S14. This experiment was originally conducted by Ippen & Dawson (1951), but it was repeated by Abdo et al. (2019) because it was suspected that the original experiment had measurement errors as a result of a technological drawbacks at the time. The original scenario with a flow rate of 0.041 m^3s^{-1}, water depth of 0.03 m and matching Froude number, F of 4.01 was used to validate the numerical model presented by the same authors. Experimental data for different flow rates of 0.038, 0.044, 0.047 and 0.050 m^3s^{-1} was also presented in the cited publication.

7.1.2 Computational Domain

The computational domain is an exact replica of the experimental setup. The flow domain is 4.0 m long, 0.6 m wide at the inlet and 0.3 m wide at the outlet, giving a contraction ratio of 2:1. The immersed boundary method ensures the no-slip condition in the contraction starting at 0.55 m from the inlet, at an angle of 6° angle and stretches until 2.0 m streamwise. The following narrower rectangular channel is 2.0 m long and 0.15 m wide, as shown in Figure 7.2.
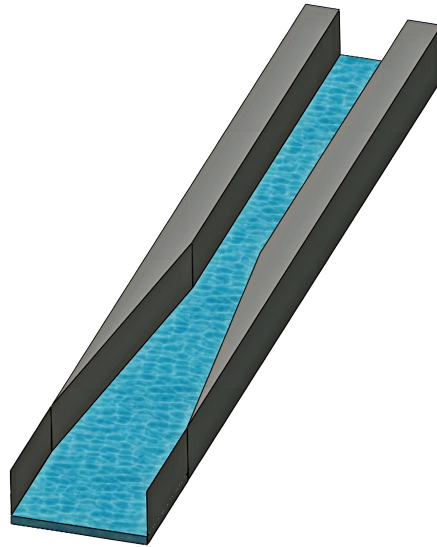
FIGURE 7.1: Domain geometry
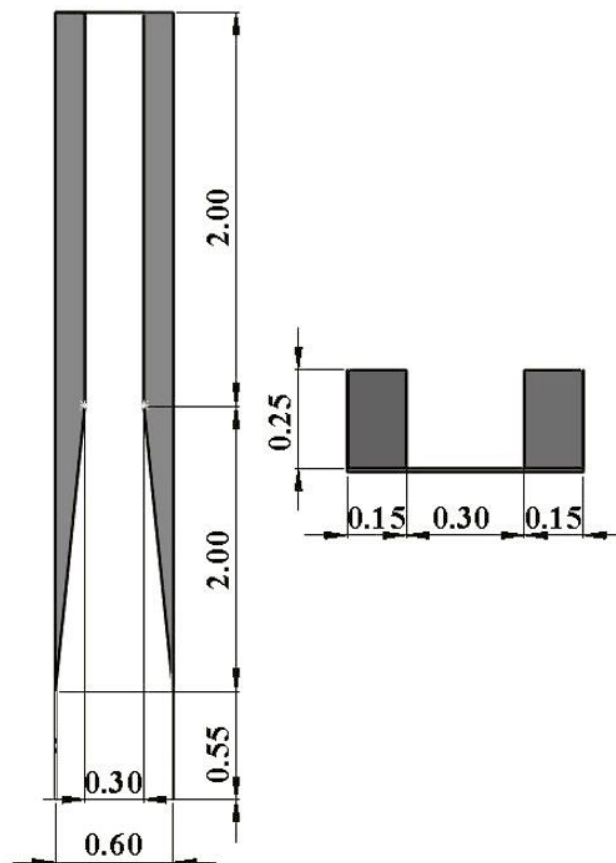
FIGURE 7.2: Domain dimensions

The initial water depth was set to 0.03 m and the prescribed bulk velocity U_b corresponds to a discharge of 0.041 m³s⁻¹. This yields a bulk Reynolds number, Re, of 130,000. The pressure gradient between upstream and downstream end

yields a global (domain-averaged) bed shear-stress, $<\tau>= 0.45$ N m^{-2} and global shear velocity of $u_*= 0.02$ m s^{-1}. At the inlet, a constant velocity inflow boundary condition was used, and a convective boundary condition was used at the outlet. The experiment used a sluice gate at the inlet, with an unknown velocity profile and turbulent fluctuations, which could be a source of inaccuracy when numerical results are compared with experimental data. No-slip boundary conditions were used at side walls and the bottom of the domain. The level-set method, with the initial location of the free-surface at 0.03 m, was used to compute the water surface elevation. A uniform grid with 800 x 240 x 100 points in x, y and z directions, respectively, discretises the flow domain and time-averaging of turbulence statistics is commenced after approximately 24 eddy turnover times ($t_e=h/u_*$), where h is the water depth.

7.1.3 Validation

Two free-surface profiles were taken at separate locations. Firstly, a profile at y=0.3 m or the centre line profile was analysed, following the second near-wall profile at 0.08 m from the wall. In the results presented, the LES model was compared to both the experimental data and the 3D model presented by Abdo et al. (2019). The wave propagation in the domain, both averaged and instantaneous is given in Figure 7.3. The figure shows a sketch of the created shock-waves originating at x= 0.58 m, i.e. shortly after the start of the contracting section. At a contraction angle of 6 °, the shock-waves are angled at 13.8°. They re-attach before the contracting section ends at approximately x=1.8 m with a crossover point at x= 1.25 m. The figure visualises the time-averaged and the instantaneous water surface in the open channel. As the flow enters the contraction, shock-waves are generated at either of the contraction edges. These are well defined on the time-averaged plot and not very obvious on the instantaneous due to the strong turbulence prevailing. As the contraction angle is relatively mild, the angles of the shock-waves are soft too, and hence the two waves cover almost the entire contraction. The edge of the reflecting wave, which occur in the narrow section are more steep and waves are shorter. The amplitude decreases towards the outlet, as reflected by shock-waves dissipation.

Comparison of experimental and numerical data at the centerline profile presented in Figure 7.4 indicate that the LES model, coupled with the level-set method and immersed boundary method results show that the approach is validated and can be used as an accurate modelling tool. It can be concluded that the LES model predicts the free-surface location at the beginning and within
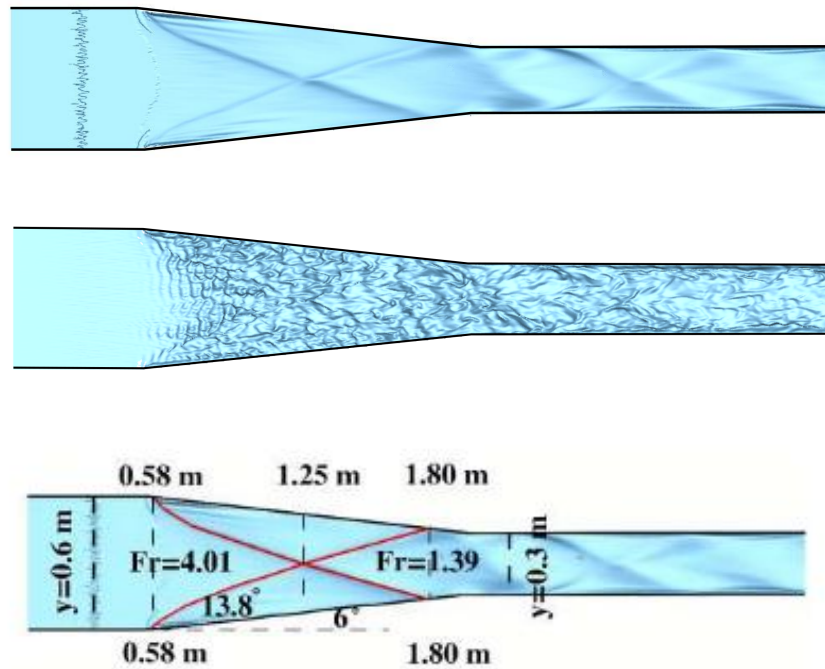
FIGURE 7.3:   Propagation of surface waves: (Top) Time-averaged, (Middle) Instantaneous, (Bottom) Shock-wave geometry

the contraction remarkably well. Peak positions of the standing waves in the channel were captured and are in good agreement with the presented data. The water surface is approximately 5% overestimated from the cross-over point towards the end of the contraction. The reflected shock waves in the narrow channel were captured reasonably well by the LES. Some discrepancies are to be expected, considering that velocity profile at the inlet is unknown. Moreover, free-surface approximations are expected to have some level of uncertainty in the results. To sum up, the LES offers improved predictions over the RANS simulation results of (Abdo et al., 2019).

The near-wall free surface profile is shown in Figure 7.5, and it can be noted that the LES model follows the same trend of the experimental data. The free surface location is slightly overestimated (around 10%). Similarly to the centerline profile, the presence of standing waves has been captured. Satisfactory agreement with experimental results exists and when contrasted with the Abdo et al. (2019) RANS model, standing waves were captured more accurately with the LES code combined with the level-set method. The LES model slightly overestimates the height of the water surface, but this could be due to the unknown inlet condition used in the experiment, which could not be embedded in the model as no description or data was provided in the publication. Overall,
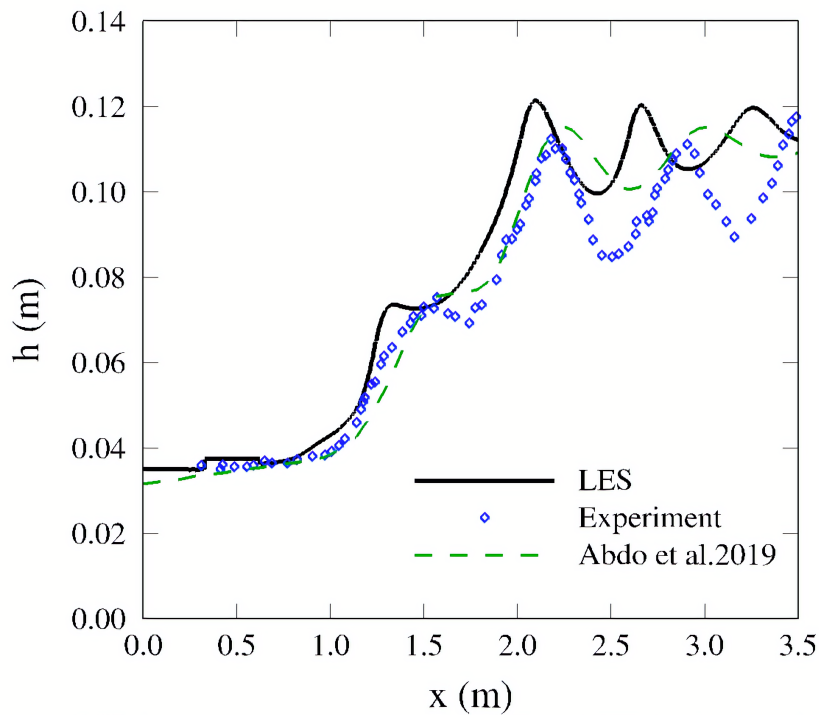
FIGURE 7.4: Centerline profile comparison of measured and time-averaged simulated water depth

from the plots presented, it can be concluded that the LES model is validated against the experimental data presented in Abdo et al. (2019).

LES model, coupled with the level-set method for free-surface tracking captured the cross-wave propagation, and the three-dimensional water surface is given in Figure 7.6.

Moreover, instantaneous streamwise velocity streamlines are shown in Figure 7.7, indicating how the instantaneous velocity changes with the water level rise.

7.2 Flow Characteristics

7.2.1 Velocity of Flow

Flow characteristics of supercritical flow through a channel contraction have not been analysed in previously published studies. A three-dimensional view of the streamwise velocity in terms of streamlines is given in Figure 7.7, showing qualitatively how the streamwise velocity changes from a very shallow fast flow to a deeper, slower flow due to the disproportional increase in water level towards the narrow section.
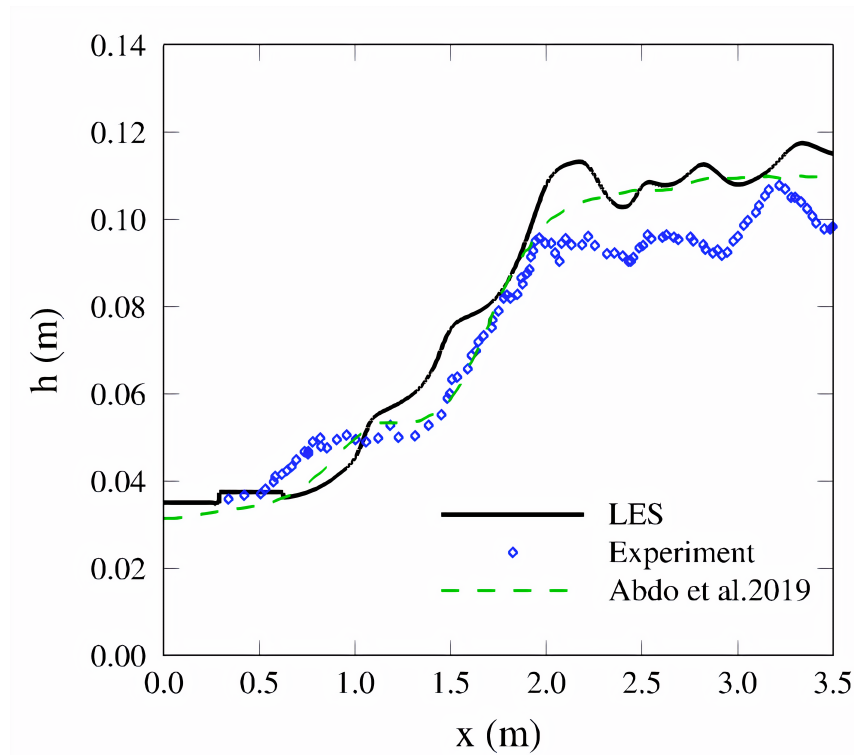
FIGURE 7.5: Near-wall profile comparison of measured and time-
averaged simulated water depth

FIGURE 7.6: Time-averaged three dimensional water surface

Near-bed and near-surface time-averaged streamwise velocity distributions are
depicted in Figure 7.8.

The results presented were normalised by the bulk velocity. Both velocity dis-
tribution plots given show that the velocity drops as the channel contracts. As
it can be seen from both near-bed and near-surface streamwise velocity distri-
bution plots, the velocity generally decreases as the channel contracts until it
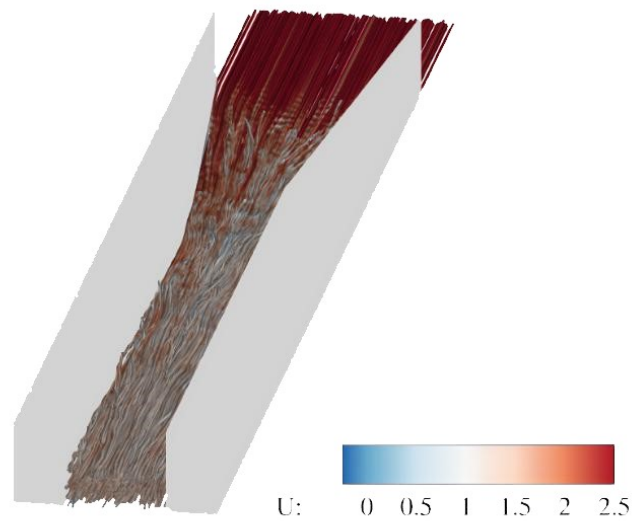
FIGURE 7.7: Streamlines of the flow

reaches a constant value near the end of the narrow section. The maximum velocity is at the inlet, and it reduces as the flow travels towards the outlet as a result of the water surface increase. Noteworthy are pockets of high velocity near the bed and near the sidewalls and low velocities following the shock-waves. Strong secondary flow develops in the contraction, and a reasonably strong water surface variation occurs in the spanwise direction which moves high-momentum fluids into the corners of the contraction while bringing low momentum fluid towards the centre of the channel.

Streamwise velocity profiles were plotted for eight different locations along the streamwise direction, and presented in Figure 7.9. Velocities shown were normalised by the bulk velocity. The flow has a constant inflow at the inlet and as it approaches the contraction, the flow accelerates. The velocity profile is not logarithmic due the strong secondary flow and the peak of the velocity profile occurs well below the water surface. This is depicted in profiles at x=1.0, x=1.25 and x=1.5. Around the shock-wave reattachment location, an additional secondary velocity peak occurs near the water surface, the result of high-momentum being transported from the corners of the channel towards the centre. This secondary peak disappears in the narrow channel section. Towards the outlet, the flow is recovering slowly towards a logarithmic velocity distribution. The figure shows that the flow acceleration reaches its maximum at the x = 1.25 m location, exactly at the shock-wave cross over point, where the peak of the time-averaged streamwise velocity is 1.36 times the local bulk velocity.
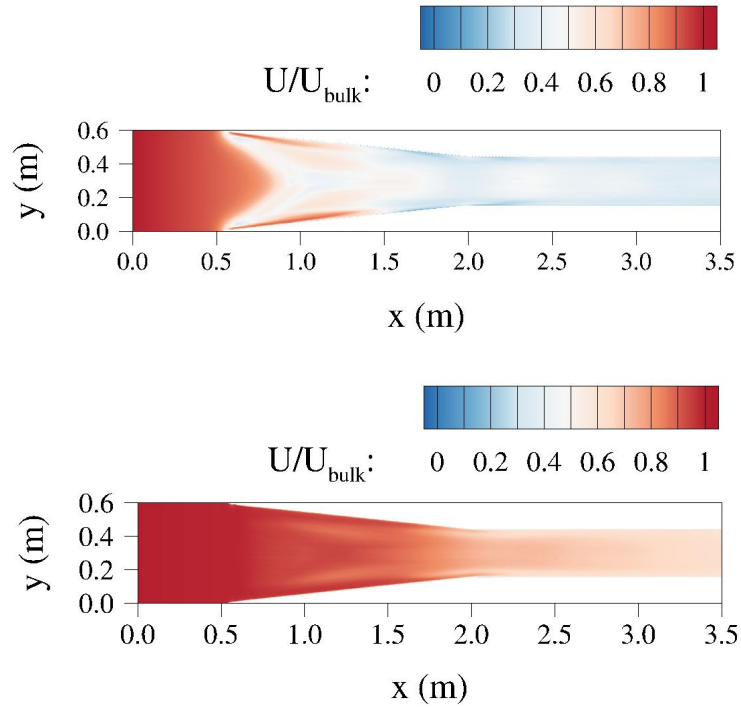
FIGURE 7.8: Time-averaged streamwise velocity distributions;
Near-bed distribution at z/h=0.1 (Top) and Near-surface distri-
bution at z/h=0.9 (Bottom)
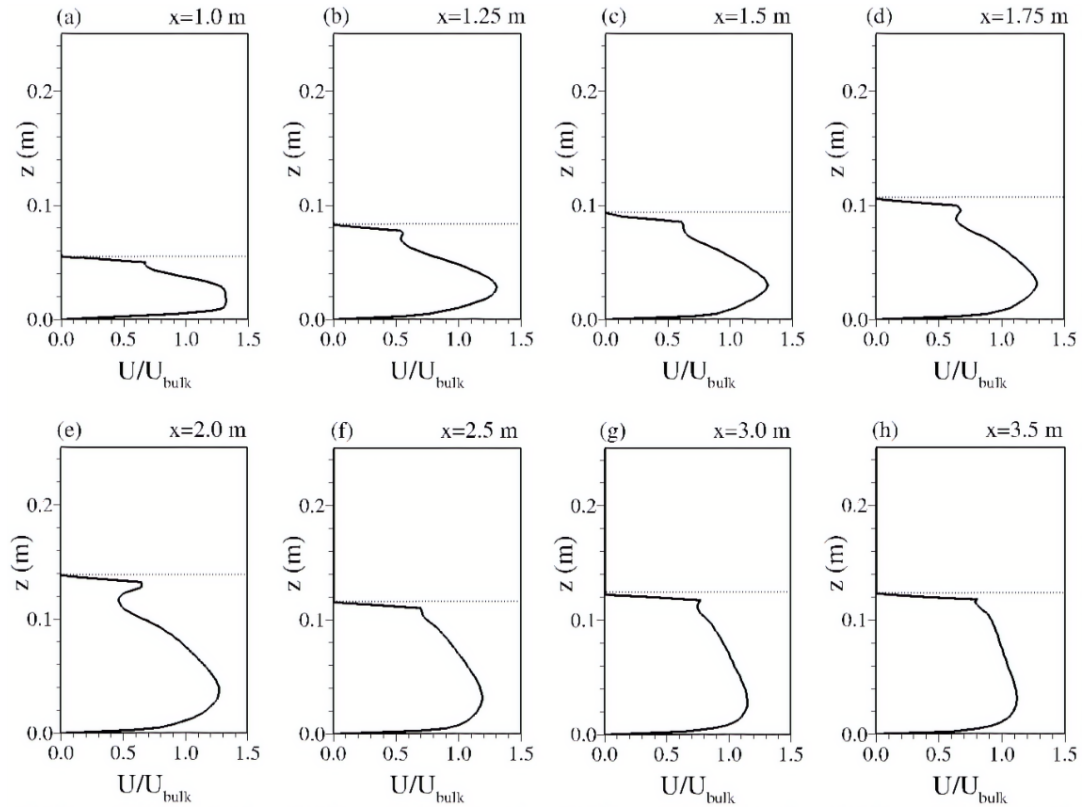
FIGURE 7.9: Time-averaged streamwise velocity profiles in the
contraction (taken at the centerline)

The distribution of the spanwise velocity in selected cross-sections in the contraction are presented in Figure 7.10. The plots indicate strong spanwise momentum at the beginning of the contraction (a) and fluid from the centre of the channel is being transported towards the walls which is where the water surface rises and generates the shockwaves. At $x = 1.25$ strong converging flow near the water surface is observed, which results in the up-flow at the wave crossover point. The water surface is depressed between the shockwaves and circulation zones are symmetrical and opposite (x=1.8). In the narrow channel, the reflected waves on either side wall result in near-surface flow towards the walls where the water surface rises.
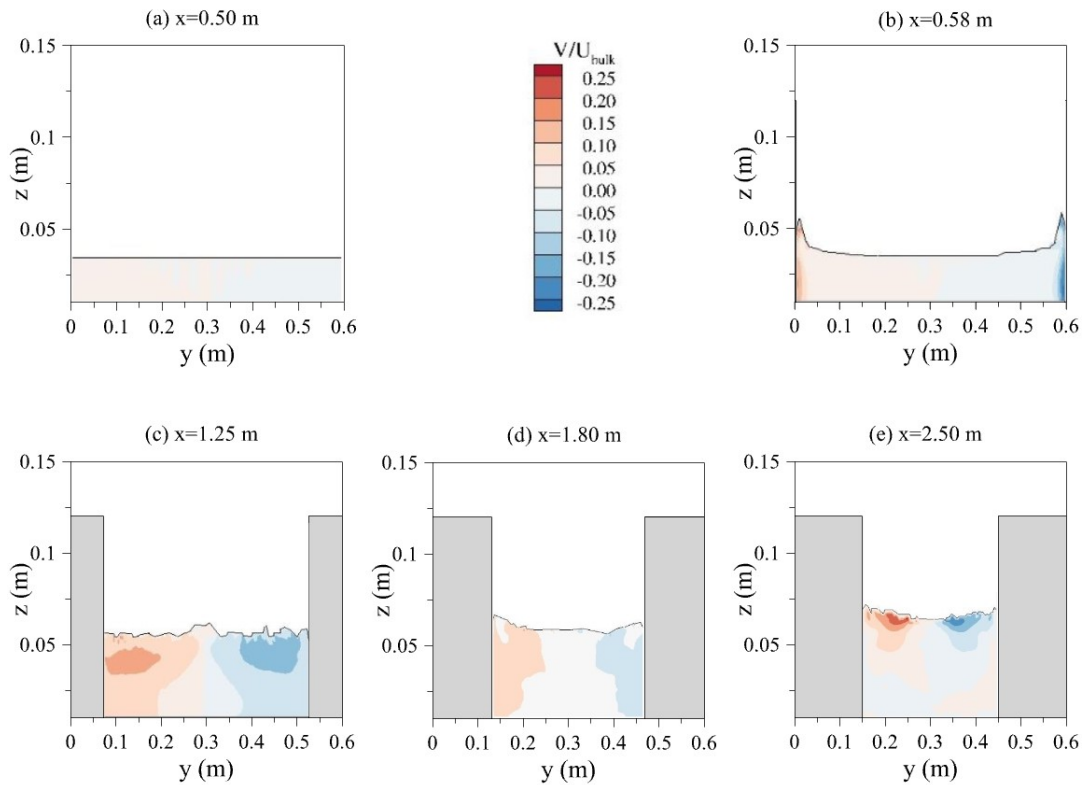
FIGURE 7.10: Contours of the time-averaged wall-normal velocity in selected cross-sections.

Contours of the vertical velocity in selected cross-sections are presented in Figure 7.11. The plots indicate up flows near the wall at the beginning of the contraction (b) and fluid from the bed of the channel is being transported towards the water surface which rises in the form of the shockwaves. At $x = 1.25$ mild up flow of fluid is seen followed by circulation zones in the contraction, lasting nearly until the end of the contracting section ($x = 1.8$ m). The water surface is depressed between the reflected shockwaves which leads to down-flows

near the walls.
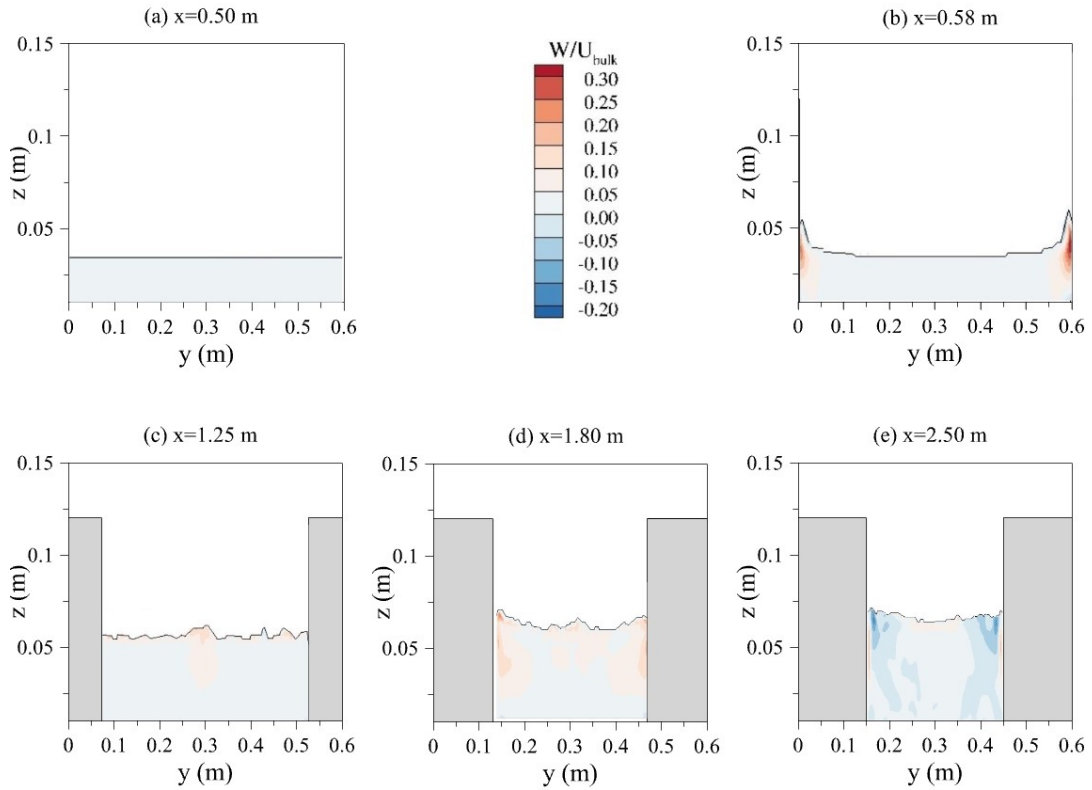
FIGURE 7.11: Contours of the time-averaged wall-normal veloc-
ity in selected cross-sections.

7.2.2   Turbulence Intensities and Shear Stresses

Distribution of turbulent kinetic energy represents the unit of kinetic energy
per unit mass, and it physically represents the root mean square of velocity
fluctuations (u', v', w'). It can be calculated from the equation:

$$tke = \frac{1}{2}(\overline{u'^2} + \overline{v'^2} + \overline{w'^2}) \tag{7.1}$$

The near-bed spatial distribution of turbulent kinetic energy is depicted in Fig-
ure 7.12. The plot was normalised by the square shear velocity, which is $u_* =$
0.02 m/s. From the figure, it can be concluded that the region of high kinetic
energy can be found in the contraction, at the same location where the water
surface starts to rise. The peak was reached between x=1.0 m and x=1.5 m,
as expected due to this being a location in the domain where the streamwise
velocities are maximum. The kinetic energy starts dissipating when the flow
reaches the uniform channel section, at x = 2.0 m.
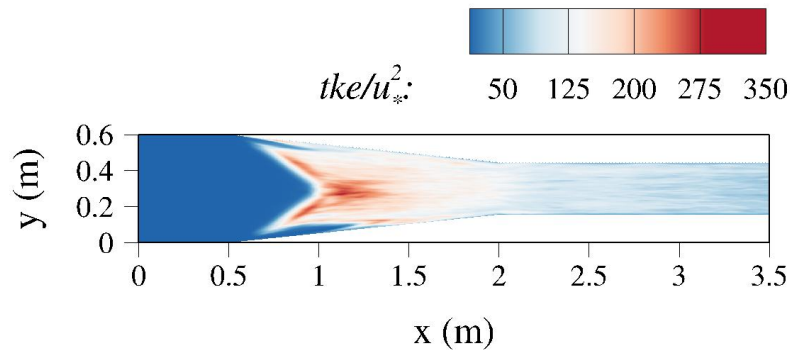
FIGURE 7.12: Normalised turbulent kinetic energy taken near
the bed at z/h=0.1

All three contributors of the turbulent kinetic energy have been analysed to see
which stress distribution has the most effect on the flow turbulence intensity.
From figures presented, it can be concluded that the most significant contrib-
utor to the turbulence kinetic energy comes from streamwise normal Reynolds
stress. Figure 7.13 indicates that the square root values of *u'u'* are almost 20
times the squared sheer velocity. The location of the maximum streamwise nor-
mal Reynolds stress was found at the same location where the maximum flow
velocity is found, at the middle of the contracting section, where the two shock-
waves cross over. As the flow approaches the outlet, the normal streamwise
stress dissipates to half of its maximum value.
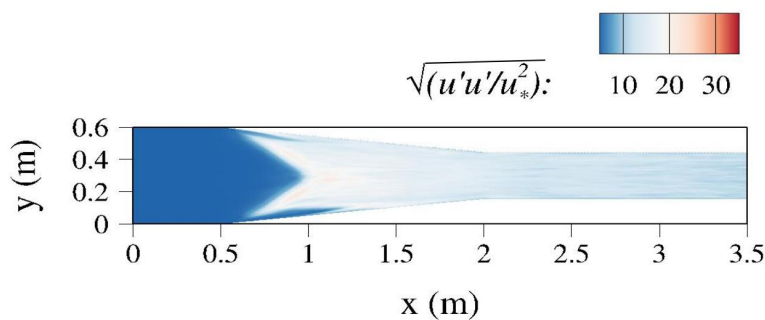
FIGURE 7.13: Normalised streamwise normal stress distribution
taken near the bed at z/h=0.1

The spanwise normal Reynolds stress was significantly smaller than the stream-
wise stresses, with the maximum value reaching $\sqrt{v'v'/u*^2} \approx 10$. The maximum
value was also located at the point in the middle of the contraction, where the
rise in the water level also reaches its maximum height. The stress drops to a
quarter of its peak near the outlet.
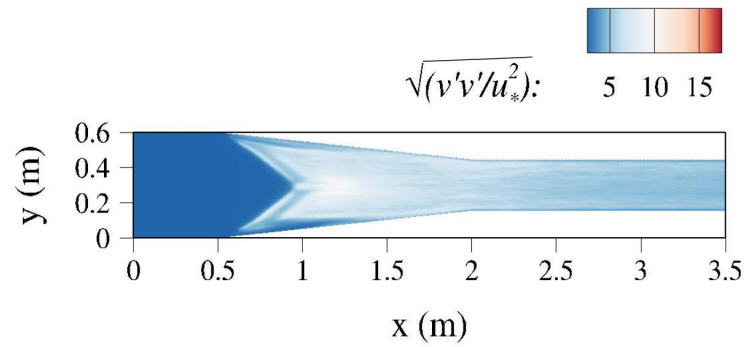
FIGURE 7.14:   Normalised spanwise normal stress distribution
taken near the bed at z/h=0.1

Near-bed distribution of vertical stresses is shown in Figure 7.15, indicating
the increase in vertical stress at points where the flow accelerates. Similarly
to streamwise and spanwise stresses, the highest magnitude of vertical stress
is found in the middle of the contraction. The largest negative stresses of
$\sqrt{w'w'/u*^2}$ reach magnitudes of 5 to 10. Vertical stress also diffuses as the
contraction turns into the uniform open-channel and moves towards the outlet.
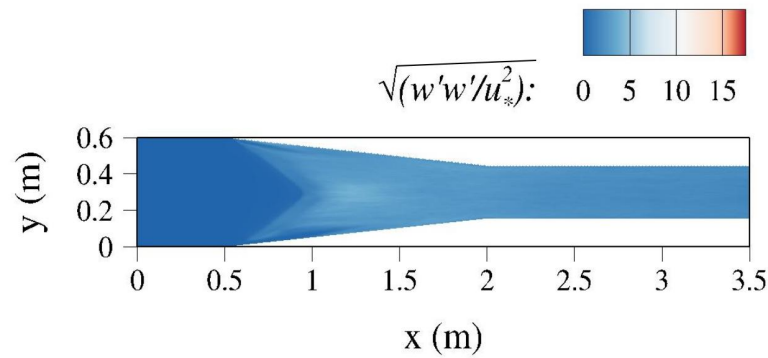
FIGURE 7.15:   Normalised vertical normal stress distribution
taken near the bed at z/h=0.1

7.3   Forces and Energy Losses

7.3.1   Pressure Distribution

A dimensionless number that depicts how relative pressure is distributed in fluid
flow is defined as the pressure coefficient, *Cp*. The pressure coefficient can be
obtained from the equation:

$$C_p = \frac{P - P_0}{0.5 \cdot \rho \cdot U_{bulk}{}^2} \tag{7.2}$$

where, Cp is the pressure coefficient, P is the pressure, P_0 is the pressure at the inlet, ρ is the density of the water and U_{bulk} is the bulk velocity.
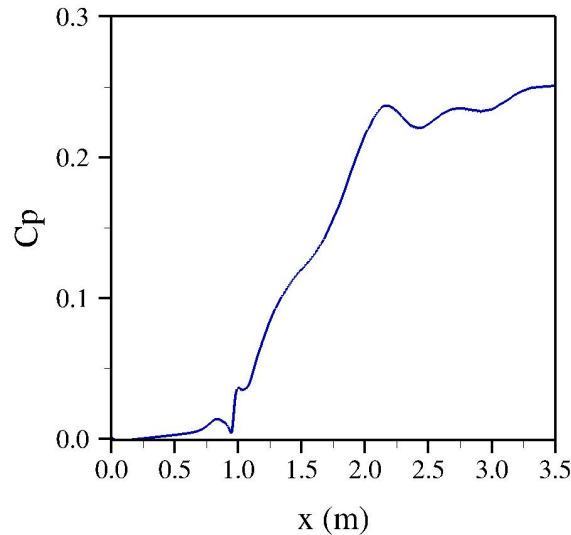
FIGURE 7.16: Pressure coefficient near-bed at z/h=0.1 taken at centerline

The pressure coefficient was taken near-bed at the centerline and plotted in Figure 7.16. As it can be identified, the pressure rises as the channel contract from 0.6 to 0.3 m width. It is to be expected that the reduction of the flow area and increase in the water-surface will also result in pressure coefficient increase along the domain.

7.3.2   Drag Forces

Drag forces act on the contraction side walls as the flow moves from the 0.6 to 0.3 m wide channel. The total drag force is contributed to by the viscous drag and form drag force.

The form drag force is a result of the changing pressure gradient, and the viscous drag is a result of side wall and bed friction. The viscous drag, F_μ is obtained from shear side wall stress ($\mu(\partial U/\partial y + \partial W/\partial y)$) and shear bed stress ($\mu(\partial U/\partial z + \partial V/\partial z)$). The viscous drag coefficient is obtained from Equation (7.3), where C_f is the viscous coefficient, F_μ is the total viscous force, ρ is the density of water and U_{bulk} is the bulk velocity of flow. The viscous, or friction coefficient for both bed and wall friction is depicted in Figure 7.17. From the figure, it

can be concluded that the bed friction coefficient tends to become uniform as the fluid moves towards the outlet. Wall friction peaks at the beginning of the contraction, more specifically, at the location of the sharp corner. This is anticipated as the contraction corner is the point of peak shear velocity in the domain.

$$C_f = \frac{F_\mu}{0.5 \cdot \rho \cdot U_{bulk}^2} \tag{7.3}$$
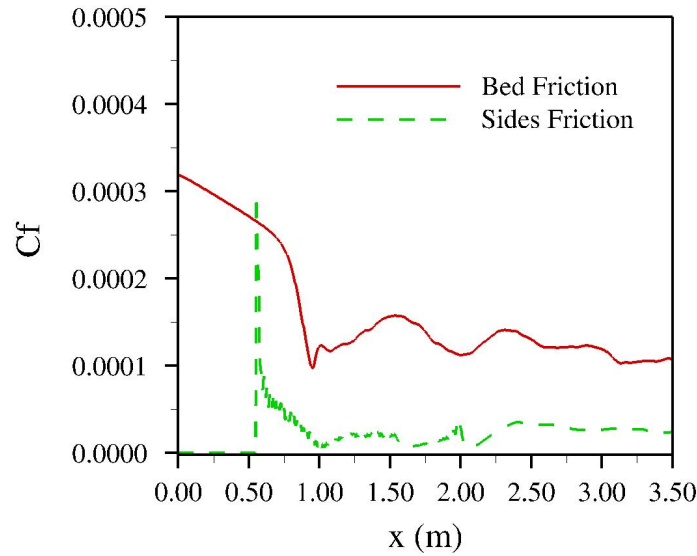
FIGURE 7.17: Viscous drag coefficient form both bed and walls

The form drag, F_p was analysed for the contraction area from x=0.55 m to 2 m. The form drag was found by calculating the pressure gradient over the length of the contraction walls and integrated over the depth of flow. The form drag coefficient was calculated using Equation (7.4), where C_{pd} is the form drag coefficient, F_p is the form drag, ρ is the density of water and U_{bulk} is the bulk velocity of flow.

$$C_{pd} = \frac{F_p}{0.5 \cdot \rho \cdot U_{bulk}^2} \tag{7.4}$$

The comparison of form drag coefficient and viscous drag coefficient in the contraction is presented in Figure 7.18. It can be noted that the form drag coefficient peaks at the centre of the contracting sides. The form drag coefficient becomes more uniform as the flow approaches the uniform width section, and this is to be expected as the form drag in the 0.3 m wide section is constant due to the flow being parallel to the side walls. From the figure, it can also be concluded that the form drag coefficient is significantly larger than the viscous

drag, and this is an expected effect of a high Reynolds number. At the point of maximum form drag coefficient, at x = 1.5 m, the friction drag coefficient is about 2% of the C_{pd}. At the location of the contraction start, where the sharp corner is located, the viscous drag coefficient is about nine times larger than the form drag coefficient.
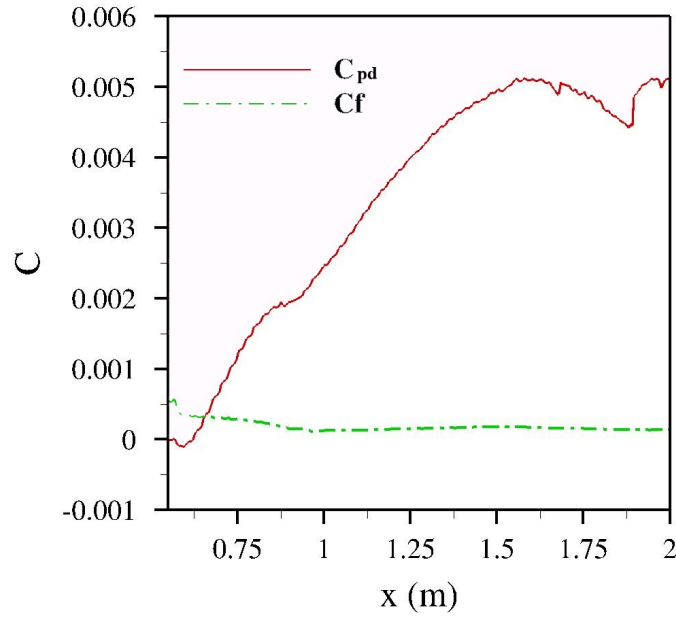
FIGURE 7.18: Form drag coefficient C_{pd} and Viscous drag coefficient C_f in the contraction

7.3.3 Energy Line

One of the objectives of the numerical simulation of supercritical flow through a straight wall channel contraction is to quantify the energy loss inside the contraction. The energy at centerline along the x-direction was calculated using Equation (7.5), where E is the energy, U is the streamwise velocity, and g is the gravitational acceleration.

$$E = z + \frac{U^2}{2g} \tag{7.5}$$

The variation of energy along the centerline is shown in Figure 7.19, showing how the energy drops as the flow moves from inlet to the outlet. The data analysed was spanwise averaged. The total head loss is quantified as the difference in energy at the inlet and outlet of the domain. It can be noted that high energy loss is found in the region where the contraction is found. Noteworthy are the plateaus of the energy line around the shock-wave cross-over and the

reattachment point of the shock-waves, respectively. The total loss along the
domain is 0.11 m.
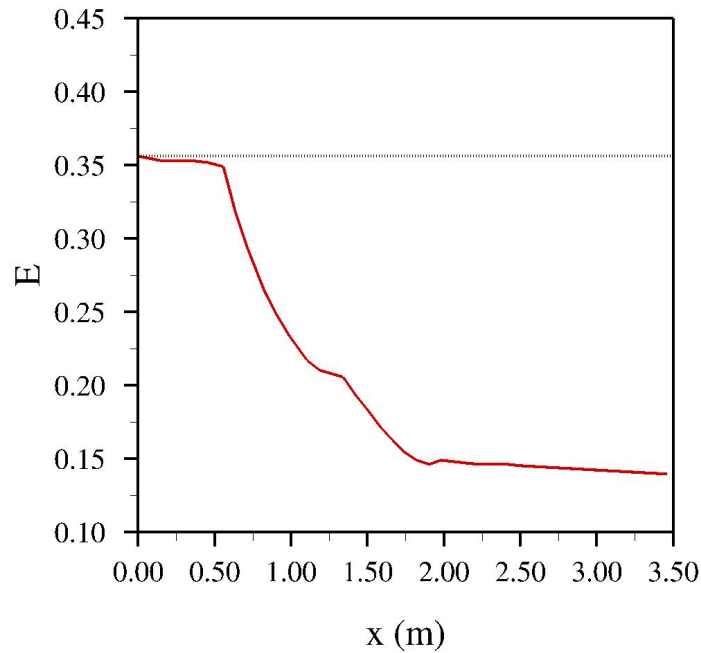
FIGURE 7.19: Energy of spanwise averaged flow

$$h_l = K_l * \frac{U^2}{2g} \tag{7.6}$$

The loss coefficient is another approach to calculating the energy loss in the
contraction. This loss coefficient can be calculated using Equation (7.6), where
h_l is the head loss, K_l is the loss coefficient, U is the streamwise velocity and g is
the gravitational acceleration. From the simulation results, the mean spanwise
averaged velocity at the start of the contraction at x=0.55 m is 2.48 m/s and
the water level is 0.037 m. At the end of the contraction, at x location of 2
m, the mean velocity is 1.89 m/s and the water level is at 0.1097 m. Hence,
the head loss in the contraction alone is 0.059, and the total contraction loss
coefficient is 0.32.

7.4   Angle of Contraction Effect

7.4.1   Free-surface

Numerical modelling of a straight wall contraction was described in the previous
section. The validation case used entailed the use of a 6° contraction depicted
in Figure 7.2. To analyse the effect of the contraction angle on the free-surface

and flow energy losses in the contraction, several other angles were also used in the model.

The comparison of the position of the free-surface for different angles is given below. All contractions started at the same point, but the angled contraction was placed at different locations with respect to the angles used. Points of contraction start and end are summarised in Table 7.1.

TABLE 7.1: Contraction start and end locations

Angle	Contraction start	Contraction end	Channel end
5°	x=0.285 m	x=2.0 m	x=3.5 m
6°	x=0.550 m	x=2.0 m	x=3.5 m
8°	x=0.933 m	x=2.0 m	x=3.5 m
10°	x=1.15 m	x=2.0 m	x=3.5 m
12°	x=1.29 m	x=2.0 m	x=3.5 m

The overview of free-surfaces for 5°, 8°, 10° and 12° is shown in Figure 7.20.
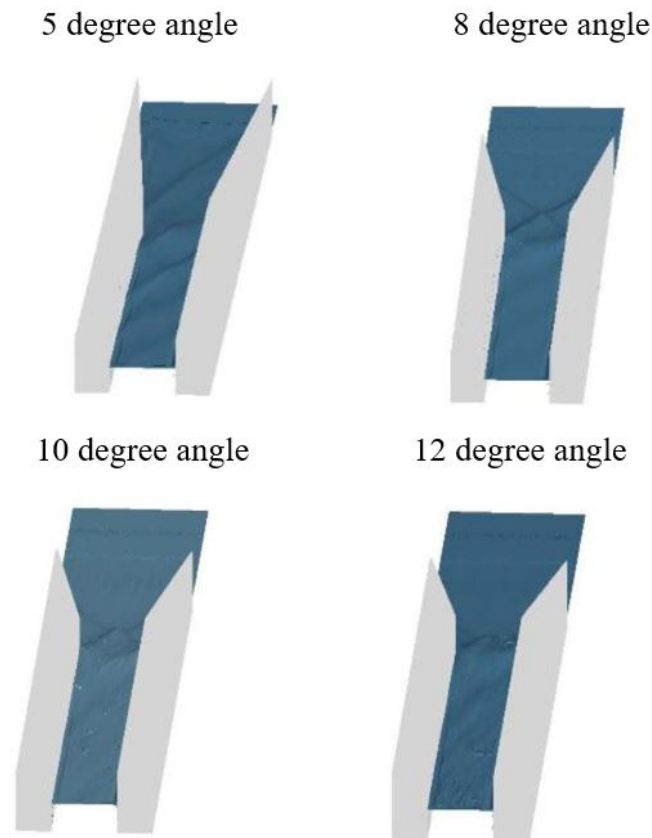
FIGURE 7.20: Comparison of 5°, 8°, 10° and 12° free-surfaces
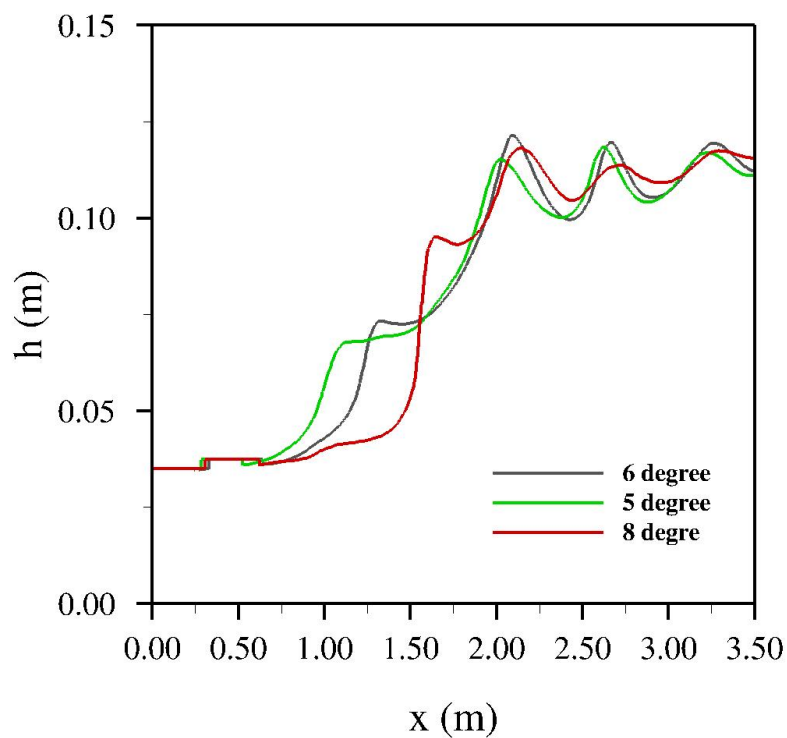
FIGURE 7.21: Comparison of 5°, 6° and 8° contraction angles
in a straight wall contraction
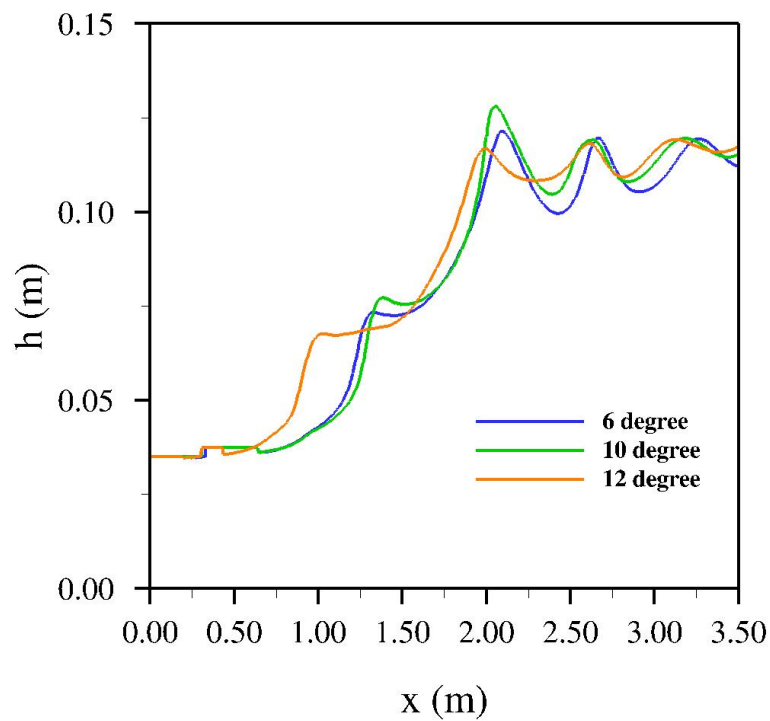
FIGURE 7.22: Comparison of 6°, 10° and 12° contraction angles
in a straight wall contraction

From Figure 7.21, it can be noted that both phase and size of shockwaves is different for angles of 6°, 5° and 8°. The phase of 6 and 5° contraction angles is similar, with the 5° angle resulting in lower peaks. The phase and shape of the wave produced from the 8° contraction results in more notable differences, but the peak and overall height of the wave is similar to the original contraction angle of 6°. From the Figures depicting the free surface at the centerline of the domain, it can be concluded that the angle of contraction has an effect on both the height and the phase of the surface waves. It can be noted that for 10° and 12° angles of contraction, the initial formation of the shock wave is in a different location to the location for 6° contraction angle. The figure indicates that for the angle of 12° produces a taller standing wave than other angles. The phase of the standing wave is the same as for 6° angle. The 10 ° angle of contraction produces a wave of similar average height as the angle of 6°, but the peaks of the wave have different locations.

7.4.2 Energy Loss

The variations of energy along the centerline for different angles are shown below. The velocities used for analysis were spanwise averaged, and the total head loss h_l, is quantified as the difference from start to end point of interest. It can be noted that the energy line corresponding to the angle of 6 ° is smoother than lines from other angle simulations. Some artificial energy was noted in simulations run for angles of 5 °, 8 °, 10 ° and 12 °, and not in the original case study for the angle of 6°. This is because the 6° simulation case was averaged for a longer period of time and achieved better convergence of results. However, enough information to calculate loss coefficients and head losses was obtained from the presented results for all angles of contraction.
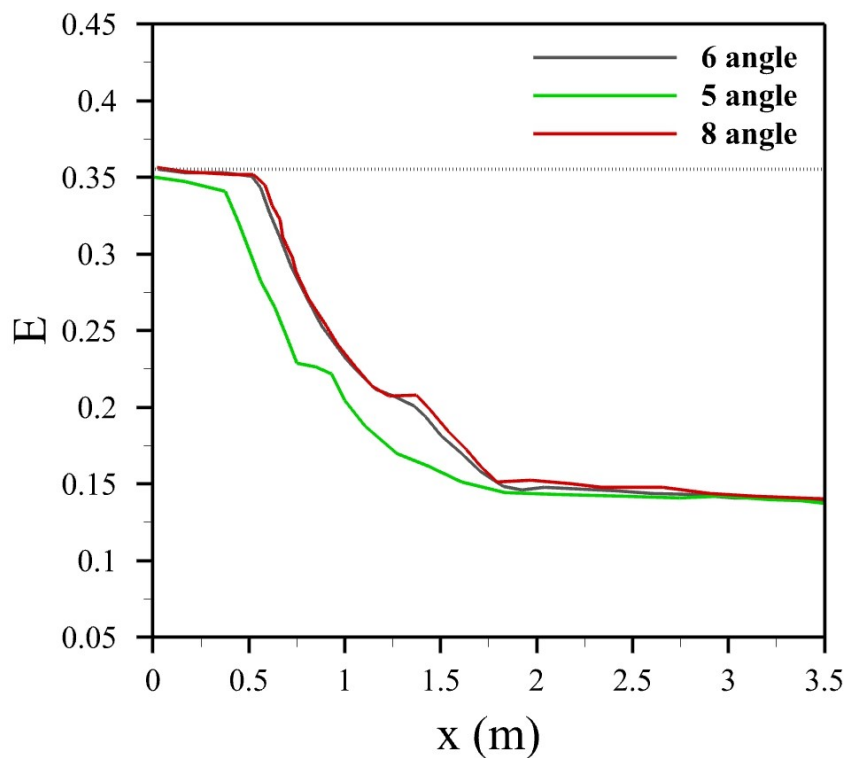
FIGURE 7.23: Comparison of 5°, 6° and 8° contraction angles
energy in a straight wall contraction
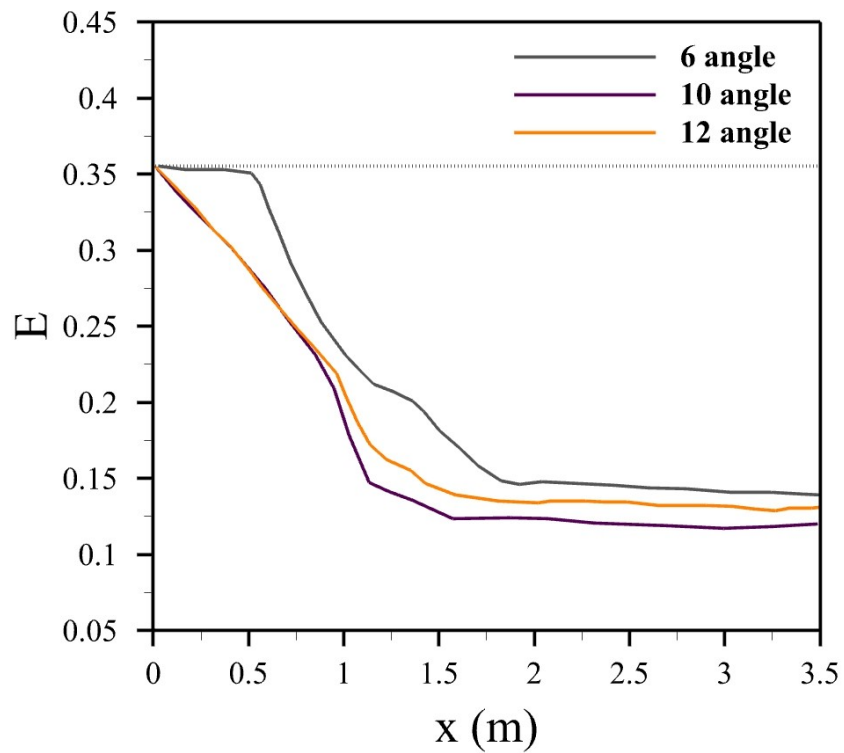
FIGURE 7.24: Comparison of 6°, 10° and 12° contraction angles
energy in a straight wall contraction

The total head losses in the contractions, together with energy loss coefficients, are summarised in Table B.1, where h_1 is water depth at contraction start in m, h_2 is water depth at contraction end in m, U_1 is the spanwise averaged velocity at contraction start in m/s U_2 is the spanwise averaged velocity at contraction end in m/s, h_l is the head loss in the contraction in m and K_l is the loss coefficient.

TABLE 7.2: Loss coefficients and head loss

Angle	h_1	h_2	h_l	U_1	U_2	K_l
5°	0.0375	0.1152	0.179	2.285	0.439	18.22
6°	0.037	0.1097	0.059	2.48	1.89	0.32
8°	0.0382	0.108	0.043	1.545	0.425	4.63
10°	0.0409	0.113	0.021	1.411	0.411	2.45
12°	0.0407	0.128	0.013	1.459	0.4106	1.51

Although the energy graphs show similar line trends, Table B.1 indicates that the contraction angle of 6° has by far the smallest contraction loss coefficient of 0.32. The next best performing, when loss coefficients are compared, angle of contraction is the angle of 12° and the worst-performing is the angle of 5°. If head losses are compared, the same angle of 6° outperforms other simulated set ups and hence is recommended for use when designing contraction channels such as accelerator channel used in spillway turbine design.

7.5   Summary of Flow in Open-Channel Contraction Simulation

The method of large-eddy simulation in combination with level-set and immersed boundary methods were employed to simulate supercritical flow in a straight-wall open-channel contraction. The LES was validated first with experimental data in terms of water level along the channel and simulated water levels agreed reasonably well with measured data. The formation of a pair of shockwaves, a common water surface feature in channel contractions was quite accurately obtained as well as subsequent reflected waves in the narrow section of the channel.

The time-averaged flow is significantly affected by the flow acceleration and the shockwaves, the maximum streamwise acceleration occurs in the middle of the contracting section, around the shockwave crossover location. The velocity profile in the contraction deviates significantly from a logarithmic profile due to the presence of strong secondary currents and shows the peak of the streamwise

velocity well below the water surface. The streamwise velocity profile recovers only slowly towards the outlet.

Contour plots of the second-order statistics in terms of *tke* and its three normal stress contributors confirmed that the highest turbulence occurs in the vicinity of the shockwave crossover location, which is where the maximum streamwise velocity gradients are found. The energy line and drag force analyses suggest that the flow loses the majority of its energy in the form of pressure drag.

The analysis of the effect of different contraction angles on the energy loss inside the contraction indicates that the angle of 6° produces the lowest loss coefficient and should be used when designing contracting channel section such as the accelerator channel used in spillway turbine design.

Chapter 8

Conclusions and Recommendations for Future Work

8.1 Conclusions

The incentive to increase the production of electricity from renewable energy sources has been identified as the main motivation for starting the research presented in this thesis. The question of how to sustainably contribute to world energy demands with minimal environmental harm has been the fundamental driver behind the idea of developing the novel spillway turbine.

The overview of the existing small scale hydropower turbine technology revealed a potential for developing a turbine for use in steeply sloped man-made channels, such as chute spillways. The advantages of using small scale solutions over building large hydropower plants come from many environmental and social implications such large developments entail. The spillway turbine presented in this thesis is envisioned as an impulse turbine, inspired by the shape of the Savonius turbine, the design of the cross-flow turbine and the hydrodynamics of the Pelton Wheel. The idea behind the spillway turbine comes from creating an impulse turbine but without a need for a nozzle most impulse turbines have.

The design process of the spillway turbine entailed three stages of laboratory testing, numerical simulation and final recommendations presented in field application proposal. For purposes of describing the design process and methodology behind this product development, conclusions and recommendations were presented at the end of each design version section in Chapter 4. The design version III was the final design of spillway turbine tested in the laboratory and the efficiency achieved was 43.38 %, and the calculations of the specific speed and the speed factor indicate that the spillway turbine can be classified as an impulse turbine. The laboratory testing led to conclusions that the nature of intake of spillway turbine runner hydrodynamics is unknown and that the

accelerator channel flow can be further investigated numerically. Numerically simulating supercritical flow through a contraction, the term that can be used to describe the flow through the accelerator channel, was considered a more sustainable approach than continuous experimental testing.

An extensive review of studies and theory of supercritical flow through an open-channel contraction showed that previously published studies struggled to correctly predict the free-surface location. The effect of contraction angles on the energy losses in the contraction was mentioned in several studies, but all authors failed to quantify these effects and give a definite conclusion. In the numerical simulation section of this thesis, it was proven that the large eddy simulation in-house HYDRO3D code is capable of capturing the free-surface of supercritical flow through an open-channel contraction accurately. The results were validated with experimental data presented in Abdo et al. (2019). Furthermore, the LES approach with level-set method shows improvements on the numerical method used by Abdo et al. (2019). The flow characteristics and turbulent quantities were also presented and analysed. Energy losses inside the contraction were quantified in terms of head loss and loss coefficient. Moreover, the effect of using different contraction angles was also discussed. From the numerical simulation part of the thesis, it was concluded that the method used is capable of correctly capturing the turbulent supercritical flow through an open-channel contraction. The accelerator channel was recommended for re-design according to the numerical modelling findings. Moreover, it was concluded that the angle of 6° results in significantly smaller loss coefficient in the contraction, and should, therefore, be used in field testing.

The design of the field testing system was presented in the Appendix C of the thesis and is the result of conclusions made from both experimental and numerical tests conducted during this research. The spillway turbine has been granted permission for testing in the described site and the full-scale runner options are shown together with the design of the spillway and its supporting structure.

A novel turbine was designed for use in low-head, low-flow, man-made channels or steeply sloped run-off river channels. The design was tested in the laboratory, analysed and revised until the efficiency of at least 40 % was achieved. Another objective was met through the investigation into high Froude number, supercritical flow through an open-channel contraction. A thorough understanding of free-surface flow was gained. Conclusions from laboratory testing and numerical simulations were implemented into field testing system design. The evaluation of the research targets set at the beginning of this thesis indicates all objectives

were fully met.

To conclude, this thesis has contributions on two fronts of hydraulic research and development. Firstly, it offers a new and innovative technological solution for extracting hydro energy with minimal social and environmental harm. Secondly, this thesis presents a new methodology for simulating the supercritical free-surface flow through an open-channel contraction. It offers an insight into the hydrodynamics of such flows that has been completely lacking from published literature.

8.2 Recommendations for Future Work

The spillway turbine development presented in this thesis has been tested in the laboratory conditions until the efficiency of at least 40% was achieved. Runner intake hydrodynamics was simulated to gain a better understanding of the flow characteristics and to support the re-design of the wedge/accelerator channel. The next step in the turbine development is to test the spillway turbine in the field as outlined in the field application section given in the Appendix C. This step would further the technological readiness of the spillway turbine and would quantify the overall influence of accelerator channel re-design on the system efficiency. The field testing was planned in detail and testing permissions were obtained. This site application will also show how the spillway turbine behaves in real-world flow conditions that are not controlled as they were in the laboratory flume.

Conclusions and recommendations will be necessary after the initial field testing and the design of the turbine could be re-adjusted again if observable issues are noted. Testing the spillway turbine on-site will also require adjustments for every site individually. Depending on if the run-off system design is required, each site will demand different structural support analysis. However, placing the spillway turbine on an existing chute spillway will require less structural design and more attention will be paid to the scaling of runner and accelerator channel components.

The initial field testing will indicate if scaling up the runners and other test variables will have an effect on the laboratory predicted performance. Like in all renewable energy projects, the environmental effects of the spillway turbine will have to be carefully evaluated. Fish friendliness and aquatic life implications will have to be carefully analysed. However, as the spillway turbine is intended

for use in man-made channels and chute spillways, its harmful effects on aquatic life are expected to be minimal.

The size and shape of runner blades are likely to have an effect on the overall efficiency of the spillway turbine. Further investigation on the runner geometry is recommended both experimentally and numerically.

During laboratory testing, it was decided that the off-shelf three-phase AC generator will be appropriate for initial phases of both laboratory and field testing. The generator used could be replaced by a custom made model in order to improve the electrical efficiency of the system. The spillway turbine will likely be connected to a DC battery charging system as this would be the simplest way of storing energy. Grid connection is also possible if the spillway turbine is installed close to a dam with already existing grid infrastructure.

The durability of the runner and accelerator channel, with maintenance schedule recommendations, will also have to be conducted after field testing is completed, but this requires continuous running of the system. Finally, after the spillway turbine is considered technologically ready, financial analysis of its performance should be conducted. Future work recommendations were summarised in the list below:

- Test the spillway turbine in the field as outlined in Appendix C.
- Adjust field testing design for every future site individually.
- Investigate if scaling up the runners and test variables has an effect on the performance.
- Conduct a report on environmental effects of the spillway turbine and fish friendliness.
- Investigate if changing the shape and size of the runner blades and runner itself would improve the efficiency.
- Investigate electricity storage options and if the generator should be replaced by a custom model.
- Investigate the durability of the turbine in a field environment.
- Conduct cost/benefit analysis of the spillway turbine and its potential for commercialisation.

During the duration of this project, several challenges were identified. Firstly, the originality of the idea had to be carefully evaluated, as the industrial sponsor required a brand new piece of technology which will eventually be patented. Secondly, the laboratory conditions had to be adjusted, meaning that the available flume had to be made into a sloping spillway channel. Tight laboratory schedule

posed many testing time limitations, so a detailed testing methodology had to be conducted. Moreover, numerically simulating free-surface, supercritical flow in a channel contraction was a complicated task. Not only the supercritical flow conditions created instabilities and difficulties in flow simulations, but the free-surface approximations further complicated the task. The field testing in North Carolina was planned for completion in March, but the unpredictable world-wide pandemic made this impossible and the field testing had to be postponed. Overall, the objectives set at the beginning of the project were successfully completed through both experimental and numerical approaches.

Further questions arised from this research such as: How technologically ready is the spillway turbine?; Can the efficiency be improved by changing the shape and size of the runner and runner blades?; Could changing the electrical components in the system lead to better performance?. All of these uncertainties could be answered through completing further work recommendations. As this project focused on runner intake hydrodynamics in depth, conducting future research that will focus on improving the runner geometry would be beneficial.

Bibliography

Abdo, K., Riahi-Nezhad, C. and Jasim, I. (2019). Steady supercritical flow in a straight-wall open-channel contraction. *Journal of Hydraulic Research, 57(5).* 647-661.

Acharya, N., Kim, C., Thapa, B. and Lee, Y. (2015). Numerical analysis and performance enhancement of cross-flow hydro turbine. *Renewable Energy, 80.* 819-826.

Adzic, F. Stoesser, T., Runge, S. and Morris, E. Design and Performance of a Novel Spillway Turbine.*Journal of Power and Energy Engineering, 8.* 14-31.

Akwa, J., Vielmo, H. and Petry, A. (2012).A review on the performance of Savonius wind turbines. *Renewable and Sustainable Energy Reviews, 16(5).* 3054-3064.

Alcrudo, F. and Garcia-Navarro, P. (1993). A high-resolution Godunov type scheme in finite volumes for the 2D shallow-water equations. *International Journal of Numerical Methods and Fluids, 16(6).* 489-505.

Alessandrini, B., & Delhommeau, G.A. (1996). A multigrid velocity-pressure free-surface-elevation fully coupled solver for calculation of turbulent incompressible flow around a hull. *Proceedings of the 21st Symposium on Naval Hydrodynamics.* Trondheim, Norway.

Alexander, A.J. and Holownia, B. (1978). Wind tunnel tests on Savonius rotor. *Journal of Industrial Aerodynamics, 3(4).* 343-351.

Alexander, K., Giddens, E. and Fuller, A. (2009). Axial-flow turbines for low head micro-hydro systems. *Renewable Energy, 34(1).* 35-47.

Ansar, A., Flyvbjerg, B., Budzier, A. and Lunn, D. (2014). Should we build more large dams? The actual cost of hydropower megaproject development. *Energy Policy, 69.* 43-56.

Bajracharya, T., Archarya, B., Joshi, C., Saini, R. and Dahlhaug, O. (2008). Sand erosion of Pelton turbine nozzles and buckets: A case study of Chilime hydropower plant. *WEAR, 264(3-4). 177-184.*

Bakken, T., Sundt, H., Ruud, A. and Harby, A. (2012). *Development of small versus large hydropower in Norway-comparison of environmental impacts.* Energy Procedia, 20. *185-199.*

Berger, R. and Stockstill, R. (1993). *A 2D numerical model for high-velocity channels.* Technical Report REMR-HY-12,US Army Corps of Engineers, Waterways experiment Station,Vicksburg,MS.

Baucher, Y., Ksayer, Voulawz, E. and Clodic, D. (2010). *Characterisation of frictional loss in Pelton turbines. International R&AC conference, Purdue University, Purdue, 2274. 1-8.*

Bhalamudi, S.M. and Chaudhry, M.H. (1992). *Computation of flows in open-channel transitions.* Journal of Hydraulic Research, 30(1). *77-93.*

Bonsor, K. (2001). *How Hydropower Plants Work. HowStuffWorks.com. Available at:* <https://science.howstuffworks.com/environmental/energy/hydropower-plant.htm>*[Online. Accessed 22 January 2020].*

Boris, J.P., & Book, D.L. (1973). *Flux-corrected transport. I.SHASTA,a fluid transport algorithm that works.* Journal of Computational Physics, 11(1). *38-69.*

Bozhinova, S. Hecht, V., Kisliakov, D., Muller, G. and Schneider, S. (2013). *Hydropower converters with head differences below 2.5 m.* Energy, 168(3). *107-119.*

Bozorgi, A., Javidpour, E., Riasi, A., Nourbakhsh, A. (2013). *Numerical and experimental study of using axial pump as turbine in Pico hydropower plants.* Renewable Energy, 53. *258-264.*

Bomminayuni, S. & Stoesser, T. (2011). *Turbulence statistics of open-channel flow over a rough bed.* Journal of Hydraulic Engineering, 137(11). *1347-1358.*

Breeze, P. (2018). *Hydropower. 1st edition. Elsevier Ltd.*

British Standards. (2014). *BS ISO:4762- Hexagon socket head cap screws. London: British Standards Institute.*

British Standards. (2017). *BS ISO:1438- Hydrometry- Open channel flow measurement using thin-plate weirs. London: British Standards Institute.*

Bryan, C. and Kendra, S. (2013). *Impulse (Turgo and Pelton) turbine performance characteristics and their impact on pico-hydro installations.* Renewable Energy, 50. *959-964.*

Causon, D., Mingham, C. and Ingram, D.(1999). *Advances in calculation methods for supercritical flow in spillway channels.* Journal of Hydraulic Engineering, 128(3). *1039-1050.*

Chang, Y.C, Hou, T.Y., Merriman, B. et al. (1996). *A level set formulation of Eulerian interface capturing methods for incompressible fluids.* Journal of Computational Physics, 124(2). *449-464.*

Chow, V.T. (1959). *Open-channel hydraulics.1st edition. McGraw-Hill, Inc.*

Choi, Y., Lim, J., Kim, Y. and Lee, Y. (2008). *Performance and internal flow characteristics of a cross-flow hydro turbine by the shapes of nozzle and runner blade.* Journal of Fluid Science Technology, 3(3). *398-409.*

Chua, K.V., Fraga, B., Stoesser, T., Hong, S.H. & Sturm, T. (2019). *Effect of Bridge Abutment Length on Turbulence Structure and Flow through the Opening.* Journal of Hydraulic Engineering, 145(6). *04019024.*

Cevheri, M., McSherry, R. and Stoesser, T. (2015). *A local mesh refinement approach for large-eddy simulations of turbulent flows.* International Journal for Numerical Methods in Fluids, 82(5). *261-285.*

Christensen, N. (2019). *Western power grid would bring Saskatchewan cheap, clean hydropower from B.C. and Manitoba. Regina Leader-Post. Available at:<https://leaderpost.com/opinion/columnists/wester-power-grid-would-bring=saskatchewan-cheap-clean-hydro-power-from-b-c-and-manitoba. [Online. Accessed: 3rd August 2019].*

Corsatea, T. and Magagna, D. (2019). *Overview of European innovation activities in marine energy technology. Available at:* https://publications.jrc.ec.europa.eu/respiratory/bitstream/JRC86301/ldna26342enn.pdf *[Online. Accessesd: 20th September 2019].*

Daly, B.J. (1967). *Numerical study of two fluid Rayleigh-Taylor instability.* The Physics of Fluids, 10(2). *297-307.*

Dam removal Europe. (2020). *Available at:*https://damremoval.eu/ *[Online. Accessed: 17th March 2020].*

Date, A., Date, A. and Akbarzadeh, A. (2013). *Investigating the potential for using a simple water reaction turbine for power production from low head hydro resources.* Energy Conversion and Management, 66. *257-270.*

Dawson, J.H. (1943). *The effect of lateral contraction on super-critical flow in open channels. Master's thesis. Lehigh University, Bethlehem, Pennsylvania.*

De Andrade, J. Curiel, C. Kenyery, F. Aguillon, O., Vasquez, A. and Asuaje, M. (2011). *Numerical investigation of the internal flow in a Banki Turbine.* International Journal of Rotating Machinery. *1-12.*

Dixon, S. and Hall, C., (2010).*Fluid mechanics and thermodynamics of turbomachinery.6th edition. Butterworth-Heinmann, Elsevier.*

Douglas, J., Swaffield, J. and Gasiorek, J. (2001). *Fluid Mechanics. 4th edition. Essex, England: Pearson Education.*

Dursun B, Gokcol C. (2011). *The role of hydroelectric power and contribution of small hydropower plants for sustainable development in Turkey.* Renewable Energy, 36(4).*1227–35.*

Ecoursesonline.(2019). *SWCS: Lesson 21. Chute Spillway. Available at:*http : //ecoursesonline.iasri.res.in/mod/page/view.php?id=2189 *.[Online. Accessed: 2nd April 2019].*

International- *U.S. Energy Information Administrations (EIA). Available at:*https://www.eia.gov/beta/international/. *[Online. Accessed: 2nd July 2019].*

Energy.gov (2019). *History of Hydropower.Available at:* https://www.energy.gov/eere/water/history-hydropower *.[Online. Accessed: 9th July 2019].*

European Commission, *Directive 2009/28/EC of the European Parliament and of the Council of 23rd April 2009 on the promotion of the use of energy from renewable sources and amending and subsequently repealing Directives 2001/77/EC and 2003/30. Official Journal of the European Union, Belgium; 2009.* htpps://doi:10.3000/1725 2555.L_2009.140.eng.

European Union climate action. https://ec.europa.eu/clima/citizens/eu_en..

Farmer, J., Martinelli, L. & Jameson, A. (1993). *A fast multigrid method for the non-linear ship wave problem with a free surface.* Proceedings of the

Sixth International Conference on Numerical Ship Hydrodynamics). *Iowa, USA,1993, 155-172.*

Fiuzat, A. and Akerkar, B. (1991). *Power outputs of two stages of cross-flow turbine.* ASCE Journal of Energy Engineering, 117(2). *57-70.*

Ferziger, J., & Perić, M. (2002). Computational methods for fluid dynamics. *3rd edition. New York: Springer-Verlag.*

Fulgosi, M., Lakehal, D., Banerjee, S. et al. (2003). *Direct numerical simulation of turbulance in a sheared air-water flow with a deformable interface.* Journal of Fluid Mechanics, 482. *319-345.*

Gerland, P, Raffery, A.E,, Sevickova, H., Li, N., Gu, D., Spoorenberg, T., Alkema, L., Fosdick, B.K., Chunn, J., Lalic, N., Bay, G., Buttner, T., Neilig, B.K. & Wilmoth, J. (2014). *World population stabilization unlikely this century.* Science, 346(6206). *234-237.*

Gharangik, A.M. and Chaudhry, M.H. (1991). *Numerical simulation of hydraulic jump.* Journal of Hydraulic Engineering, 117(9). *1195-1211.*

Gibson, J. (2019). *Llyn Brianne dam spillway (C) John Gibson. Available at:*Geograph.org.uk. Available at: https://www.geograph.org.uk/photo/925456. *[Online. Accessed: 21ˢᵗ March 2019].*

Giosio, D., Henderson, A., Walker, J., Brandner, P., Sargison, J. and Gautam, P. (2015).*Design and performance evaluation of a pump-as-turbine micro-hydro test facility with incorporated inlet flow control.* Renewable Energy, 78. *1-6.*

Goswami, D. and Kreith, F. (2017). *Energy conversion. 2ⁿᵈ edition. CRC Press.*

Grand Coulee power plant. (2019. Bureau of Reclamation. Available at:https://www.usbr.gov/pn/grandcoulee/tpp/history.html.*[Online. Accesses: 12ᵗʰ December 2019.]*

Grande-Dixence (2019). Available at: http://www.grande-dixence.ch/en. *[Online. Accessed: 27ᵗʰ September 2019].*

Graves, D. and Iglesias, G. (2018). *Wave and tidal energy.1ˢᵗ edition. John Wiley & Sons Ltd.*

Harlow, F.H., & Welch, J.E. (1965). *Numerical calculation of time-dependant viscous incompressible flow of fluid with free surface.* The Physics of Fluids, 8(12). *2182-2189.*

Harvey, A., Brown, A., Hettiarachi, P. and Inversin, A. (2009). *Micro-hydro design manual.* Practical Action Publishing.

Harries, T., Kwan, A., Brammer, J. and Falconer, R. (2016). *Physical testing of performance characteristics of a novel drag-driven vertical axis tidal stream turbine; with comparisons to a conventional Savonius.* International journal of marine energy, 14. *215-228.*

Hindasageri,V., Ramesh, H. and Kattimani, S.C. (2011). *Performance of Savonious rotors for utilising the orbital motion of ocean waves in shallow waters.*Journal of Sustainable Energy & Environment, 2. *117-119.*

Hinson, (2018). *Tidal Lagoons House of Commons library.*

Hirt, C.W., & Nichols, B.D. (1981). *Volume of fluid (VOF) method for the dynamics of free boundaries.* Journal of Computational Physics, 39(1). *205-225.*

Hodges, B.R., & Street, R.L. (1999). *On simulation of turbulent non-linear free-surface flows.* Journal of Computational Physics, 151(2). *425-457.*

Severn Tidal Power (2010). *HM Government - Department of energy and climate change.*

Hsu, M., Ten, W. and Lai, C. (1998). *Numerical simulation of supercritical shock wave in channel contraction.* Computers & Fluids, 27(3). *347-365.*

Hou, T.Y., Lowengrub, J.S. and Shelly, M.J. (2001). *Boundary integral methods for multi-component fluids and multi-phase materials.* Journal of Computational Physics, 169. *302-362.*

Hydrolink. (2009). *Small hydro power - HHP V type – vertical compact Pelton turbine. Available at:* $http://www.hydrolink.cz/en/pelton-turbines/hhp-v-type-vertical-compact-pelton-turbine-5.html.$ *[Online. Accessed: 31st January 2020.]*

Key world energy statistics. Available at: $https://www.iea.org/publications/freepublications/publications/KeyWorld2017.pdf.$ *[Online. Accessed: 15th July 2018].*

Global energy & C0$_2$ report. Available at:$https://www.iea.org/geco/electricity/.$ *[Online. Accessed: 2nd July 2019].*

Ikeda, T., Iio, S. and Tatsuno, K.(2010). *Performance of nano-hydraulic turbine utilising waterfalls.* Renewable Energy, 35(1). *293-300.*

*International rivers (2019). Human impacts of Dams. Available at:*https://wwww.internationalrivers.org/human-impacts-of-dams *. [Online. Accessed: 11th October 2019].*

Ippen, A.T. and Dawson, J.H. (1951). High-velocity flow in open-channels.A symposium: Design of channel contractions. Transactions of the American Society of Civil Engineers, 116(1). *326-346.*

*Itaipu Binacional. (2019). Generating units. Available at:*https://www.itaipu.gov.br/en/energy/generating-units. *[Online. Accessed: 12th December 2019.]*

Jawahar, C. and Michael, P. (2010). A review on turbines for micro hydro power plant. Renewable and Sustainable Energy Reviews, 72. *882-887.*

Jiménes, O.F. (1987). Computation of supercritical flow in open channels. (Master's thesis). Washington State University.

Jiménes, O.F. and Chaudhry, M.H. Computation of supercritical free-surface flows. Journal of Hydraulic Engineering, 114(1). *377-395.*

Johns, B., Soulsby, R.L. and Xing, J. (1993). A comparison of numerical model experiments of free surface flow over topography with flume and field observations. Journal of Hydraulic Research, 31(2). *215-228.*

Johnson, W. Ely, R. and White, F. (1982). Design and testing of an inexpensive cross-flow turbine. Small hydropower fluid machinery, American Society of Civil Engineers Winter annual meeting of Phonex, AZ. *129-133.*

Kang, S., & Sotiropoulos, F. (2015). Large eddy simulation of three-dimensional turbulent free surface flow past a complex stream restoration structure. Journal of Hydraulic Engineering, 141(10). *04015022.*

Kara, S., Stoesser, T., & Sturm, T.W. (2012). Turbulence statistics in compound channels with deep and shallow overbank flows. Journal of Hydraulic Research, 50. *482-493.*

Kara, S., Stoesser, T., Sturm, T.W., & Mulahasan, S. (2015a). Flow dynamics through a submerged bridge opening with overtopping. Journal of Hydraulic Research, 53(2). *186-195.*

Kara, M., Stoesser, T. & McSherry, R. (2015b). Calculation of fluid-structure interaction: methods, refinements, applications. Proceedings of the Institution of Civil Engineers. Engineering and Computational Mechanics, 168. *59–78.*

Kara, S., Kara, M.C., Stoesser, T., Sturm, T.W., (2015c). *Free-Surface versus Rigid-Lid LES Computations for Bridge-Abutment Flow.* Journal of Hydraulic Engineering 141(9). *04015019.*

Kaldellis, J. and Zafirkais, D. (2011). *The wind energy (r)evolution:A short review of a long history.* Renewable Energy, 36(7). *1887-1901.*

Kerikous, E. and Thévenin, D. (2019). *Optimal shape of thick blades for a hydraulic Savonius turbine.* Renewable Energy, 134. *629-638.*

Khare, V., Khare, C., Nema, S. and Baredard, P. (2019). *Tidal Energy Systems.* Elsevier.

Khosrowpanah, S., Fiuzat, A. and Alberson, M. (1988). *Experimental study of corss-flow turbine.* ASCE Journal of Hydraulic Engineering, 114(3). *299-314.*

Kim, D., Kim, J.H. & Stoesser, T. (2010). *Large eddy simulation of flow and solute transport in ozone contact chambers.* ASCE Journal of Environmental Engineering, 136(1). *22-31.*

Kim, D., Kim, J.H. & Stoesser, T. (2013). *The effect of baffle spacing on hydrodynamics and solute transport in serpentine contact tanks* Journal of Hydraulic Research, 51(5). *558-568.*

Kotousov, L. (2005). *Measurement of the water jet velocity at the outlet of nozzles with different profiles.* Technical Physics, 50(9). *1112-1118.*

Krüger, S. and Rutschmann, P. (2006). *Modelling 3D supercritical flow with extended shallow-water approach.* Journal of Hydraulic Engineering, 132(9). *916-926.*

Kumar, A. and Saini, R.P. (2016). *Performance parameters of Savonius type hydrokinetic turbine- A review.* Renewable and Sustainable Energy Reviews, 64. *289-310.*

Lewis, B. (2014). *Major historical development in the design of water wheels and Francis hydro-turbines.* IOP Conference Series: Earth and Environmental Science..

Lashofer, A., Kaltenberger, F., and Pelikan, B. (2011). *State of technology and design guidelines for the Archimedes screw turbine.* Wasserwirtschaft 101(7–8). *76–81 (in English-originally in German).*

McKee, S., Tome, M.F., & Ferreira, V.G. (2003). *The MAC method.* Computers and FLuids, 37(8). *907-930.*

McSherry, R.J., Chua, K., & Stoesser, T (2017). *Large eddy simulation of free-surface flows.* Journal of Hydrodynamics, 29(1). *1-12.*

Mendoza, C. and Shen, H.W. (1990). *Investigation of turbulent flow over dunes.* Journal of Hydraulic Engineering, 116(4). *459-477.*

MJ2 Technolgies. (2011). *Very Low Head turbine. Available at:* $http://www.vlh-turbine.com/$ *.[Online. Accessed: 30th March 2020.]*

Mockmore, C. and Merryfield, F. (1949). *The Banki water turbine.* Engineering experiment station bulletin series, 25.. *Oregon state college, Corvallis.*

Molls, T. and Chaudhry, M.H. (1995). *Depth-Averaged Open Channel Flow Model.* Journal of Hydraulic Engineering, 121(6). *453-465.*

Molls, T. and Zhao, G. (1996). *Depth-Averaged Bossinesq equations applied to flow in converging channel.* North American Water and Environment Congress and Destructive Water. *453-465. Anaheim, CA.:ASCE.*

Moran, E., Lopez, M., Nathan, M., Muller, N. and Hyndman, D. (2018). *Sustainable hydropower in the 21st century.* Proceedings of the National Academy of Sciences of the United States of America 115(45). *11891-11898.*

Møork, G., Barstow, S., Kabuth, A. and Pontes, M.T. *Assesing the global wave energy potential. American Society of Civil Engineers 2010 29th International Conference on Ocean, Offshore and Arctic Engineering. 447-54. American Society of Mechanical Engineers; 2010.*

Motwani, K., Jain, S. and Patel, R. (2013). *Cost analysis of pump as turbine for pico hydropower plants - a case study.*Procedia Engineering, 51.*721- 726.*

Müller, G., Denchfield, S., Marth, R. and Shelmerdine, R. (2007). *Stream wheels for applications in shallow and deep water. Proceedings of 32nd IAHR Congress, Venice, Italy, Theme C2c. Paper 291.*

Nakajima, M., Shouichiro, I. and Ikeda, T. (2008). *Performance of Savonius rotor for environmentally friendlly hydraulic turbine.* Journal of fluid science and technology, 3(3). *420-429.*

Nakase, Y., Fukutomi, J., Watanabe, T., Suetsugu, T. and Kubota, T. (1982). *A study of cross-flow turbine (effect of nozzle shape on its performance).* Small Hydropower Fluid Machinery, American Society of Civil Engineers Winter Annual Meeting of the American Society of Civil Engineers, Phonex, AZ. *13-18.*

National Geographic (2019). Geothermal energy information and facts. Available at: *https://www.nationalgeographic.com/environment/global-warming/geothermal-energy/*.[Online. Accessed: 2nd July 2019].

Nichols, B.D., & Hirt, C.W. (1973). Calculating three-dimensional free surface flows in the vicinity of submerged and exposed structures. Journal of Computational Physics, 12(2). 234-246.

Nicoud, F. and Ducros, F. (1999). Subgrid-scale stress modelling based on the square of the velocity gradient tensor.Flow, Turbulence and Combustion, 62(3). 183-200.

Noh, W.F., & Woodward, P. (1979). SLIC (simple line interface calculations. Lecture Notes in Physics, 59). 330-340.

Novak et al. (1996). Hydraulic structures.2nd edition. E & FN Spon.

Nunez, C. (2019). Renewable Energy, explained. National Gepraphic. Available at: *https://www.nationalgeographic.com/environment/energy/reference/renewable-energy/*.[Online. Accessed: 20th January 2020].

Okot, D. Review of small hydropower technology. Renewable and Sustainable Energy Reviews, 26. 515-520.

Osher, S. & Fedkiw, R. (2002). Level set methods and dynamic implicit surfaces. New York:Springer-Verlag.

Osher, S. & Sethian, J.A. (1988). Fronts propagating with curvature-dependant speed algorithms based on Hamilton-Jacobi formulations. Journal of Computational Physics, 79(1). 12-49.

The Open University (2020). Why sustainable energy matters. Available at: *https://www.open.edu/openlearn/nature-environment/environmental-studies/why-sustainable-energy-matters/content-section-4*.[Online. Accessed: 22nd January 2020].

Ouro, P. and Stoesser, T. (2017). An immersed boundary-based large-eddy simulation approach to predict the performance of vertical axis tidal turbines. Computers and Fluids, 152. 74-87.

Ouro, P., Fraga, B., Lopez-Novoa, U. & Stoesser, T. (2019). Scalability of an Eularian-Lagrangian large-eddy simulation solver with hybrid MPI/OpenMP parallelisation. Computers and Fluids, 179). 123-136.

Paish, O. (2002). *Small hydropower: technology and current status.*Renewable and Sustainable Energy Reviews, 6(6).*537-56.*

Padhy, M., and Saini, R. (2009). *Effect of size and concentration of silt particles on erosion of Pelton turbine buckets.*Journal of Energy, 34(10). *1477-1483.*

Parkinson, E., Neury, C., Garcin, H., Vullioud, G., Weiss, T. (2006). *Unsteady analysis of Pelton runner with flow and mechanical simulations.* Hydropower & Dams, 3.

Peng, D. Merriman, B. and Osher, S. *A level set approach for computing solutions to incompressible two-phase flow.*Journal of Computational Physics, 152(2). *410-438.*

Perrig, A., Avellan, F., Kueny, J., Farhat, M. and Parkisnon, E. (2006). *Flow in a Pelton turbine bucket: numerical and experimental investigations.* Journal of Fluids Engineering, 128. *350-358.*

Pereira, N. and Borges, J. (2014). *A study on the efficiency of a cross-flow turbine based one experimental measurements. In: Proceedings of mechanical engineering. 2014; Portugal; 2014.*

Peskin, C.S. (2002). *The Immersed Boundary Method.* Acta Numerica, 11. *479-517.*

Rahman, M. and Chaudhry, M.H. (1997). *Computation of flow in open-channel transitions.* Journal of Hydraulic Research, 35(2). *243-256.*

Raven, H.C. (1996).* A solution method for the nonlinear ship wave resistance problem *(Doctoral Theses). Delft University of technology, Delft, Netherlands.*

Raven, H., & Van Brummelen, E. (1999). *A new approach to computing steady free-surface viscous flow problems.* 1st MARNET-CFD Workshop).*Barcelona, Spain.*

Rauen, W. Lin, B. and Falconer, R. (2008).*Transition from wavelets to ripples in a laboratory flume with a diverging channel.*International Journal of Sediment Research 23(1). *1-12.*

Razak, J., Alghoul, M., Zainol, M. and Yusoff, A. (2010). *Application of cross-flow turbine in off-grid pico hydro renewable energy system.* Proceedings of recent advances in applied mathematics.

Rodi, W., Constantinescu, G. and Stoesser, T. *Large-Eddy simulation in hydraulics.* CRC Press.

Robinson, A. and Gilkes, S. (2018). *Development of a Turgo Turbine.* Hydropower& Dams, 1. *90-93.*

Runge, S. (2018). *Performance and Technology Readiness of a Free-stream turbine in a canal environment. PhD thesis. Cardiff University, 2018.*

Runge, S., Stoesser, T, Morris, E and White, M. (2018). *Technology Readiness of a Vertical-Axis Hydro-Kinetic Turbine.* Journal of Energy and Power Engineering, 6(8).*63-85.*

Russo, G. and Smereka, P. *A remark on computing distance functions.* Journal of Computational Physics, 163(1). *51-67.*

Saha, U.K., Thotla, S. and Maity, D. (2008). *Optimum design configuration of Savonius rotor through wind tunnel experiments.* Journal of Wind Engineering and Industrial Aerodynamics 96(8-9). *1359-75.*

Salameh, Z. (2014). *Renewable energy system design. 1st edition.* Academic Press.

Sammartano, V., Arico, C. Carravetta, A., Fecarotta, O. and Tucciarelli, T. (2013). *Banki-Michell optimal design by computational fluid dynamics testing and hydrodynamic analysis.* Energies, 6(5). *2362-2385.*

Sanjou, M. & Nezu, I. (2010). *Large eddy simulation of compound open-channel flows with emergent vegetation near floodplain edge.* 9th International Conference on Hydrodynamics. *Shanghai, China. 565-569.*

Santolin, A., Cavazzini, G., Ardizzon, G. and Pavesi, G. (2009). *Numerical investigation of the interaction between the jet and bucket in a Pelton turbine.* Journal of Power and Energy, 223(A). *721-728.*

SLS (Selective Laser Sintering): 3D Printing Powder-based Process. *Available at:https://www.sculpteo.com/en/glossary/selective-laser-sintering-sls-definition/[Online. Accessed:16th July 2020].*

Senior, J., Saenger, N., and Müller, G. (2010). *New hydropower converters for very low-head differences.* Journal of Hydraulic Research, 48(6) *703-714.*

Sethian, J.A.& Smereka, P. (2003). *Level set methods for fluid interfaces.* Annual Review of Fluid Mechanics, 35(1). *341-372.*

Shafiee, S. and Topal, E. (2009). *When will fossil fuel reserves be diminished?.* Energy Policy, 37(1). *181-189*

Shi, J., Thomas, T.G. & Williams, J.J.R. (2000). *free-surface effects in open channel flow at moderate Froude and Reynold's numbers.* Journal of Hydraulic Research, 38(6). *465-474.*

Sinagra, M. Sammartano, V. Arico, C. and Collura, A. (2015). *Experimental and numerical analysis of a cross-flow turbine.* Journal of Hydraulic Engineering, 142(1).

Staubli, T. and Abgottspon, A. (2008). *Efficiency differences of upper and lower injectors and scan of tailrace temperature distribution. International conference on hydraulic efficiency measurements, IGHEM 2008-Milano.*

Stoesser, T., Braun, C., Garcia-Villalba, M. & Rodi, W. (2008). *Turbulence structures in flow over two dimensional dunes.* Journal of Hydraulics Engineering, 134(1). *42-55.*

Stoesser, T. & Nikora, V.I. (2008). *Flow structure over square bars at intermediate submergence: Large eddy simulation study of bar spacing effect.* Acta Geophysica, 56(3). *876-893.*

Stoesser, T. (2010). *Physically realistic roughness closure scheme to simulate turbulent channel flow over rough beds within the framework of LES.* Journal of Hydraulic Engineering, 136(10). *812-819.*

Stoesser, T. (2014). *Large-eddy simulation in hydraulics: Quo Vadis?.* Journal of Hydraulic Research, 25(4). *441-452.*

Stoesser, T., McSherry, R. & Fraga, B. (2016). *Secondary currents and turbulence over a non-uniformly roughened open-channel bed.* Water, 7(9). *4896-4913.*

Suh, J., Yang, J. & Stern, F. (2011). *The effect of air-water interface on the vortex shedding froma vertical circular cylinder.* Journal of Fluids and Structures, 27(1). *1-22.*

Sussman, M., Smerka, P. and Osher, S. *A level set approach for computing solutions to incompressible two-phase flow.* Journal of Computational Physics, 114(1). *146-159.*

Suwanit, W. and Gheewala, S. (2011). *Life cycle assessment of mini-hydropower plants in Thailand.* International Journal of Life Cycle Assessment, 16.. *849–858.*

Tanwar, N. (2006). *Clean development mechanism and off-grid small-scale hydropower projects: Evaluation of additionality.* Energy Policy, 35. *714–721.*

Telukdar, P., Sardar, A., Kulkarni, V. and Saha, U. (2018). *Parametric analysis of model Savonius hydrokinetic turbines through experimental and computational investigations.* Energy Conversion and Management, 158. *36-49.*

Tesla, N.(2012). *My inventions and other writings. London: Penguin Classics.*

Three Gorges dam hydro electric power plant, China. (2019). Power-technology/ Available at: https://www.power-technology.com/projects/gorges/ *.[Online. Accessed: 15th December 2019].*

Thirugnanasambandam, M., Iniyan, S. and Goic, R. (2010). *A review of solar thermal technologies.* Renewable and Sustainable Energy Reviews, 14(1). *312-322.*

Tomé, M.F. and McKee, S. (1994). *GENSMAC: A computational marker-and-cell method for free surface flows in general domains.* Journal of Computational Physics, 110(17). *171-186.*

Totapally, H. and Aziz, N. (1994). *Refinement of cross-flow turbine parameters.* Journal of Fluid Energy, 116(3). *133-147.*

Tutar, M. and Veci, I. (2016). *Performance analysis of a horizontal axis 3-bladed Savonius type wave turbine in an experimental wave flume.* Renewable Energy, 86. *8-25.*

Quaranta, E. and Müller, G. (2018). *Sagebien and Zuppinger water wheels for very low head hydropower applications.* Journal of Hydraulic Research, 56(4). *526-536.*

Ubbink, O.(1997). Numerical prediction of two fluid systems with sharp interfaces *(Doctoral theses). Imperial College of Science, Technology and Medicine, London, UK.*

Ulhmann, M. (2005). *An immersed boundary method with direct forcing of the simulation of particulate flows.* Journal of Computational Physics, 209(2). *448-476.*

United Nations framework convention on climate change (2016). Paris Agreement.Available at: https://unfccc.int/sites/default/files/english_paris_agreement.pdf.

Varga, J. (1959). Tests with the Banki water turbine. Acta Technica 27(1-2). *79-102.*

*Viollet, P.L. (2017). From the water wheel to turbines and hydroelectricity. Technological evolution and revolutions.*Comptes Rendus Mecanique, 345. *570-580.*

Wiemann, P., Müller, G. and Senior, J. (2007). Review of current developments in low head, small hydropower. 32nd IAHR Conference 2007. 01 - 06 Jul 2007. *10 pp .*

Williamson, S., Stark, B. and Booker, J. (2013).Performance of a low-head pico hydro Turgo turbine. Applied Energy, 102(2013). *1114-1126.*

*Wilson, P. (1967). Turgo, a high speed impulse turbine.*Water Power, January.

Xie, Z., Lin, B. & Falconer, R.A. (2014). Turbulence characteristics in free-surface flow over two-dimensional dunes. Journal of Hydro-Environmental Research, 8(3). *200-209.*

*Xie Z. (2015) A two-phase flow model for three-dimensional breaking aves over complex topography.*Proceedings of the Royal Society A., 471: 20150101..

Xie, Z. & Stoesser, T. (2020). A three-dimensional Cartesian cut-cell/volume-of-fluid method for two-phase flows with moving bodies. Journal of Computational Physics, 416. *109536.*

Youngs, D.L., Morton, K.W., & Baines, M.J. (1982). Time-dependent multi-material flow with large fluid distortion. Numerical methods for fluid dynamics. *New York,USA: Academic Press. 273-285.*

Yoon, J.Y. and Patel, V.C. (1996). Numerical model of turbulent flow over sand dune. Journal of Hydraulic Engineering, 122(1). *10-18.*

Yue, W.S., Lin, C.L. & Patel, V.C. (2005). Coherent structures in open-channel flows over a fixed dune. Journal of Fluids Engineering, 127(5). *858-864.*

Zarfl, C., Lumsdon, A.,Berlekamp, J., Tydecks, L. and Tockner, K. (2015). A global boom in hydropower dam construction. Aquatic Sciences, 77(1). *161-170.*

Zhao, D., Shen, H., Tabios, G. and Tan, W. (1994). Finite volume two dimensional unsteady flow model for river basin. Journal of Hydraulic Engineering, 120(7). *863-883.*

Zhao, D., Shen, H., Lai, J. and Tabious, G. (1996). Approximate Riemman solver in FVM for 2D hydraulic shock wave modelling. Journal of Hydraulic Engineering, 122(12). *692-702.*

Zhao, D., Chen, T., Merriman, B. Osher, S. (1996). A variation level set approach to multi-phase motion. Journal of Computational Physics, 127(1). *179-195.*

Zhao, H., Chen, T., Merriman, B. & Osher, S. (1996). A variational level set approach to multi-phase motion. Journal of Computational Physics 127(1). *179-195.*

Zhang, Z. (2007). Flow friction theorem of Pelton turbine. Journal of Power and Energy, 221(A). *1173-1180.*

Zhang, Z. (2009). Flow dynamics of free surface flow in the rotating buckets of Pelton turbine. Journal of Power and Energy, 221(A). *1173-1180.*

Zhang, Z. and Casey, M. (2007). Experimental studies of the jet of a Pelton turbine. Journal of Power and Energy, 221(A). *1181-1192.*

Zoppé, B., Pellone, C., Maitre, T., Leroy, P. (2006). Flow analysis inside a Pelton turbine bucket. Journal of Turbomachinery, 128(3). *500-511.*

Zotlöterer Energy Systems. (2010). Gravitation water vortex power plant. Available at: http://www.zotloeterer.com/welcome/gravitation-water-vortex-power-plants/realisation/.

Appendix A

Laboratory Testing Overview

A.1 Design I Testing

Test	Q(m³/s)	h(m)	x(m)	y(m)	z(m)	Wedge	Runner	E(%)
1	0.0123	0.518	-	0.385	0.005	-	R1	8.54
2	0.0139	0.518	-	0.385	0.005	-	R1	13.89
3	0.0139	0.526	-	0.385	0.005	-	R1	22.94
4	0.0174	0.531	-	0.385	0.005	-	R1	23.26
5	0.0174	0.545	-	0.385	0.005	-	R1	30.94
6	0.0211	0.546	-	0.385	0.005	-	R1	25.09
7	0.0113	0.522	0.04	0.385	0.005	W3	R1	29.39
8	0.0129	0.528	0.04	0.385	0.005	W3	R1	23.94
9	0.0156	0.531	0.04	0.385	0.005	W3	R1	21.91
10	0.0192	0.545	0.04	0.385	0.005	W3	R1	17.49
11	0.0107	0.527	0.06	0.385	0.005	W3	R1	20.49
12	0.0139	0.527	0.06	0.385	0.005	W3	R1	23.90
13	0.0146	0.545	0.06	0.385	0.005	W3	R1	24.46
14	0.0166	0.547	0.06	0.385	0.005	W3	R1	17.96
15	0.0199	0.5548	0.06	0.385	0.005	W3	R1	15.44
16	0.0107	0.533	0.02	0.385	0.005	W3	R1	22.72
17	0.0136	0.536	0.02	0.385	0.005	W3	R1	25.06
18	0.0156	0.540	0.02	0.385	0.005	W3	R1	24.51
19	0.0174	0.542	0.02	0.385	0.005	W3	R1	20.21
20	0.0203	0.549	0.02	0.385	0.005	W3	R1	10.61
21	-	-	0	0.385	0.005	W3	R1	FAIL
22	0.0107	0.567	0.02	0.385	0.005	W2	R1	22.92
23	0.0129	0.522	0.02	0.385	0.005	W2	R1	24.71
24	0.0139	0.529	0.02	0.385	0.005	W2	R1	22.11

Test	Q(m³/s)	h(m)	x(m)	y(m)	z(m)	Wedge	Runner	E(%)
25	0.0181	0.549	0.02	0.385	0.005	W2	R1	13.54
26	0.0110	0.525	0.04	0.385	0.005	W2	R1	17.12
27	0.0110	0.514	0.04	0.385	0.005	W2	R1	14.54
28	0.0123	0.518	0.04	0.385	0.005	W2	R1	16.95
29	0.0153	0.527	0.04	0.385	0.005	W2	R1	13.48
30	0.0166	0.531	0.04	0.385	0.005	W2	R1	8.44
31	0.0084	0.520	0.02	0.385	0.005	W2	R1	10.29
32	0.0101	0.518	0.06	0.385	0.005	W2	R1	11.76
33	0.0120	0.518	0.06	0.385	0.005	W2	R1	16.50
34	0.0142	0.536	0.06	0.385	0.005	W2	R1	20.65
35	0.0166	0.542	0.06	0.385	0.005	W2	R1	15.66
36	0.0195	0.532	0.06	0.385	0.005	W2	R1	8.03
37	0.0098	0.510	0.06	0.385	0.005	W1	R1	7.58
38	0.0104	0.518	0.06	0.385	0.005	W1	R1	8.71
39	0.0139	0.527	0.06	0.385	0.005	W1	R1	6.46
40	0.0153	0.527	0.06	0.385	0.005	W1	R1	7.64
41	0.0177	0.536	0.06	0.385	0.005	W1	R1	6.37
42	0.0214	0.545	0.06	0.385	0.005	W1	R1	5.96
43	0.0089	0.518	0.04	0.385	0.005	W1	R1	9.09
44	0.0101	0.518	0.04	0.385	0.005	W1	R1	9.58
45	0.0139	0.518	0.04	0.385	0.005	W1	R1	8.15
46	0.0153	0.523	0.04	0.385	0.005	W1	R1	7.94
47	0.0170	0.536	0.04	0.385	0.005	W1	R1	8.32
48	0.0195	0.540	0.04	0.385	0.005	W1	R1	9.03
49	0.0226	0.544	0.04	0.385	0.005	W1	R1	7.88
50	0.0104	0.509	0.02	0.385	0.005	W1	R1	6.77
51	0.0104	0.518	0.02	0.385	0.005	W1	R1	8.47
52	0.0126	0.518	0.02	0.385	0.005	W1	R1	9.27
53	0.0152	0.527	0.02	0.385	0.005	W1	R1	9.78
54	0.0177	0.536	0.02	0.385	0.005	W1	R1	9.95
55	0.0199	0.549	0.02	0.385	0.005	W1	R1	11.16
56	0.0218	0.549	0.02	0.385	0.005	W1	R1	11.11
57	0.090	0.518	0.02	0.385	0.02	W1	R1	19.95
58	0.0104	0.520	0.02	0.385	0.02	W1	R1	22.84
59	0.0136	0.520	0.02	0.385	0.02	W1	R1	22.67
60	0.0159	0.540	0.02	0.385	0.02	W1	R1	24.43

Test	Q(m³/s)	h(m)	x(m)	y(m)	z(m)	Wedge	Runner	E(%)
61	0.0170	0.545	0.02	0.385	0.02	W1	R1	21.92
64	0.0092	0.5067	0.04	0.385	0.02	W1	R1	FAIL
65	0.0101	0.5247	0.04	0.385	0.02	W1	R1	5.81
66	0.0117	0.5211	0.04	0.385	0.02	W1	R1	12.97
67	0.0153	0.5337	0.04	0.385	0.02	W1	R1	12.54
68	0.0174	0.5427	0.04	0.385	0.02	W1	R1	14.14
69	0.0188	0.5400	0.04	0.385	0.02	W1	R1	11.78
70	0.0095	0.5130	0.06	0.385	0.02	W1	R1	8.39
71	0.0120	0.5220	0.06	0.385	0.02	W1	R1	8.96
72	0.0142	0.5202	0.06	0.385	0.02	W1	R1	9.72
73	0.0159	0.5373	0.06	0.385	0.02	W1	R1	12.61
74	0.0199	0.5427	0.06	0.385	0.02	W1	R1	10.83
75	0.0092	0.5094	0.08	0.385	0.02	W1	R1	9.69
76	0.0123	0.5139	0.08	0.385	0.02	W1	R1	9.97
77	0.0142	0.5166	0.08	0.385	0.02	W1	R1	13.43
78	0.0166	0.5337	0.08	0.385	0.02	W1	R1	11.66
79	0.0188	0.5355	0.08	0.385	0.02	W1	R1	12.54
80	-	-	-	0.385	0.02	-	R1	FAIL
81	0.0098	0.5094	0.08	0.385	0.02	W2	R1	8.89
82	0.0117	0.5202	0.08	0.385	0.02	W2	R1	14.97
83	0.0142	0.5265	0.08	0.385	0.02	W2	R1	15.36
84	0.0156	0.5373	0.08	0.385	0.02	W2	R1	10.03
85	0.0188	0.5400	0.08	0.385	0.02	W2	R1	12.44
86	0.0090	0.5112	0.06	0.385	0.02	W2	R1	10.07
87	0.0126	0.5202	0.06	0.385	0.02	W2	R1	8.13
88	0.0153	0.5265	0.06	0.385	0.02	W2	R1	7.62
89	0.0163	0.5319	0.06	0.385	0.02	W2	R1	6.99
90	0.0177	0.5427	0.06	0.385	0.02	W2	R1	10.55
91	0.0092	0.5130	0.04	0.385	0.02	W2	R1	5.81
92	0.0110	0.5121	0.04	0.385	0.02	W2	R1	8.33
93	0.0136	0.5310	0.04	0.385	0.02	W2	R1	8.33
94	0.0153	0.5328	0.04	0.385	0.02	W2	R1	7.69
95	0.0181	0.5400	0.04	0.385	0.02	W2	R1	9.48
96	0.0090	0.5130	0.02	0.385	0.02	W2	R1	8.04
97	0.0113	0.5175	0.02	0.385	0.02	W2	R1	5.92
98	0.0126	0.5229	0.02	0.385	0.02	W2	R1	9.62

Test	Q(m³/s)	h(m)	x(m)	y(m)	z(m)	Wedge	Runner	E(%)
99	0.0153	0.5247	0.02	0.385	0.02	W2	R1	10.04
100	0.0177	0.5445	0.02	0.385	0.02	W2	R1	8.28
101	0.0117	0.5130	0.08	0.385	0.02	W3	R1	4.82
102	0.0149	0.5337	0.08	0.385	0.02	W3	R1	5.06
103	0.0177	0.5337	0.08	0.385	0.02	W3	R1	3.65
104	0.0113	0.5184	0.06	0.385	0.02	W3	R	4.81
105	0.0146	0.5265	0.06	0.385	0.02	W3	R1	5.72
106	0.0166	0.5301	0.06	0.385	0.02	W3	R1	6.53
107	-	-	0.06	0.385	0.02	W3	R1	FAIL
108	0.0136	0.5301	0.04	0.385	0.02	W3	R1	10.14
109	0.0170	0.5265	0.04	0.385	0.02	W3	R1	14.62
110	0.0184	0.5319	0.04	0.385	0.02	W3	R1	16.89
111	0.0214	0.5400	0.04	0.385	0.02	W3	R1	16.26
112	0.0129	0.5211	0.02	0.385	0.02	W3	R1	10.77
113	0.0159	0.5310	0.02	0.385	0.02	W3	R1	6.58
114	0.0188	0.5427	0.02	0.385	0.02	W3	R1	7.03
115	0.0218	0.5400	0.02	0.385	0.02	W3	R1	11.11
116	0.0078	0.4980	0.02	0.385	0.02	W1	R1	8.52
117	0.0090	0.5022	0.02	0.385	0.02	W1	R1	12.54
118	0.0110	0.5130	0.02	0.385	0.02	W1	R1	12.20
119	0.0120	0.5240	0.02	0.385	0.02	W1	R1	15.51
120	0.0156	0.5193	0.02	0.385	0.02	W1	R1	10.51
121	0.0084	0.6620	0.04	0.385	0.02	W1	R1	14.08
122	0.0095	0.5130	0.04	0.385	0.02	W1	R1	13.82
123	0.0123	0.5175	0.04	0.385	0.02	W1	R1	11.67
124	-	-	0.04	0.385	0.02	W1	R1	FAIL
125	0.0274	0.5265	0.04	0.395	0.04	W3	R2	1.30
126	0.0291	0.5490	0.04	0.395	0.04	W3	R2	2.19
127	0.0308	0.5445	0.04	0.395	0.04	W3	R2	3.06
128	0.0322	0.5472	0.04	0.395	0.04	W3	R2	3.94
129	0.0254	0.5445	0.06	0.395	0.04	W3	R2	0.58
130	0.0279	0.5508	0.06	0.395	0.04	W3	R2	2.02
131	0.0313	0.5517	0.06	0.395	0.04	W3	R2	2.44
132	0.0304	0.5472	0.06	0.395	0.04	W3	R2	2.29
133	0.0279	0.5490	0.02	0.395	0.04	W3	R2	0.77
134	0.0300	0.5580	0.02	0.395	0.04	W3	R2	1.59

Test	Q(m³/s)	h(m)	x(m)	y(m)	z(m)	Wedge	Runner	E(%)
135	0.0344	0.5607	0.02	0.395	0.04	W3	R2	2.10
136	0.0362	0.5652	0.02	0.395	0.04	W3	R2	1.86
137	0.0166	0.5220	0.06	0.395	0.04	W2	R2	5.49
138	0.0199	0.5112	0.06	0.395	0.04	W2	R2	3.53
139	0.0218	0.5364	0.06	0.395	0.04	W2	R2	6.17
140	0.0254	0.5337	0.06	0.395	0.04	W2	R2	5.17
141	0.0287	0.5454	0.06	0.395	0.04	W2	R2	4.40
142	0.0181	0.5184	0.04	0.395	0.04	W2	R2	2.10
143	0.0195	0.5279	0.04	0.395	0.04	W2	R2	4.34
144	0.0222	0.5427	0.04	0.395	0.04	W2	R2	4.96
145	0.0238	0.5454	0.04	0.395	0.04	W2	R2	3.37
146	0.0283	0.5481	0.04	0.395	0.04	W2	R2	1.39
147	-	-	0.02	0.395	0.04	W2	R2	FAIL
148	0.0192	0.5265	0.02	0.395	0.04	W2	R2	2.11
149	0.0218	0.5445	0.02	0.395	0.04	W2	R2	1.4
150	0.0262	0.5400	0.02	0.395	0.04	W2	R2	1.29
151	0.0279	0.5472	0.02	0.395	0.04	W2	R2	3.95
152	0.0113	0.5148	0.06	0.395	0.04	W1	R2	4.52
153	0.0142	0.5139	0.06	0.395	0.04	W1	R2	5.67
154	0.0163	0.5319	0.06	0.395	0.04	W1	R2	7.76
155	0.0184	0.5337	0.06	0.395	0.04	W1	R2	7.23
156	0.0214	0.5373	0.06	0.395	0.04	W1	R2	6.44
157	0.0283	0.5364	0.06	0.395	0.04	W1	R2	5.08
158	0.0120	0.5157	0.04	0.395	0.04	W1	R2	2.69
159	0.0142	0.5175	0.04	0.395	0.04	W1	R2	1.79
160	0.0170	0.5229	0.04	0.395	0.04	W1	R2	2.74
161	0.0188	0.5310	0.04	0.395	0.04	W1	R2	5.88
162	0.0211	0.5364	0.04	0.395	0.04	W1	R2	5.34
163	0.0274	0.5472	0.04	0.395	0.04	W1	R2	3.8
164	0.0120	0.5031	0.02	0.395	0.04	W1	R2	3.79
165	0.0139	0.5175	0.02	0.395	0.04	W1	R2	2.96
166	0.0163	0.5175	0.02	0.395	0.04	W1	R2	2.52
167	0.0184	0.5292	0.02	0.395	0.04	W1	R2	5.85
168	0.0199	0.5319	0.02	0.395	0.04	W1	R2	5.27
169	0.0266	0.5499	0.02	0.395	0.04	W1	R2	3.05
170	0.0078	0.4995	0.02	0.395	0.02	W1	R2	5.61

Test	Q(m³/s)	h(m)	x(m)	y(m)	z(m)	Wedge	Runner	E(%)
171	0.0104	0.4950	0.02	0.395	0.02	W1	R2	4.35
172	0.0123	0.5157	0.02	0.395	0.02	W1	R2	5.64
173	0.0142	0.5157	0.02	0.395	0.02	W1	R2	4.58
174	0.0159	0.5355	0.02	0.395	0.02	W1	R2	4.14
175	0.0092	0.4995	0.04	0.395	0.02	W1	R2	5.57
176	0.0104	0.5022	0.04	0.395	0.02	W1	R2	3.86
177	0.0120	0.5175	0.04	0.395	0.02	W1	R2	3.58
178	0.0149	0.5175	0.04	0.395	0.02	W1	R2	3.39
179	0.0163	0.5283	0.04	0.395	0.02	W1	R2	4.85
180	0.0090	0.5040	0.06	0.395	0.02	W1	R2	7.23
181	0.0104	0.5022	0.06	0.395	0.02	W1	R2	7.75
182	0.0120	0.5067	0.06	0.395	0.02	W1	R2	8.61
183	0.0149	0.5166	0.06	0.395	0.02	W1	R2	7.12
184	0.0170	0.5220	0.06	0.395	0.02	W1	R2	8.53
185	0.0078	0.4950	0.06	0.395	0.02	W2	R2	6.61
186	0.0101	0.5085	0.06	0.395	0.02	W2	R2	7.83
187	0.0117	0.5085	0.06	0.395	0.02	W2	R2	9.42
188	0.0146	0.5166	0.06	0.395	0.02	W2	R2	8.58
189	0.0174	0.5256	0.06	0.395	0.02	W2	R2	8.09
190	0.0090	0.4923	0.04	0.395	0.02	W2	R2	7.17
191	0.0095	0.5022	0.04	0.395	0.02	W2	R2	9.03
192	0.0120	0.5157	0.04	0.395	0.02	W2	R2	8.5
193	0.0142	0.5148	0.04	0.395	0.02	W2	R2	8.11
194	0.0166	0.5202	0.04	0.395	0.02	W2	R2	8.00
195	0.0092	0.5040	0.02	0.395	0.02	W2	R2	6.89
196	0.0095	0.5058	0.02	0.395	0.02	W2	R2	10.09
197	0.0120	0.5067	0.02	0.395	0.02	W2	R2	9.88
198	0.0139	0.5157	0.02	0.395	0.02	W2	R2	9.13
199	0.0159	0.5301	0.02	0.395	0.02	W2	R2	7.47
200	0.0087	0.5063	0.06	0.395	0.02	W3	R2	1.45
201	0.0101	0.5040	0.06	0.395	0.02	W3	R2	5.14
202	0.0110	0.5139	0.06	0.395	0.02	W3	R2	7.59
203	0.0146	0.5157	0.06	0.395	0.02	W3	R2	9.15
204	0.0170	0.5220	0.06	0.395	0.02	W3	R2	9.44
205	0.0078	0.4959	0.04	0.395	0.02	W3	R2	2.92
206	0.0113	0.4986	0.04	0.395	0.02	W3	R2	3.66

Test	Q(m³/s)	h(m)	x(m)	y(m)	z(m)	Wedge	Runner	E(%)
207	0.0120	0.5130	0.04	0.395	0.02	W3	R2	6.85
208	0.0136	0.5202	0.04	0.395	0.02	W3	R2	7.98
209	0.0163	0.5202	0.04	0.395	0.02	W3	R2	8.46
210	0.0090	0.4986	0.02	0.395	0.02	W3	R2	1.41
211	0.0095	0.5022	0.02	0.395	0.02	W3	R2	5.25
212	0.0120	0.5112	0.02	0.395	0.02	W3	R2	7.31
213	0.0149	0.5157	0.02	0.395	0.02	W3	R2	8.1
214	0.0170	0.5220	0.02	0.395	0.02	W3	R2	8.2
215	-	-	-	0.395	0.02	-	R2	FAIL
216	0.0203	0.5355	-	0.395	0.005	-	R2	1.87
217	0.0076	0.4905	0.04	0.395	0.005	W1	R2	4.06
218	0.0092	0.4986	0.04	0.395	0.005	W1	R2	3.84
219	0.0113	0.5040	0.04	0.395	0.005	W1	R2	3.18
220	0.0126	0.5166	0.04	0.395	0.005	W1	R2	6.53
221	0.0153	0.5157	0.04	0.395	0.005	W1	R2	7.53
222	0.0078	0.4950	0.02	0.395	0.005	W1	R2	7.1
223	0.0084	0.5166	0.02	0.395	0.005	W1	R2	7.77
224	0.0120	0.5067	0.02	0.395	0.005	W1	R2	6.16
225	0.0133	0.5148	0.02	0.395	0.005	W1	R2	5.94
226	0.0156	0.5202	0.02	0.395	0.005	W1	R2	5.88
227	0.0076	0.4941	0.05	0.395	0.005	W1	R2	4.73
228	0.0092	0.5040	0.05	0.395	0.005	W1	R2	5.34
229	0.0104	0.5175	0.05	0.395	0.005	W1	R2	6.13
230	0.0260	0.5175	0.05	0.395	0.005	W1	R2	6.10
231	0.0166	0.5265	0.05	0.395	0.005	W1	R2	5.05
232	0.0084	0.4977	0.05	0.395	0.005	W2	R2	5.12
233	0.0098	0.5166	0.05	0.395	0.005	W2	R2	6.84
234	0.0113	0.5103	0.05	0.395	0.005	W2	R2	8.35
235	0.0153	0.5166	0.05	0.395	0.005	W2	R2	6.07
236	0.0163	0.5607	0.05	0.395	0.005	W2	R2	6.12
237	0.0090	0.4941	0.04	0.395	0.005	W2	R2	6.59
238	0.0098	0.5076	0.04	0.395	0.005	W2	R2	8.04
239	0.0120	0.5157	0.04	0.395	0.005	W2	R2	8.54
240	0.0139	0.5166	0.04	0.395	0.005	W2	R2	8.58
241	0.0166	0.5337	0.04	0.395	0.005	W2	R2	5.16
242	0.0084	0.4959	0.02	0.395	0.005	W2	R2	8.18

Test	Q(m³/s)	h(m)	x(m)	y(m)	z(m)	Wedge	Runner	E(%)
243	0.0101	0.5022	0.02	0.395	0.005	W2	R2	9.05
244	0.0120	0.5202	0.02	0.395	0.005	W2	R2	8.27
245	0.0159	0.5292	0.02	0.395	0.005	W2	R2	4.15
246	0.0170	0.5274	0.02	0.395	0.005	W2	R2	5.68
247	0.0092	0.4995	0.05	0.395	0.005	W3	R2	4.26
248	0.0107	0.5085	0.05	0.395	0.005	W3	R2	6.69
249	0.0117	0.5256	0.05	0.395	0.005	W3	R2	8.49
250	0.0139	0.5220	0.05	0.395	0.005	W3	R2	3.95
251	0.0177	0.5247	0.05	0.395	0.005	W3	R2	8.11
252	0.0092	0.4923	0.04	0.395	0.005	W3	R2	5.72
253	0.0098	0.5049	0.04	0.395	0.005	W3	R2	8.02
254	0.0120	0.5193	0.04	0.395	0.005	W3	R2	8.55
255	0.0142	0.5085	0.04	0.395	0.005	W3	R2	9.43
256	0.0166	0.5220	0.04	0.395	0.005	W3	R2	8.99
257	0.0087	0.4977	0.02	0.395	0.005	W3	R2	4.63
258	0.0954	0.5031	0.02	0.395	0.005	W3	R2	8.96
259	0.0117	0.5094	0.02	0.395	0.005	W3	R2	9.99
260	0.0136	0.5193	0.02	0.395	0.005	W3	R2	8.92
261	0.0170	0.5229	0.02	0.395	0.005	W3	R2	6.68

Q-Discharge; h-Head; x-Distance of runner to wedge/accelerator channel; y- Distance of runner to channel bed; z-Distance of runner to spillway; E-Efficiency

A.2   Design II Testing

Test	Q(m³/s)	h(m)	x(m)	y(m)	z(m)	Wedge	Runner	E(%)
262	0.0058	0.4905	0.03	0.385	0.005	A O	A	1.3
263	0.0068	0.5040	0.03	0.385	0.005	A O	A	3.03
264	0.0076	0.5067	0.03	0.385	0.005	A O	A	5.14
265	0.0092	0.5175	0.03	0.385	0.005	A O	A	7.72
266	0.0117	0.5220	0.03	0.385	0.005	A O	A	8.95
267	0.0149	0.5265	0.03	0.385	0.005	A O	A	9.84
268	0.0166	0.5427	0.03	0.385	0.005	A O	A	11.42
269	0.0184	0.5490	0.03	0.385	0.005	A O	A	11.86
270	0.0086	0.5154	0.02	0.385	0.005	A E	A	11.78
271	0.0115	0.5184	0.02	0.385	0.005	A E	A	13.61
272	0.0126	0.5256	0.02	0.385	0.005	A E	A	17.44
273	0.0151	0.5304	0.02	0.385	0.005	A E	A	17.29
274	0.0171	0.5400	0.02	0.385	0.005	A E	A	16.37
275	0.0085	0.5121	0.03	0.385	0.005	A E	A	7.14
276	0.0108	0.5160	0.03	0.385	0.005	A E	A	12.48
277	0.0125	0.5301	0.03	0.385	0.005	A E	A	20.47
278	0.0139	0.5376	0.03	0.385	0.005	A E	A	23.7
279	0.0168	0.5400	0.03	0.385	0.005	A E	A	17.42
280	0.0069	0.5058	0.04	0.385	0.005	A E	A	2.73
281	0.0102	0.4866	0.04	0.385	0.005	A E	A	5.11
282	0.0126	0.5211	0.04	0.385	0.005	A E	A	5.63
283	0.0139	0.5340	0.04	0.385	0.005	A E	A	15.73
284	0.0170	0.5388	0.04	0.385	0.005	A E	A	19.33
285	0.0084	0.5190	0.04	0.385	0.005	A E	A	11.36
286	0.0101	0.5238	0.04	0.385	0.005	A E	A	14.36
287	0.0123	0.5301	0.04	0.385	0.005	A E	A	16.89
288	0.0147	0.5376	0.04	0.385	0.005	A E	A	19.82
289	0.0169	0.6030	0.04	0.385	0.005	A E	A	20.64
290	0.0085	0.5163	0.03	0.385	0.005	A E	A	18.78
291	0.0101	0.5256	0.03	0.385	0.005	A E	A	20.81
292	0.0122	0.5289	0.03	0.385	0.005	A E	A	23.96
293	0.0140	0.5436	0.03	0.385	0.005	A E	A	23.86
294	0.0161	0.5424	0.03	0.385	0.005	A E	A	21.71
295	0.0081	0.5196	0.02	0.385	0.005	A E	A	20.04

Test	Q(m³/s)	h(m)	x(m)	y(m)	z(m)	Wedge	Runner	E(%)
296	0.0101	0.5289	0.02	0.385	0.005	A E	A	22.43
297	0.0120	0.5130	0.02	0.385	0.005	A E	A	22.53
298	0.0146	0.5382	0.02	0.385	0.005	A E	A	18.34

Q-Discharge; h-Head; x-Distance of runner to wedge/accelerator channel; y- Distance of runner to channel bed; z-Distance of runner to spillway; E-Efficiency

A.3   Design III Testing

Test	Q(m³/s)	h(m)	x(m)	y(m)	z(m)	Wedge	Runner	E(%)
299	0.0084	0.5226	0.02	0.375	0.005	A	A	31.60
300	0.0095	0.5307	0.02	0.375	0.005	A	A	43.38
301	0.0120	0.5412	0.02	0.375	0.005	A	A	39.41
302	0.0136	0.5472	0.02	0.375	0.005	A	A	37.81
303	0.0085	0.5157	0.03	0.375	0.005	A	A	26.43
304	0.0100	0.5325	0.03	0.375	0.005	A	A	31.39
305	0.0110	0.5343	0.03	0.375	0.005	A	A	38.52
306	0.0131	0.5508	0.03	0.375	0.005	A	A	39.07
307	0.0158	0.5502	0.03	0.375	0.005	A	A	38.93
308	0.0082	0.5247	0.04	0.375	0.005	A	A	16.59
309	0.0099	0.5292	0.04	0.375	0.005	A	A	24.47
310	0.0110	0.5301	0.04	0.375	0.005	A	A	30.66
311	0.0148	0.5430	0.04	0.375	0.005	A	A	27.73
312	0.0164	0.5472	0.04	0.375	0.005	A	A	33.46
313	0.0084	0.5178	0.03	0.385	0.005	A	A	16.74
314	0.0103	0.5244	0.03	0.385	0.005	A	A	21.67
315	0.0118	0.5328	0.03	0.385	0.005	A	A	26.81
316	0.0134	0.5445	0.03	0.385	0.005	A	A	29.97
317	0.0157	0.5451	0.03	0.385	0.005	A	A	32.16
318	0.0086	0.5145	0.02	0.385	0.005	A	A	32.71
319	0.0097	0.5277	0.02	0.385	0.005	A	A	34.49
320	0.0119	0.5298	0.02	0.385	0.005	A	A	34.76
321	0.0148	0.5427	0.02	0.385	0.005	A	A	33.44
322	0.0162	0.5514	0.02	0.385	0.005	A	A	32.92
323	0.0069	0.5223	0.03	0.385	0.005	B	A	14.55
324	0.0086	0.5295	0.03	0.385	0.005	B	A	19.29
325	0.0102	0.5388	0.03	0.385	0.005	B	A	23.43
326	0.0121	0.5496	0.03	0.385	0.005	B	A	29.82
327	0.0140	0.5580	0.03	0.385	0.005	B	A	33.25
328	0.0079	0.5274	0.02	0.385	0.005	B	A	30.10
329	0.0095	0.5439	0.02	0.385	0.005	B	A	33.25
330	0.0111	0.5445	0.02	0.385	0.005	B	A	37.32
331	0.0133	0.5574	0.02	0.385	0.005	B	A	38.56
332	0.0148	0.5655	0.02	0.385	0.005	B	A	37.17

Test	Q(m³/s)	h(m)	x(m)	y(m)	z(m)	Wedge	Runner	E(%)
333	0.0078	0.5424	0.03	0.375	0.005	B	A	18.47
334	0.0087	0.5469	0.03	0.375	0.005	B	A	29.00
335	0.0105	0.5547	0.03	0.375	0.005	B	A	29.03
336	0.0122	0.5640	0.03	0.375	0.005	B	A	39.02
337	0.0151	0.5778	0.03	0.375	0.005	B	A	35.32
338	0.0077	0.5334	0.02	0.375	0.005	B	A	22.48
339	0.0092	0.2939	0.02	0.375	0.005	B	A	32.10
340	0.0104	0.5598	0.02	0.375	0.005	B	A	34.91
341	0.0124	0.5646	0.02	0.375	0.005	B	A	34.82
342	0.0147	0.5694	0.02	0.375	0.005	B	A	30.18
343	0.0082	0.5274	0.02	0.375	0.005	C	C	26.30
344	0.0099	0.5213	0.02	0.375	0.005	C	C	34.36
345	0.0126	0.5436	0.02	0.375	0.005	C	C	31.47
346	0.0144	0.5427	0.02	0.375	0.005	C	C	28.16
347	0.0161	0.5574	0.02	0.375	0.005	C	C	22.19
348	0.0100	0.5241	0.04	0.375	0.005	C	C	22.25
349	0.0120	0.5379	0.04	0.375	0.005	C	C	26.08
350	0.1413	0.5427	0.04	0.375	0.005	C	C	26.21
351	0.0073	0.5388	0.03	0.375	0.005	C	C	29.14
352	0.0086	0.5394	0.03	0.375	0.005	C	C	29.49
353	0.0103	0.5460	0.03	0.375	0.005	C	C	26.51
354	0.0121	0.5568	0.03	0.375	0.005	C	C	16.89
355	0.0075	0.5256	0.03	0.385	0.005	C	C	18.73
356	0.0087	0.5325	0.03	0.385	0.005	C	C	20.35
357	0.0100	0.5427	0.03	0.385	0.005	C	C	21.39
358	0.0122	0.5475	0.03	0.385	0.005	C	C	19.11
359	0.0105	0.5481	0.04	0.385	0.005	C	C	14.83
360	0.0123	0.5550	0.04	0.385	0.005	C	C	15.68
361	0.0146	0.5592	0.04	0.385	0.005	C	C	16.71
362	0.0085	0.5325	0.02	0.385	0.005	C	C	20.64
363	0.0108	0.5361	0.02	0.385	0.005	C	C	18.66
364	0.0127	0.5571	0.02	0.385	0.005	C	C	16.76
365	0.0106	0.5379	0.03	0.365	0.005	A	1	20.83
366	0.0124	0.5415	0.03	0.365	0.005	A	1	24.79
367	0.0144	0.5469	0.03	0.365	0.005	A	1	24.35
368	0.0080	0.5259	0.02	0.375	0.005	A	1	18.92

Test	Q(m³/s)	h(m)	x(m)	y(m)	z(m)	Wedge	Runner	E(%)
369	0.0101	0.5301	0.02	0.375	0.005	A	1	21.16
370	0.0125	0.5451	0.02	0.375	0.005	A	1	22.43
371	0.0147	0.5475	0.02	0.375	0.005	A	1	22.42
372	0.0087	0.5271	0.03	0.375	0.005	A	1	13.57
373	0.1003	0.5352	0.03	0.375	0.005	A	1	16.60
374	0.0122	0.5364	0.03	0.375	0.005	A	1	22.03
375	0.0144	0.5457	0.03	0.375	0.005	A	1	21.67
376	0.0096	0.5211	0.03	0.385	0.005	A	1	15.38
377	0.0115	0.5376	0.03	0.385	0.005	A	1	17.94
378	0.0144	0.5355	0.03	0.385	0.005	A	1	21.35
379	0.0164	0.5415	0.03	0.385	0.005	A	1	20.23
380	0.0079	0.5760	0.02	0.385	0.005	A	1	13.74
381	0.0097	0.5190	0.02	0.385	0.005	A	1	16.11
382	0.0118	0.5283	0.02	0.385	0.005	A	1	19.90
383	0.0140	0.5349	0.02	0.385	0.005	A	1	21.96

Q-Discharge; h-Head; x-Distance of runner to wedge/accelerator channel; y- Distance of runner to channel bed; z-Distance of runner to spillway; E-Efficiency

Appendix B

Turbine Manufacturing

Spillway turbine rotors, the inserts and Design I wedges were manufactures from a polyamide powder using selective laser sintering (SLS) technique. The manufacturing was completed internally, in the MEC laboratories at Cardiff University. This 3D printing technique has several advantages, such as fast manufacturing time and low production costs. The SLS process is shown in Figure B.1 (Runge, 2018).
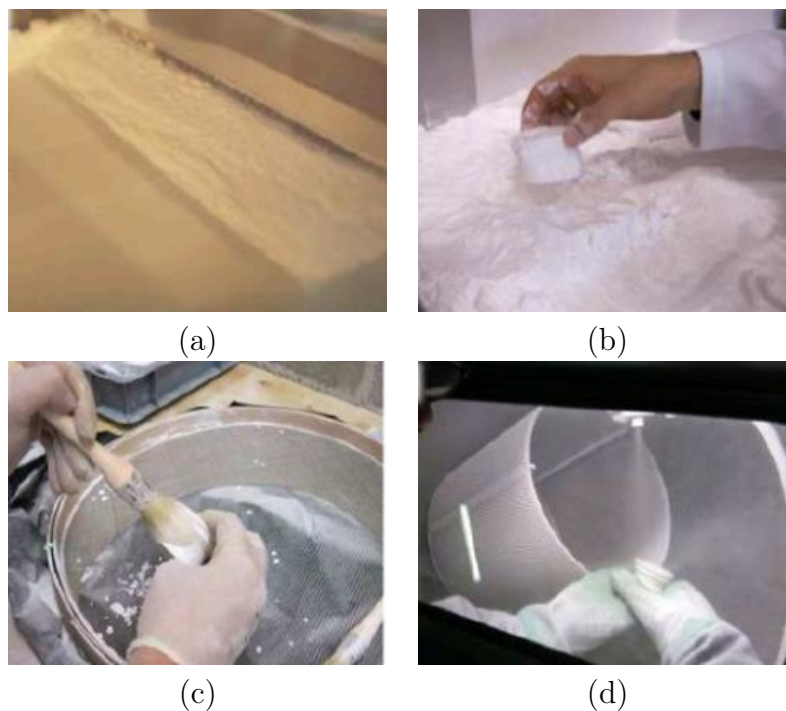
FIGURE B.1: (a) Sinter process ; (b) Object Removal ; (c) Brushing ; (d) Sandblasting (Sculpteo.com , 2020)

Firstly, a polymer powder is placed into the process chamber. A laser then scans a very thin layer of powder, joining powder particles in a shape of the desired shape. This is called sintering of the first 3D layer of the shape. This process is repeated for the next layer of the part, which joined to the first layer and made

into a solid section. This is shown in the sinter process B.1. The next step is to remove the object made from sintering. Brushing and sandblasting is finally used on the shape to remove loose powder particles, resulting in a smooth solid object. The materials properties of PA2200 powder used were summarised in Table B.1.

TABLE B.1: Material Properties PA 2200

General Material Properties			
Acrylic grain size	ISO 13320-11	56	μm
	Laser diffraction	2.20	mil
Bulk Density	EN ISO 60	0.45	g/cm^3
Density of laser-sintered part	EOS method	0.93	g/cm^3
		58	lb/ft^3
Mechanical Properties			
Tensile modulus	EN ISO 527	1700	MPa
	ASTM D638	247	ksi
Tensile strength	EN ISO 527	48	MPa
	ASTM D638	6962	psi
Elongation at break	EN ISO 527	24	%
Elongation at break	ASTM D638	24	%
Flexural modulus	EN ISO 527	1500	MPa
	ASTM D638	217	ksi
Flexural strength	EN ISO 527	58	MPa
	ASTM D638	8412	psi
Charpy-Impact strength	EN ISO 179	53	kJ/m^3
Charpy-Notched impact strength	EN ISO 179	4.8	kJ/m^3
Izod-Impact strength	EN ISO 180	32.8	kJ/m^3
Izod-Noticed impact strength	EN ISO 180	4.4	kJ/m^3
Ball indentation hardness	EN ISO 2039	78	N/mm^2
Shore D-hardness	EN ISO 868	75	-
	ASTM D2240	75	-
Thermal Properties			
Melting point	EN ISO 11357-1	172-180	°C
Vicat softening temperature B/50	EN ISO 306	163	°C
	ASTM D1525	325	°F
Vicat softening temperature a/50	EN ISO 306	181	°C
	ASTM D1525	358	°F

Appendix C

Field Application

C.1 Testing Site

The Spillway turbine design was planned for field testing on a site located in North Carolina, US. The testing permit was obtained for a privately owned property of the East Fork Road, Brevard County in North Carolina. Satellite map view of the area is shown in Figure C.1.

FIGURE C.1: Satellite view of testing site area

A Laurel Branch stream is present on-site and a water run-off channel was to be designed to test the spillway turbine. The design flow rate is estimated to be 100 l/s, and an overview of the site is shown in the Figure C.2.

The design of the spillway turbine intended for field testing is the optimised runner design described in Design III section shown in Chapter 4. The accelerator channel design was revised according to the conclusions made in the numerical modelling section. Therefore, the runner with 2 cup inserts was scaled to fit the site specifications, and the accelerator channel was designed to have a 6 ° contraction angle.

FIGURE C.2: Visualisation of the site including the two-section
flume next to the stream and two spillway turbines

C.2 Flume Construction

The flume (Figure C.3) is to be constructed for the purpose of testing the spillway turbine on-site in North Carolina. The flume will be constructed next to an existing stream of water, the Laurel Branch, and its water will be used to drive the turbine runners. The flume is to be constructed from treated wood and it will be supported by five steel frames placed on concrete foundations. The wooden flume will follow the stream's course along its right bank and will comprise of two main sections which are connected by a transition.

The constructed flume will have two main sloping sections, in accordance with the topography of the site, as shown in Figure C.4. Section 1 is the section that will be connected to the planned pipe inlet and section 2 is downstream of an approximately horizontal section of the stream and includes the outlet that returns the water back to the stream. Detailed dimensions of the flume are given in section C.3 and turbine positions along the constructed flume are shown in C.4.

The flume will be supported through concrete foundations linked to steel beam supports. The foundations are planned to be 1 m wide, 1 m long and 0.3 m deep squares of concrete, but can be adapted to fit site conditions. Anchorage of concrete squares to the bedrock and steel reinforcements are also recommended.
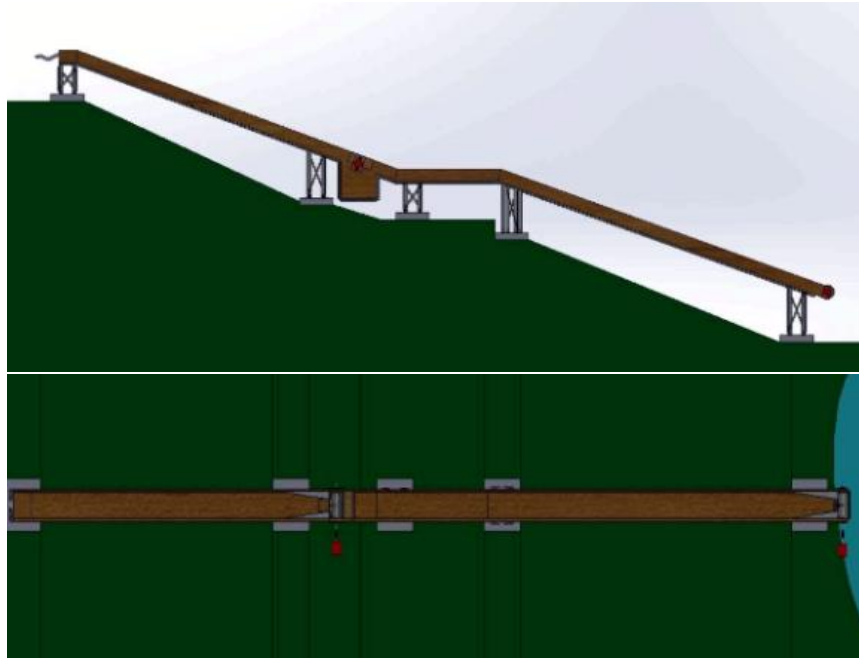
FIGURE C.3: Flume side (top) and top (bottom) views
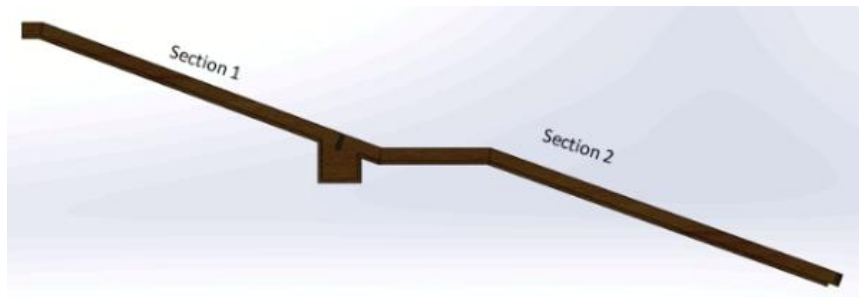
FIGURE C.4: Flume sections

The flume is to be bolted to the steel via steel rails mounted underneath the flume. The detailed dimensions of steel supports, steel rail and attachments are shown in section C.6.

C.3   Flume Dimensions

The general flume design was presented in the previous section and the detailed dimensions for sections 1 side view, section 2 side view, the entire flume side view and the flume top view are given in Figures C.5, C.6, C.7 and C.8 respectively.

Drawing of the side view of section 1 shows that the flume will have walls of 0.35 m height. The inlet was designed to be 0.56 m long but can be adjusted to fit site topography. After the inlet, the first sloping section stretches for 9.45 m. The height difference between section 1 starting and end points is around 3.5
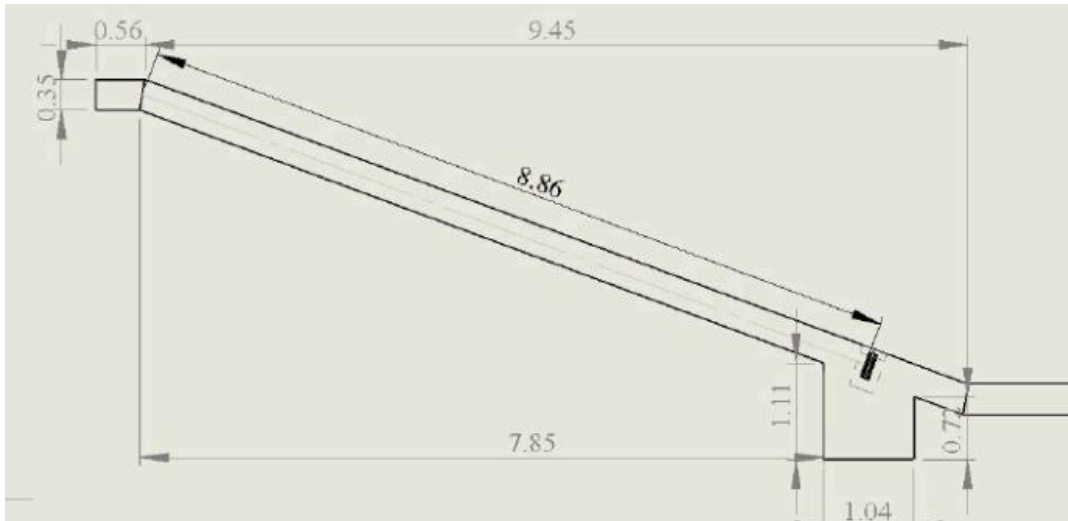
FIGURE C.5: Flume section 1 side view; all dimensions in metres

m. A box for water collection will be constructed 8.37 m downstream from the inlet. The box is 1.11 m deep and 1.0 m wide. Steel frame supports are placed just before and just after the collection box to keep the flume above ground.
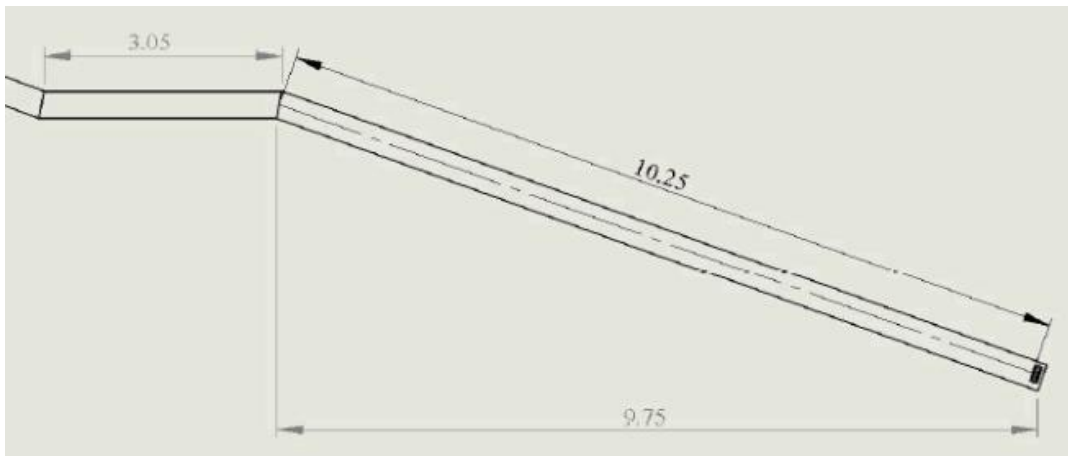
FIGURE C.6: Flume section 2 side view; all dimensions in metres

The second sloping section stretches for 9.81 m as shown in Figure C.6. The water collection box is not necessary in this section, as the water will go to outlet after hitting the second runner. The height difference from section 2 start and end points is 3.5 m. Two steel supports will be used for slope 2, one at the beginning of the section and one just after the collection box.

As it can be noted from Figure C.7, sections 1 and 2 are connected by a 3.04 m section that is almost straight. Section 2 will finish with the water spilling back to the stream.
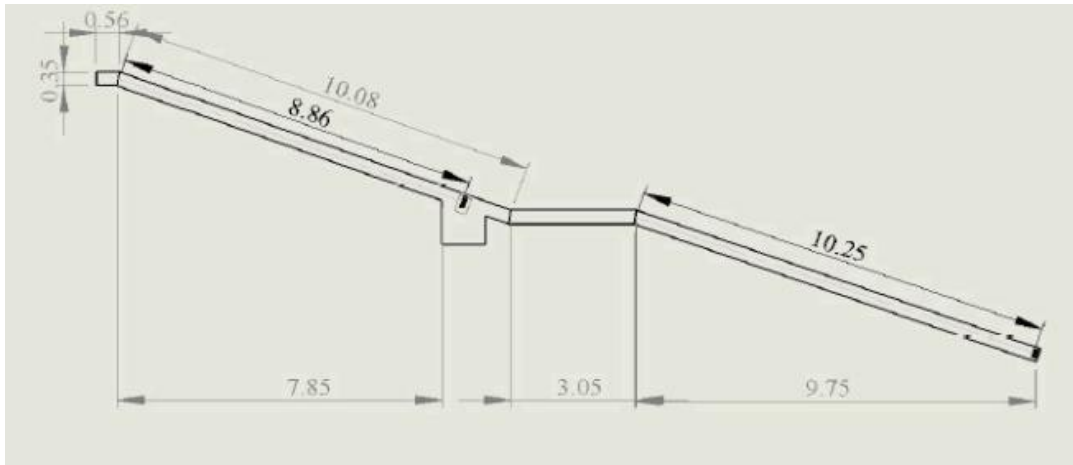
FIGURE C.7: Entire flume length side view; all dimensions in metres
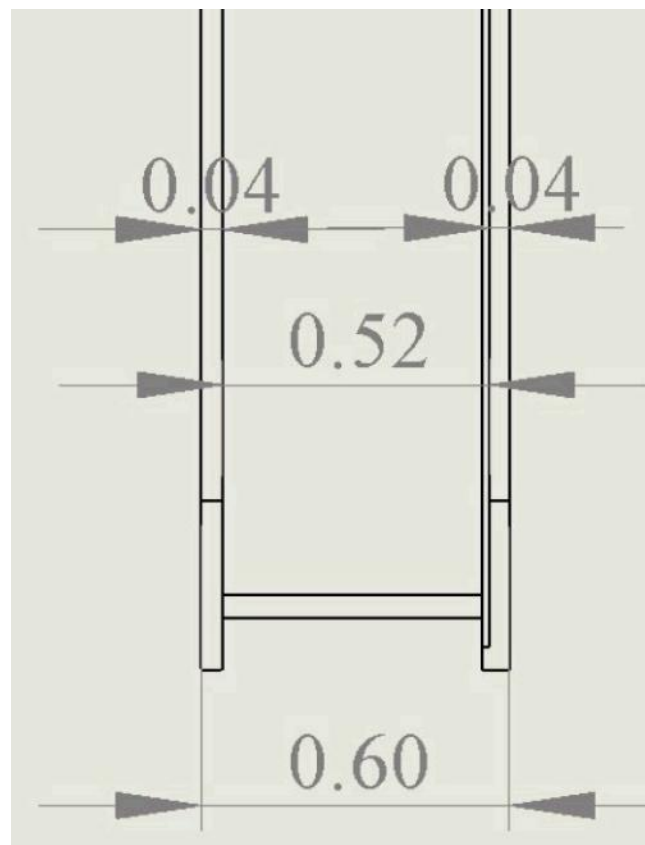
FIGURE C.8: Flume top view, width of channel and walls; all dimensions in metres

The wooden flume is 0.6 m wide with walls of 0.04 m thickness as shown in Figure C.8. The total channel width is 0.52 m which will fit a 0.5 m wide runner with discs and bolts inside the channel.

C.4 Turbine Positions Along the Channel

Slots were cut into the flume sidewalls so bearings can be mounted to keep the runners in place. The exact location of the slots needs to be determined once the flume is fully constructed. The approximate dimensions and positioning of the slots is shown in figures below.
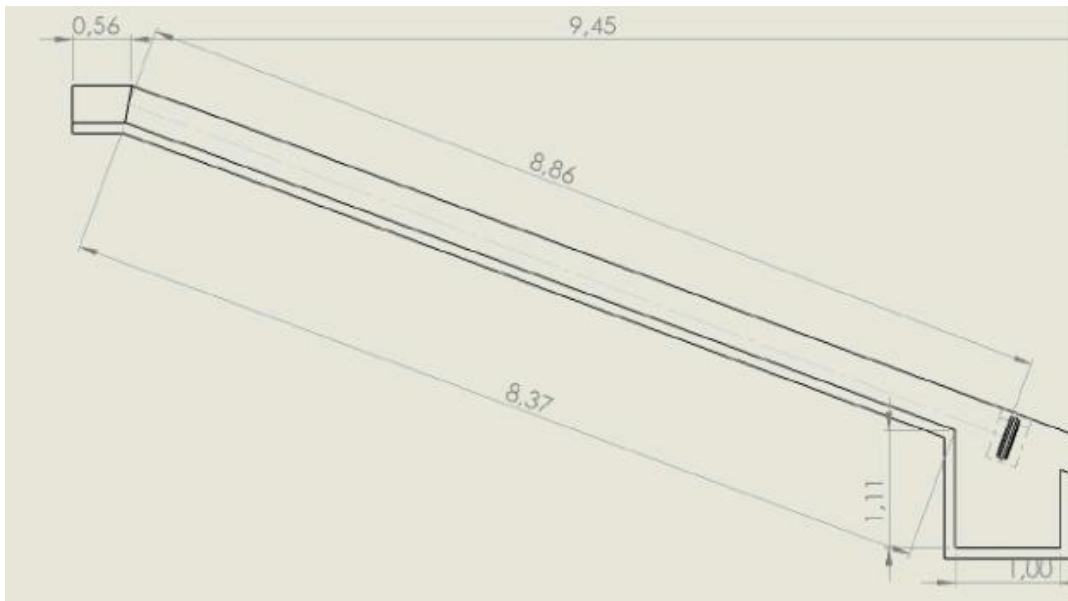
FIGURE C.9: Section 1 flume side view with the position of the slots for runner placement and box placement distance; all dimensions in metres
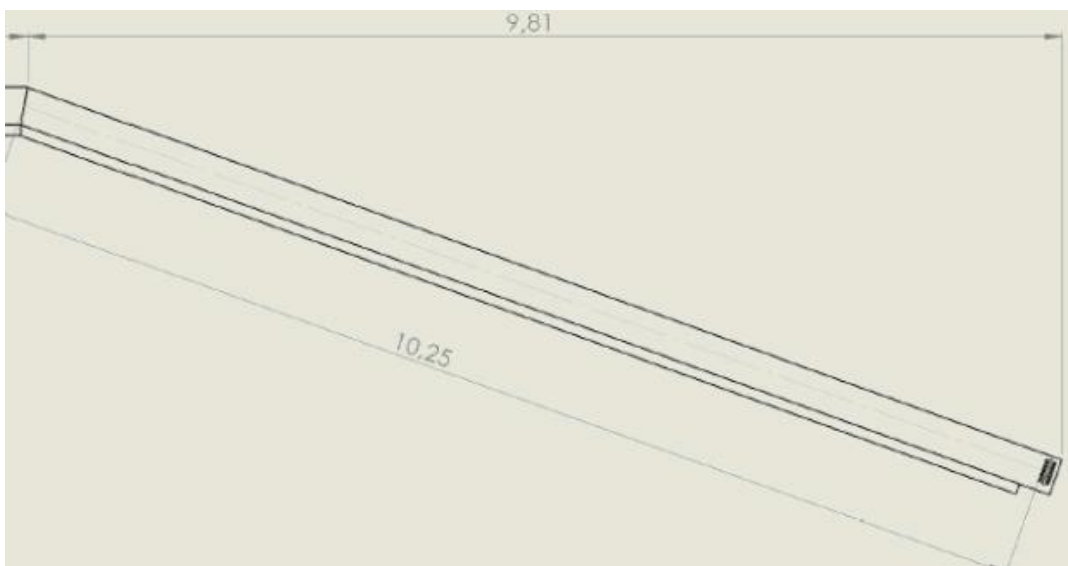
FIGURE C.10: Section 2 flume side view with the position of the slots for runner placement and box placement distance; all dimensions in metres

Turbine slots in the wooden frame shell be reinforced with metal plates presented in Figure C.11. The plates will have a thickness of 0.04 m.
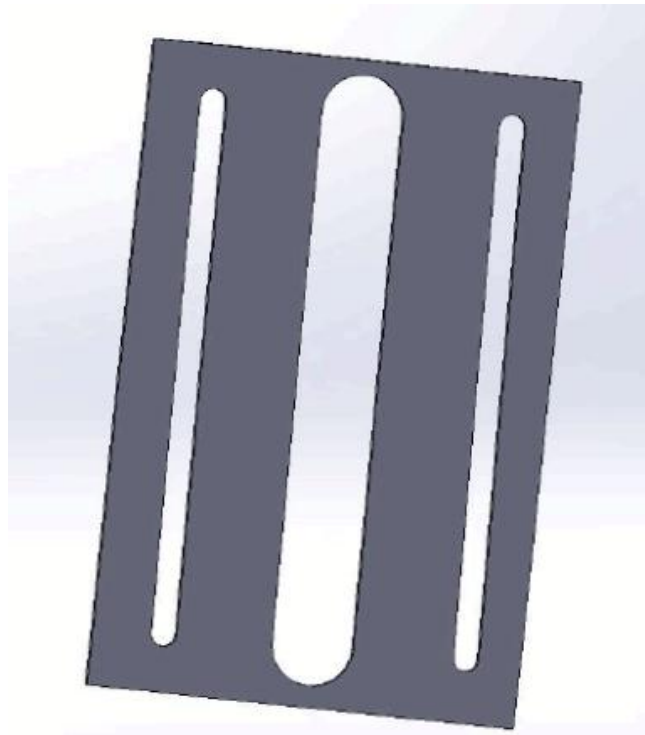
FIGURE C.11: Metal reinforcement for flume sections with runner slots

The slot dimensions are the same for both sections. The slots are 0.4 m long. The middle slots are cut to fit a 0.06 m diameter shaft. The distance from the middle slot to the bearing slots is 0.075 m. The width of the bearing slots is 0.02 m which are used to mount the bearings that hosts the shaft.
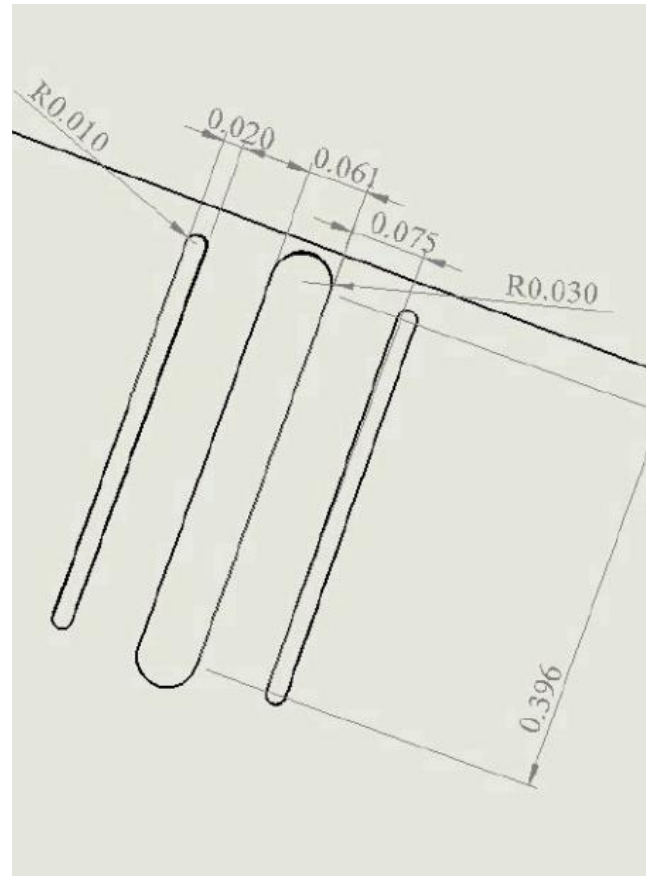
FIGURE C.12: Slot dimensions for runner installation

C.5 Accelerator Channel Design and Placement

From the conclusions made from the numerical simulation of turbine intake hydrodynamics, it was decided that the accelerator channel will entail a 6 ° contracting walls, as shown in Figure C.13. The contracting walls will be placed directly before the runner to accelerate and direct the flow towards the runner blades. The suggested material for the accelerator wedge is steel or acrylics.

The detailed design of the contraction is given in Figure C.14. The contraction consists of 2 triangular sections of 1.43 m length and 0.14 m width. The height of the wedge sections matches the height of the flume. The contractions are designed to be hollow sections with a horizontal reinforcement in the middle. The accelerator channel contraction connection to the flume is given in Figure C.15. Three brackets depicted in Figure C.16 will be used for each contraction, and bolts will be used for the upstream ends of the contractions.
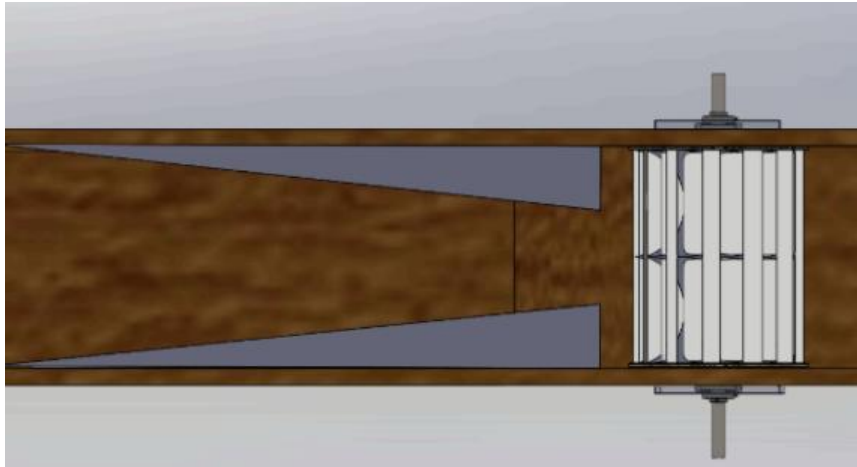
FIGURE C.13: Contracting accelerator channel
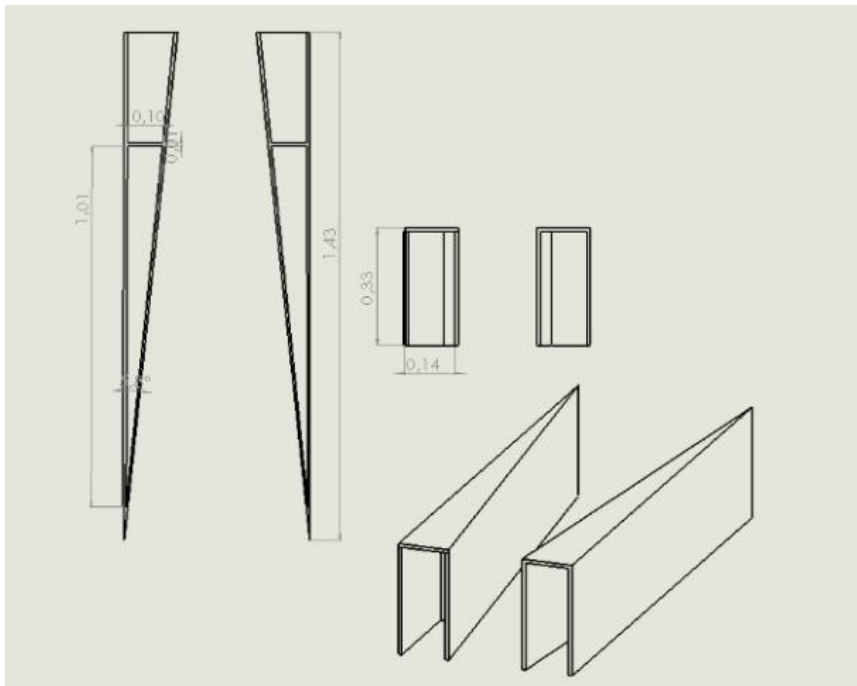
FIGURE C.14: Contracting section dimensions
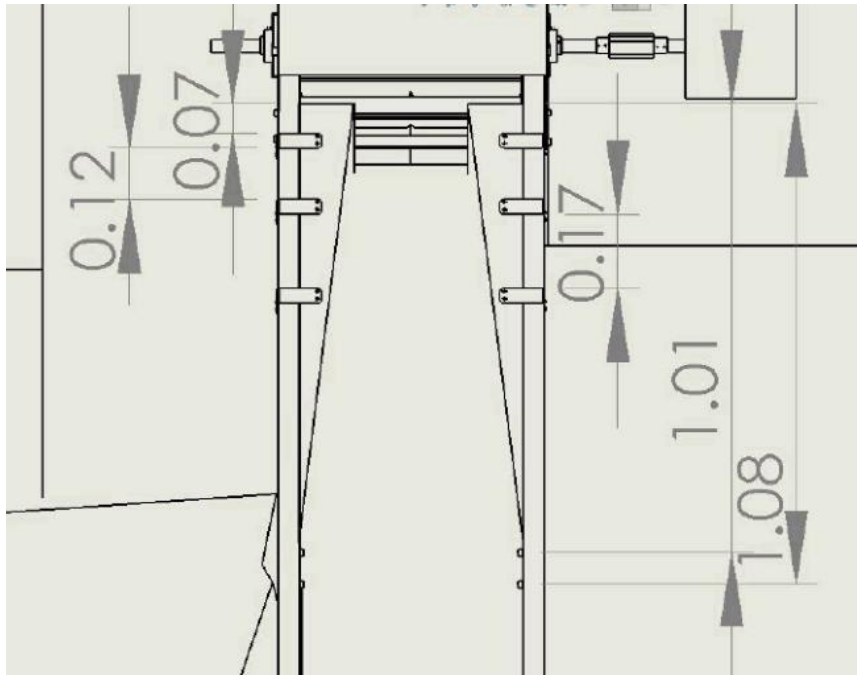
FIGURE C.15: Contraction to flume connection; all dimensions in meters
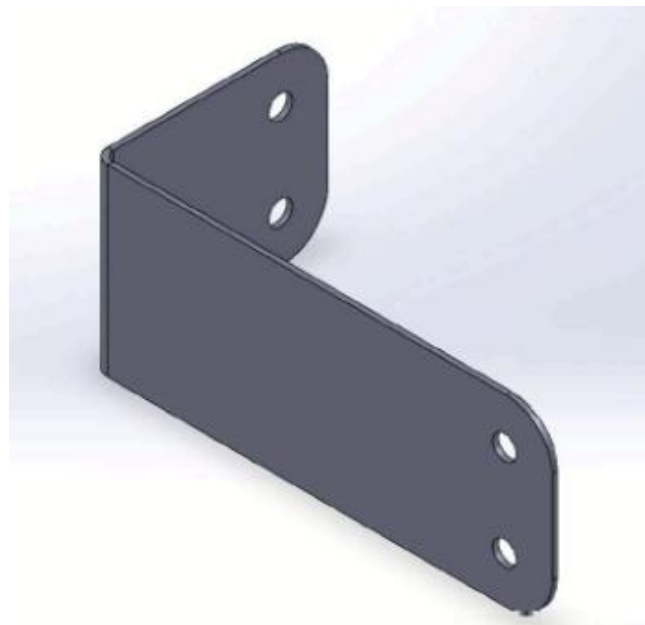
FIGURE C.16: Contraction connection L-bracket

C.6   Support Structure

The steel frame is designed to have a main beam length of 0.9 m for flat sections, and can be extended for sloping sections depending on exact site topography. The support consists of 8 L-shaped steel beams of 0.04 m depth and 0.1 m width. The columns in the steel supports are connected by mild-steel bars of the same dimensions.

The steel railing was composed of 2 T-profile steel beams and run along the entire flume length. It was connected to the flume through countersunk M16 screws. Countersunk holes are created along the steel section going from the face of the beams through the wood. The hole depths were 0.07 m.
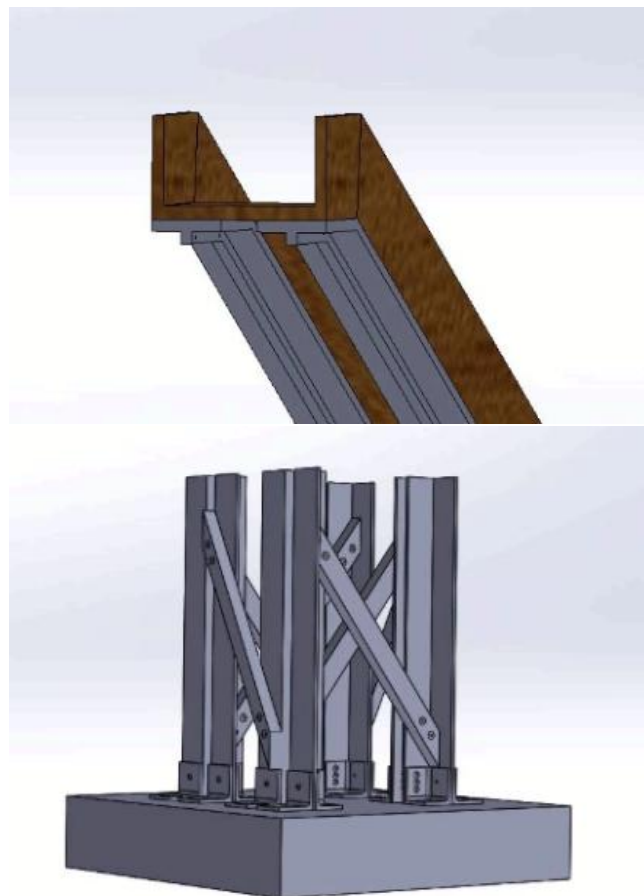
FIGURE C.17: Steel support (top) and T-section steel rail (bottom)

The steel support was connected to the concrete foundations through 2 types of steel brackets. Steel to concrete connection was made with countersunk screws and steel to steel connections were achieved with bolts, as shown in Figure C.18. As previously described, steel frames will be used to support the flume and

FIGURE C.18: Steel to steel and steel to concrete connections

support rails will be attached to the bottom of the flume to provide reinforcement and an attachment point for the support rails. The T-shape section rails run along the entire flume and detailed drawing of the dimensions is shown in Figure C.19.
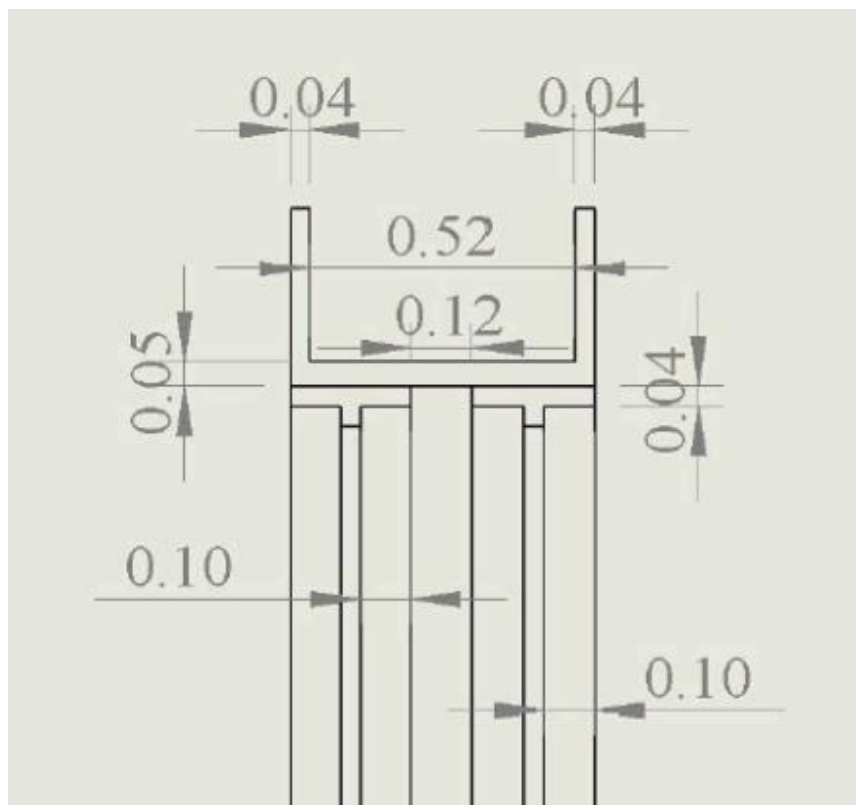
FIGURE C.19: T-shape steel sections run along the flume bottom; all dimensions in metres

The steel frame dimensions are depicted in Figure C.20. The main beam length is 0.9 m for flat sections but will be extended for sloping section according to the site topography. The support consists of 8 L-shaped steel beams of 0.04

m depth and 0.1 m width. The columns are connected by mild steel bars of similar dimensions,
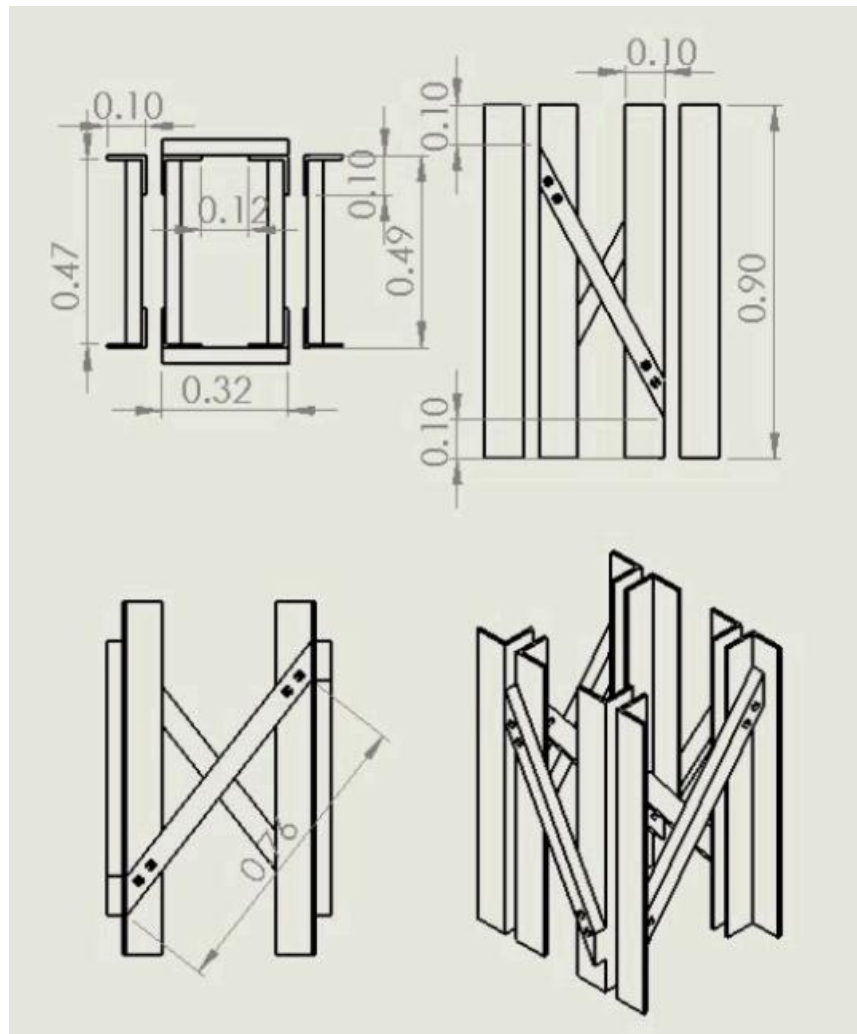
FIGURE C.20: Steel support; all dimensions in metres

C.7   Flume Support Connections

The steel rail composed of 2 T-shape profile steel beams, running along the entire flume length will be screwed to the wooden flume. Countersunk holes were created along the steel section, stretching from the face of the beams through the wood. The hole depths are 0.07 m and the positions are shown in Figures C.21, C.22 and C.23. The holes are placed 0.15 m from the sharp edges and are 0.5 m apart. The holes are placed in the middle of the T-section rails sides, 0.05 m from the edges. Countersunk M16 screws of 0.07 m length were used for attachment.
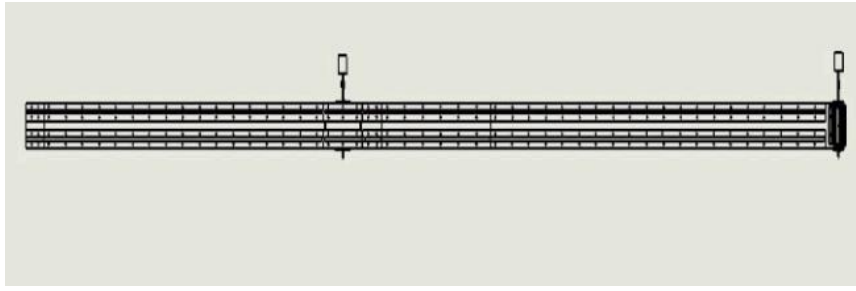
FIGURE C.21: Support rail with hole positions; bottom view
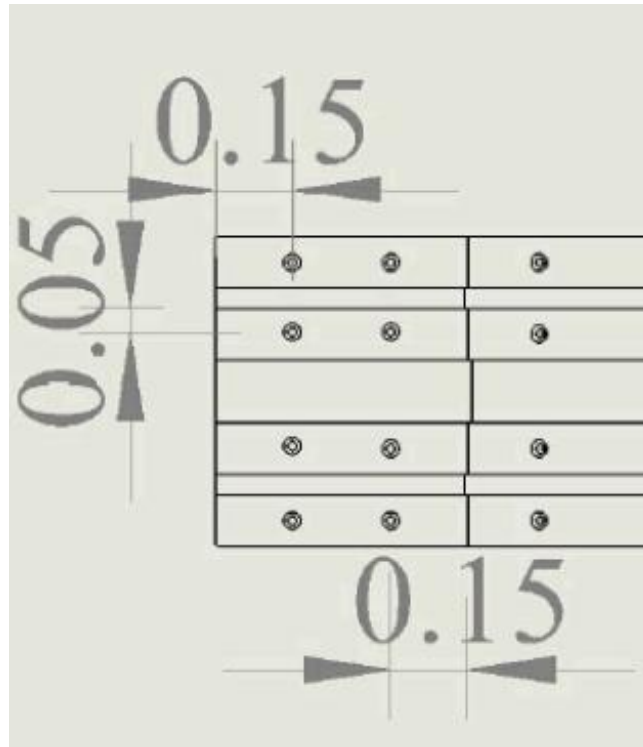
FIGURE C.22: Positioning of screw holes close to the edges

The steel support was connected to the concrete foundation through 2 types of steel brackets. Steel to concrete connection was achieved with countersunk screws and steel to steel connection was achieved through bolting, as shown in figures below.

The screws used to attach both brackets to the concrete foundations had slots in the middle of the bracket, 0.03 m from the sides. Countersunk hex head M8 screws, 0.2 m long were used in all 8 locations, with total of 16 concrete to steel screws.

M6 bolts were used to attach the tops of brackets 1 to the L section steel beams. The positions of the hole was in the centre of the top bracket side. M6 bolts with 0.04 m depth were also used in the bracket 2 to L-steel connections, with 3 bolts in series, 0.02 m apart from each other. The steel support was attached
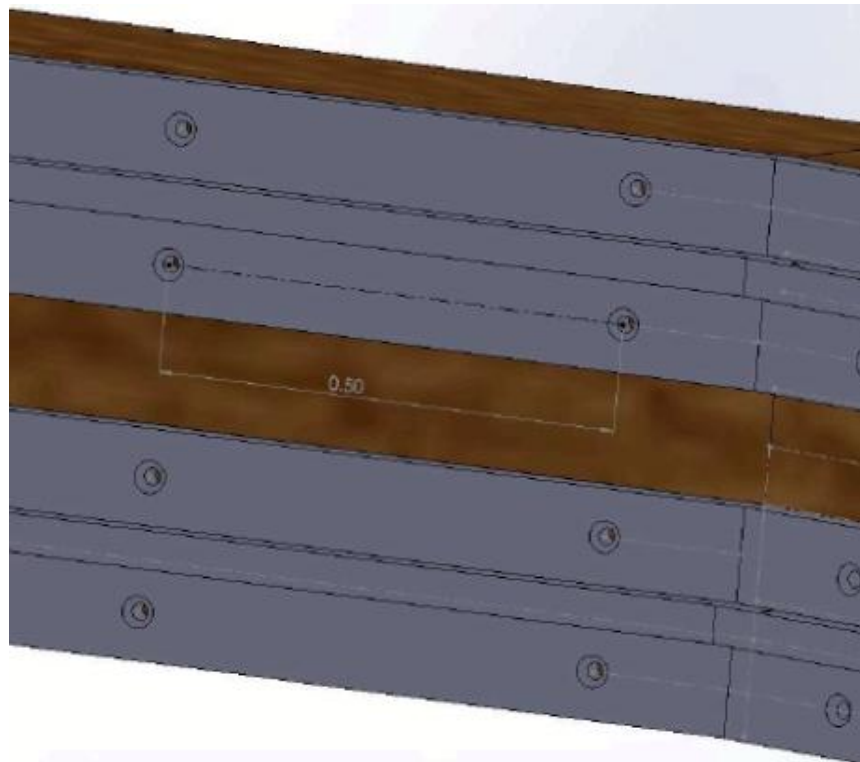
FIGURE C.23: Positioning of screw holes away from the edges

FIGURE C.24: Positioning of screw holes away from the edges

to the metal railing though M12, 0.07 m bolts as shown in Figure C.28
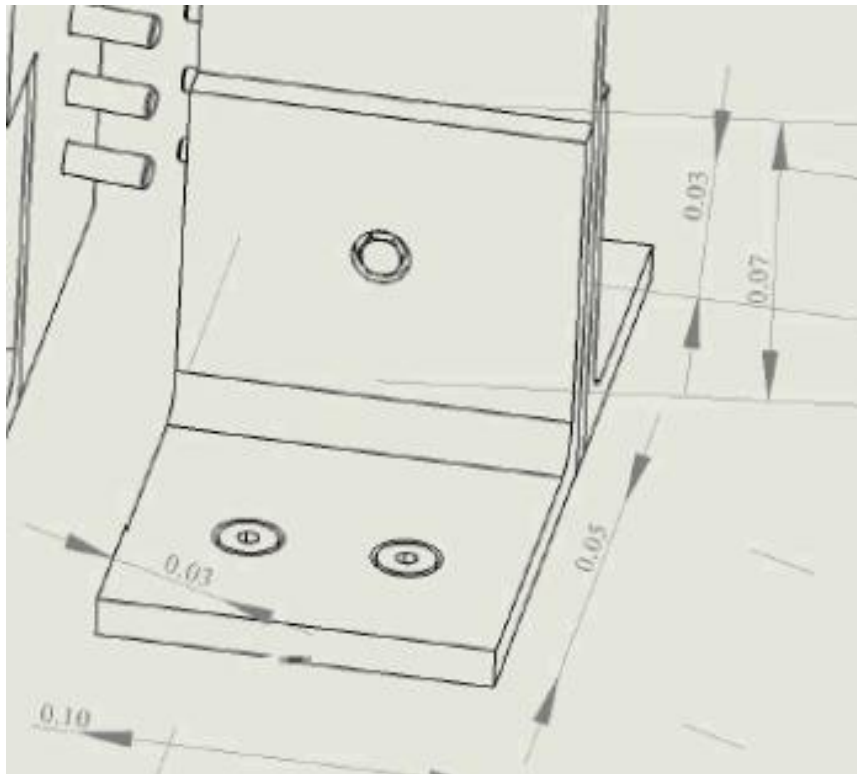
FIGURE C.25: Bracket 1, used on the outside of steel L-sections

FIGURE C.26: Overview of steel to steel and steel to concrete
connections
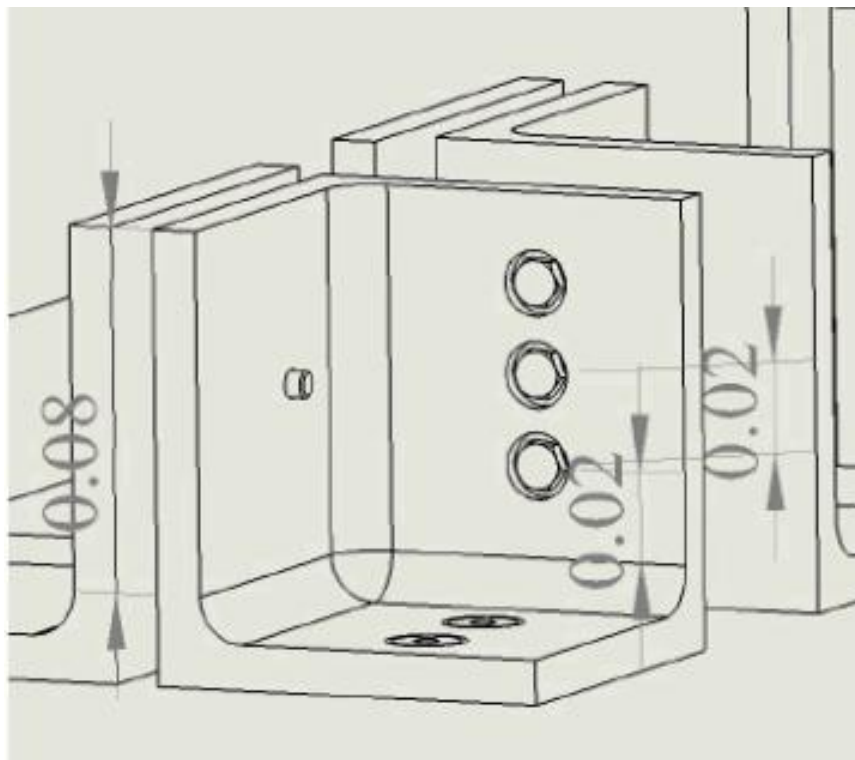
FIGURE C.27: Bracket 2, used on the inside of the steel L-sections
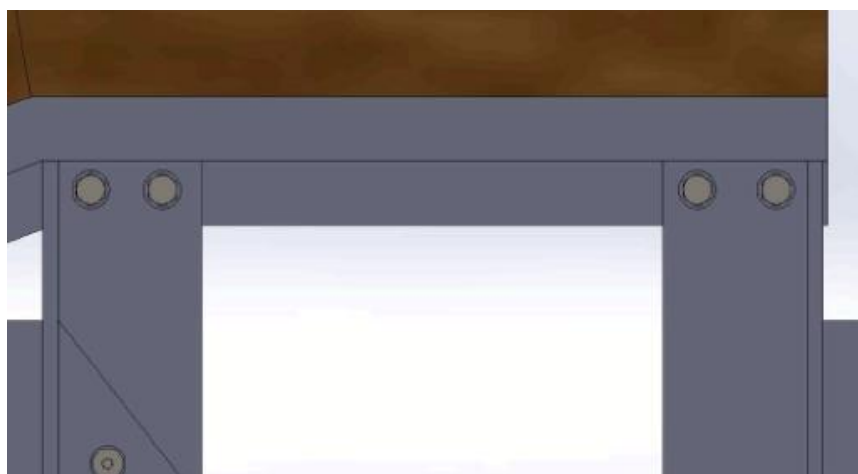
FIGURE C.28: Rail to steel support attachment

C.8 Bearings for Runner Attachment

Bearings needed to hold the runner shaft in position are given in Figure C.29. Detailed dimensions of bearings are given in Figure C.30
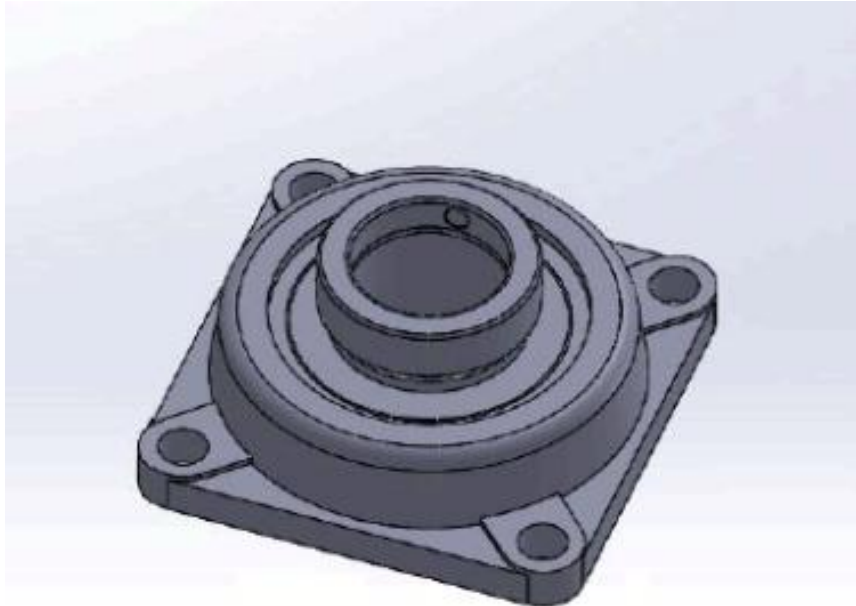
FIGURE C.29: Shaft bearing
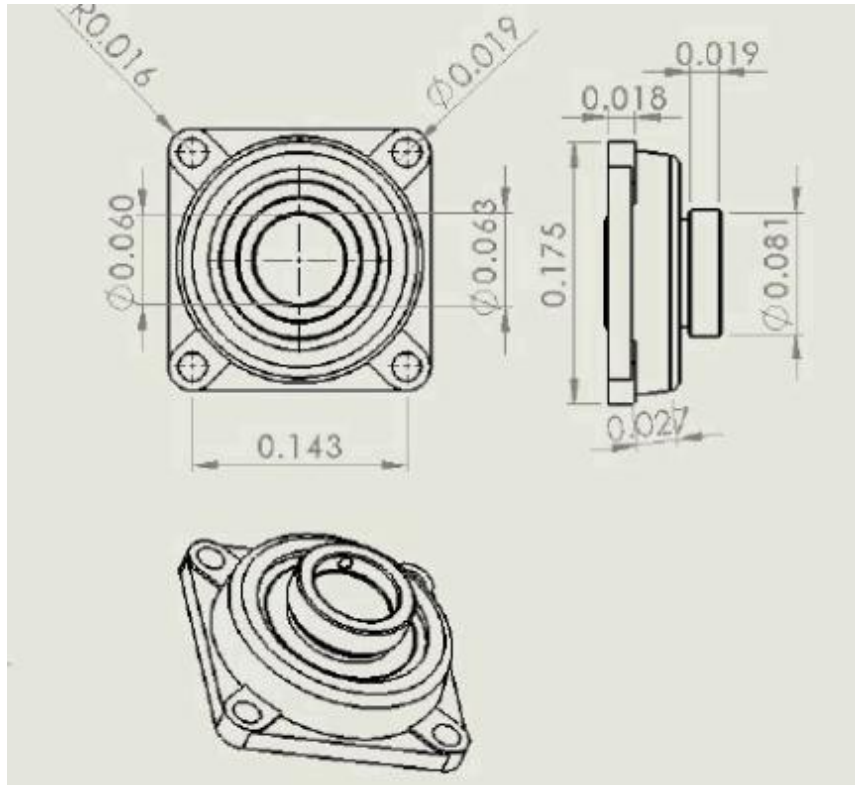
FIGURE C.30: Bearing dimensions; all in meters

C.9   Runner Shaft

The runner shaft is shown in Figure C.31. It features a key that connects the runner to the shaft and prevents the relative rotation between two parts still enabling torque transmission. The dimensions of the shaft are shown in Figure C.32.

The runner shaft is made of stainless steel and has 0.06 m diameter. The total length of the shaft is 0.7 m. The proposed key is of 0.05 m length and 0.008 m width. The slots for the shaft key will be cut into either side of the runner.

FIGURE C.31: Runner shaft, 0.06 m diameter stainless steel
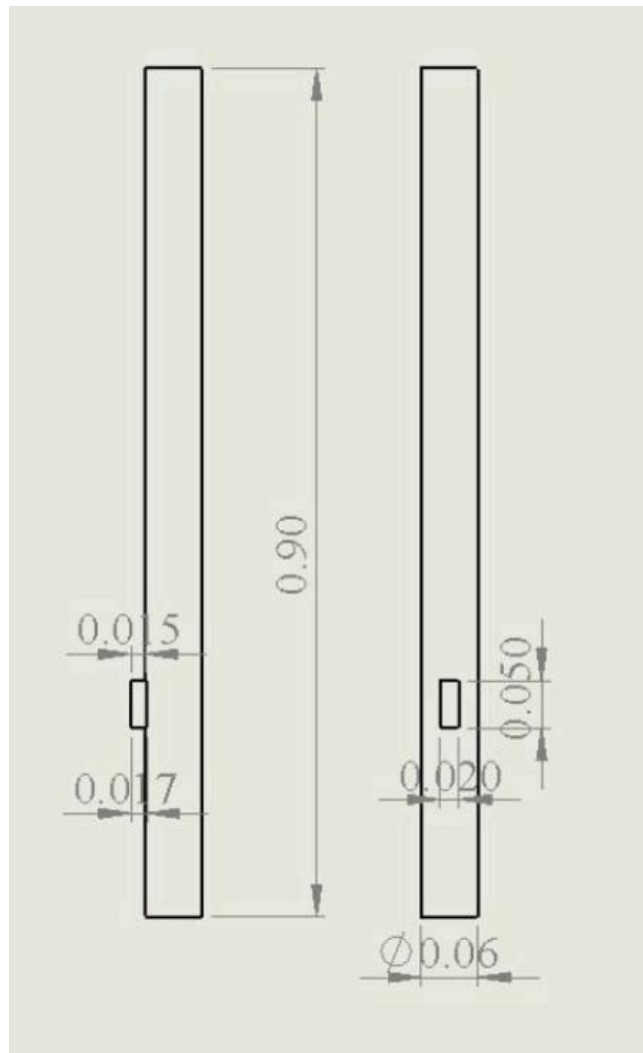
FIGURE C.32: Shaft dimensions; all in metres
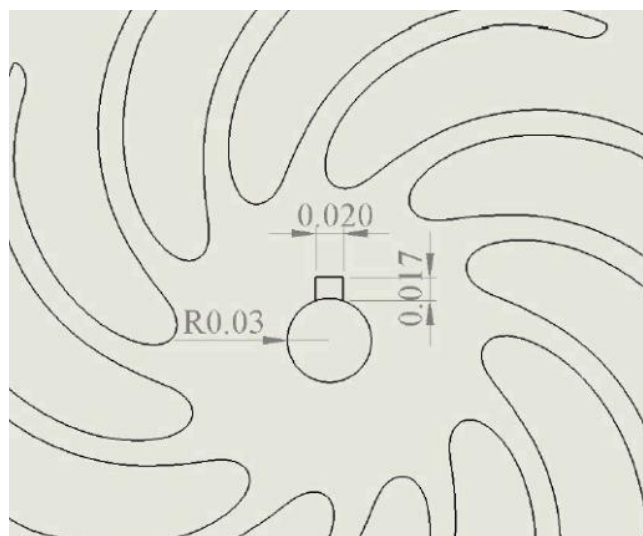
FIGURE C.33: Dimensions of shaft key slots in the runner; all in metres

C.10   Scaled Turbine Runners

The runners planned for field testing were designed according to runners tested in the laboratory. Two runners were manufactured for field testing, both with inserts presented in Chapter 4. As the diameter of the runner has been scaled to double of the original diameter and triple for Runner F1 and Runner F2 intended for field testing. As the diameter was scaled up, the number of blades was also scaled from 6 to 12 blades. The minimum blade clearance was kept above 0.1 m, as concluded from laboratory test analysis.

The F1 runner is a 12 bladed runner with 0.4 m diameter, 0.5 m length and a blade thickness of 0.01 m. The design and drawings of Runner F1 are shown in Figure C.34 and further disk and insert drawings with dimensions are shown in subsection C.10.1.

The F2 runner is also a 12 bladed runner with a 0.6 m diameter, 0.5 m length and 0.015 m blade thickness. As the laboratory set up and schedule did not allow for further runner re-design and testing, it was decided that a runner with a blade clearance of 0.15 m will be tested in field. This runner is given in Figure C.39, with detailed dimensions shown in subsection C.10.2

C.10.1   Runner F1

Runner F1 with 0.4 m diameter and 12 blades dimensions are given in figures below. Dimensions of runner inserts and disks are also presented.
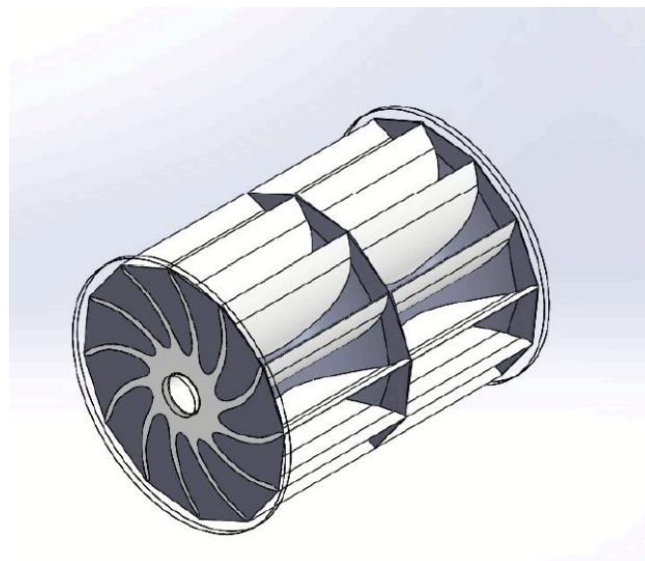

FIGURE C.34: 12 bladed, 0.4 m diameter runner
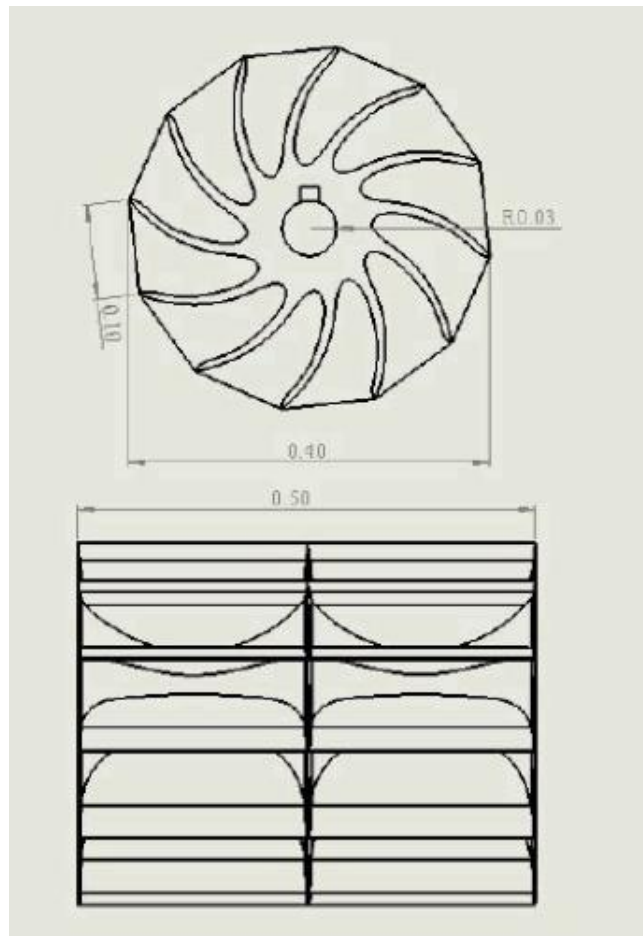
FIGURE C.35: 0.4 m diameter runner dimension; all in metres
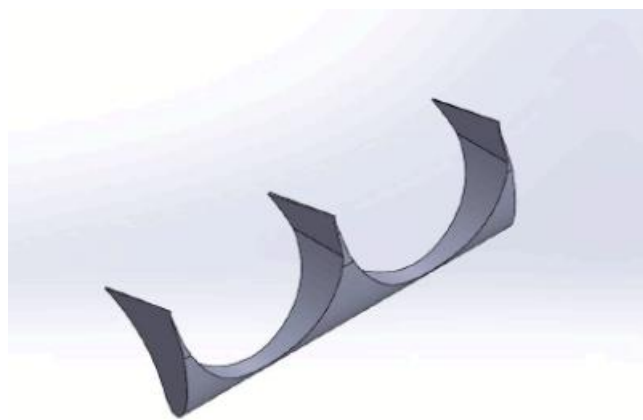

FIGURE C.36: Insert for Runner F1
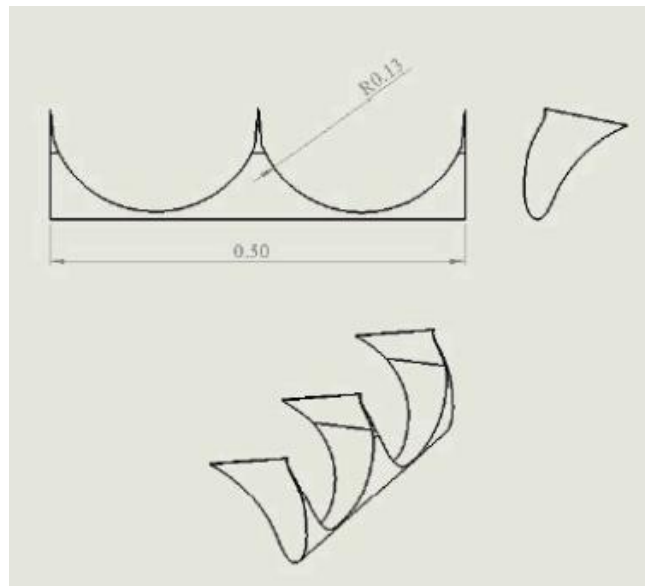
FIGURE C.37: Insert for Runner F1 dimensions; all in metres
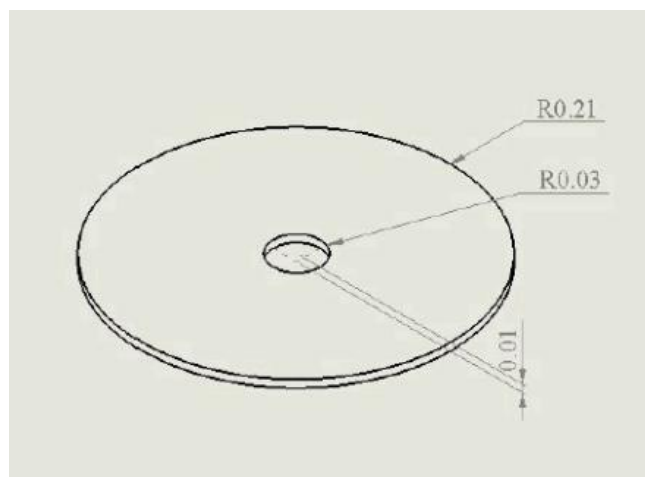
FIGURE C.38: Disks for Runner F1; all in metres

C.10.2   Runner F2

Runner F2 with 0.6 m diameter and 12 blades dimensions are given in figures below. Dimensions of runner inserts and disks are also presented.
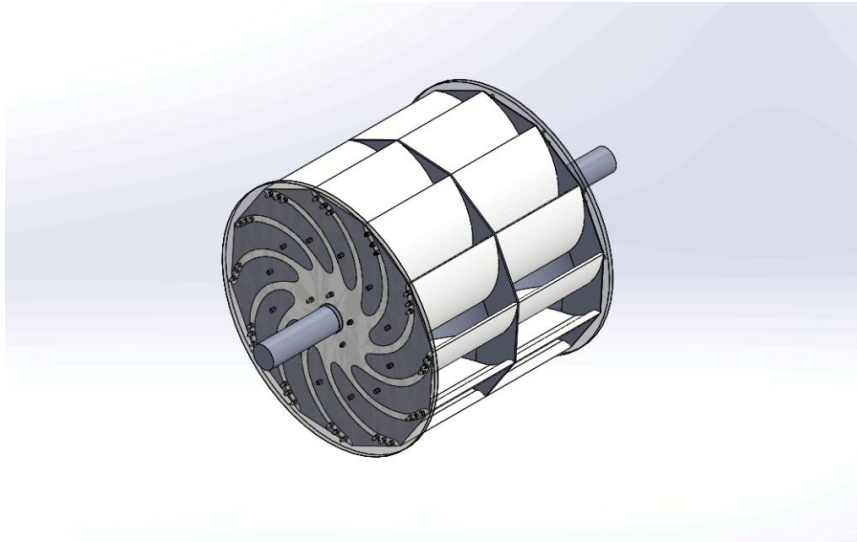
FIGURE C.39: 12 bladed, 0.6 m diameter runner
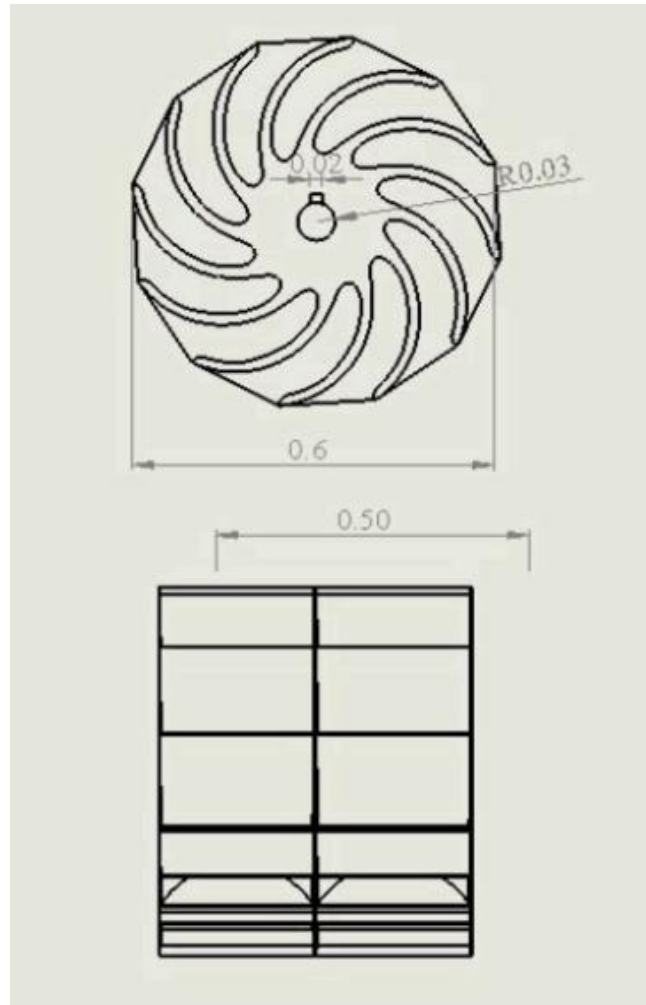
FIGURE C.40: 0.6 m diameter runner dimension; all in metres


FIGURE C.41: Insert for Runner F2
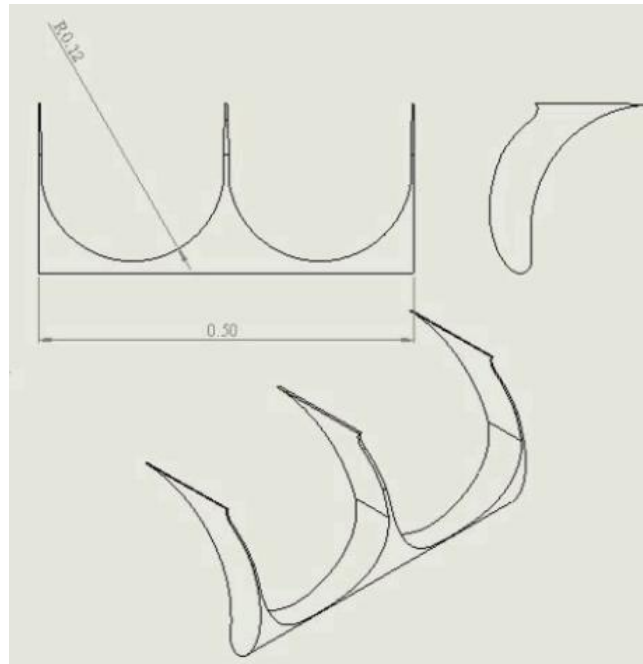
FIGURE C.42: Insert for Runner F2 dimensions; all in metres
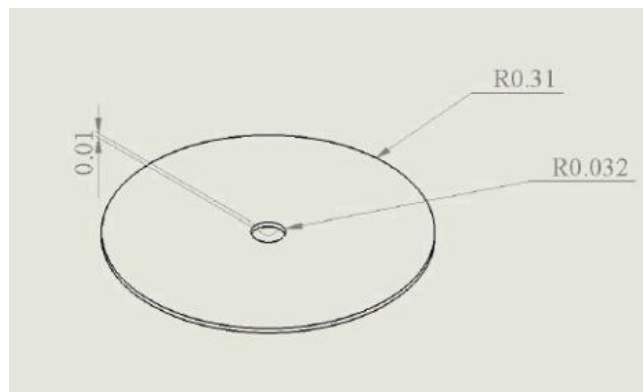
FIGURE C.43: Disks for Runner F2; all in metres

C.11 Splash Cover

A splash cover is required in the flume to protect the generator and a torque transducer from getting wet. The splash cover is made of acrylic and it is 0.002 m thick. The splash cover will be screwed to the flume and is easily removable, so easy access to the runner is assured.
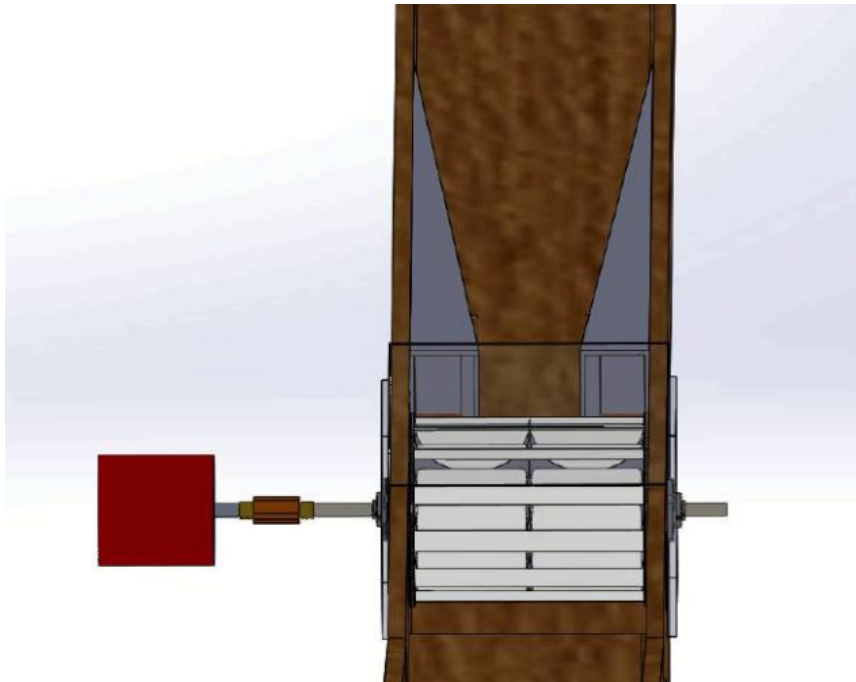
FIGURE C.44: Installed turbine system with a splash cover on top
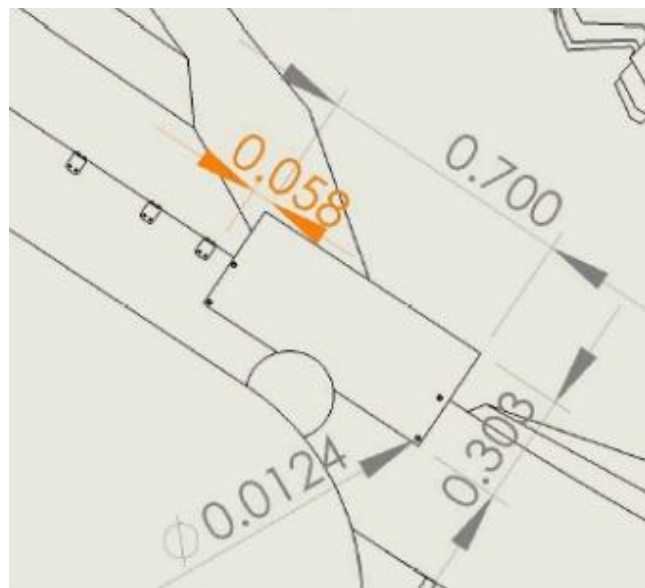
FIGURE C.45: Splash cover dimensions; all in metres

204

Appendix D

Technical Sheets
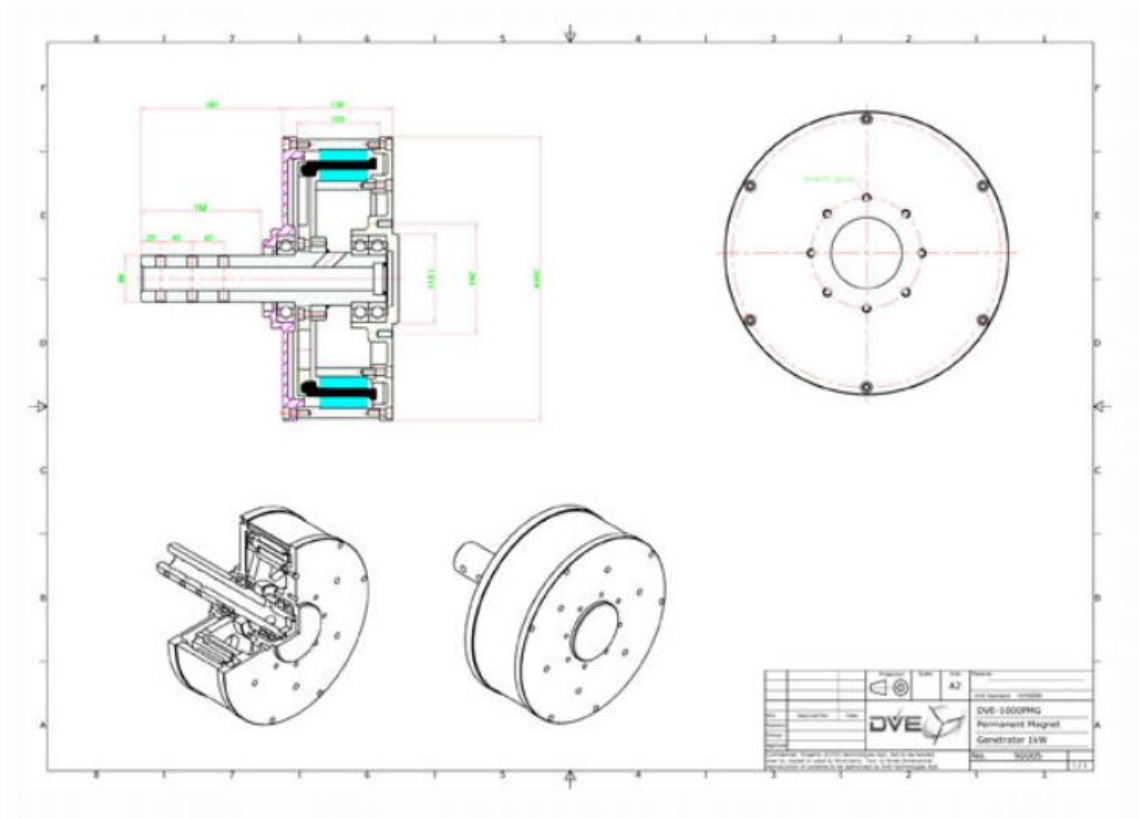
Figure D.1: DVE Generator

FUTEK
ADVANCED SENSOR TECHNOLOGY, INC.

MODEL TRS605
**Non-Contact Shaft-to-Shaft Rotary Torque Sensor
with Encoder**

FEATURES

- Utilizes strain gauge technology
- Angle speed feedback
- Compact size
- Can operate up to 7000 RPM

Active end

– Output (CCW)
+ Output (CW)
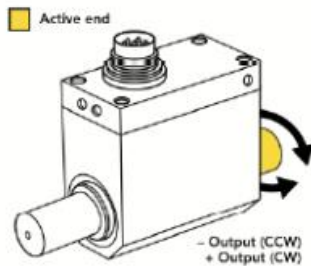
SPECIFICATIONS	
PERFORMANCE	
Nonlinearity	±0.2% of RO
Hysteresis	±0.1% of RO
Nonrepeatability	±0.2% of RO
Rotational Speed	7000 Max
ELECTRICAL	
Rated Output (RO)	±5 VDC
Excitation	11–26 VDC, 1 Watt
Connector	12 pin Binder Series #581 (09-0331-90-12)
MECHANICAL	
Safe Overload	150% of RO
Zero Balance	±1% of RO
Material	Aluminum (Housing), Steel Alloy (Shaft)
IP Rating	IP40
TEMPERATURE	
Operating Temperature	–13 to 176°F (–25 to 80°C)
Compensated Temperature	41 to 122°F (5 to 50°C)
Temperature Shift Zero	±0.01% of RO/°F (±0.02% of RO/°C)
Temperature Shift Span	±0.01% of RO/°F (±0.02% of RO/°C)
CALIBRATION	
Calibration Test Excitation	12 VDC
Calibration (standard)	Certificate of Conformance
Calibration (available)	5 pt CW & CCW
Shunt Calibration Value	With sensor fully connected apply 11–26 VDC to Pins A & K to generate 5 VDC nom output
ENCODER	
Output	Impulse (TTL)
Pulses per Revolution	2 × 360
Excitation	5 VDC, 40 mA max
Angle 1	Leading Pulse
Angle 2	Trailing Pulse (90°)
CONFORMITY	
RoHS	2014/30/EU
CE	Declaration of Conformity

Sensor Solution Source
Load - Torque - Pressure - Multi-Axis - Calibration - Instruments - Software

www.futek.com

CE RoHS ANSI 2540-1 ISO 17025 ISO 9001 ISO 13485 U.S. Manufacturer

FIGURE D.2: Futek Torque and Encoder